Development of a 10 J, 10 Hz sub-picosecond CPA laser based on Yb^{3+} doped gain media

The PFS pump laser

Mathias Krüger

München 2021

Development of a 10 J, 10 Hz sub-picosecond CPA laser based on Yb^{3+} doped gain media

The PFS pump laser

Mathias Krüger

Dissertation
an der Fakultät für Physik
der Ludwig–Maximilians–Universität
München

vorgelegt von
Mathias Krüger
geboren in Suhl

München, den 10.05.2021

Erstgutachter: Prof. Dr. Stefan Karsch
Zweitgutachter: Prof. Dr. Malte Kaluza
Tag der mündlichen Prüfung: 06.07.2021

To my beloved family

Zusammenfassung

Der Petawatt-Field-Synthesizer (PFS) wurde am Max-Planck-Institut für Quantenoptik (MPQ) mit dem Ziel entwickelt, Lichtpulse zu erzeugen, welche eine zentrale Wellenlänge von ~900 nm besitzen, eine Energie von bis zu 500 mJ, eine Pulsdauer von 6 fs sowie eine Wiederholrate von 10 Hz. Mit diesen Lichtpulsen sollen Intensitäten im Strahlfokus von bis zu 10^{20} W/cm^2 erreicht werden, mit einem zeitlichen Kontrast von mehr als 10^{11}. Die Hauptanwendung ist die Erzeugung von hoch-energetischen, isolierten Attosekundenpulsen durch die Wechselwirkung der Lichtpulse mit einem Plasma auf Festkörperoberflächen.

Das Kernelement des PFS Systems sind mehrere Verstärkerstufen, die auf dem Prinzip der optischen parametrischen Verstärkung gestreckter Pulse (OPCPA) basieren. Die vorliegende Dissertation behandelt die Entwicklung eines Lasers, welcher die einzelnen OPCPA Stufen auf einer Zeitskala von einer Pikosekunde pumpt. Das Ziel dieses "Pumplasers" ist die Erzeugung von Lichtpulsen mit 10 J, 10 Hz und 1 ps bei einer Wellenlänge von 1030 nm. Darüber hinaus müssen diese Pulse auf 515 nm konvertiert werden, mit einer Restenergie von mindestens 4 J. Da ein Laser mit solchen Parametern kommerziell nicht erhältlich ist, musste der gesamte Pumplaser als Eigenentwicklung gebaut werden.

Die zunächst Pikosekunden langen Pulse werden auf mehrere Nanosekunden gestreckt, bevor in verschiedenen Laserverstärkern die Pulsenergie erhöht wird. Die Verstärker des Pumplasers beinhalten ausschließlich Verstärkermedien, welche mit Ytterbium dotiert sind. Diese Medien ermöglichen eine effiziente Speicherung von Energie mit Hilfe von Diodenlasern. Darüber hinaus reduzieren sie die Anforderungen an die Kühlung deutlich im Vergleich zu klassischen Verstärkermedien, die mit Titan oder Neodym dotiert sind. Ytterbium dotierte Medien besitzen zudem eine spektrale Bandbreite der Verstärkung, welche eine komprimierte Pulsdauer von weniger als einer Pikosekunde erlaubt.

Diese Dissertation behandelt die Umsetzung von drei neuen Laserverstärkern. Der Schwerpunkt liegt auf der Wahl geeigneter Verstärkermedien sowie deren Kühlung, und auf der Entwicklung von opto-mechanischen Systemen. Hieraus sind mehrere, essenzielle Technologien entstanden. Yb:KYW wird als vergleichsweise untypisches Verstärkermedium für hohe Energien in einem Vorverstärker eingesetzt. Die hiermit erzeugten, besonders breitbandigen Pulse ermöglichen eine effiziente Kompensation der Verschmälerung des Spektrums im Yb:YAG basierten Hauptverstärker. Die Verstärkermedien werden in Wärmesenken gehaltert, welche vakuum-injiziertes Flüssigmetall enthalten. Hierdurch wird eine effiziente Kühlung und eine hohe Strahlqualität erreicht. Die optischen Systeme basieren unter anderem auf dem neuartigen Prinzip der „Typ 2 Abbildung“, welches eine reduzierte Größe der Verstärker ermöglicht.

Die neuen Laserverstärker erlauben es, mit dem Pumplaser eine Pulsenergie von bis zu 10 J bei 2.5 Hz und 1030 nm zu erreichen, oder bis zu 5 J bei 10 Hz. Diese Pulse können mit einer Effizienz von 86 % auf eine Dauer von ~670 fs komprimiert werden, was einer Spitzenleistung von 11 TW entspricht. Dies sind die energiereichsten Pulse mit Sub-Pikosekunden Pulsdauer, welche jemals mit einem auf Yb:YAG basierten Laser erzeugt wurden.

Abstract

The Petawatt-Field-Synthesizer (PFS) is a light source developed at the Max-Planck-Institut für Quantenoptik (MPQ) that aims at generating light pulses centered at ~900 nm with an energy of up to 500 mJ, at a pulse duration of 6 fs and a repetition rate of 10 Hz. The system is designed to deliver intensities in the focus of up to $1 \times 10^{20}\,\mathrm{W/cm^2}$ with a temporal contrast better than 1×10^{11}. The main application for such ultrashort and ultra-intense light pulses is the generation of isolated attosecond pulses with an unrivaled energy via the high harmonic generation on solid surfaces (SHHG).

The core of the PFS system is a cascade of several optical parametric chirped pulse amplification (OPCPA) stages which are seeded and pumped on a timescale of one picosecond. This thesis is dedicated to the development of a suitable pump source for the OPCPA stages, the "PFS pump laser". The goal of this pump laser is an output energy of 10 J at a central wavelength of 1030 nm, with a pulse duration of less than 1 ps and a repetition rate of 10 Hz. Furthermore, the pulses must be converted to 515 nm via second harmonic generation (SHG) with at least 4 J of energy left. Since no commercial systems with these parameters exist, the entire pump laser had to be developed in-house.

The initial picosecond long pulses of the PFS pump laser are stretched to several nanoseconds before energy is added in a chirped pulse amplification (CPA) scheme. The pump laser contains a series of amplifiers which exclusively rely on ytterbium doped gain media such as Yb:Glass, Yb:KYW or Yb:YAG. This type of gain media enables an efficient energy storage by diode lasers and a more relaxed thermal management in comparison to titanium or neodymium doped media. Furthermore, the amplification bandwidth of ytterbium doped gain media ensures an output spectrum of the pump laser that supports a compressed pulse duration of less than a picosecond for an operation at room temperature.

In this thesis, the design and implementation of three new amplifiers for the PFS pump laser is presented, with a focus on the choice of gain media, the optical and opto-mechanical systems, and the thermal management. Several key technologies were developed for each amplifier. The broadband Yb:KYW is used as a comparably new gain medium for high energies to replace Yb:YAG in a pre-amplification stage of the pump laser. This enables a broadband and gain narrowing compensating seed for the final Yb:YAG based 10 J amplification stage. The gain media are mounted in heatsinks based on vacuum injected liquid metal as the interface material. This ensures a superior cooling performance and a high quality of the amplified beam profile and wavefront. Furthermore, the implementation of a new optical system termed "Type 2 imaging" allows for a compact size of the amplifiers and an overall high quality of the amplified beam.

The new amplifiers and technologies push the output energy of the PFS pump laser to the targeted 10 J at a repetition rate of 2.5 Hz or alternatively to 5 J at the targeted 10 Hz. The output pulses can be compressed to ~670 fs with an efficiency of 86 %, which corresponds to a peak power of ~11 TW. To the best knowledge of the author, these are the most energetic sub-picosecond pulses from a CPA laser based on Yb:YAG worldwide.

Contents

Chapter 1

Introduction

The laser has come a long way since its first prediction by Schawlow and Towns in 1958 [1] and its first demonstration by Maiman in 1960 [2]. The exploitation of the light amplification by stimulated emission of radiation (laser) gave rise to a vast variety of new optical applications with unprecedented light properties, such as ultra-high intensities for example. Nowadays, the laser is a device of many extremes and one of the corner stones of modern technology. Being initially the size of a human fist, modern lasers exist that are smaller than a micrometer or bigger than an entire building complex. Lasers with a continuous emission of light are used with only a few milliwatts of average power for optical disc drives or with several kilowatts for welding and cutting metals. Lasers can also concentrate the emitted energy in short light pulses rather than in a continuous emission. The most energetic laser in the world, the national ignition facility (NIF), is able to generate light pulses with a pulse duration of only a few nanoseconds and with an energy of two million joules in an attempt to trigger nuclear fusion, the process that powers the sun [3].

The maximum achievable energy of a pulsed laser is mostly limited by the damage threshold of the implemented optics. Depending on the pulse duration, the intensity of the light pulse can become so high that the bulk material of the laser optics or their coatings are melted, evaporated, or ionized [4]. As a consequence, either larger laser beams or longer pulse durations are required to safely add more energy. However, both methods grow impractical at some point since they require ever larger optics or pulse durations that are too long for certain applications.

The breakthrough invention of the chirped pulse amplification (CPA) technique by Strickland and Mourou solves this limitation of pulsed lasers [5]. The intensity of the light pulse is reduced by making the pulse longer in time before energy is added, the so-called ”stretching”. In the process, a slightly different delay in time is introduced for each wavelength that is contained within the pulse, the ”chirp”. After energy is added, the stretched pulse is shortened in time, ideally to the initial pulse duration, the so-called ”compression”. This way, only the last optics in the laser are required to be large in order to withstand the intense light pulses. The CPA technique gave rise to a whole new class of pulsed lasers which can generate several petawatts of peak power. When such light pulses are tightly focused, intensities of more than $1 \times 10^{22}\,\mathrm{W/cm^2}$ can be achieved [6]. These are the most intense events created by humankind.

Another major breakthrough for pulsed lasers was the invention of ”chirped mirrors” which grant an unprecedented precision and control of the time delay of each wavelength during stretching and compression [7]. With chirped mirrors the fundamental limit of the minimum possible pulse duration can be achieved which is set by the spectral bandwidth of the light pulse. This limit is also called the ”Fourier transform limit”. Nowadays, light pulses with a duration as short as ~5 fs can be generated directly from a laser that employs chirped mirrors.

Such ultrashort pulses that only last a few optical cycles, also called "few-cycle" pulses, enable the investigation of natural processes on an unprecedented timescale such as the motion of electrons [8].

The most common laser or "gain" medium to generate and amplify ultrashort pulses is a crystal made of titanium doped sapphire (Ti:Sa). It exhibits the broadest amplification bandwidth of all available gain media and therefore grants the shortest achievable pulse duration. However, the output energy at the minimum possible duration of ~5 fs is limited to the range of nanojoules [9]. During further amplification the spectral bandwidth of the light pulse becomes narrower because of the shape of the amplification spectrum of Ti:Sa, the so-called "gain narrowing". As a result, Ti:Sa lasers with an output energy in the range of millijoules or joules typically achieve a minimum pulse duration of only 20 to 30 fs. This is also the current limit in general for high energy light pulses from a conventional laser since no other applicable gain medium was found so far with a broader amplification bandwidth.

The optical parametric amplification (OPA) technique is a way to overcome the bandwidth limitations of conventional lasers. In an OPA based light source a weak, broadband "seed" pulse is amplified by temporally overlapping it with an energetic, narrowband "pump" pulse in a crystal that exhibits strongly non-linear optical properties [10, 11]. In contrast to conventional lasers no optical energy is stored in this type of crystal, it merely acts as a converter for the energy between the two pulses. The amplification bandwidth can be chosen rather freely. It is mostly set by the parameters of the seed and pump pulses as well as their overlapping angle in the non-linear crystal. Furthermore, the OPA process is instantaneous and therefore only limited to the timescale of the seed and pump pulses. Altogether, this enables an amplification of high contrast and high energy pulses over a broader spectral bandwidth than in a conventional laser. A remarkable example of an OPA based light source is the Light-Wave-Synthesizer 20 (LWS20) which generates an output energy of 80 mJ at a pulse duration of 4.5 fs and a repetition rate of 10 Hz [12].

The Petawatt-Field-Synthesizer

The Petawatt-Field-Synthesizer (PFS) is a light source based on OPA that intends to push the output energy of few-cycle pulses and their temporal contrast to new regions [13, 14]. The PFS system was developed and operated at the Max-Planck-Institut für Quantenoptik (MPQ) in Germany. The final design intended to generate light pulses with an energy of 500 mJ and a pulse duration of less than 6 fs at a repetition rate of 10 Hz. This corresponds to a peak power of ~100 TW and a focused intensity of up to $1 \times 10^{20}\,\mathrm{W/cm^2}$.

The main application of PFS for such ultrashort and ultra-intense pulses is a process called high harmonic generation on solid surfaces (SHHG) [15, 16]. Focusing the pulses for example on a fused silica substrate generates a plasma on the surface which partially reflects the incident pulse. The strong electromagnetic field of the pulse furthermore causes a relativistic oscillation of the plasma mirror (ROM). As a result, the incident light pulse gets Doppler-shifted upon reflection and higher harmonics are generated with wavelengths that can cover a range from the extreme ultraviolet (XUV) region to the soft X-ray region. Furthermore, the higher harmonics can have pulse durations of only a few attoseconds and they can be isolated from other harmonics. Such "isolated attosecond pulses" enable the investigation of some of the shortest natural processes [17].

The core of the PFS system is a cascade of several OPA stages in which the initial microjoule level pulses with a wavelength range of 700 to 1400 nm are consecutively amplified to the final 500 mJ. The OPA stages are seeded and pumped on a timescale of one picosecond. Together with thin, large diameter OPA crystals this maximizes the achievable output energy and the temporal contrast. The seed pulses are generated by a Ti:Sa based laser frontend. The initial

pulse duration of ~5 fs is stretched to one picosecond and recompressed after amplification in the OPA stages. Therefore, the OPA scheme of PFS is also called "optical parametric chirped pulse amplification" (OPCPA).

The pump pulses are sourced by a separate CPA laser. The goal of this "pump laser" is to generate pulses with an energy of up to 10 J at a repetition rate of 10 Hz, a pulse duration of 1 ps and a center wavelength of 1030 nm. The pump pulses are further converted with an efficiency of ~50 % to a center wavelength of 515 nm in a process called "second harmonic generation" (SHG) to pump the OPA stages. The pump laser shares the same Ti:Sa frontend as the OPA. The narrowband, picosecond long pulses are stretched to several nanoseconds before they are amplified in a series of conventional laser amplifiers.

A distinctive feature of the PFS pump laser is the exclusive implementation of gain media which are doped with ytterbium ions, such as Yb:Glass, Yb:KYW and Yb:YAG. The doping with ytterbium enables the storage of optical energy by highly efficient diode lasers rather than inefficient flashlamps as in Ti:Sa based lasers. Furthermore, crystals such as Yb:KYW and Yb:YAG exhibit a comparably high thermal conductivity. Altogether, this greatly relaxes the overall thermal management of the implemented amplifiers.

Motivation of this thesis

Most of the PFS pump laser had to be developed in-house since an ytterbium based CPA laser with the required parameters did not and still does not exist commercially. A major part of the development was conducted prior to this thesis by C. Wandt and S. Klingebiel, who set up the CPA components as well as several amplifiers. At the beginning of this thesis, the PFS pump laser was able to deliver pulses with an energy of ~1 J, a repetition rate of 2 Hz, a central wavelength of 1030 nm and a compressed pulse duration of less than one picosecond.

This thesis is dedicated to the development of new amplifiers for the pump laser, with the goal to increase the available pulse energy to 10 J at a repetition rate of 10 Hz. The essential development steps that were required for the new amplifiers can be divided into four categories:

1. **Choice of proper gain medium and operational parameters.** The gain medium, its size and the doping concentration set the rough boundaries of the achievable output energy and the spectral bandwidth of the amplifier. Furthermore, a proper set of operational parameters such as input energies, beam shapes and the power of the diode lasers must be found to satisfy the specifications of the amplifier.
2. **Thermal management of the gain medium and the amplifier.** Since the laser process introduces energy losses in the form of heat, a suitable cooling scheme and heatsink design is required to extract the heat from the gain medium. Furthermore, a proper thermal management must be applied to the entire amplifier to prevent a misalignment of optics due to thermal effects.
3. **Design and implementation of a suitable optical system.** The optical system ultimately determines how much of the theoretically possible output energy and bandwidth can be achieved. It sets the efficiency of the energy storage in the gain medium as well as the efficiency of the amplification process. The optical system also determines the achievable quality of the amplified pulses, such as the beam profile and the wavefront.
4. **Mechanical design and implementation of the amplifier.** The mechanical implementation of the amplifier determines the maintenance effort to operate it, the general robustness against daily misalignments or external influences, and the mechanical stability of the amplified pulses. The development ranges from simple opto-mechanical components such as mirror mounts to entire vacuum chambers.

Outline of this thesis

Over the course of this thesis, three amplifiers were developed for the PFS pump laser with output energies of roughly 0.1 J, 1 J and 10 J, and with Yb:KYW or Yb:YAG as gain medium. At the time of this thesis, all three amplifiers were the most energetic of their kind worldwide for the amplification of pulses that can be compressed to less than one picosecond. To give an in-depth description of the development steps that were involved, the thesis is structured as follows:

Chapter 2, The PFS system: This chapter provides an overview of the entire PFS system in its final state. It furthermore gives a comprehensive description of the PFS pump laser, with a detailed depiction of all amplifiers and beam manipulation stages that are implemented. The contributions of previous works and in particular of this thesis are explicitly marked to allow for a better classification of what is new.

Chapter 3, Fundamentals of Yb:YAG and Yb:KYW: The chapter emphasizes on the fundamental physics that are involved when Yb:YAG or Yb:KYW is used as gain medium. A detailed overview of the material properties is given as well as a summary of the most important optical effects that must be considered when using these gain media in an amplifier.

Chapter 4, Heatsink development: This chapter is dedicated to the development of suitable heatsinks which mount the gain media and extract the generated heat from them. A thorough theoretical and experimental study of the achievable temperatures is given for different heatsink designs. The mechanical implementation of each developed heatsink is presented, with an emphasis on a new technology that incorporates vacuum injected liquid metal as thermal interface between the heatsink and the gain medium.

Chapter 5, Optical systems of laser amplifiers: This chapter summarizes the most common optical systems of laser amplifiers and evaluates their feasibility for the PFS pump laser. A detailed description is given for the preferred optical system termed ”Type 2 imaging” that is implemented in two of the three developed amplifiers. Furthermore, an extensive case study of the fundamental optical properties is presented for an amplifier based on such a system.

Chapter 6, The SuperBooster: The chapter summarizes the technology and the performance of the new ”SuperBooster” amplifier which incorporates Yb:KYW as gain medium. In addition, a thorough theoretical study is given for the application of Yb:KYW and its ability to replace Yb:YAG. The SuperBooster allows for an unprecedented output energy of ~140 mJ with this comparably new gain medium for a high energy amplifier.

Chapter 7, The Cube: The chapter summarizes the technology and the performance of the amplifier ”The Cube” which incorporates Yb:YAG and allows for a maximum output energy of 2 J. This amplifier was explicitly developed to replace the original 1 J amplification stage of the PFS pump laser in order to grant a more reliable day-to-day operation. The Cube also served as the main amplifier of the PFS pump laser for most of the experimental results that were achieved with the PFS system.

Chapter 8, The BigMama: This chapter is dedicated to the development of the final 10 J amplifier of the PFS pump laser, the ”BigMama”. An extensive theoretical study is given for the application of suitable Yb:YAG crystals as the gain medium. Furthermore, the opto-mechanical implementation is described in detail as well as several experimental campaigns that were conducted with the amplifier.

Chapter 9, Conclusion and outlook: This chapter gives a brief summary of the most important achievements of this thesis as well as a short outlook for further activities.

Chapter 2

The PFS system

The original PFS system intended to reach an output energy of more than 3 J, with a pulse duration of 5 fs and a repetition rate of 10 Hz [13, 14]. Over the course of the project, the specifications were continuously reduced which resulted in a final design with a more relaxed goal of ~500 mJ at sub-6 fs and 10 Hz. Although this goal is considerably lower than the initial one, it is still an extraordinary parameter set for the exploration of attosecond science.

The new goal also reduced the complexity of the required OPCPA stages and the pump laser. The final design only requires one pump beam which delivers 10 J at 1030 nm, 10 Hz and 1 ps, or after frequency doubling more than 4 J at 515 nm.

This chapter gives an overview of the latest state of the PFS project with an emphasis on the pump laser of the OPCPA stages.

Overview

2.1 The PFS system at MPQ and CALA:
Brief overview of the PFS project with the latest operational stage and an intended upgrade.
2.2 The 1 J pump laser of the operating PFS system at MPQ:
Detailed description of the CPA laser chain that was used to pump the OPCPA stages of PFS at MPQ.
2.3 The standalone 10 J pump laser at the CALA facility:
Detailed description of the pump laser that was re-built at the new CALA facility as a standalone laser without a subsequent OPCPA system.

2.1 The PFS system at MPQ and CALA

The left side of figure 2.1 shows the PFS system as it was built at the Max-Planck-Institut für Quantenoptik (MPQ). It was successfully used on a daily basis until its disassembly at the end of 2017. Experiments were conducted with an output energy of up to 42 mJ and a pulse duration below 7 fs, in particular in the field of surface high harmonic generation (SHHG) [18–20].

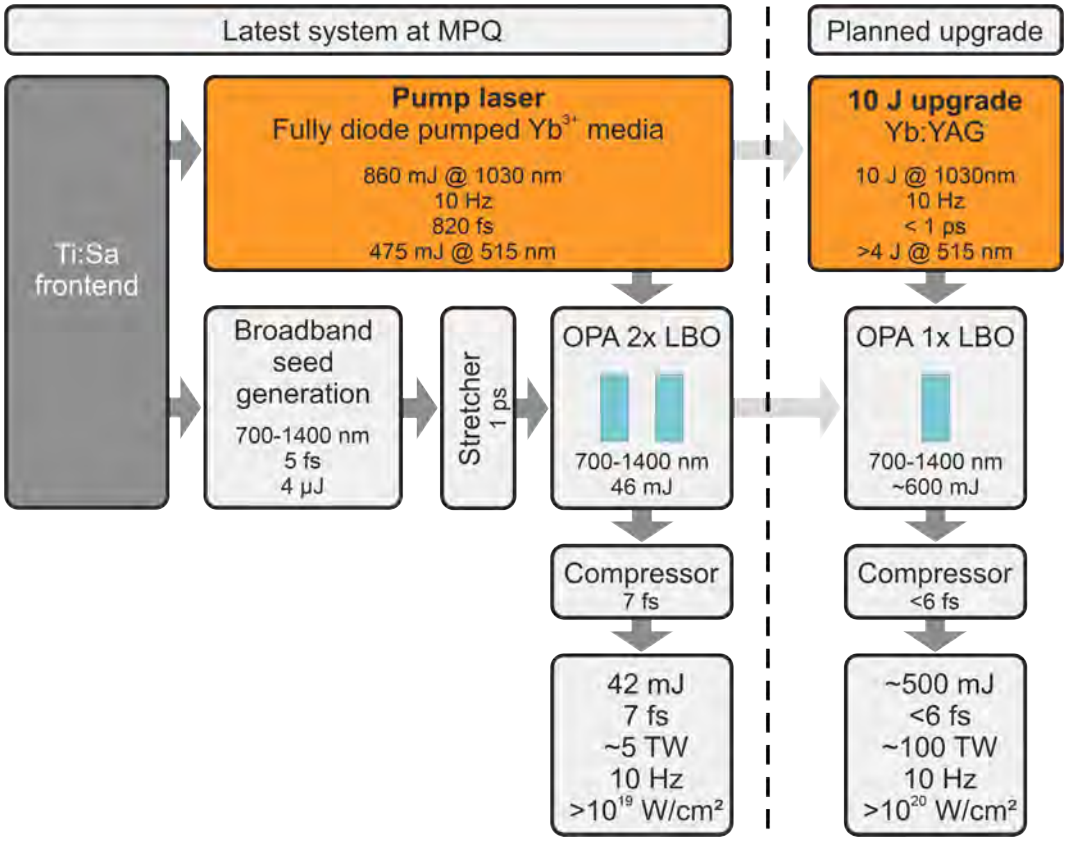

Figure 2.1: *Schematic of the PFS system with all sub-systems. Left: the latest PFS version that was built and successfully operated at the Max-Planck-Institut für Quantenoptik (MPQ) till the end of 2017. Right: planned upgrade after relocating PFS to the Center for Advanced Laser Applications (CALA) in 2018, with an additional* 10 J *pump laser amplifier and a new OPCPA stage with ten times higher output energy.*

The core of the system is a cascaded two stage OPCPA based on LBO crystals, which operates at a bandwidth of 700 to 1400 nm and at a time window of one picosecond [21, 22]. The two OPCPA stages are pumped at 515 nm by a CPA laser chain that is fully based on diode pumped Yb^{3+} gain media [23, 24]. The OPCPA stages and the pump laser are both seeded by a commercially available Ti:Sa oscillator (”CEP4 SEED, Rainbow™”, FEMTOLASERS GmbH). This way, an optical synchronization is achieved and the timing jitter of the overlap in the OPCPA stages is minimized. In order to meet the spectral requirements of the OPCPA seed, the output of the oscillator is further amplified and then broadened by a series of non-linear stages, including hollow-core fibers and XPW [22, 25].

The right side of figure 2.1 shows the final stage of PFS that was planned for the new laboratory at the Center for Advanced Laser Applications (CALA), after the move of PFS in 2018. It intended to reach the final goal of 500 mJ and sub-6 fs, which calculates to 100 TW. This required an additional OPCPA stage and an upgraded pump laser that delivers more than 4 J of pump energy at the second harmonic (515 nm), or 10 J at the fundamental (1030 nm). The development and commissioning of this pump laser was the main subject of this thesis.

2.2 The 1 J pump laser of the operating PFS system at MPQ

The pump laser of PFS at MPQ was able to deliver pulses centered at 1030 nm, with up to 860 mJ at 10 Hz and 820 fs. After converting the pulses to 515 nm up to 475 mJ remained for pumping the two OPCPA stages. A distinctive feature of the PFS pump laser is a series of amplifiers which exclusively contain fully diode-pumped, Yb^{3+} doped gain media. Also, the gain medium Yb:YAG is used for the first time in the main amplifier of a CPA laser chain. This allows to reach the targeted output energies in the joule-level while maintaining a repetition rate of 10 Hz and a compressed pulse duration of less than a picosecond.

Major development steps towards the targeted parameters were conducted by C. Wandt and S. Klingebiel prior to this thesis [23, 24, 26]. A detailed schematic of the final PFS pump laser at MPQ is presented in figure 2.2. New contributions of this thesis are marked in blue.

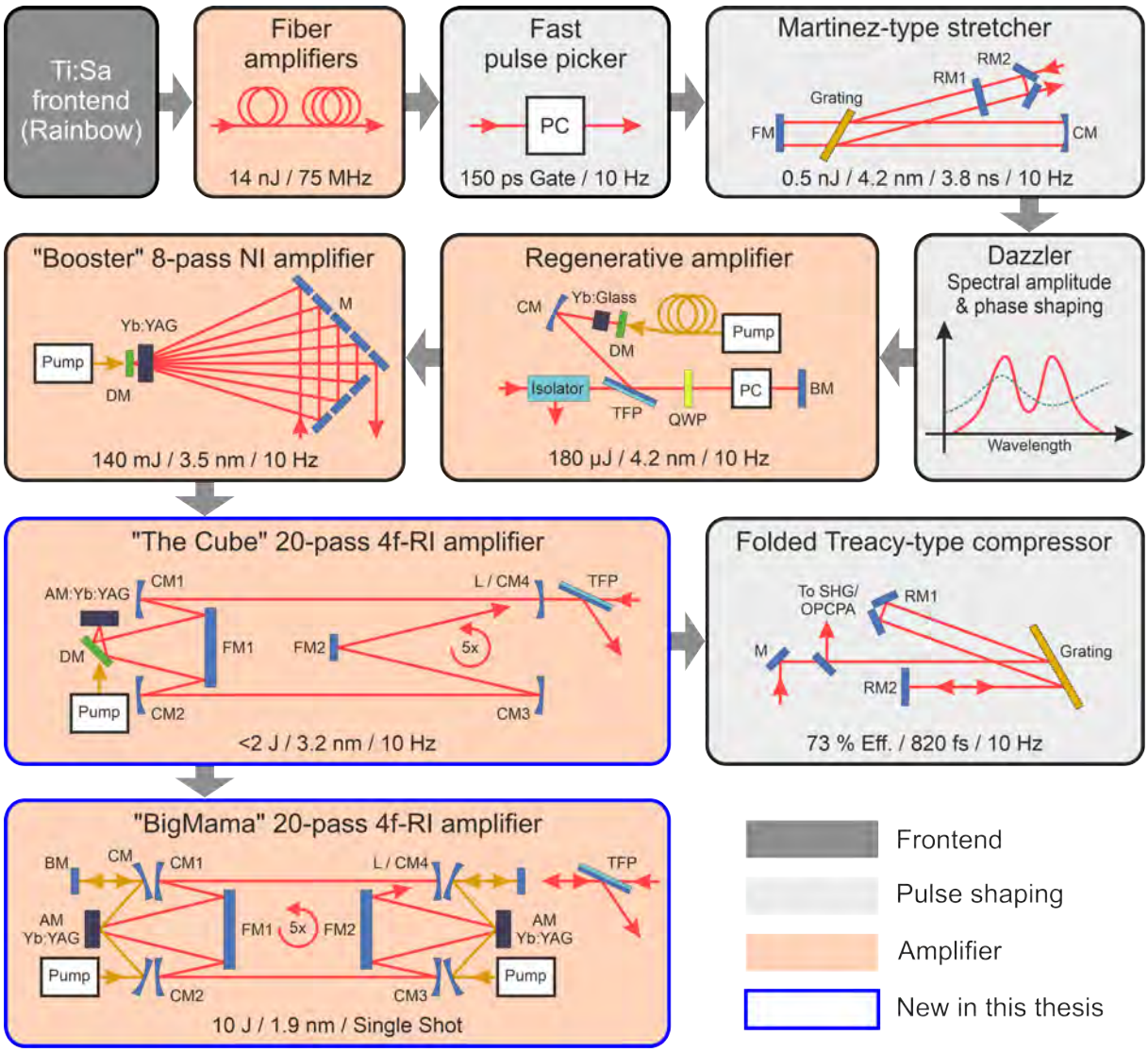

Figure 2.2: *Schematic of the PFS pump laser in its final version at MPQ. The CPA laser chain contains only diode-pumped, Yb^{3+} gain media based amplifiers and additional pulse shaping devices. It also contains a first prototype of the 10 J upgrade. NI: Non-imaging, 4f-RI: 4f relay-imaging, PC: Pockels Cell, FM: Folding mirror, RM: Roof mirror, CM: Concave mirror, DM: Dichroic mirror, M: Mirror, TFP: Thin-Film-Polarizer, QWP: Quarter-wave plate, BM: Backreflecting mirror, L: Lens, AM: Active mirror, SHG: Second harmonic generation, OPCPA: Optical parametric chirped pulse amplification (stages).*

Ti:Sa oscillator
A Ti:Sa based oscillator ("CEP4 SEED, Rainbow™", FEMTOLASERS GmbH) delivers broadband pulses centered at 790 nm to seed the OPCPA part of PFS. The oscillator furthermore delivers pulses with up to 4 pJ at 1030 nm which are used to directly seed the Yb^{3+} based amplifier chain of the pump laser. Since the OPCPA part of PFS and the pump laser are sourced by the same oscillator, an optical synchronization of both is achieved.

Yb:Glass fiber amplifiers
The first amplification stage of the pump laser consists of two cascaded, Yb^{3+} doped fiber amplifiers which boost the initial pJ-scale oscillator pulses to a more useful pulse energy of 14 nJ at a repetition rate of 75 MHz and a center wavelength 1030 nm. The fiber amplifiers were developed by the Institute for Applied Physics (IAP) at the Friedrich-Schiller-Universität Jena (FSU). They are pumped with 180 mW and 5 W respectively, at a wavelength of 980 nm.

Fast Pockels cell "FPC"
A so called "fast Pockels cell" (FPC) only transmits a 150 ps time window centered around the few picosecond long output pulses of the fiber amplifiers. Doing so before stretching the pulses cuts out most of the constant amplified spontaneous emission (ASE) background that is induced by the continuously pumped fiber amplifiers. The fast Pockels cell furthermore reduces the repetition rate to the desired 10 Hz.

Stretcher
The cleaned pulses are stretched in a Martinez-type stretcher to a pulse duration of 3.8 ns [24]. The stretcher grating has 1740 lines/mm and is hit under an angle of 60°, with a virtual grating separation of 6 m. The pulses pass two times through the entire stretcher. The dispersion terms typically are: 4.94×10^8 fs^2 for the group delay dispersion (GDD), -1.03×10^{10} fs^3 for the third order dispersion (TOD) and 3.55×10^{11} fs^4 for the fourth order dispersion (FOD). The output energy drops to 0.5 nJ because of the limited diffraction efficiency of the grating, the overall 8 passes on the grating as well as the artificial limitation of the spectral bandwidth to 4.2 nm.

Dazzler
A fine-tuning of the spectral phase is done with an acousto-optic modulator (FASTLITE "Dazzler" [27]). It allows to pre-compensate for additional dispersion from the subsequent amplifiers and thus to achieve an optimum compression at the end. Furthermore, the spectral amplitude of the pulses is shaped with a deep hole around the central wavelength of 1030 nm to counteract gain narrowing of the high energy Yb:YAG amplifiers. Due to this strong shaping, roughly 10 to 20 % of the initial energy remains.

180 µJ Yb:FP glass regenerative amplifier "Regen"
In the second amplification stage, a regenerative amplifier ("Regen") boosts the spectrally shaped pulses to an energy of 180 µJ over roughly 140 roundtrips through the cavity [26]. The Regen is based on a 8 mm thick Yb:FP glass that is doped with Yb^{3+} at a concentration of $6 \times 10^{20}\,1/\mathrm{cm}^3$ [30]. The glass is pumped at 976 nm with a peak power of 5 W and a pulse duration of 1.5 ms. The beam in the cavity has a 1/e²-diameter of 1.5 mm and the focus size on the Yb:FP has a 1/e²-diameter of roughly 100 µm. Owing to the large bandwidth of Ytterbium in a glass matrix, the bandwidth and spectral shape of the pulses are maintained during amplification.

140 mJ Yb:YAG amplifier "Booster"
The third amplification stage ("Booster") increases the pulse energy to 140 mJ in an 8-pass half bow-tie amplifier geometry [26]. The amplifier is based on a radially water cooled, 3 at.% doped Yb:YAG crystal with a size of $Ø15 \times 8$ mm as the gain medium. The crystal is pumped at 940 nm with a peak power of 2.5 kW and a pulse duration of 1.5 ms. The beam size of the seed is increased to roughly 4.3 mm full width at half maximum (FWHM) to ensure a safe operation

below the laser induced damage threshold (LIDT). Due to the Yb:YAG specific gain narrowing, the spectral bandwidth is narrowed down to 3.5 nm.

2 J Yb:YAG main amplifier "The Cube"
The fourth and last amplification stage ("The Cube") boosts the energy to an absolute maximum of 2 J, of which typically 1.2 J is used for daily operations of the OPCPA chain. A bandwidth of up to 3.2 nm ensures a compressibility of the amplified pulses to less than a picosecond.

The Cube was developed over the course of this thesis to replace the original 1 J amplification stage ("The Tube") that was developed by C. Wandt [28]. The new amplifier is based on the same 20-pass relay-imaging geometry but incorporates several, significant improvements to solve most of the beam quality and maintenance issues of the original amplifier.

The Cube incorporates a 2 at.% doped Yb:YAG crystal with a diameter of Ø38 mm and a thickness of 3 mm, or alternatively, an Yb:YAG ceramic with an ASE absorbing cladding. A pump module with 33 kW peak power, a pump duration of ~0.35 ms and a center wavelength of 934 nm is used to pump the crystal at a repetition rate of 10 Hz within an area of $13 \times 13\,\mathrm{mm}^2$ FWHM. An efficient cooling is achieved by attaching the high-reflective (HR) back side of the crystal to a newly designed, water cooled heatsink. This technique is also commonly known as "active-mirror" cooling. A comprehensive study of the new heatsinks is given in chapter 4. A more detailed description of the whole amplifier is presented in chapter 7.

Compressor
Pulses with up to 1.2 J were compressed on a daily basis to 820 fs with an efficiency of 73 % in a folded Treacy-type compressor [24, 29]. The $800 \times 400\,\mathrm{mm}^2$ compressor grating is hit under an angle of 60° and has a line density of 1740 lines/mm. A roof mirror in the compressor (RM1 in figure 2.2) folds the beam path such that only one grating is required for the compression. Furthermore, the folding reduces the overall length of the compressor to 3 m despite the virtual grating separation of 6 m. Everything is housed inside a vacuum chamber to reduce the impact of air fluctuations on the beam pointing and on the timing jitter between the pump laser and the OPCPA.

Second harmonic generation (SHG)
On record, a compressed pulse energy of up to 860 mJ at 1030 nm was converted to 475 mJ at 515 nm in a second harmonic generation (SHG) stage. The stage consists of a DKDP type II crystal with a thickness of 4 mm and an optimum angle of 54.4°. This results in an efficiency of up to 55 %. Afterwards, the 515 nm pulse energy is split between the two subsequent OPCPA stages.

10 J Yb:YAG amplifier prototype "BigMama"
A first prototype of the 10 J amplifier was developed in parallel to the operating PFS pump laser as part of this thesis. It is called "BigMama", referring to the almost ten times higher output energy than the operating main amplifier The Cube. The prototype shares most of the concept of The Cube, but it incorporates larger optics, a new pump geometry and a second 2 at.% doped, $Ø38 \times 3$ mm Yb:YAG crystal to reach an output energy of 10 J. Each crystal is pumped in a FWHM diameter of 24.5 mm and in single-shot mode at a pump power of 27 kW, a pump duration of 1 ms and a wavelength of 936 nm.

The prototype reached the desired output energy of 10 J in a test campaign with single shots. However, the tests also revealed several drawbacks of the amplifier concept and of its heatsink design which required a major re-development. Nevertheless, the prototype proved to be a valuable experimental platform that paved the way for the final version of the BigMama, which is thoroughly described in chapter 8.

2.3 The standalone 10 J pump laser at the CALA facility

The move of the PFS system to the CALA facility in 2018 required to set up most of the pump laser from scratch, but it also allowed for a major revision and to implement several upgrades. Furthermore, the pump laser was set up as a standalone system since the assembly of the OPCPA part of PFS was put on hold.

The latest version of the pump laser is able to achieve an output energy of up to 10 J at 2.5 Hz, and a compressed pulse duration of 670 fs. The energy is currently limited to 5 J at the targeted repetition rate of 10 Hz due to the risk of laser induced damages. A detailed schematic of the revised and upgraded pump laser is given in figure 2.3.

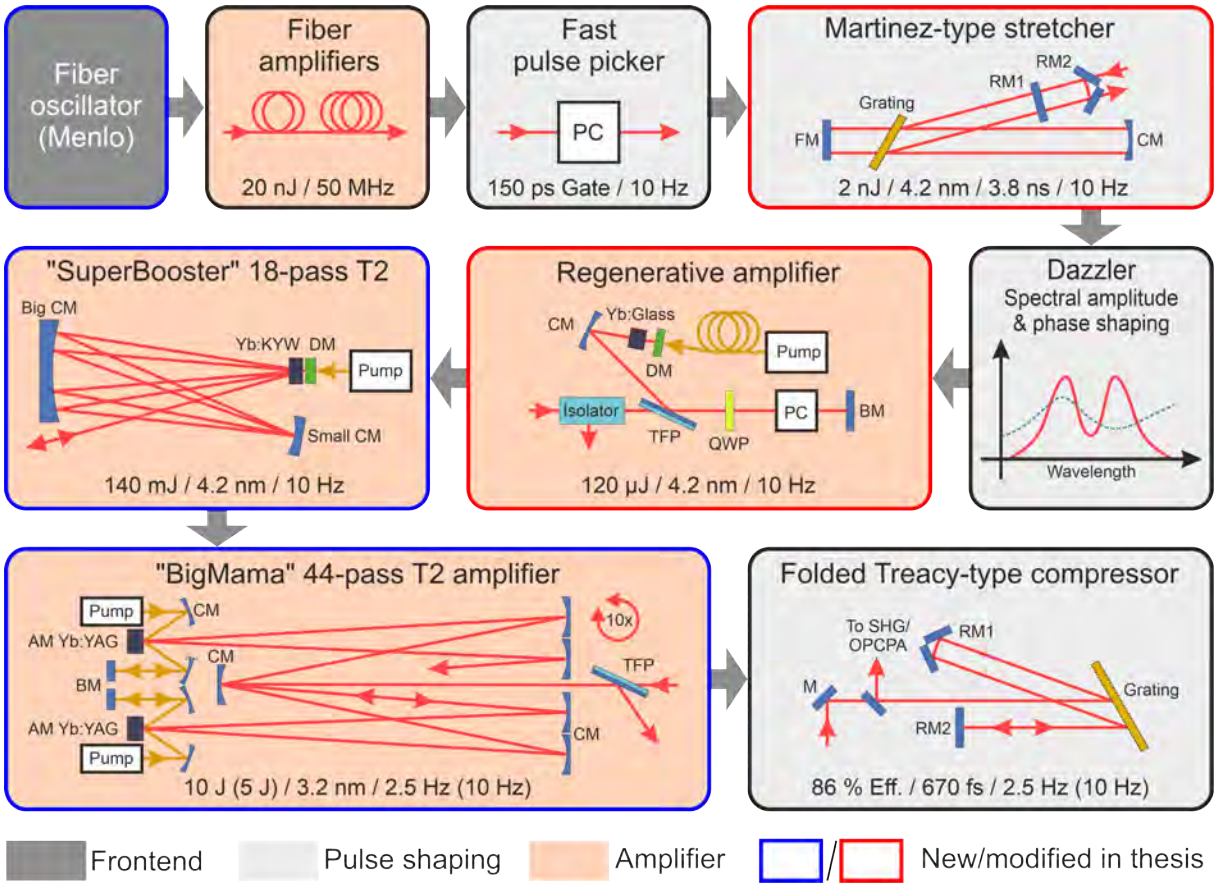

Figure 2.3: *Schematic of the standalone PFS pump laser at CALA. The new CPA laser chain is based on the original pump laser, with a new high energy oscillator, major improvements to the stretcher and the regenerative amplifier as well as two new amplifiers. T2: Type 2 imaging, PC: Pockels Cell, FM: Folding mirror, RM: Roof mirror, CM: Concave mirror, DM: Dichroic mirror, M: Mirror, TFP: Thin-Film-Polarizer, QWP: Quarter-wave plate, BM: Backreflecting mirror, L: Lens, AM: Active mirror, SHG: Second harmonic generation, OPCPA: Optical parametric chirped pulse amplification (stages).*

Modifications of the original pump laser concept

The pump laser at the CALA facility is seeded with a narrowband, high energy fiber oscillator that is optimized for a center wavelength of 1030 nm (Menlo Systems GmbH "YLMO High Power"). Although the new oscillator increases the output energy of the subsequent fiber amplifiers only slightly due to saturation effects, the higher seed energy significantly improves the ASE contrast of the amplified pulses in comparison to the previous Ti:Sa-based oscillator.

A major revision was conducted for the stretcher. The fundamental setup was left unchanged but a thorough re-alignment was conducted and several opto-mechanics were exchanged. In the

process, a considerable degradation of the stretcher grating in the form of numerous scratches and coating defects was discovered. These are assumed to be the main cause for the originally low throughput of the stretcher of only ~10 %. The throughput could be boosted by a factor of three to a total of ~30 % by re-aligning the stretcher and replacing the grating with an original spare one. Together with the new high energy oscillator, up to 2 nJ of energy is left after stretching, compared to 0.5 nJ of the previous pump laser at MPQ.

Another major modification was done to the regenerative amplifier. The cavity length was increased from 9 ns to 10 ns which is more suitable for the slow rise and fall times of the Pockels cell. In the original setup, the shorter cavity length frequently caused a temporal cut-off at the beginning or the end of the amplified pulse, which translates to a spectral cut-off via the pulse chirp. The increased cavity length improves the optimization range of the Pockels cell gate time, which also leads to a better suppression of pre- and post-pulses. Beside this, the output energy was limited to a maximum of 120 µJ to prevent laser induced damages, which occasionally happened at the original 180 µJ.

140 mJ Yb:KYW amplifier "SuperBooster"

A new amplifier ("SuperBooster") was developed for the 100 mJ-class pre-amplification stage. Instead of Yb:YAG, the amplifier incorporates the more broadband gain medium Yb:KYW which does not exhibit any noticeable gain narrowing. As a result, the pulses are amplified to a maximum of 140 mJ while maintaining their initial bandwidth of 4.2 nm as well as their pre-shaped spectral amplitude hole at 1030 nm. The output spectrum can therefore be used to efficiently compensate for the gain narrowing in the final 10 J amplifier. More information on Yb:KYW and its beneficial properties are found in the subsequent chapter 3.

The pump module of the new SuperBooster was taken from the original "Booster" amplifier and equipped with a new beam homogenizer. The 5 at.% doped, Ø8 × 3 mm Yb:KYW crystal is pumped at 2.3 kW, 10 Hz and 934 nm within a hexagon of 2.7 mm FWHM. A new, liquid metal interfaced, radial water cooling is applied which is described in detail in section 4.7.

The geometry of the new amplifier was changed from the original non-imaging half bow-tie to a so called "Type 2 imaging" which is described in detail in chapter 5. This new geometry allows for up to 18 re-imaged amplification passes with a superior beam quality. A thorough description of the design and performance of the amplifier is given in chapter 6.

10 J Yb:YAG main amplifier "BigMama"

The latest version of the 10 J amplifier ("BigMama") is able to deliver output energies as high as 10 J at a repetition rate of 2.5 Hz, and a spectral bandwidth that allows for a compression of the pulses to ~670 fs. An operation at 10 Hz is possible, but at a reduced output energy of 5 J due to the risk of laser induced damages.

The fundamental geometry is based on the Type 2 imaging of the SuperBooster and incorporates two Ø38 × 3 mm, 2 at.% Yb:YAG crystals. This translates to a total of 44 re-imaged amplification passes. One pump module with 27 kW peak power is used per crystal, with a pump duration of ~1 ms, a wavelength of ~936 nm and a pump diameter of 24.5 mm FWHM. An efficient cooling is achieved with a novel, liquid metal interfaced, active-mirror heatsink that is presented in section 4.6. An in-depth overview of the entire amplifier is given in chapter 8.

Compressor

The compressor is mostly identical to the original version at MPQ. The roof mirrors were exchanged with bigger versions to account for the higher pulse energy of 10 J. Furthermore, the entire setup was built with a mirrored arrangement of all optics to account for the different positioning of the input and output beams in the CALA facility. As a side-effect of the modifications, the throughput of the compressor increased from 73 % to a maximum of 86 %.

Chapter 3

Fundamentals of Yb:YAG and Yb:KYW

The main advantage of Yb^{3+} doped gain media over classical gain media like Ti:Sa or Nd:YAG is the long lifetime of the upper laser level in the range of ~1 ms. As a result, a direct pumping via highly efficient diode lasers is possible. Furthermore, a high optical-to-optical efficiency can be achieved by matching the narrowband diode emission with the absorption spectrum of Yb^{3+}. Altogether, this lowers the overall heat load within the system and allows for higher repetition rates at high energies compared to traditional flash lamp pumped systems.

Previous experiments at PFS showed that Yb:YAG is a promising material for reaching the targeted output energy of 10 J at 10 Hz and a spectral bandwidth of ~3 nm that supports sub-picosecond pulse durations [28, 31, 32]. Thus, also the 10 J amplifier that was developed over the course of this thesis is based on Yb:YAG. The experiments also revealed a strong gain narrowing of Yb:YAG for the high energy gain that is required to reach 10 J, in particular when several amplifiers are cascaded. The issue is solved in this thesis by implementing Yb:KYW as gain medium in the pre-amplification stage of the 10 J main amplifier. This effectively confines any gain narrowing to the main amplifier where the overall energy gain is moderate. Thus, a spectral bandwidth greater than 3 nm can be achieved even at an output energy of 10 J.

This chapter is dedicated to a general description and comparison of Yb:YAG and Yb:KYW crystals, since they are the most important gain media in the PFS pump laser. Also, the fundamental processes that are involved in storing and extracting the energy from these crystals are introduced. Furthermore, a general overview is given for the most important optical effects that must be considered for the implementation of any gain medium in an amplifier.

Overview

3.1 Material properties of Yb:YAG and Yb:KYW:
Detailed comparison of the mechanical and optical properties of Yb:YAG and Yb:KYW, including absorption and emission cross-sections.
3.2 Pump and amplification process:
Fundamentals of the pump and amplification processes and how to calculate them.
3.3 Amplified spontaneous emission (ASE):
Origin, influence, and compensation of forward and transverse emitted ASE.
3.4 Material and thermally induced wavefront deformations:
Different effects that cause wavefront deformations of a beam when travelling through a gain medium.
3.5 Depolarization effects:
Origin of thermally induced depolarization and how to compensate it.

3.1 Material properties of Yb:YAG and Yb:KYW

The optical and mechanical properties of Yb:YAG and Yb:KYW crystals are comparable. However, they differ significantly in two aspects. The first is the much broader emission bandwidth of Yb:KYW with similar absorption and emission cross-sections as Yb:YAG. The second aspect is the isotropic nature of Yb:YAG whereas Yb:KYW is anisotropic and birefringent with three unique crystal axes. Therefore Yb:KYW exhibits different mechanical and optical properties along each axis.

3.1.1 Comparison of optical and thermal properties

A detailed comparison of the optical and thermal properties of both crystal materials is given in table 3.1. The three principal optical axes of Yb:KYW are named N_m, N_g and N_p.

Table 3.1: *The most important optical and thermal properties of Yb:YAG and Yb:KYW. Note: All values are rounded. Precise values are found in the respective literature.*

	Yb:YAG	**Yb:KYW**		
Optical axis	Isotropic	N_m	N_g	N_p
Refractive index at 1030 nm	1.8153 [33]	2.02 [34]	2.06	1.98
Fluorescence time in µs	951 [35]	359 [36]		
Emission cross-section at 1030 nm, 300 K, in 10^{-20} cm²	2.2 [37]	2.5 [36]	0.4	1.1
Absorption cross-section at 941 nm, 300 K, in 10^{-20} cm²	0.8	1.9	0.4	1.0
Pump saturation intensity at 941 nm, 300 K, in kW/cm²	22	26	126	52
Seed saturation fluence at 1030 nm, 300 K, in J/cm²	8	7	50	17
Undoped thermal conductivity at 300 K in W/mK	11 [38]	2.6 [38]	-	-
Undoped thermal expansion coefficient in 10^{-6} 1/K	6.1 [39]...8.2[40]	10.8 [41]	17.4	2.0
Undoped thermo-optic coefficient at ~1064 nm in 10^{-6} 1/K	7.8 [38]...12.1 [39]	-8.9 [42]	-12.4	-14.6

Optical properties
Both crystals exhibit a high refractive index, with ~1.8 for Yb:YAG and ~2 for Yb:KYW.

A distinctive feature of Yb:KYW is the reduced fluorescence lifetime of only ~360 µs compared to ~950 µs for Yb:YAG. Although this elevates the requirements for the pump module, it is partially compensated by the almost 2.5 times higher absorption cross-section of Yb:KYW at the optimum Yb:YAG pump wavelength of 941 nm. This compensation manifests for example in the similar pump saturation intensity which is required for a sufficient excitation of the material. As a consequence, an existing pump module of Yb:YAG can also be used for Yb:KYW. This is further shown in chapter 6 where a comparable output energy of the 100 mJ-class pre-amplifier of the PFS pump laser is achieved by replacing Yb:YAG with Yb:KYW.

A closer look to the three principal optical axes of Yb:KYW reveals that the highest cross-sections are achieved when the pump and seed beams are linearly polarized along the N_m axis. For this axis, the emission cross-section and the seed saturation fluence at 1030 nm are comparable to Yb:YAG. Therefore, both materials behave similar in terms of amplification. The N_p

axis can also be used but the overall efficiency will be lower. The N_g axis poses no applicability for the wavelength region around 1030 nm.

As a result, an N_g cut of the Yb:KYW crystal lattice is preferred for an amplification at 1030 nm. In this cut, the N_g axis is oriented perpendicular to the crystal surface and the higher performing N_m and N_p axes can be easily accessed by choosing an appropriate polarization orientation of the amplified beam.

Thermal properties

While the published data for the optical properties of both crystal materials is comprehensive and rather coherent across the literature, it is not the case for the thermal properties. A significant scattering and lack of suitable data especially of the thermal properties of KYW is found. Furthermore, most of the data for KYW is for the undoped case, whereas values may strongly vary depending on the doping concentration. This particularly affects the thermal conductivity. As a consequence, in the following paragraphs only the thermal properties of undoped YAG and KYW are compared against each other.

In general, KYW shows slightly inferior thermal properties. The thermal conductivity is by a factor of ~4 lower than YAG, which indicates a less suitable application for high average powers. In addition, the thermal conductivity of YAG can be significantly increased by applying cryogenic temperatures, whereas KYW only shows a moderate effect, see figure 3.1.

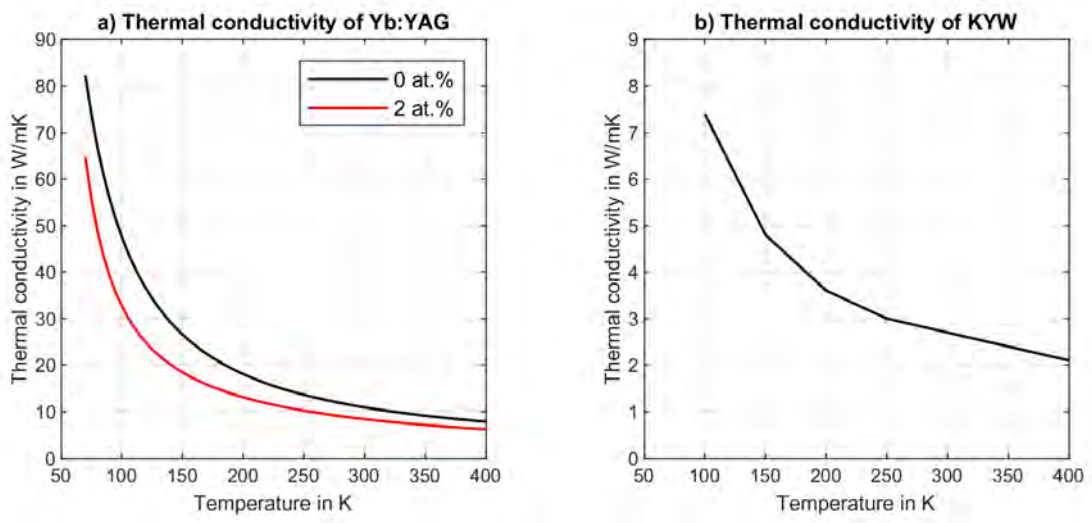

Figure 3.1: *Thermal conductivity curves at different temperatures for a) undoped YAG and 2 at.% doped Yb:YAG [38] and b) undoped KYW [38]. Values for KYW beyond* 300 K *are linear extrapolations from the published data.*

The thermal expansion of KYW is in the order of YAG but varies strongly along the three principal optical axes, with a ratio of ~5 between the accessible N_m and N_p axes in the case of an N_g cut. Another interesting difference is a positive thermo-optic coefficient for YAG and a negative one for KYW. Thus, the thermal lens induced by the thermo-optic effect will be defocusing for KYW. Depending on the overall parameters, this can be beneficial since it partially compensates the focusing thermal lens that is induced by the thermal expansion or bulging of the material [43].

3.1.2 Comparison of absorption and emission cross-sections

The main reason for the application of Yb:KYW in a pre-amplifier of the PFS pump laser is the more broadband emission spectrum, which allows to efficiently counteract the gain narrowing in the Yb:YAG based 10 J main amplifier. The individual cross-sections of Yb:YAG and the N_m axis of Yb:KYW can be found in figure 3.2 for a temperature range between 293 K and 393 K. This is the typical operating range for the developed amplifiers of PFS. For a better visibility, only the important wavelength ranges of the pump and amplification processes are shown. More comprehensive data sets and plots are published in [36] and [37].

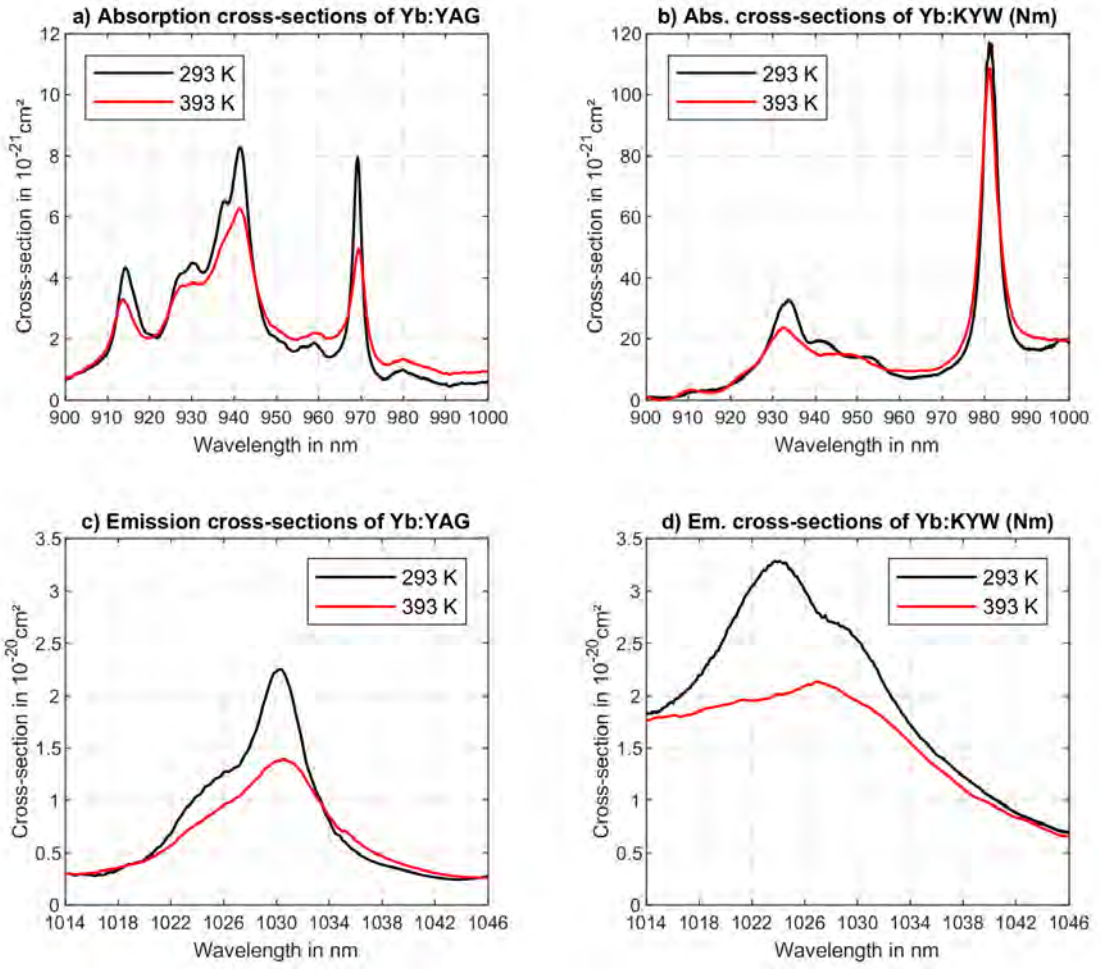

Figure 3.2: *Measured absorption and emission cross-sections of Yb:YAG [37] and the N_m axis of Yb:KYW [36] at* 293 K *and* 393 K. *Note: Yb:KYW cross-sections for* 393 K *are linear extrapolations from the measured data at* 293 K.

As mentioned before, Yb:KYW has a 2.5 times higher absorption cross-section than Yb:YAG at the typical pump wavelength of 941 nm and it has a similar pump saturation intensity. The cross-section increases even further with a local maximum at a pump wavelength of 933 nm. This proves to be beneficial if the Yb:KYW crystal is planned as a drop-in replacement in an existing Yb:YAG infrastructure. The pump module of an Yb:YAG based amplifier is typically optimized for a center wavelength of 941 nm at a pump duration around ~1000 µs. The shorter lifetime of Yb:KYW of ~360 µs however requires shorter pump pulses. As a result, the pump diodes experience a lower thermal load, which causes a shift of the emitted wavelength from 941 nm towards 933 nm.

A highly efficient pump operation is found for the zero-phonon-line (ZPL) of Yb:KYW at 981 nm. It features a six times higher absorption cross-section than at 941 nm and outnumbers the absorption cross-section of the ZPL of Yb:YAG by a factor of 15. Furthermore, the corresponding quantum defect is ~4.7 % and therefore lower than the 6 % of Yb:YAG.

For the PFS pump laser a spectral bandwidth of ~3 nm centered at 1030 nm is required to achieve sub-picosecond pulses. The ability of Yb:KYW to preserve this bandwidth during amplification can be directly deduced from the shape of its emission spectrum. In the region around 1030 nm, the curve of the spectrum does not abruptly change direction nor does it exhibit a peak as in the case of Yb:YAG. Instead, the curve is rather smooth and broad with slightly higher cross-section for shorter wavelengths. Thus, no noticeable gain narrowing for an amplification around 1030 nm occurs, which will be proven later in chapter 6.

In terms of temperature dependency both materials behave similar over the important range of 293 K to 393 K, with in general decreasing cross-sections for higher temperatures.

3.2 Pump and amplification process

The energy levels that are involved in the pump and amplification process of Yb:YAG and Yb:KYW are arranged in a quasi-three-level system, which in turn is a special case of a four-level system [44]. In a simplified model shown in figure 3.3 a), only four, discrete energy levels are involved in the laser cycle. Other possible interactions or cross-relaxations are omitted.

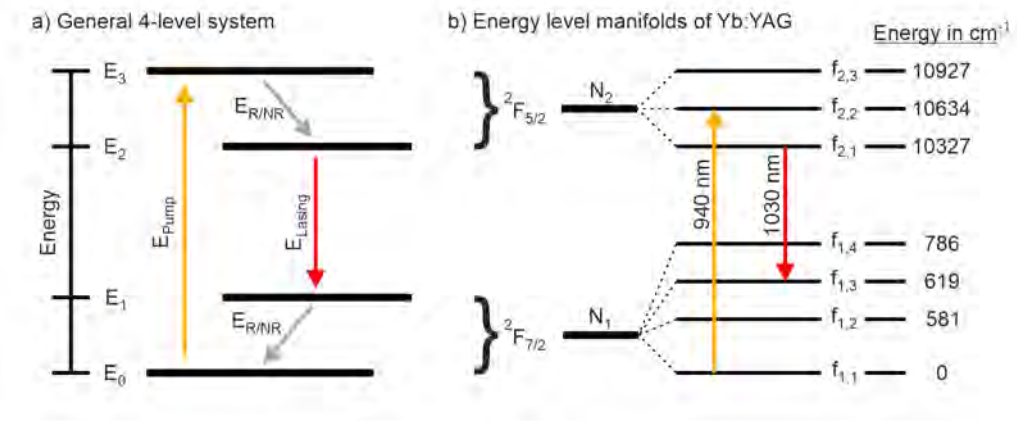

Figure 3.3: *a) Simplified energy level scheme of a four-level system with the most important transitions for a typical laser cycle: the pump transition with a photon energy E_{Pump}, the lasing transition with a photon energy E_{Lasing} and the radiative/non-radiative transitions with an energy of $E_{R/NR}$. b) Energy level scheme of Yb:YAG with the energy manifolds $^2F_{7/2}$ (ground state) and $^2F_{5/2}$ (excited state) as well as their sub-levels f. N_1 and N_2 are the ion densities in each state, respectively. Energy values are taken from [45].*

In a four-level system, all energy levels above the ground state E_0 are assumed to be separated enough so their thermal population can be neglected. Thus, in a thermal equilibrium all ions are in the ground state or lower pump level E_0. From this level, ions can be excited or "pumped" to the upper pump level E_3 by an incoming photon whose energy matches the energy difference of both levels. After pumping, a fast radiative or non-radiative decay to the upper laser level E_2 occurs. This level typically has a long lifetime before the ions decay by spontaneous emission to the lower laser level E_1. Afterwards, a fast radiative or non-radiative decay occurs to the ground state and the laser cycle is complete.

With a sufficiently high pump rate of photons it is possible to populate the upper laser level E_2 faster than it decays by spontaneous emission. If its population exceeds the one in the lower laser level E_1, which is close to zero in thermal equilibrium, a so-called inversion is achieved. This is the fundamental requirement for a laser, since now this excessive population can be used to coherently add photons to an incoming photon flux by stimulated emission.

The system is called a quasi-three-level system if the energy difference between the ground state E_0 and the lower laser level E_1 is small enough such that E_1 is thermally populated in thermal equilibrium. This is for example the case for Yb:YAG at room temperature where the energy difference is in the range of $\sim kT$, with k being the Boltzmann constant and T the temperature. As a consequence of the additional thermal population of E_1, a higher population of the upper laser level E_2 is required before an inversion is achieved. Also, the inversion threshold becomes temperature dependent.

The structure of the energy levels in Yb:YAG is shown in figure 3.3 b), with the two energy manifolds ${}^2F_{7/2}$ (ground state) and ${}^2F_{5/2}$ (excited state) [46]. Both manifolds are split into several sub-levels f, between which the pump and laser transitions occur. Each sub-level is thermally populated in accordance to the Boltzmann distribution. For a lasing at 1030 nm, the sub-level $f_{2,1}$ corresponds to the upper laser level E_2 in the simplified sketch of a), and sub-level $f_{1,3}$ corresponds to the lower laser level E_1. At room temperature, the sub-level $f_{1,3}$ is thermally populated by ~5 %. Therefore, to achieve an inversion, the sub-level $f_{2,1}$ must be populated higher than this by the pump process.

3.2.1 Calculation of the pump process

The mathematical description of the pump process closely follows the excellent work of J. Körner. A more comprehensive description can be found in [47, 48].

The combined rate equation that describes the change of the population density of the lower and upper laser levels over time is given for a full laser cycle as [49]:

$$\frac{\mathrm{d}N_2}{\mathrm{d}t} = -\frac{\mathrm{d}N_1}{\mathrm{d}t} = \underbrace{\sigma_\mathrm{a}(\lambda_\mathrm{P})\, c\Phi_\mathrm{P}\,(f_{1\mathrm{P}}N_1 - f_{2\mathrm{P}}N_2)}_{Pump} \underbrace{-\frac{N_2}{\tau_\mathrm{f}}}_{Sp.\ emission} \underbrace{-\sigma_\mathrm{e}(\lambda_L)\, c\Phi_L\,(f_{2L}N_2 - f_{1L}N_1)}_{Amplification} \quad (3.1)$$

N_1 is the density for example of Yb^{3+} ions in the ground state (lower manifold) and N_2 the density in the excited state (upper manifold). The sum of both is the total density of doped ions N_{dop}. The indices P and L correspond to the pump beam and the laser or seed beam, respectively. σ_a and σ_e are the cross-sections for absorption and emission at the wavelength λ, c is the speed of light, Φ is the photon density, f_1 and f_2 are the Boltzmann occupation factors for the lower and the upper energy sub-levels that are involved in the transitions, and τ_f is the fluorescence life time.

If the pump is pulsed rather than continuous, the process of amplification can be neglected during pumping, since the seed pulse typically arrives after the pump is switched off. Therefore, equation (3.1) reduces to:

$$\frac{\mathrm{d}N_2}{\mathrm{d}t} = -\frac{\mathrm{d}N_1}{\mathrm{d}t} = \sigma_\mathrm{a}(\lambda_\mathrm{P})\, c\Phi_\mathrm{P}\,(f_{1\mathrm{P}}N_1 - f_{2\mathrm{P}}N_2) - \frac{N_2}{\tau_\mathrm{f}} \quad (3.2)$$

A more convenient representation of the pump process is obtained by implementing several substitutions. First, a relative excitation β is defined as the ratio between the density of excited ions and the overall density of doped ions:

$$\beta(t,z) = \frac{N_2(t,z)}{N_{dop}} \quad (3.3)$$

where t denotes the dependency on the time and z the dependency on the position along the optical axis within the gain medium.

Second, the pump rate R is defined as:

$$R(t,z) = \sigma_a c \Phi_P(t,z) \tag{3.4}$$

Third, an equilibrium excitation β_{eq} for the pump process is introduced. It is defined as the ratio between the absorption cross-section and the sum of the absorption and emission cross-sections at the pump wavelength:

$$\beta_{eq} = \frac{\sigma_a}{\sigma_a + \sigma_e} \tag{3.5}$$

The equilibrium excitation of the pump process is the upper limit of the excitation at which no further increase of the population in the upper laser level is achieved by an ongoing pumping. In the classical example of a hypothetical two level laser, β_{eq} would be 0.5 or 50 %.

Implementing all substitutions into the rate equation (3.2) yields an expression for the evolution of the material excitation over time:

$$\frac{\mathrm{d}\beta(t,z)}{\mathrm{d}t} = R(t,z) f_{1\mathrm{P}} - \beta(t,z) \cdot \left(\frac{R(t,z) f_{1\mathrm{P}}}{\beta_{\mathrm{eq}}(z)} + \frac{1}{\tau_{\mathrm{f}}} \right) \tag{3.6}$$

To obtain a similar expression for the evolution of the pump rate, the change of the pump photon density must be considered when the pump beam propagates through the gain medium:

$$\frac{\mathrm{d}\Phi}{\mathrm{d}z} = -\sigma\Phi \cdot (f_1 N_1 - f_2 N_2) \tag{3.7}$$

Together with the equation (3.4) of the pump rate and the substitutions, the evolution of the pump rate over time and penetration depth of the material is expressed as:

$$\frac{\mathrm{d}R(t,z)}{\mathrm{d}z} = -N_{\mathrm{dop}}\, \sigma_{\mathrm{a}}(z) \cdot \left(1 - \frac{\beta(t,z)}{\beta_{\mathrm{eq}}(z)} \right) R(t,z) \tag{3.8}$$

Now, solving the differential equation (3.6) of the material excitation yields:

$$\begin{aligned} \beta(t,z) = & \exp\left[-\int_0^t \frac{R(t',z) f_{1P}}{\beta_{eq}} \,\mathrm{d}t' - \frac{t}{\tau_f} \right] \\ & \cdot \left\{ \int_0^t R(t',z) f_{1P} \cdot \exp\left[\int_0^{t'} \frac{R(t'',z) f_{1P}}{\beta_{eq}} \,\mathrm{d}t'' - \frac{t'}{\tau_f} \right] \mathrm{d}t' + \beta_0(z) \right\} \end{aligned} \tag{3.9}$$

where β_0 is the initial material excitation. The equation allows to precisely calculate the material excitation over time and across the gain medium. To simplify the calculation, the Boltzmann occupation factor f_{1P} can be approximated with 1, since the excitation of ions typically starts from the lowest energy level of the ground state.

Solving the differential equation (3.8) of the pump rate yields:

$$R(t,z) = \underbrace{R_0(t) \cdot e^{-N_{\mathrm{dop}}\, \sigma_a z}}_{R_a} \cdot \underbrace{\exp\left(N_{\mathrm{dop}}\, \sigma_a \cdot \int_0^z \frac{\beta(t,z')}{\beta_{\mathrm{eq}}(z')} \mathrm{d}z' \right)}_{R_{\mathrm{b}}} \tag{3.10}$$

where R_0 is the pump rate at the entrance face of the gain medium, R_a is the decay of the pump rate according to the Lambert-Beer law and R_b is a correcting term to this law which

takes a non-zero excitation into account. The equation allows to calculate the time and position depending pump rate during the pump process.

The two final equations for the material excitation and the pump rate are dependent on each other and several integrations are involved. For this reason, an analytical solution is not possible. Instead, an iterative, numerical approach is required. For this, two extreme cases of the excitation are considered. One case starts with a zero excitation at all times and estimates the minimum material excitation with each iteration. The other case starts at the maximum possible excitation β_{eq} and estimates the maximum material excitation in the material. The extreme cases are written as:

$$R_b^1 = R_b\left(\beta_{\text{low}}^0(t,z) = 0\right) = 1 \tag{3.11}$$

$$R_b^1 = R_b\left(\beta_{\text{high}}^0(t,z) = \beta_{eq}\right) = \frac{1}{R_a} \tag{3.12}$$

By iterating then with the following formalism:

$$R_b^{(m+1)}(t,z) = R_b\left(\beta_{low/high}^m(t,z)\right) \tag{3.13}$$

$$\beta_{low/high}^{(m+1)}(t,z) = \beta\left(R_a R_b^{(m+1)}(t,z)\right) \tag{3.14}$$

successive, more precise estimations of the minimum and maximum material excitation are obtained. The higher the number of iterations is, the closer both cases get to the eventual excitation of the material. The iteration process is stopped at a predefined precision.

3.2.2 Calculation of the amplification process

A suitable algorithm to precisely calculate the amplification process is given by L. Frantz and J. Nodvik [50]. Applying it to the quasi-three-level scheme of Yb:YAG and implementing the aforementioned substitutions yields two equations. One is for the photon density Φ over time of the amplified seed pulse and the other is for the remaining excitation β of the gain medium after the pulse propagated through it [48]:

$$\phi(t) = \frac{\phi_0(t)}{1 - \left(1 - e^{-\sigma_e \int_0^{l_{mat}} N_{dop} \frac{\beta_0(x') - \beta_{eq}}{1-\beta_{eq}} dx'}\right) \cdot e^{-\frac{c\sigma_e}{1-\beta_{eq}} \cdot \int_{-\infty}^{t-\frac{x}{c}} \phi_0(t')dt'}} \tag{3.15}$$

$$\beta(x) = \frac{\left(\beta_0(x) - \beta_{eq}\right) \cdot e^{-\sigma_e \int_0^x N_{dop} \frac{\beta_0(x') - \beta_{eq}}{1-\beta_{eq}} dx'}}{e^{-\sigma_e \int_0^x N_{dop} \frac{\beta_0(x') - \beta_{eq}}{1-\beta_{eq}} dx'} + e^{\frac{c\sigma_e}{1-\beta_{eq}} \cdot \int_{-\infty}^{\infty} \phi_0(t')dt'} - 1} + \beta_{eq} \tag{3.16}$$

where Φ_0 is the initial photon density of the seed pulse over time, l_{mat} is the total thickness of the gain medium, and β_{eq} is the equilibrium excitation at the seed wavelength, above which a gain is achieved. Since these are general expressions, also effects like saturation and arbitrary pulse shapes are accounted for.

3.2.3 Common figures of merit

Several, commonly used figures of merit can be deduced from the previous equations:

Pump saturation intensity
The pump saturation intensity defines the pump intensity that is required to achieve a material excitation of $\beta_{eq}/2$ for an infinite pump duration. It is typically used to estimate the magnitude of the pump intensity that is required for an efficient pump operation. It can be calculated from the pump rate and is given by:

$$I_{\mathrm{Sat}} = \frac{h\nu}{f_{1\mathrm{P}}\tau_f \cdot (\sigma_a + \sigma_e)} \tag{3.17}$$

where h is Planck's constant and ν the photon frequency of the pump.

Storage efficiency
The storage efficiency of the pump process is calculated by [51]:

$$\eta_L = \frac{1 - \exp\left\{-\tau_P/\tau_f\right\}}{\tau_P/\tau_f} \tag{3.18}$$

with τ_P the pulse duration of the pump. It shows that pump pulses shorter than the fluorescence lifetime τ_f offer a more efficient storage of energy in the gain medium. However, shorter pump pulses require a higher pump power to store enough energy within the shorter time which increases the overall costs of a pump module.

Small signal gain
The small signal gain (SSG) is an extreme case of the amplification process that is only valid for low photon densities of the input beam, at which no saturation effects are observed. With this simplification, equation (3.15) reduces to:

$$\Phi = \Phi_0 \cdot e^{N_{dop} f_2 \cdot [\sigma_e \beta - \sigma_a (1-\beta)] z} \tag{3.19}$$

which shows an exponential growth of the photon density during amplification. The term in the exponent is also commonly called the small signal gain coefficient g_0:

$$g_0 = N_{dop} f_2 \cdot [\sigma_e \beta - \sigma_a (1-\beta)] \tag{3.20}$$

Similar to the pump process, the Boltzmann occupation factor f_2 can be typically approximated with 1.

Seed saturation fluence
The seed saturation fluence defines an energy fluence of the amplified beam, upon which the small signal gain is reduced to 1/e by saturation effects. It is calculated by:

$$F_{Sat} = \frac{h\nu}{\sigma_a + \sigma_e} \tag{3.21}$$

A fluence above this value is favorable, as it translates into a higher energy extraction efficiency. In case of a multi-pass amplifier the fluence of the beam is added up for every pass and therefore, the efficiency is increased. If the fluence of the amplified beam approaches the seed saturation fluence, the gain is significantly altered and therefore, the small signal gain approximation cannot be used anymore.

3.3 Amplified spontaneous emission (ASE)

The fundamental process of a laser is the stimulated emission of radiation. An incident photon stimulates the decay of the inverted upper laser level which then coherently adds a photon of the same energy. Thus, an amplification is achieved.

However, a gain medium does not distinguish where the incident photon comes from. This can be either an external beam that is to be amplified, or just the spontaneous emission from the medium itself. Consequently, in an excited gain medium with a population inversion, also the spontaneously emitted photons will experience an amplification and depopulate the upper laser level. This radiation is also called amplified spontaneous emission (ASE). It is part of any laser since it is directly linked to the fundamental laser process itself. As a consequence, it must be always considered when developing or using a laser, as it may severely limit the operational regime [52–56].

In general, ASE is emitted in every direction. For an application it typically makes sense to divide these directions into two types. The first type is the forward or backward emitted ASE in the direction of the amplified beam, which acts as a background or overlay to the amplified beam. The second type is the transverse emitted ASE, also often called transverse or parasitic lasing, which propagates perpendicular to the amplified beam across the gain medium. The transverse ASE can further oscillate between the borders of the gain medium or in more complex gallery modes, which may strongly depopulate the upper laser level [51].

A simplified sketch of the possible paths of an ASE photon is shown in figure 3.4. The gain medium is disc-shaped and only pumped in the central area. It is surrounded by air or vacuum, which causes reflections of the ASE at the borders.

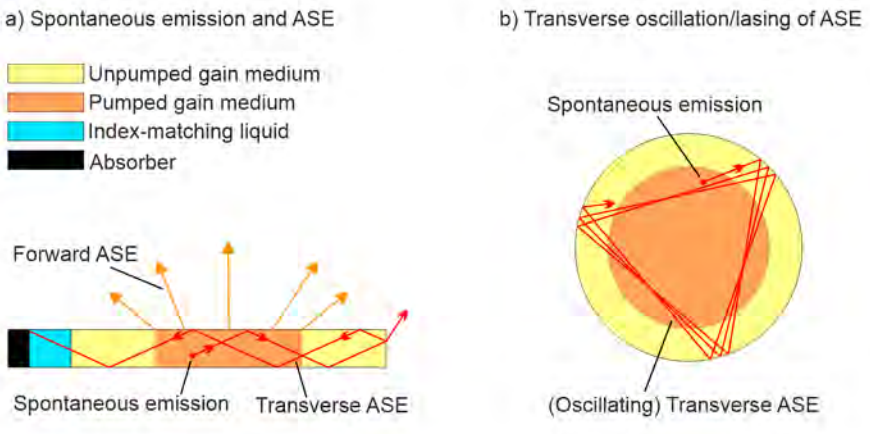

Figure 3.4: *Simplified sketch of the possible paths of ASE photons in a partially excited/pumped gain medium with a disc shape. a) Cross-sectional view of the gain medium with forward emitted ASE, multiple reflections of the transverse ASE, as well as an additional index-matching liquid and absorber to couple out and absorb ASE. b) Top view of the gain medium with oscillating, transverse ASE.*

3.3.1 Forward ASE and ASE background

The forward emitted ASE overlaps with the direction of the amplified beam. In most cases it acts as a comparably weak background signal that does not pose any danger of laser induced damages. If, however, the forward emitted ASE experiences a sufficient feedback, for example by parasitic backreflections or a multi-pass geometry, it can be amplified further and eventually

overpower the actual amplified laser beam. Thus, care must be taken to suppress any feedback of ASE. This is particularly important in amplifiers with imaging optical systems since they allow for multiple passes through a gain medium with comparably low optical losses. A common practice in such systems is the implementation of pinholes in the focus plane which filter out any parasitic reflections or ASE that do not match the propagation properties of the amplified beam.

Even if a feedback is sufficiently suppressed, the weak ASE background stills limit the achievable temporal contrast of an amplified laser pulse. This contrast is particularly important for ultrahigh-intensity laser systems that are used e.g. for laser-electron acceleration [57], laser-ion acceleration [58] or in general laser-plasma interactions [19]. If the ASE background is too high, it can trigger an interaction with the target of the experiment already before the arrival of the ultra-intense laser pulse and may render the experiment useless.

An excellent study of the ASE background and the achievable temporal contrast in an amplifier is given by Keppler et.al [59]. Here, the more intuitive inverted temporal contrast TIC^{-1} is used which defines the time dependent pulse intensity, e.g. before or after the main pulse, normalized to the peak intensity of the main pulse. Thus, a high temporal contrast has a low TIC^{-1}. The minimum achievable TIC^{-1} of an amplifier due to ASE is expressed by the ratio between P_{ASE}, the power of the underlying ASE, and P_{Pulse}, the power of the main pulse:

$$\begin{aligned} \mathrm{TIC}_{\mathrm{ASE}}^{-1} &= \frac{I_{\mathrm{ASE}}}{I_{\mathrm{Pulse}}} = \frac{P_{\mathrm{ASE}}}{P_{\mathrm{Pulse}}} \\ &= I_{\mathrm{Sat}}\, K_{\Delta\Omega} K_p K_{\Delta\nu} \gamma(g_0, L)\, \frac{\tau_{\mathrm{Pulse}}}{E_{\mathrm{Seed}}} \end{aligned} \tag{3.22}$$

with

$$\gamma(g_0, L) = \frac{\ln\left[g_0/(1-L)\right]}{g_0 - 1} \tag{3.23}$$

I_{Sat} is the saturation intensity, $K_{\Delta\Omega}$ the spatio-angular acceptance of the amplifier, $K_{\Delta\nu}$ the spectral acceptance, K_P the probability of an ASE photon to match the preferred polarization of the amplifier, τ_{Pulse} the compressed pulse duration, E_{Seed} the seed energy, g_0 the small signal gain coefficient and L the reabsorption losses.

Several measures to reduce the ASE background in an amplifier can be deduced from the equations:

- In general, a high input energy and a high gain combined with low losses is preferred.
- Spatial filters, such as the aforementioned pinholes in the focus plane of an imaging amplifier, reduce the spatio-angular acceptance of the amplifier and limit the collected ASE.
- If possible, optical coatings should be limited to only the required wavelengths of the pump and amplification processes.
- For isotropic gain media the emitted ASE is equally distributed over every state of polarization. Thus, a combination of a well-defined state of polarization of the amplified beam and a polarization coupling of the input and output beams can half the ASE background. For anisotropic gain media this method is typically less efficient since the distribution of ASE may have a preferred state of polarization.

3.3.2 Transverse ASE

An excellent and comprehensive study of the transverse ASE can be found in the research works of D. Albach [51, 60]. Here, only a short overview of the studies is given with the most critical insights.

In general, any spontaneously emitted photon that is amplified during the pump process will contribute to an increased depopulation of the gain medium before the seed pulse arrives. This effect can also be understood as an increased fluorescence probability or a shorter lifetime of the gain medium, as it causes a faster decay of the upper laser level. In the simplest case, the ASE impact is taken into account by the lifetime correcting factor M_{ASE} in the rate equation of the pump process:

$$\frac{\mathrm{d}\hat{n}}{\mathrm{d}t} = \left.\frac{\mathrm{d}\hat{n}}{\mathrm{d}t}\right|_{P} - \left.\frac{\mathrm{d}\hat{n}}{\mathrm{d}t}\right|_{SE} \cdot M_{ASE} \tag{3.24}$$

Here, $\hat{n}$ denotes the density of excited ions, P the pump process and SE the spontaneous emission. The M_{ASE} factor can be calculated in a rough approximation by:

$$M_{ASE} \approx e^{\{\sigma_e \hat{n} L\}} \tag{3.25}$$

with the emission cross-section σ_e for the ASE and the length L along the characteristic dimension of the gain medium, e.g. the diameter for a disc shape. The ASE corrected fluorescence lifetime is:

$$\tau_{f,\,\mathrm{corr}} = \frac{\tau_f}{M_{ASE}} \tag{3.26}$$

This approximation of M_{ASE} only holds true if the impact of ASE is fairly low. In case of a strong depopulation of the gain medium by the transverse ASE, the M_{ASE} factor will significantly vary temporally and spatially. Furthermore, the calculation of the M_{ASE} factor does not take saturation effects into account. Therefore, the impact of ASE is typically overestimated.

The approximation also does not account for multiple reflections of ASE between the front and back surfaces of the gain medium. In a disc-shaped gain medium this can be the dominant process for the depopulation by ASE. A suitable tool to also account for these reflections is HASEonGPU [61]. In addition to the time resolved simulation of the pump process, it incorporates a sophisticated ray tracing simulation of the spontaneously emitted and amplified photons. Thus, the impact of ASE can be precisely calculated over time and across the gain medium.

The only requirement for the simulation is the absence of transverse oscillations of the ASE, since the ray tracing does not include reflections from the transverse borders of the gain medium, e.g. the barrel of a disc. These oscillations can be avoided by a suitable choice of the gain medium and additional countermeasures that suppress the feedback of the transverse ASE, as described in the following.

Oscillation threshold of transverse ASE

A useful formalism to evaluate the probability of transverse oscillations is the estimation of the small signal gain G of the transverse ASE. It is defined for the path of a photon along the characteristic dimension of the gain medium until hitting a border:

$$G = (1 - \mathrm{Loss}) \cdot e^{(g_0 \cdot L)} \tag{3.27}$$

g_0 is the small signal gain coefficient at the ASE wavelengths, L is the characteristic length that an ASE photon travels until hitting the border, and *Loss* is for example the energy loss after a reflection at the border. In a disc-shaped medium that is pumped across the entire aperture, L is the diameter. In case the disc is only partially pumped for example in the center, the calculation

of the product g_0L must be split into the pumped, excited region and the unpumped, absorbing region around. Multiple reflections between the front and back surface that increase the path length are typically neglected in this approximation.

Oscillations of the ASE will occur, if the small signal gain of the ASE exceeds the losses at the border of the gain medium. As a figure of merit, the product g_0L is used and compared against the losses:

$$g_0L < -\ln(1-\text{Loss}) \tag{3.28}$$

The maximum allowed values of g_0L for a YAG disc that is surrounded by air, water or oil are summarized in table 3.2. For an operation near the given g_0L or above, transverse oscillations of ASE are expected.

Table 3.2: *Maximum values of g_0L for a YAG disc that is surrounded by air, water or oil. Oscillations of the transverse ASE are expected for values above these. The reflection losses assume a perpendicular angle of incidence on a polished barrel of the disc.*

Interface	**Refr. index n_0 / n_1**	**Losses in %**	**max. g_0L**
YAG/air	1.8153 / 1	91.4	2.5
YAG/water	1.8153 / 1.33	97.6	3.7
YAG/oil	1.8153 / 1.5	99.1	4.7

Liquids with a higher refractive index that better match YAG can further improve the suppression of oscillations. However, these types of liquids are often hazardous and less convenient to use. In addition, for high g_0L values, the ASE significantly depopulates the gain medium already in a single pass. Thus, a working point below a g_0L of 4 should always be pursued [51].

3.3.3 Methods for minimizing ASE

ASE cannot be avoided since it is a fundamental part of the laser process itself. It can only be minimized by suitable countermeasures. However, parasitic oscillations of ASE can and must be avoided [51]. It is therefore important to plan for ASE at the beginning of the design phase of an amplifier and to exclude undesirable working points, for example high g_0L values.

In general, a suitable working point of an amplifier requires a longitudinal gain of the amplified beam that is significantly higher than the transverse or longitudinal gain of the ASE. For disc-shaped gain media this requires the application of multiple passes of the amplified beam since the gain for a single pass is typically low.

Partial pumping of the gain medium

To minimize the impact of ASE, lossless paths of the emitted ASE should be avoided. For an Yb:YAG disc for example, it is advisable to only pump the center region, as previously depicted in figure 3.4. This way, the transverse ASE experiences reabsorption in the unpumped Yb:YAG material around. Ideally, the induced absorption and the losses at the transverse border are too high for the onset of an oscillation and no further measures are required.

Index-matching and absorbing cladding

A similar effect can also be achieved by incorporating an absorbing element into the path of the transverse ASE. One way is to couple out the ASE with the help of an index-matching liquid around the borders of the gain medium. This can also be done by anti-reflection coatings or wedged facets. An external absorber then absorbs the ASE and prevents any feedback [62, 63].

Another way is to incorporate the absorbing element directly into the gain medium itself. A prominent example are cladded Yb:YAG ceramics, where an ASE absorbing, chromium-doped

YAG element is bonded to the borders [64–66]. This cladding effectively absorbs any transverse ASE and limits the impact to a single pass through the excited region [67, 68].

Avoiding external reflections
A more general, sometimes neglected measure against oscillations of the transverse or forward emitted ASE is to avoid high reflective surfaces in the vicinity of the gain medium, for example from a mirror mount or the surrounding heatsink. Furthermore, parasitic reflections from windows or mirrors that are aligned parallel to the gain medium can cause external oscillations of ASE and therefore must be avoided, which will be shown in chapter 7.

Additional undoped material
Although the previous methods suppress transverse oscillations, they do not alter the propagation of ASE inside the excited region of the gain medium. However, for disc-like geometries, the total internal reflection between the front and back surface can be the dominant process for the depopulation by ASE.

To avoid this, the confinement of the ASE inside the excited region must be decreased. This can be achieved for example by attaching additional, undoped YAG to the front of an Yb:YAG crystal [69, 70]. Instead of being reflected multiple times between the front and back surfaces of the excited region, the ASE is coupled out and travels most of its path in the undoped YAG. Thus, only the initial path towards the undoped region can cause a depopulation.

3.4 Material and thermally induced wavefront deformations

A beam that passes through a gain medium experiences wavefront deformations. In the simplest case, this can be caused by imperfections of the bulk material such as growth defects or by an insufficient surface polish. Several more complex effects arise when the gain medium is actively pumped.

The emerging thermal effects during pumping are one of the main contributions to wavefront deformations in high energy or high power lasers. In a gain medium a part of the absorbed pump energy is always converted into heat. The origin can be the quantum defect between the pump wavelength and the lasing wavelength or reabsorption, for example of ASE. Depending on the heat flow of the cooling scheme this heat may cause spatially varying temperature profiles across the gain medium. Since the mechanical and optical properties of the medium depend on the temperature, a beam that is passing through experiences deformations of its wavefront.

In general, the most important effects on the wavefront, that emerge when a gain medium is actively pumped, can be classified into four categories:

- A mechanical effect on the overall shape of the gain medium. It is induced by the thermal expansion of the gain medium which may lead to either a bulging of the bulk material or a bending of the surfaces, similar to a bi-metal [71].
- A photo-elastic effect on the refractive index. It is induced by the mechanical stress from the thermal expansion and can cause stress induced birefringence. It is particularly strong for regions with steep temperature gradients because of the increased local stress.
- A thermo-optical effect which is induced by the temperature dependence of the refractive index.
- An ”electronic-optical” effect on the refractive index. It emerges from the excitation or inversion of the gain medium which causes a change of the polarizability of the material [72, 73].

The commonly used term ”thermal lens” refers to the overall change of the beam wavefront that is induced by all four effects. However, it is often used for only the mechanical effect and the

thermo-optical effect due to their typically strong contribution and the similarity of the resulting wavefront deformation to the one caused by a lens.

A comprehensive study of all four effects can be found in [51] and [74]. In general, their influence can be described as a change of the optical path length for a beam that passes through the medium. In the unpumped or cold state, the path length for a rod-like gain medium is expressed as:

$$\delta^{off} = n_0(T_c)\,L + d \tag{3.29}$$

with n_0 the refractive index of the medium at the cold temperature T_c, L the length of the cold gain medium and d the additional free space propagation length after the medium. In the pumped or hot state, the path length can be expressed as:

$$\delta^{on}_{r,\theta} = \int_0^{L+\Delta L} (n_0(T_c) + n_T + n_s + n_e)\,\mathrm{d}z + d - \Delta L(r) \tag{3.30}$$

with (r,θ) the cylindrical coordinates of the rod and z the coordinate along the direction of the beam. The mechanical deformation of the gain medium by thermal expansion is expressed as ΔL. The first term n_T inside the bracket describes the change of the refractive index that is induced solely by the change of temperature. It is directly linked to the thermo-optical coefficient and can be calculated at a constant strain of the medium with:

$$n_T = \left(\frac{\mathrm{d}n_{r,\theta}}{\mathrm{d}T}\right)(T(r,z) - T_c) \tag{3.31}$$

where T is the hot state temperature at the point of interest. The second term n_s describes the influence of mechanical stress on the refractive index [75]. This stress is typically induced by the thermal expansion of the material and linked to the photo-elastic effect. It is given as:

$$n_s = \sum_{j=r,\theta,z} \left(\frac{\mathrm{d}n_{r,\theta}}{\mathrm{d}\varepsilon_j}\right)\varepsilon_j(r,z) \tag{3.32}$$

with the strain ε for the respective coordinate. The third and last term n_e takes the electronic-optical effect into account, which is the change of the refractive index by the inversion $\hat{n}$ of the material [72, 73]. It is expressed by:

$$n_e = \left(\frac{\mathrm{d}n_{r,\theta}}{\mathrm{d}\hat{n}}\right)\hat{n}(r,z) \tag{3.33}$$

Typically, the electronic-optical effect has only little impact on the wavefront for high energy amplifiers since the pump beam profile ideally is homogeneous and flat. In this case, it only contributes to a constant phase offset across the entire beam.

The mechanical and thermo-optical effects are considerably stronger but often lead to wavefront deformations which can be well compensated by either the amplifier geometry itself, see for example section 5.4, or by additional optical elements. The influence of the photo-elastic effect is more complex and strongly depends on the application. A more detailed explanation how to compensate for it is given in the following sub-section.

3.5 Depolarization effects

The term depolarization describes the change of an initially well-defined state of polarization of an input beam when it propagates through an amplifier. This change of polarization ultimately leads to an energy loss if polarization dependent optical elements or processes are used after the amplifier. In a gain medium, two sources of depolarization are found: intrinsic material properties or the thermally induced, photo-elastic effect when the medium is actively pumped.

3.5.1 Depolarization by intrinsic birefringence

Even without an active pumping, the bulk material of the gain medium can be a source of depolarization. During the growth process or the manufacturing, mechanical stress can build up inside the material which causes a local change of the refractive index by the photo-elastic effect. These regions are often also called growth lines or schlieren. Within them, the material changes its refractive index and behaves birefringent. For crystals that are grown with the Czochralski method this effect is particularly pronounced around the center or ”core region” of the crystal boule [76, 77].

As an example, figure 3.5 shows an imperfect Yb:YAG crystal that is examined between two crossed polarizers to visualize any birefringence. The bulk material exhibits significant growth lines which cause a locally different optical path length for different states of polarization. If such a crystal is used in an amplifier this translates into a local wavefront deformation and depolarization of the amplified beam. Thus, the growth lines are also imprinted into the beam profile.

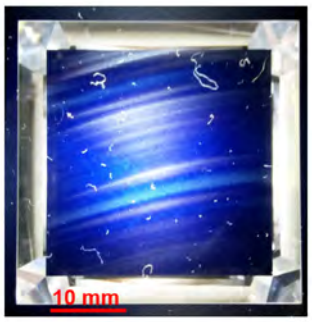

Figure 3.5: *Visible growth lines in a* 1 % *doped,* 5 mm *thick Yb:YAG crystal that is placed between two crossed polarizers.*

To avoid such material effects, the maximum allowed birefringence must be specified before purchasing suitable gain media. Furthermore, for large discs, e.g. the Ø38 mm Yb:YAG crystals of the 10 J amplifier of PFS, the core region of a crystal boule must be avoided. Alternatively, core-free growing methods can be used [78] or the crystal can be cut along the growth lines to minimize their impact.

3.5.2 Depolarization by thermally induced stress-birefringence

Another origin of depolarization is the mechanical stress that is induced by the thermal expansion of the gain medium during the pump process. The resulting photo-elastic effect changes the optical indicatrix of the refractive index in a typically non-uniform manner and thus, creates local birefringence. It is particularly strong for regions with steep temperature gradients, as these regions also exhibit the highest internal stress due to the different thermal expansion of the surrounding material.

A thorough, analytical analysis of the thermally originating, stress induced birefringence can be found in [79] and a practical study in [51]. Here, the description of the underlying process is only limited to a shorter, more intuitive approach. In figure 3.6 a disc-shaped gain medium is assumed that is only pumped in the center region. The thermal expansion creates two types of mechanical stress which are perpendicular to each other: the radial stress due to the elongation of the material and the tangential stress due to the widening of the diameter.

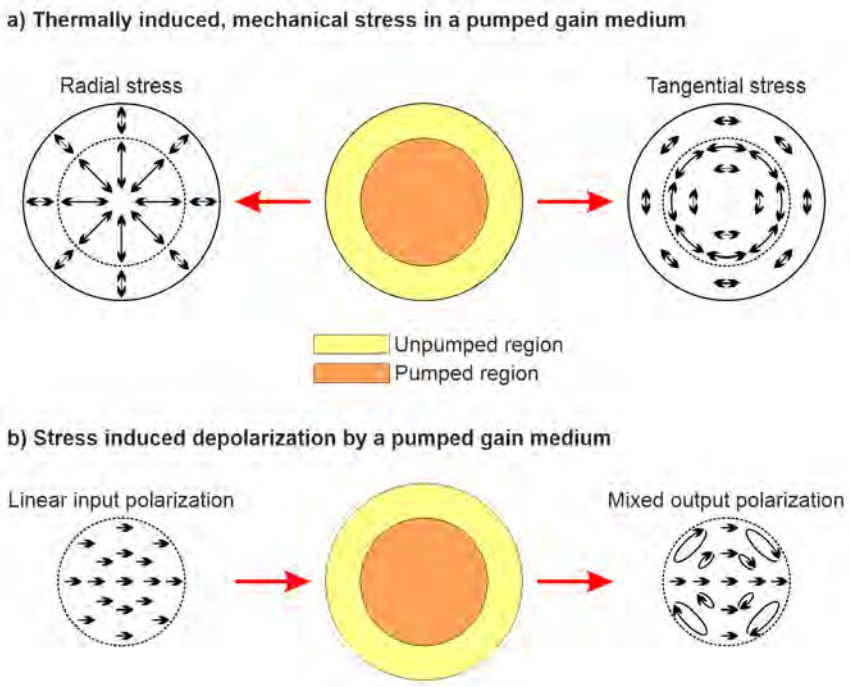

Figure 3.6: *Simplified sketch of a) the mechanical stress in a pumped gain medium due to thermal expansion and b) the depolarization of an incident beam that results from the stress-induced birefringence.*

Both types of stress typically have a different magnitude. As a result, the photo-elastic effect has a different impact for both directions on the refractive index. Because of this, even a normally isotropic material like YAG can behave birefringent under the influence of mechanical stress.

This behavior is particularly pronounced for regions with steep temperature gradients, for example at the borders of the pumped region in figure 3.6. Around this region the thermal expansion of the material strongly changes which further enhances the induced mechanical stress. In simple words, the hot material tries to thermally expands to the outside, but the surrounding ring of cold material resists this expansion.

If a linearly polarized beam passes through such a pumped gain medium, two things are observed:

- The local components of the beam with a polarization that is oriented along the direction of the tangential stress or the radial stress will not experience a change of the state of polarization. For both directions, the polarization is aligned along a principal refractive index of the optical indicatrix.
- Any other component with a different orientation is transversely depolarized due to the influenced of two different refractive indices of the optical indicatrix. The effect becomes stronger with increasing angle of the polarization towards one of the principal axes and also with the distance to the center, as the mechanical stress increases with the radius.

3.5.3 Methods for compensation

Several methods exist to minimize or to compensate for the induced depolarization.

Optimized crystal cut
An intrinsic minimization is achieved by choosing a suitable cut of the crystal lattice that exhibits the least influence of depolarization on a beam. This is even possible for cubic crystals like YAG since they behave non-isotropic if stress is applied [67, 80, 81]. For YAG the [111] cut proves to be the optimum since the depolarization losses are independent on the rotational orientation of the polarization. A further minimization of the losses can be achieved with the [110] cut, but it is very sensitive to the orientation of the polarization and to any misalignment.

Compensating quarter-wave plate
A compensation of the induced depolarization can be done by implementing a quarter-wave plate after the gain medium. It is positioned in such a way that a principal axis of the waveplate aligns with the linear polarization of the beam [82–84]. Therefore, the beam components with a linear polarization are not influenced, but any changes due to depolarization experience a partial compensation by the phase shift of the waveplate.

Pre-compensating quarter-wave plate and half-wave plate
A similar method is applied for the 1 J amplifier presented in chapter 7 which was originally inspired by [85]. Instead of implementing a quarter-wave plate after the gain medium inside of the multi-pass amplifier, a quarter-wave plate and a half-wave plate are positioned at the entrance of the amplifier. With them, an arbitrary state of polarization of the input beam can be generated. This allows to find a specific state of polarization for which the effects of depolarization are minimized. This method proved to work exceptionally well for moderate cases of depolarization.

Quartz rotator
For the final 10 J amplifier the previous method alone is not sufficient due to the significantly stronger thermal effects. Instead, a Quartz rotator is used to further compensate the depolarization [44, 86–88]. The quartz rotator is cut along the c-axis and therefore does not exhibit any birefringence for the incoming beam. It does however show an optical activity which rotates the polarization of an incoming beam by a well-defined angle, independent of the state of polarization. The amount of rotation is only defined by the wavelength of the incoming beam and the thickness of the rotator.

The compensation with a quartz rotator only works in combination with multiple passes of a beam through a gain medium, or the rotator is placed between two identical gain media. Typically, a 90° rotation angle is used. After the first pass, the state of polarization is rotated by 90° which effectively exchanges the radial and the tangential components. After the second pass, each component experienced once the influence of the radial stress and once the influence of the tangential stress of the material. Thus, both components accumulate the same phase retardation and the state of polarization is preserved.

The fundamental difference of using a quartz rotator instead of a waveplate is the ability to achieve the same rotation angle for any orientation or state of polarization, and thus for any position within the depolarized beam. More details on the implementation in the 10 J amplifier can be found in section 8.7.

Chapter 4

Heatsink development

The previous chapter showed that the material properties of Yb:YAG and Yb:KYW are temperature dependent. In particular the absorption and emission cross-sections decrease with increasing temperature. Therefore, it is important to apply a proper cooling to maximize the efficiency of the pump and amplification processes. The cooling and mounting of the gain medium in a heatsink also affects the beam profile and wavefront of an amplifier. The increased temperatures under operation may cause a thermal expansion, mechanical bending, thermal lensing, or depolarization. Besides this, the efficiency of the heat removal typically is the limiting factor for the achievable repetition rate of high energy amplifiers in general.

As a consequence, one of the most crucial and challenging development step of the new amplifiers of this thesis was the design and implementation of proper heatsinks for the gain media, which is the subject of this chapter.

Overview

4.1 Existing heatsink technology:
An overview of existing heatsink technology of comparable laser systems, description of the original heatsink of the 1 J amplifier of PFS.
4.2 Thermal measurements and simulations:
Temperature measurements of Yb:YAG crystals, performance of different heatsink materials, estimation of the heat generation within the crystals.
4.3 New heatsinks with glue or liquid metal interface:
CAD models and performance of the first iteration of new heatsinks for the new 1 J amplifier ”The Cube”, based on glue or liquid metal as thermal interface material.
4.4 Troubleshooting of the MKIII and AMKI:
Drawbacks of the two new heatsink designs MKIII and AMKI.
4.5 The seven golden rules for the perfect heatsink:
Seven design rules for the ideal heatsink of the high energy amplifiers of PFS.
4.6 One heatsink to rule them all – the hybrid MKX:
The latest heatsink design for the 10 J amplifier ”BigMama”, based on a hybrid combination of the gluing and liquid metal methods.
4.7 The transmissive MKVII heatsink:
A heatsink for the 100 mJ ”SuperBooster” amplifier with transmissive crystals, based on the technology of the MKX heatsink.
4.8 Troubleshooting of the MKX/MKVII and liquid metal:
Drawbacks of the latest heatsinks and of liquid metal for long-term operations.

4.1 Existing heatsink technology

Numerous techniques exist to efficiently extract the heat from a gain medium. The most prominent ones for high energy systems that are comparable to the PFS pump laser are:

- Direct water cooled, active-mirror Yb:YAG slabs in the LUCIA system [51, 96].
- Room temperature, high velocity helium-gas cooled multi-slabs of Yb:S-FAP in the MERCURY system [97].
- Cryogenic cooling with a gas flow around multi-slabs of Yb:YAG in the DiPOLE system [98, 99] or Yb:CaF_2 in the PEnELOPE system [93].
- Indium contacted Yb:YAG slabs on metal heatsinks in the TRAM amplifiers of the ILE [100].

There are several reasons why these techniques are not suitable for the PFS pump laser. The application of a cryogenic cooling is forbidden since pulse durations of less than a picosecond cannot be achieved with Yb:YAG due to the decreased bandwidth at cryogenic temperatures. Some of these techniques furthermore rely on transmissive gain media whereas the main amplifiers of PFS heavily rely on reflective, active-mirror gain media to minimize the required footprint of the laser. In the scope of this thesis, "active-mirror" describes a high-reflective (HR) coating on the back side of the gain medium which is contacted to a heatsink. Thus, the heat is extracted through this "active-mirror".

A direct water cooling of the active-mirror requires a highly sophisticated and complex heatsink design to allow for a homogeneous water flow and thus, for a uniform cooling of large sized crystals. The direct stream of water can furthermore enhance the impact of water vibrations on the beam stability. Also, the contact with water may cause a long-term degradation of the HR coating due to chemical and mechanical processes.

Of the listed techniques, the thermal contact between the crystal and a heatsink via an indium-foil is the most suitable one for PFS. However, it requires either high pressure or an elevated temperature to achieve a sufficient bonding and thermal contact between the two components. Thus, care must be taken to not introduce additional deformations of the gain medium that may affect the reflected beam profile or wavefront.

A similar heatsink technique was applied by C. Wandt for the original 1 J amplifier "The Tube" of PFS [28]. The heatsink is a polished copper mirror that is sold commercially for CO_2-lasers, see figure 4.1. The crystal is fixed to the copper surface with a UV-hardening acrylic glue (Panacol Vitralit 6127). Although the glue has a low thermal conductivity of $\sim 0.2\,\mathrm{W/(m\,K)}$, a layer thickness of less than 1 µm ensures a good thermal contact. The heat is extracted by water at room temperature, which flows through a single, U-shaped channel inside the copper mirror. This heatsink design proved to work in principle and an output energy of more than 1 J was achieved at a repetition rate of 2 Hz, a pump peak power of 10.5 kW and a pump pulse duration of 1.25 ms. This corresponds to an average pump power of ~30 W. Besides this success, the heatsink design also showed several drawbacks:

- To achieve the required layer thickness in the range of a micrometer, a considerable pressure has to be uniformly applied to the crystal which frequently causes deformations of the crystal surfaces and therefore also of the wavefront of the amplified beam.
- The thermal expansion coefficient of copper with $16\,\mathrm{K^{-1}}$ differs strongly from that of YAG with ~6 to $8\,\mathrm{K^{-1}}$. Under thermal load, this causes mechanical stress between the crystal and the heatsink which may induce further wavefront deformations.
- The gluing process is prone to fail and irreversible once the glue is hardened.

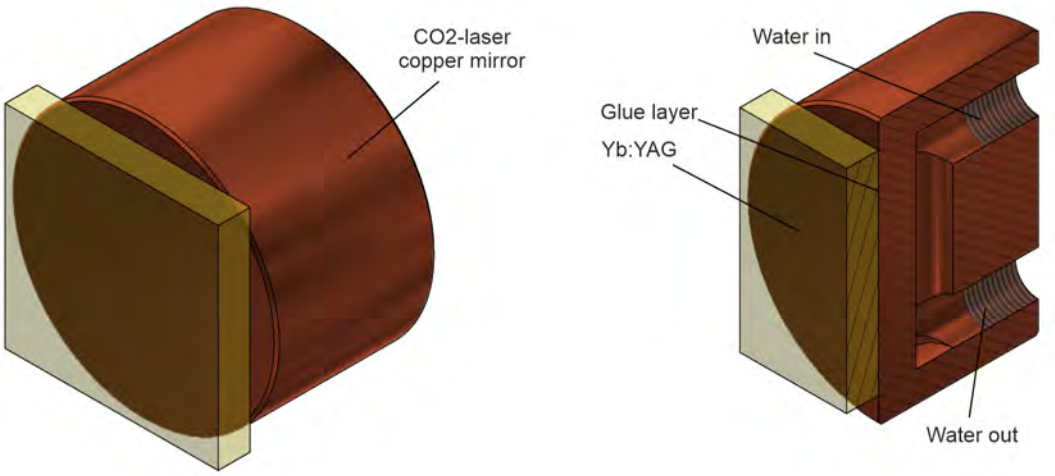

Figure 4.1: *CAD model of the original heatsink of the* 1 J *amplifier of PFS, in an isometric and section view with 1:1 scale. The heatsink consists of a* $40 \times 40 \times 6\,\mathrm{mm}^3$*,* 2 *% doped Yb:YAG crystal that is glued onto a water cooled,* CO_2*-laser copper mirror. The cooling water flows through a single, U-shaped channel.*

An example of the degraded beam quality due to the aforementioned drawbacks is shown in figure 4.2. The left picture is a recorded beam profile in the output image plane of the operating 1 J amplifier and the right picture shows the beam profile on an infrared detection card after 8 m of free space propagation.

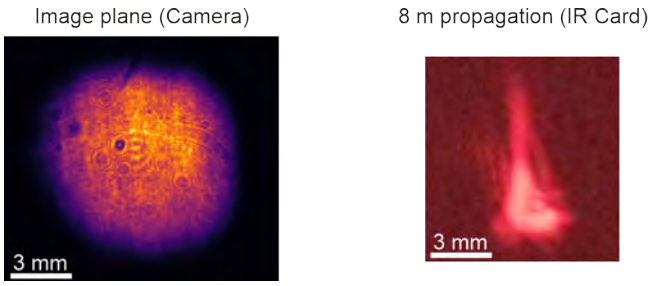

Figure 4.2: *Output beam profiles of the original* 1 J *amplifier recorded with a camera in the image plane (left) and with an infrared card after* 8 m *of additional free space propagation (right). Wavefront deformations are induced by the glued heatsink.*

The higher thermal loads of an operation beyond 2 Hz further impaired the beam profile and also revealed an insufficient thermal management of the amplifier in general. Thus, the desired repetition rate of 10 Hz could not be achieved with the original 1 J amplifier. As a consequence, a new heatsink concept as well as a better thermal management was required for the redeveloped version of the 1 J amplifier and the final 10 J amplifier of PFS.

4.2 Thermal measurements and simulations

The goal of any heatsink design is to efficiently extract the heat from the actively pumped gain medium. Since the temperature of the gain medium is directly linked to the stored heat, a more efficient heat extraction results in a lower temperature and hence a better efficiency of the pump and amplification processes. Also, a lower temperature reduces effects like thermally induced stress, thermal lensing or thermal drifts.

In order to simulate the generated heat and the resulting temperature in an active gain medium, a precise knowledge of all involved parameters is required. This includes:

- the exact dimensions, doping concentration, and cross-sections of the gain medium
- the precise pump parameters, especially the amount of pump energy that is converted to heat
- most importantly, the precise knowledge of the spatio-temporal evolution of ASE during the pump process since it contributes to reabsorption within the gain medium
- the exact dimensions and material properties of any part of the heatsink
- the parameters of the water cooling system
- the three dimensional evolution of the heat transfer through the gain medium and heatsink

It is obvious that most of these points cannot be determined with absolute precision. Thus, from experience, a simulation of the generated heat from scratch typically delivers insufficient results. It is therefore important to support the simulation with empirical data, for example with the measured average temperature of the gain medium in a comparable setup.

4.2.1 Measurement method for the gain medium temperature

A highly versatile method to measure the space and time resolved temperature of an active medium was developed by J. Körner et. al. [95]. In short, an enlarged probe beam with precisely known and stabilized wavelength is sent to the gain medium, an image of the beam is recorded after it passed the medium, and the space and time resolved absorption is measured. The amount of absorption depends directly on the absorption cross-section at the probing wavelength, which in turn is temperature dependent. Thus, the precise knowledge of this cross-section allows to retrieve the temperature.

The retrieved temperature is the average over the thickness of the gain medium. This method also allows to conduct the measurements directly in the amplifier and even in a vacuum environment, since the probe beam requires only little space. The accuracy is typically around $\pm 2\,^{\circ}\mathrm{C}$ for the temperature, 100 µm for the spatial resolution and below one second for the temporal resolution.

The application of this measurement method for PFS is sketched in figure 4.3. The measurement setup is built around an imaging 8-pass pump geometry, which is presented in detail in section 8.3. The geometry grants a pump absorption of almost 100 % in the implemented Yb:YAG crystal. The crystal is pumped by up to 30 kW at 938 nm, 10 Hz and a pulse duration of up to 1.5 ms. In addition, the whole system can be evacuated.

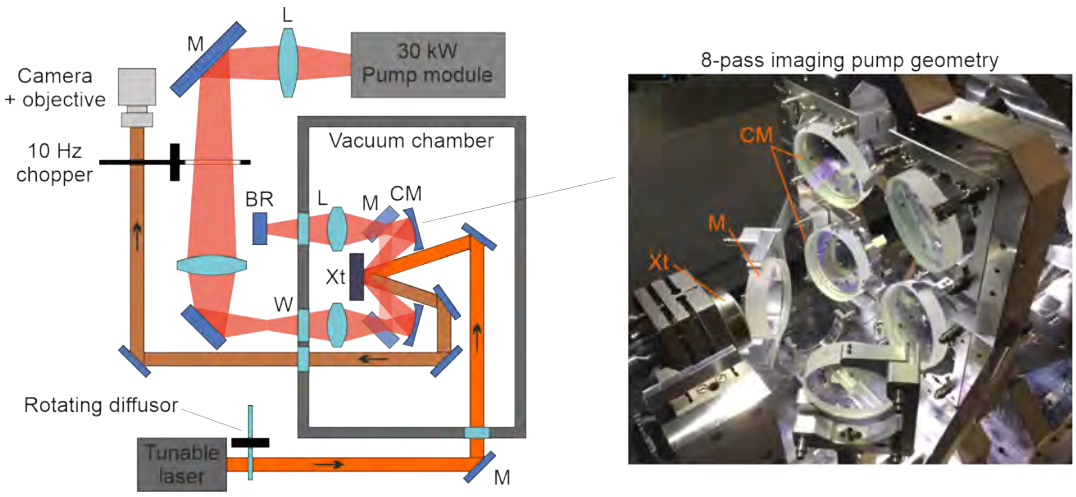

Figure 4.3: *Setup to measure the space and time resolved temperature distribution of an Yb:YAG crystal under thermal load. The crystal (Xt) is mounted in an imaging 8-pass pump geometry that ensures a pump absorption of almost* 100 *%. A tunable laser sends an enlarged probe beam with a narrowband spectrum stabilized at* 969 nm *to the crystal. A rotating diffuser minimizes the effects of coherent speckles on the beam profile. Upon passing the crystal, the beam is partially absorbed and afterwards recorded with a camera. An additional chopper wheel blocks any pump light during recording. The relative temperature change of the crystal is calculated from the intensity change of the sampling beam profile, which in turn is based on how the absorption cross-sections of Yb:YAG change with the temperature. M: Mirror, CM: Concave mirror, L: Lens, BR: Backreflector, Xt: Crystal, W: Window.*

The probe beam is sourced by a tunable diode laser that is stabilized at the 969 nm zero-phonon line of Yb:YAG in order to achieve the maximum absorption. A rotating diffusor in the probe beam path reduces the effects of coherent speckles in the recorded camera image and a chopper wheel blocks any pump light during recording.

An exemplary measurement with the setup is presented in figure 4.4. It shows the spatio-temporal temperature evolution of a Ø38 $\times$ 3 mm, 2 % doped Yb:YAG crystal that is mounted in a heatsink prototype and pumped at 30 kW, 10 Hz and 1.4 ms in a diameter of 23 mm FWHM. These parameters correspond to the worst case scenario for reaching an output energy of 10 J with the final 10 J amplifier of PFS. After switching on the pump module, it takes 16 s to reach a steady average temperature of 133 °C, at which point the pump module is switched off again and the gain medium cools down to the cooling water temperature of 16 °C.

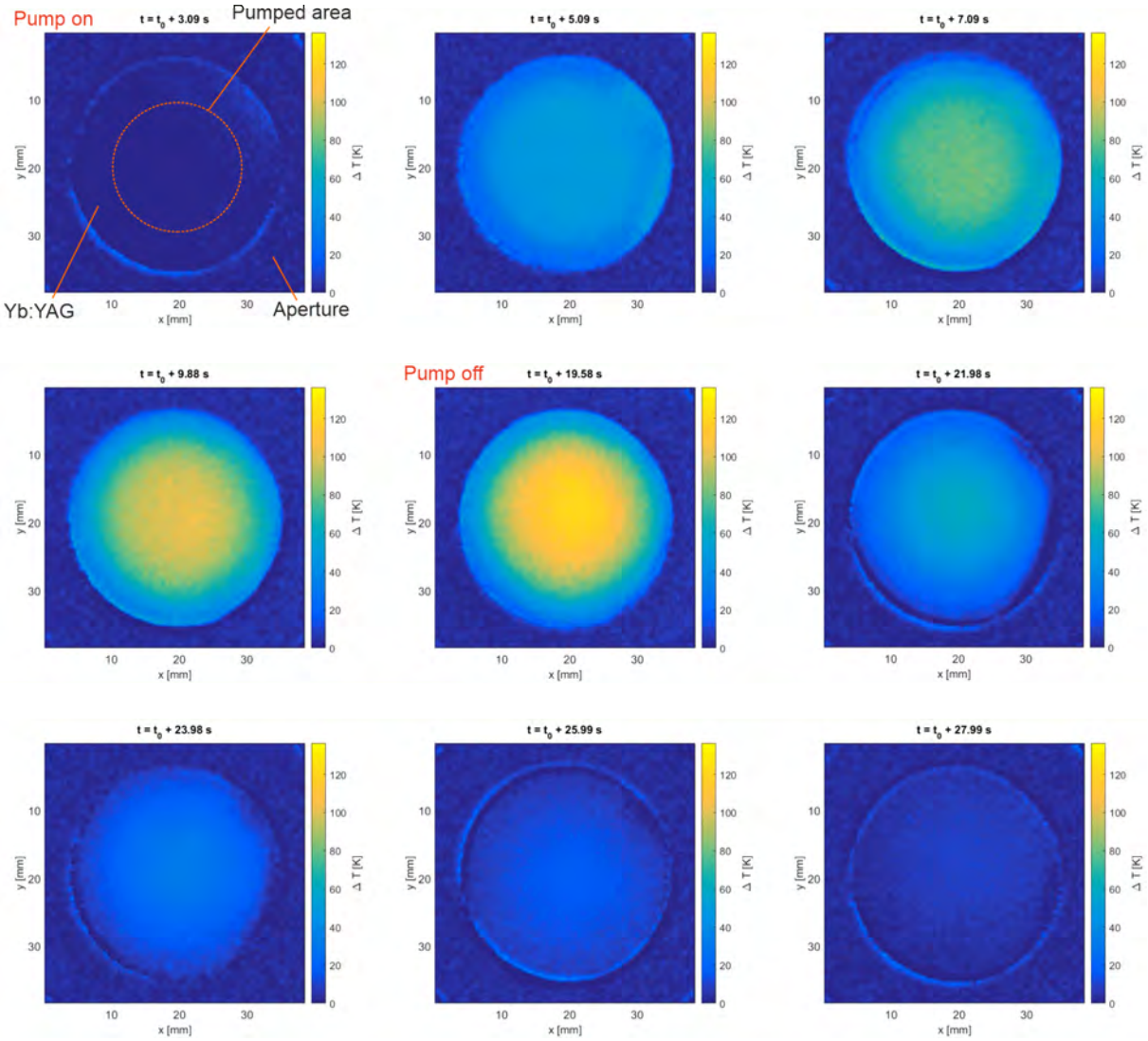

Figure 4.4: *Exemplary, spatio-temporal temperature evolution of a* Ø38 × 3 mm, 2 % *doped Yb:YAG crystal that is mounted in a heatsink prototype. The crystal is pumped at* 30 kW, 10 Hz *and* 1.4 ms *in a diameter of* 23 mm *FWHM and is cooled at a water temperature of* 16 °C. *The on and off times of the pump module are indicated in the respective sub-figure.*

4.2.2 Thermal performance of different heatsink materials

The temperature measurement setup was extensively used to evaluate the thermal performance of different heatsink materials, in particular for the critical interface between the heatsink and the crystal. For this purpose, a heatsink prototype was developed that allows for the combination of different materials and also to suppress ASE by channeling the cooling water around the barrel of the Yb:YAG crystal. A sketch of the prototype is shown in figure 4.5.

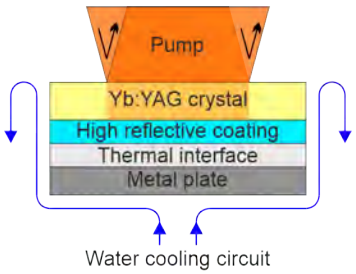

Figure 4.5: *Sketch of a heatsink prototype that is used to evaluate the performance of different heatsink materials. The crystal is surrounded by cooling water to guide out and suppress ASE.*

For the measurement campaign, a Ø38 × 3 mm, 2 % doped Yb:YAG crystal with reflective coating on the back side was used. The most promising heatsink materials that were evaluated are:

- A metal plate made from a sinter-alloy that contains 70 % molybdenum and 30 % copper (MoCu 70/30), which exhibits a similar thermal expansion coefficient as YAG and a thermal conductivity comparable to copper.
- An interface made of a silicone-free thermal paste that is commonly used for CPU heatsinks (”Hydronaut” from Thermal Grizzly Holding GmbH).
- An interface made of liquid metal with extraordinarily high thermal conductivity (”Conductonaut” from Thermal Grizzly Holding GmbH).
- An interface made of the same UV-hardening glue as in the original heatsink (”Vitralit 6127” from Panacol-Elosol GmbH).
- A direct water cooling without the metal plate and the interface layer.

In figure 4.6 the results of a measurement with the MoCu 70/30 metal plate and the thermal paste as interface material are shown. The crystal is pumped at 30 kW, 10 Hz and 1.4 ms in a diameter of 23 mm FWHM. Graph a) shows the evolution of the crystal temperature over time. After the pump module is switched on, the crystal takes 8 s to reach 90 % of the maximum temperature and another 8 s for the remaining 10 %. After that, the average temperature in the center of the crystal stays at ~133 °C. After the pump module is switched off, it only takes around 10 s to completely cool down the crystal.

Graph b) shows a cross-section of the lateral temperature profile of the crystal after it reached the highest temperature. The profile is rather smooth and center-symmetric, which indicates a homogeneous cooling performance of the heatsink prototype and also a uniform pump beam profile of the implemented 8-pass imaging geometry. The temperature profile follows an approximatetely spherical shape within a central diameter of 16 to 18 mm. Outside, the profile has a strongly non-spherical shape with steep edges in particular around the border of the pumped crystal region.

A comparison of the performance of all tested interface materials and the direct water cooling is presented in table 4.1. The table includes two settings of the pump module: one for the worst

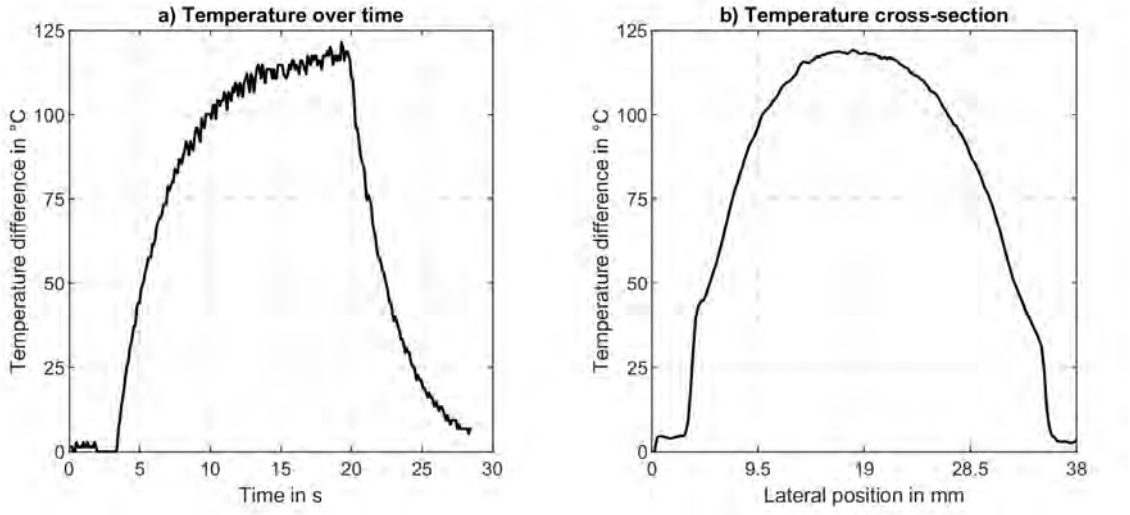

Figure 4.6: *Temperature measurement of a Ø38 × 3 mm, 2 % doped Yb:YAG crystal that is mounted in the heatsink prototype with a MoCu 70/30 metal plate and the thermal paste as interface material. a) Change of the average temperature over time. The pump is switched on at* 3 s *and off at* 20 s*. b) Cross-section of the temperature profile* 17 s *after switching on the pump module. Both data sets are taken in the center area of the crystal. The pump is set to* 30 kW *at* 10 Hz *and* 1.4 ms *within a pump profile diameter of* 23 mm *FWHM. The cooling water is set to* 16 °C*.*

case scenario of the 10 J amplifier with 30 kW, 10 Hz and a pump duration of 1.4 ms, and one for a more probable case with a pump duration of only 1 ms.

Table 4.1: *Different thermal interface materials and their performance in the heatsink prototype in combination with a Ø38 × 3 mm, 2 % doped Yb:YAG crystal. The crystal is pumped at* 30 kW, 10 Hz *and pump duration of* 1 ms *or* 1.4 ms *within a diameter of* 23 mm *FWHM. The cooling water temperature is set to* 16 °C*. TC: Thermal conductivity, Thickness: Thickness of interface layer, ΔT_{max}: Maximum temperature difference between crystal and cooling water upon reaching thermal equilibrium.*

Interface material	**TC in W/(mK)**	**Thickness in µm**	**ΔT_{max} at 1 ms in °C**	**Time to ΔT_{max} in s**	**ΔT_{max} at 1.4 ms in °C**	**Time to ΔT_{max}in s**
Thermal paste	11	100...300	72	12	117	16
Paste w/ vacuum	11	100...300	82	14	122	18
Glue	0.2	1	21	9	29	9
Liquid metal	70	100	17	8	28	9
Direct water	-	-	11	8	16	8

As expected, the best cooling performance is achieved with a water jet guided directly to the back side of the Yb:YAG crystal. The temperature rises by a maximum of 11 °C for a pump duration of 1 ms and by a maximum of 16 °C at the worst case pump duration of 1.4 ms. However, due to the non-optimized water jet a spatially inhomogeneous cooling is achieved which imprints severe intensity modulations into the amplified beam profile.

Slightly higher temperatures but high quality beam profiles are achieved with the glue and the liquid metal interface. Both implement a 3 mm thick MoCu 70/30 metal plate which acts as a low pass filter for spatial fluctuations of the cooling water flow. The thickness of the interface layers is set to values that can be reliably created. For liquid metal and glue as interface material, a maximum temperature increase of 28 to 29 °C is observed at a pump duration of

1.4 ms which reduces to 17 to 21 °C at 1 ms. Considering the accuracy of the measurement setup, both interface materials can be considered as equally performing.

The worst performance is achieved with the silicone-free thermal paste. As mentioned before, the temperature rises by a maximum of 117 °C in ambient air conditions. Theoretically, the thermal paste should only cause a 5 °C higher temperature than liquid metal. The origin of the extraordinarily high temperatures was found in a high thermal contact resistance between the paste and the crystal, which is caused by an insufficient mechanical or chemical contact on a microscopic scale. Thus, an efficient heat exchange between both materials is prohibited. This also manifests in a longer cooldown time after the pump module is switched off. The contact issues are also observed when detaching the metal plate. Most of the thermal paste sticks to the metal plate and almost no stains remain on the crystal.

Interestingly, the evacuation of the vacuum chamber only causes a minor temperature increase of 5 °C with the thermal paste at a pulse duration of 1.4 ms. This indicates the low contribution of air convection to the overall heat extraction from the crystal.

In conclusion, the heatsink materials of choice for PFS are a MoCu 70/30 metal plate combined with a thermal interface made of glue or liquid metal. Both variants offer an equally good cooling performance and a superior quality of the beam profile. Although the direct water cooling achieves lower temperatures, the more complex heatsink design and the potential degradation of the crystal coating by the constant water stream makes it a less desirable choice for PFS.

4.2.3 Estimation of the maximum heat load within an Yb:YAG crystal

The results from the temperature measurements were also used to estimate the amount of the generated heat inside of an Yb:YAG crystal under thermal load in a 10 J operation. Ideally, only the quantum defect of around 9 % between the ~940 nm pump and the 1030 nm seed is converted to heat. Due to reabsorption of spontaneously emitted photons and ASE, the actual amount of heat is much higher and can easily reach more than 50 % of the absorbed pump energy. Therefore, the knowledge of the generated heat in the crystal is critical for the design of new heatsinks.

A practical tool to simulate the crystal temperatures and the heat transfer across the heatsink assembly is Autodesk CFD. The tool allows to calculate the heat transfer in three dimensions and to include the flow dynamics of the cooling water. For this purpose, the CAD models of the crystal and heatsink are directly loaded into the tool and the material properties and boundary conditions are defined. Many of the material properties are typically only estimations based on data sheets or distributor notes. The impact of their limited accuracy on the simulation results, however, can be significant. It is therefore useful to simulate a worst-case scenario from which a maximum possible heat load within the crystal can be estimated. Thus, a heatsink design that is based on this heat load will safely achieve the required cooling in a worst case scenario, and probably perform even better in a real case scenario.

Measurement and simulation parameters

In the following, the maximum heat load of a Ø38 × 3 mm, 2 % doped Yb:YAG is estimated. For this, the crystal temperature is measured first in the previously presented setup. Afterwards, the heat load is estimated by implementing the crystal-heatsink assembly and the measured temperatures into a simulation with Autodesk CFD.

The crystal is pumped at 30 kW, 10 Hz, and 1.4 ms within a pump diameter of 23 mm FWHM. This corresponds to the worst case scenario of reaching an output energy of 10 J with the final 10 J amplifier. A heatsink similar to the prototype of figure 4.5 is used, where the crystal is glued on top of a thermal expansion matched MoCu 70/30 metal plate. For the measurement

and simulation, only the back side of the metal plate is cooled. No water flows around the barrel. Figure 4.7 shows the simplified CAD model of the heatsink assembly that is implemented in the thermal simulation.

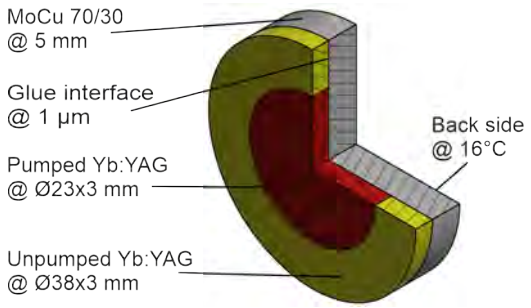

Figure 4.7: *Simplified CAD model for the thermal simulation of a Ø38 × 3 mm, 2 % doped Yb:YAG crystal that is mounted on a heatsink prototype.*

In order to estimate the heat load within the crystal, the following approach is used:

- A first guess of the heat load within the pumped region of the crystal is done based on the pump parameters. An additional heat load in the unpumped area is assumed to account for reabsorption effects of spontaneously emitted photons and ASE.
- The 3D heat transfer of the entire heatsink assembly is simulated in Autodesk CFD.
- The resulting temperature profile across the crystal is compared to the temperature measurements. If necessary, the heat load is adapted accordingly and the assembly is simulated again.
- Upon a close match between the temperatures, the simulation is stopped and the final heat load is retrieved

The following, ideal simulation parameters allow for a maximum heat transfer through the heatsink:

- The thermal conductivity of 2 % doped Yb:YAG is set to $8\,\mathrm{W/(m\,K)}$.
- The thermal conductivity of MoCu 70/30 is set to $190\,\mathrm{W/(m\,K)}$.
- The thermal conductivity of the UV glue is set to $0.2\,\mathrm{W/(m\,K)}$.
- The water cooling is considered ideal and the back side of the heatsink is always at 16 °C.

As a result, the simulation will retrieve the maximum possible heat load within the crystal, since a lower heat transfer also requires a lower heat load to generate the measured temperatures.

Measurement and simulation results

The measurement and simulation results are plotted in figure 4.8. The best match between both is found for a homogeneous heat load of 78.5 W in the pumped area of the crystal, which calculates to 18.5 % of the total absorbed pump energy. This means that 9.5 % of the generated heat is due to reabsorption of spontaneously emitted photons and ASE. In the unpumped area of the crystal, a heat load of 67 W must be set in the simulation to recreate the measured, lateral temperature cross-section. Overall, 35 % of the total absorbed pump energy is converted to heat in this worst case scenario.

The actual heat load within the crystal is expected to be lower than this. In the simulation, only a simplified CAD model of the heatsink is used. Furthermore, ideal values are assumed for the water cooling as well as for the thermal properties and thermal contact of all materials. In the actual heatsink prototype of the measurement, these values will be worse due to manufacturing and material tolerances. As a consequence, the heat transfer through the prototype will be lower and therefore also the required heat load to generate the measured temperatures.

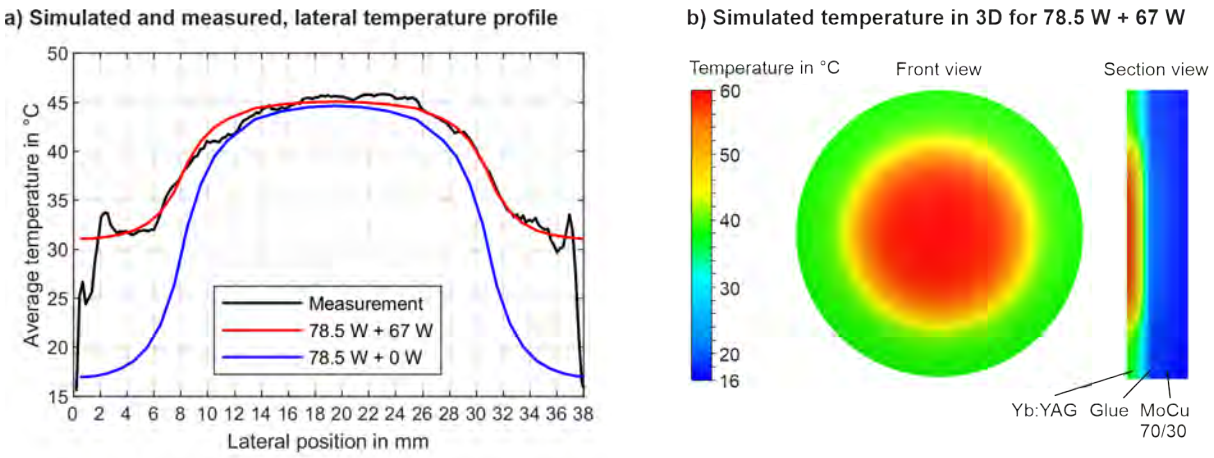

Figure 4.8: *a) Measurement and simulation of the lateral temperature profile of a Ø38 ×* 3 mm, 2 *% doped Yb:YAG crystal that is glued onto a water cooled MoCu 70/30 metal plate. The temperature is averaged over the crystal thickness. The crystal is pumped with a flat-top beam of* 23 mm *FWHM diameter at* 30 kW, 10 Hz *and* 1.4 ms *with almost* 100 *% pump absorption. Both simulations assume a heat load of* 78.5 W *in the pumped area, and one an additional heat load of* 67 W *in the unpumped area. The cooling water temperature is set to* 16 °C. *b) Simulated, absolute temperatures of the heatsink assembly in three dimensions for a heat load of* 78.5 W + 67 W.

Even though the heat load of the crystal might be lower in the actual heatsink prototype, some general conclusions can be drawn from figure 4.8:

- The biggest temperature drop of the heatsink assembly occurs in the crystal, with 57 °C on the front and 22 °C on the back. A minor drop of 1 °C is observed across the glue layer, and another drop of 5 °C across the MoCu 70/30 plate. Thus, the overall temperature is mostly determined by the crystal thickness.
- The strong temperature drop across the crystal will cause a mechanical bending in case the crystal is not fixed along the entire back side. This is particularly important for heatsink designs with thermal paste or liquid metal as interface material.
- The heat spread in the lateral direction of the crystal is minimal due to the comparably low thermal conductivity of Yb:YAG. Therefore, steep temperature gradients occur at the borders of the pumped region. In accordance with the fundamentals shown in sections 3.4 and 3.5, these gradients will cause a strongly non-spherical thermal lens and a depolarization of the amplified beam.
- The generated heat in the crystal is dominated by reabsorption of spontaneously emitted photons and ASE. Thus, the heat load and with it the temperatures of the crystal can be further decreased by applying an efficient suppression of ASE to the crystal.

4.3 New heatsinks with glue or liquid metal interface

Based on the insights of the thermal measurements and simulations, a first iteration of new heatsinks was developed, mainly for an application in the redeveloped version of the 1 J amplifier, "The Cube". Two heatsink variants where designed and manufactured in parallel: one based on the original glue concept, termed "MKIII heatsink", and one based on liquid metal as the thermal interface material, termed "AMKI heatsink". Both follow the goal of a reliable 10 Hz operation of the 1 J amplifier to enable daily experiments with the PFS system. The developed heatsink designs furthermore allow to implement them in the 10 J amplifier and thus, to evaluate their performance at a roughly ten times higher heat load.

4.3.1 The thermal expansion matched MKIII heatsink

As a starting point for the glue based MKIII heatsink, the following constraints were adopted, based on the experience with the original copper mirror heatsink:

- The crystal must be of active-mirror type.
- To minimize mechanical stress under thermal load, a heatsink material must be used that has a thermal expansion coefficient similar to YAG.
- The gluing process must be optimized in order to avoid a deformation of the surfaces and therefore, of the amplified beam wavefront.
- The heatsink must support a crystal thickness between 3 and 6 mm as well as a diameter of up to 40 mm to account for the large crystals of the 10 J amplifier.

There are two suitable heatsink materials with a high thermal conductivity and a thermal expansion coefficient similar to YAG. One is WCu 90/10, a sinter-alloy made from 90 % tungsten and 10 % copper. The other is MoCu 70/30, a sinter-alloy made from 70 % molybdenum and 30 % copper. The following table 4.2 summarizes the most important properties of the two alloys and compares them to Yb:YAG as well as pure copper, which is used in the original copper mirror heatsink.

Table 4.2: *Material properties of copper, WCu 90/10, MoCu 70/30 and Yb:YAG.*

	Copper	**WCu 90/10**	**MoCu 70/30**	**Yb:YAG**
Thermal conductivity in W/mK	390	170	>190	8...12
Thermal expansion coeff. in 10^{-6}/K	16	7.5	8.2	6...8
Youngs modulus in GPa	117	290	210	300
Density in g/cm^3	8.96	16.5	9.8	4.56

The MoCu 70/30 sinter-alloy was chosen for the heatsinks of PFS although WCu offers a higher tensile strength at roughly the same thermal properties. The main reason is the easier and less hazardous machining of MoCu 70/30 for the in-house workshop. The thermal expansion coefficient of MoCu 70/30 almost perfectly matches that of Yb:YAG. In comparison to pure copper, the thermal conductivity is reduced by a factor of two, but it can be compensated by a reduced material thickness of the heatsink due to the higher Youngs modulus. The MoCu 70/30 for the heatsinks of this thesis is supplied by the company H.C. Starck GmbH.

Mechanical design of the MKIII

The CAD model of the developed MKIII heatsink can be seen in figure 4.9. The core part is a 2" wide front plate made of MoCu 70/30. The front side is polished to a flatness below 1 µm and electro-chemically coated with nickel to increase the surface quality and to improve the gluing contact with the crystal. Both processes were done by the company LBP Optics Ltd.

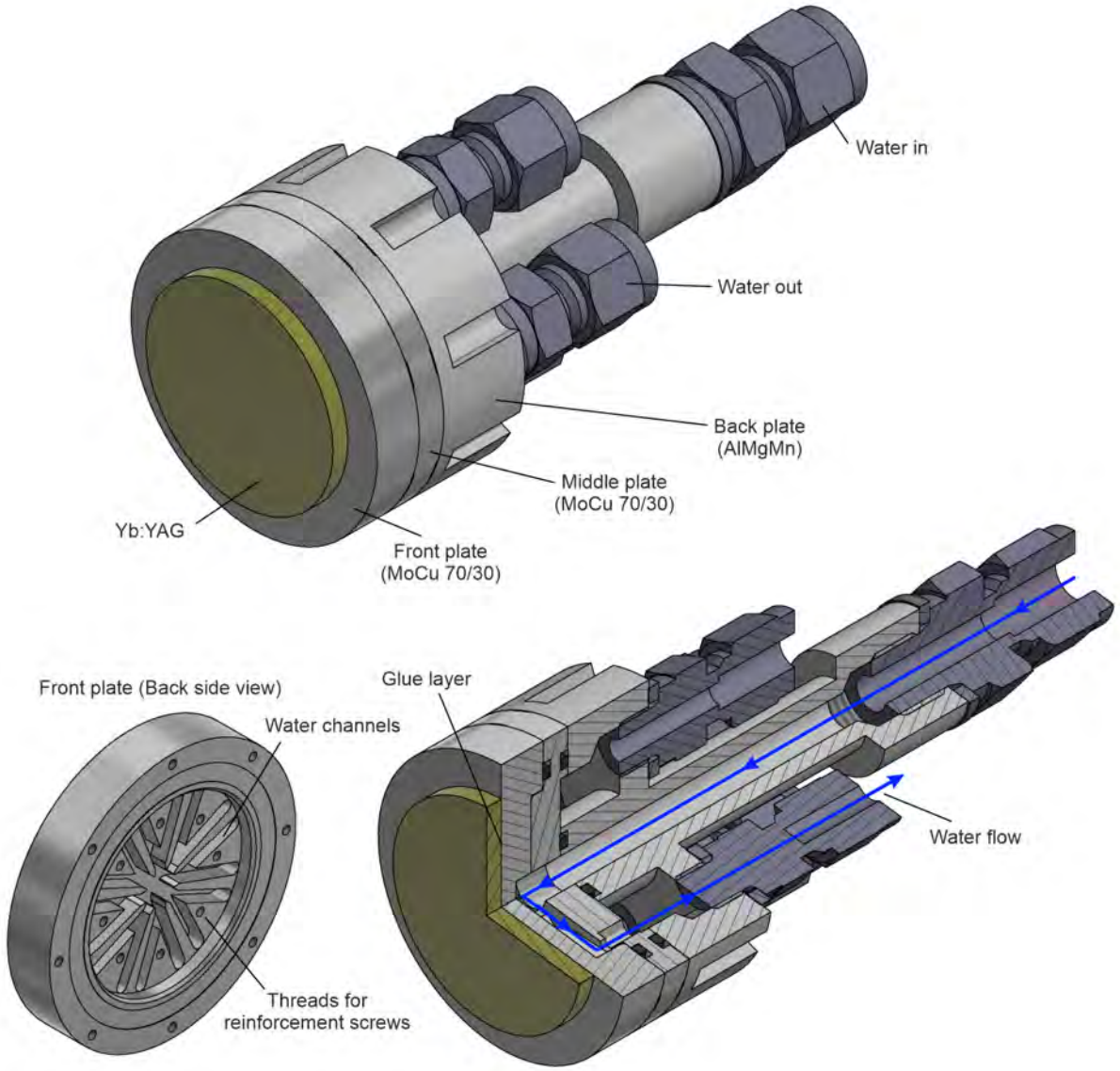

Figure 4.9: *CAD model of the MKIII heatsink with 1:1 scale. A Ø38 mm Yb:YAG crystal is glued to a thermal expansion matched, polished MoCu 70/30 metal front plate via a 1 µm layer of UV hardened glue (Panacol Vitralit 6127). The back side of the front plate contains radial symmetric water channels that spread the incoming water stream from the central part of the heatsink evenly to the outer parts. The middle plate made from MoCu 70/30 separates the water inlet from the outlet and has optional reinforcement screws that connect the front plate in order to reduce a water pressure induced bending. A reservoir in the back plate homogenizes the water flow before water exits the heatsink.*

The back side of the front plate contains water channels which guide an incoming, central water stream towards the outer areas of the heatsink. This way, a homogeneous and radial symmetric cooling profile is guaranteed. The effective thickness of the front plate is 3 mm and accounts for the two times lower thermal conductivity compared to the original, 7 mm thick copper heatsink. As a result, both heatsinks theoretically have a similar heat transfer according to Fourier's law:

$$\dot{Q} = \lambda \cdot A \cdot \frac{(T_1 - T_2)}{d} \tag{4.1}$$

where $\dot{Q}$ is the heat flux flowing from the warm side of the front plate to the cold side, λ the thermal conductivity of the material, A the area through which the heat transfer takes place, T_1 and T_2 the temperatures of the hot and cold side of the front plate and d the thickness of it.

A large water reservoir located in the back plate ensures a homogenization of the water flow before it exits the heatsink. It further improves the homogeneity of the cooling, similar to the technique used in [96]. Since the back plate does not experience any considerable temperature increase, standard AlMgMn is chosen as material. This aluminum-alloy also proves to be much more corrosion resistant to deionized water than other alloys with additional copper and lead inside.

Analysis of mechanical bending

A middle plate made from MoCu 70/30 separates the water inlet from the water outlet. Additional screws located in the center connect the front plate to the middle plate, which decreases the bending of the front plate due to water pressure. This is particularly important since the front plate only has an effective thickness of 3 mm and water pressures of the operated chillers at PFS typically reach up to 5 bar.

A mechanical stress simulation of the heatsink was done with the FEM stress analysis tool of the CAD software Autodesk Inventor. The results are shown in figure 4.10 together with a sketch of the heatsink.

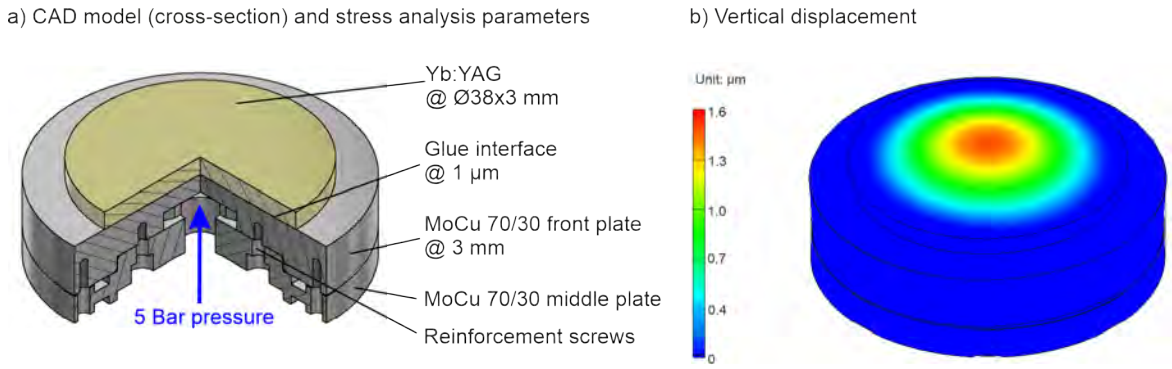

Figure 4.10: *Autodesk Inventor FEM stress analysis of the MKIII heatsink when cooling water pressure is applied. Left: Model for the stress analysis with* 5 bar *of pressure applied to the center of the front plate. Right: Vertical displacement of the front plate due to the water pressure.*

A vertical displacement of 1.6 µm in the center of the surface is observed for a 3 mm thick front plate and a water pressure of 5 bar applied to the back side of it. Assuming a spherical shape, this translates into a radius of curvature of over 1000 m which can be neglected for the operation of the 1 J amplifier.

Modified gluing process

Gluing of the crystal is done by hand with only minor pressure applied to the central area of the crystal rather than using heavy weights as with the original copper heatsink [23]. This technique has the advantage that slight deformations of the front plate are compensated by a varying thickness of the glue layer. Thus, these deformations do not affect the crystal or the wavefront of the amplified beam. With the right amount of UV glue (Panacol Vitralit 6127), an average layer thickness of less than 1 µm and a good thermal contact is achieved. To obtain an optimum wavefront, the proper order of assembly must be followed:

- First, the front plate and the middle plate must be screwed together. The induced mechanical stress, especially from the reinforcement screws, slightly deforms the front plate surface.
- Second, the crystal is glued with only minor pressure applied in order to allow the glue layer to compensate for the introduced deformations.

Performance improvements with the MKIII
Overall, the MKIII heatsink performed well in the new 1 J amplifier The Cube and solved many issues that emerged with the original heatsink. The cooling performance enabled an efficient operation of The Cube at a repetition rate of 10 Hz, which is thoroughly described in chapter 7. Furthermore, the MKIII proved to be mechanically stable in ambient air and also in vacuum.

Figure 4.11 shows the remarkable improvement of the wavefront of the amplified beam by the implementation of the new heatsink. The pictures are taken with a reduced output energy during a fully pumped 10 Hz operation of The Cube. The more homogeneous beam profile in the image plane mostly arises from higher grade crystals and a better optical system of The Cube. The actual impact of the new MKIII heatsink can be seen in the beam profile after 8 m of additional free space propagation. Besides minor features due to diffraction and bulk-effects of the crystal, the beam shape remains constant. Increasing or decreasing the thermal load does not affect the beam quality. This shows that a lower pressure during gluing and an expansion matched heatsink material are a significant improvement over the previous, copper based heatsink.

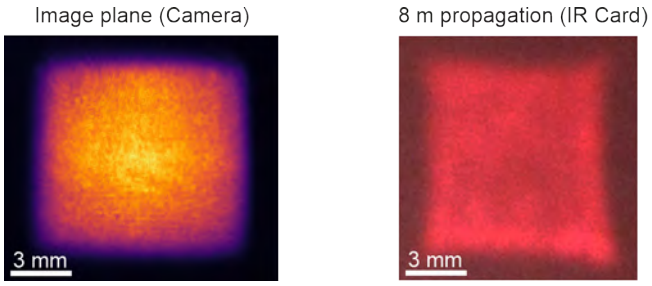

Figure 4.11: *Output beam profiles of The Cube amplifier using an MKIII heatsink with a Ø38 × 3 mm Yb:YAG crystal. Left: Beam profile in the image plane recorded with a camera. Right: Beam profile after 8 m of additional free space propagation recorded with an infrared card.*

4.3.2 The liquid metal AMKI heatsink

The AMKI heatsink was developed to solve one remaining issue with the gluing technique: the gluing process is prone to fail and irreversible. Failures can be for example trapped particles or bubbles in the glue layer or mechanical stress caused by the shrinking of the glue during hardening. Both can strongly degrade the reflected wavefront. These irreversible failures are particularly critical for the implementation of Yb:YAG ceramics with an ASE absorbing cladding, since they cost a magnitude more than crystals and can have lead times of over a year.

The issue is solved by exchanging the glue interface with a layer of liquid metal. For the AMKI, a special type of Gallinstan was chosen (”Conductonaut” from Thermal Grizzly Holding GmbH). It is an eutectic mixture of mainly indium, gallium and tin. Conductonaut has a similar viscosity as water at room temperature and above. Therefore, no force is required to generate a thermal contact between the crystal and the heatsink. The liquid metal can also be wiped off the crystal without leaving stains within the first hour after assembly. Besides this, the most distinctive feature of Conductonaut is an extraordinarily high thermal conductivity of >70 $\mathrm{W/(m\,K)}$, which is more than 300 times higher than that of typical UV hardening glue.

Mechanical design of the AMKI
The CAD model of the AMKI is presented in figure 4.12. The core part of the heatsink is a thin, water cooled MoCu 70/30 plate termed ”Cavity plate”. A ~100 µm thick cavity that is filled with liquid metal is created between this plate and the reflective back side of the crystal or ceramic.

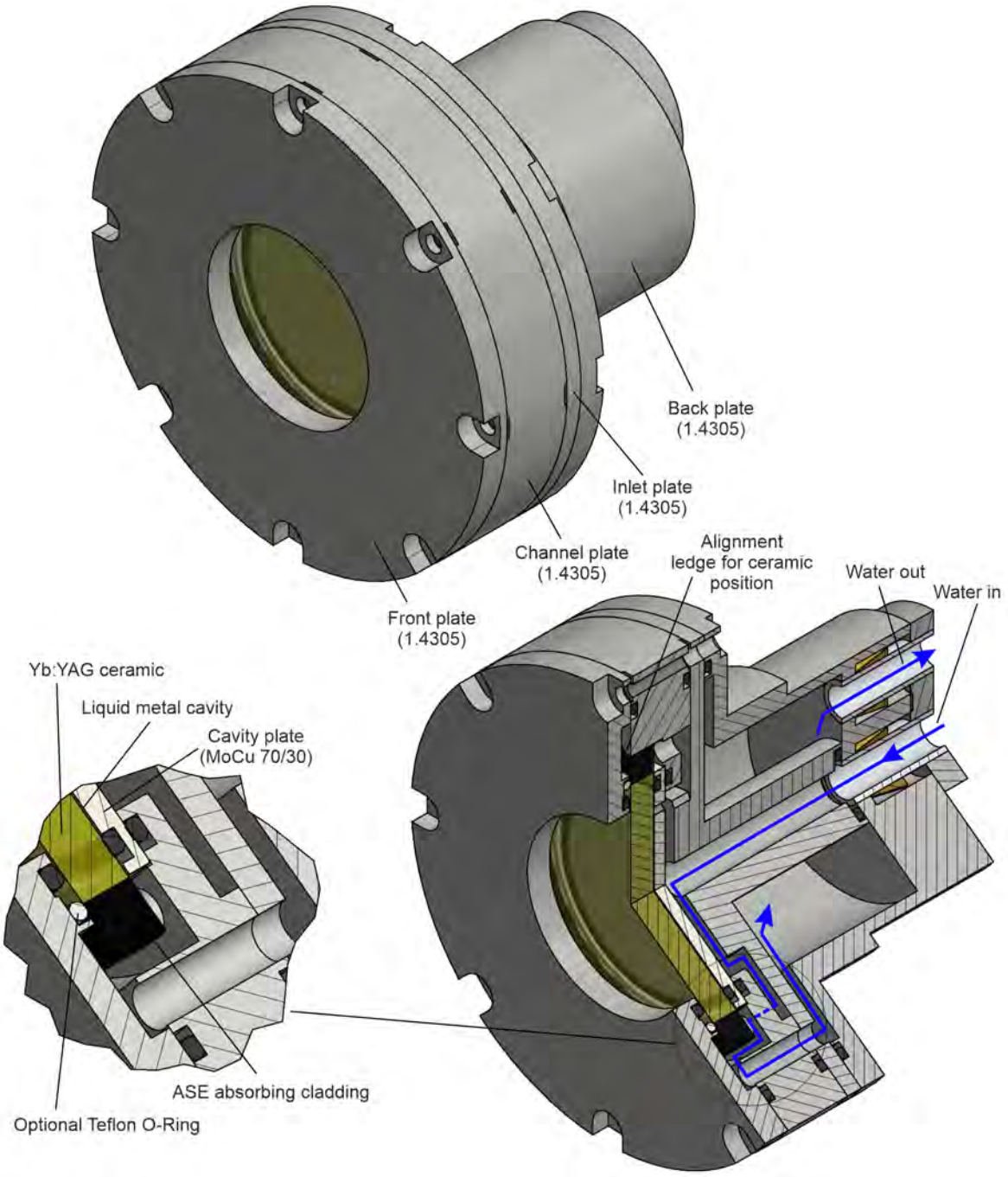

Figure 4.12: *CAD model of the AMKI heatsink with 1:1 scale. A Ø55x5 mm Cr:cladded Yb:YAG ceramic is sandwiched between the front plate, the cavity plate, and the channel plate. The empty space between the cavity plate and the ceramic is filled with liquid metal ("Conductonaut" from Thermal Grizzly Holding GmbH). The back side of the cavity plate is cooled by a central water stream. Afterwards, the water is channeled around the cladding of the ceramic which heats up due to the absorption of transverse ASE. A large water reservoir in the back plate ensures a homogenous water flow before water exits the heatsink. Only the cavity plate is made from MoCu 70/30. All other metal parts are made from V1.4305 steel to reduce corrosion from DI water.*

A total of three O-rings is implemented in the crystal-cavity-plate sub-assembly to ensure a sufficient sealing. They also permit a movement or bending of the entire sub-assembly rather than only of a single component when an over- or underpressure is applied. This keeps the cavity thickness constant when for example the amplifier is evacuated or the cooling water applies pressure to the cavity plate.

The underlying water cooling concept is similar to that of the MKIII. A central water stream is directed onto the cavity plate and diverted radially to the outer areas of the heatsink. To account for the increased heat load in the ASE absorbing cladding of a ceramic, the water stream is further channeled around the edges of the cladding. This also improves the ASE suppression for uncladded crystals since the water acts as an index-matching liquid and more ASE is coupled out of the crystal.

All parts except the cavity plate are made of V1.4305 steel, which is corrosion resistance against deionized water and also against the highly corrosive Conductonaut.

Performance of the AMKI
The implementation of the AMKI heatsink in The Cube was highly successful and showed a similar performance as the MKIII heatsink. Together with the cladded ceramics, an outstanding beam profile as well as a record output energy of up to 2 J at 10 Hz was achieved with an optical-to-optical efficiency as high as 14 %. A more detailed description of the performance is given in section 7.5.

This success proves the enormous potential of liquid metal to replace the failure prone gluing technique, despite a few challenges that exist with this new technique. These are mainly: the tendency of air bubbles in the liquid metal layer, a mechanical bending of the crystal or the ceramic due to the thermal expansion, and the easier cracking of brittle coatings due to the mechanical pressure exerted by O-rings. More details on these challenges and how to solve them are given in the following section.

4.4 Troubleshooting of the MKIII and AMKI

The two new heatsinks showed a significant improvement of the performance compared to the original copper mirror heatsink. With both designs a reliable 10 Hz operation of the redeveloped 1 J amplifier The Cube was achieved, with generally superior beam qualities. Contrary to this, several design drawbacks were found. They eventually resulted in a second, further improved iteration of new heatsinks. The most important drawbacks are described in this section.

4.4.1 Drawbacks of the MKIII and the gluing process

One of the major challenges for the MKIII design is still the gluing process. At least half of the gluing attempts failed due to different issues that affect the beam profile and wavefront. These issues are best explained with figure 4.13 which shows the amplified beam profile in the image plane of the 10 J amplifier. Two MKIII heatsinks are used with Ø38 × 3 mm Yb:YAG crystals glued on top. Each crystal is passed 10 times by the laser beam. The features seen in the beam profile of figure 4.13 a) originate from both heatsinks and can be divided into two categories:

- High intensity spots are scattered across the beam profile. They exhibit intensities up to 10 times higher than the surrounding area and originate from one heatsink.
- Newtonian like rings and bright, deformed lines appear in the image plane as well as in the propagated beam. They originate from the other heatsinks.

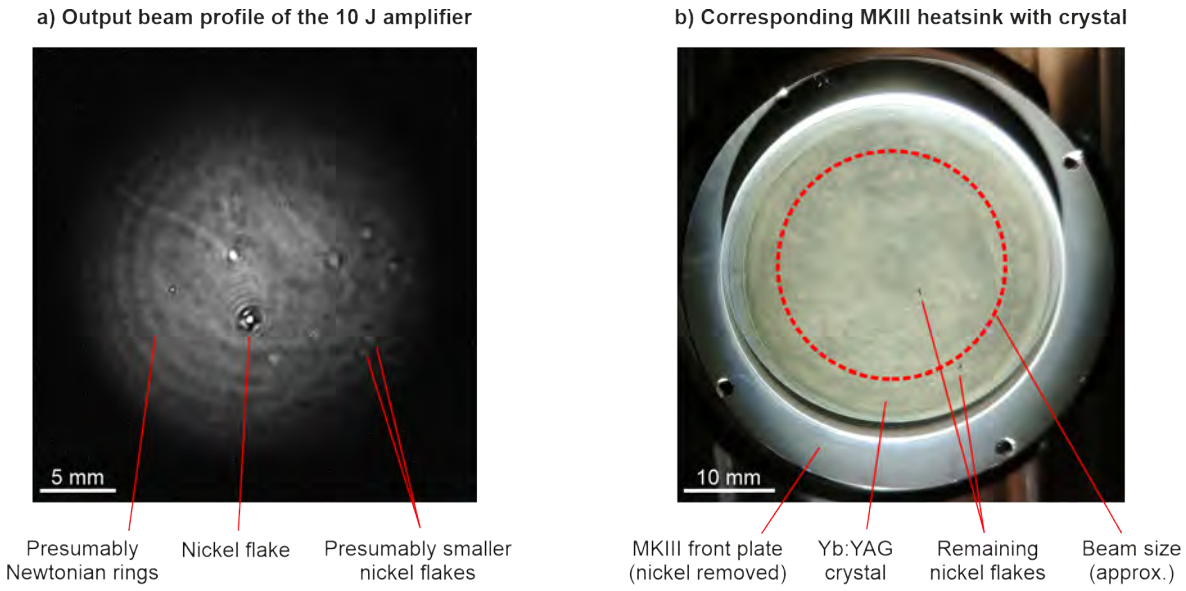

Figure 4.13: *a) Amplified output beam profile of the* 10 J *amplifier that shows several features which originate from the two implemented MKIII heatsinks. b) Camera picture of one implemented heatsink with a Ø*38 × 3 mm *Yb:YAG crystal glued on top. The nickel coating of the front plate was removed before gluing, but several visible nickel flakes remained on the surface.*

All of the features appear after gluing the crystals to the heatsinks. Imperfections of the crystals can be excluded, since preceding quality control measurements of the bare crystals in the same amplifier showed a flawless bulk material, polish, and coating.

Some of the high intensity spots are connected to less than 2 µm thick nickel flakes on the surface of one MKIII heatsink. These flakes remained after removing the nickel coating via ultra-sonic etching. This step was necessary since the nickel coating occasionally lost adhesion to the porous MoCu 70/30 sinter-alloy surface in some areas. The brightest spot in the beam profile of figure 4.13 a) for example corresponds to the big, visible nickel flake in the center of figure 4.13 b). Although there are many more, comparably large features and bright spots in the beam profile, not all of them have a visible counterpart on the surface of one of the two heatsinks or the crystals. Their origin is still a topic of ongoing investigations.

The same is also true for the Newtonian like rings in the beam profile, which still lack a conclusive explanation. Interestingly, these rings align well with actual Newtonian rings that can be seen in one heatsink when it is illuminated with a coherent light source. The actual Newtonian rings originate from an interference in the glue layer between the slightly spherical heatsink surface and the flat crystal back side.

In other heatsink assemblies, features like dark spots in the beam profile or sine-wave patterns in the wavefront emerged after gluing. Thorough investigations of the origin of all features were conducted with different UV glues, heatsink materials, surface topologies and gluing techniques. For this purpose, a separate diagnostic system was developed, which enables 6 imaging passes on the heatsink. This allows to investigate the effects on the beam profile and the wavefront before, during and after the hardening of the UV glue. Two of the conducted measurements are presented in appendix A.

The following conclusions can be drawn from the conducted investigations:

- If the UV glue Panacol Vitralit 6127 is applied, features in the beam profile and the wavefront appear as soon as the hardening process is initiated with UV light, not before.
- If the UV glue Epotek OG 142-82 is applied, no features appear before, during and up to 7 hours after hardening. Between 7 and 72 hours, the same features appear, but with a lower magnitude.
- Features are observed with pumped or unpumped crystals as well as with standard HR mirrors that are glued along their coated side.
- The emerging features are virtually independent of the mechanical pressure that is applied to generate a thin glue layer.
- Surface imperfections of the heatsink with a height of less than a micrometer are sufficient to cause significant modulations in the beam profile and the wavefront.
- A varying thickness of the glue layer between 1 µm and 10 µm has no observable effect on the emergence and magnitude of the features.

As stated before, there is no conclusive explanation for all features yet and investigations are still ongoing. Part of the features can be explained with the mechanical force that is exerted on the crystal by a shrinking ratio of the UV glue. For the applied two glues, this ratio is specified as less than 3 %. This shrinking may cause a deformation of the crystal surface and therefore also of the reflected wavefront of the beam. The fact that these wavefront deformations turn into an intensity modulation in the image plane can be explained to some extent with the imaging system itself. The alignment precision is limited and each pass might have a slightly shifted image position along the optical axis. Thus, a perfect re-imaging is not achieved. Furthermore, high spatial frequencies are filtered out by the apertures of the imaging optics.

A different explanation is required for the Newtonian like rings or sine-waves of the wavefront, and also for the extraordinarily high intensity modulations that are connected for example to the nickel flakes. For this, the leakage of the laser beam through the HR coating of a crystal or mirror could be responsible which may cause an etalon-like interference effect between the coating and the reflective heatsink surface. This effect potentially influences the optical properties of the coating, such as the reflectivity and the penetration depth of the beam. The impact strongly depends on the distance and alignment between both surfaces and their reflectivities. As a consequence, a locally varying distance that is caused for example by a nickel flake may result in a locally varying reflectivity and penetration depth of the beam. As a consequence, also the intensity and wavefront of the reflected beam vary locally.

In order to prove this theory a comprehensive simulation is required which allows to investigate the properties of the multi-layer stack of the HR coating when it is contacted to the reflective heatsink surface. This is possible for example with the Optilayer software (OptiLayer GmbH) and future activities on this topic are planned.

As a conclusion from the observations, the chances of a successful gluing are maximized when the heatsink surface is perfectly flat and without any features. Also, the crystal must be aligned as parallel as possible to the surface. A UV glue with the lowest possible shrinking ratio is preferred.

4.4.2 Drawbacks of the AMKI and liquid metal

The AMKI heatsink with liquid metal avoids all of the issues that arise with the gluing method. Furthermore, the liquid metal proves to be a thermal interface material with an exceptional potential for the cooling of laser crystals. Most of the drawbacks that emerged with the AMKI heatsink are directly related to the mechanical design rather than the liquid metal. The most important ones are summarized in figure 4.14.

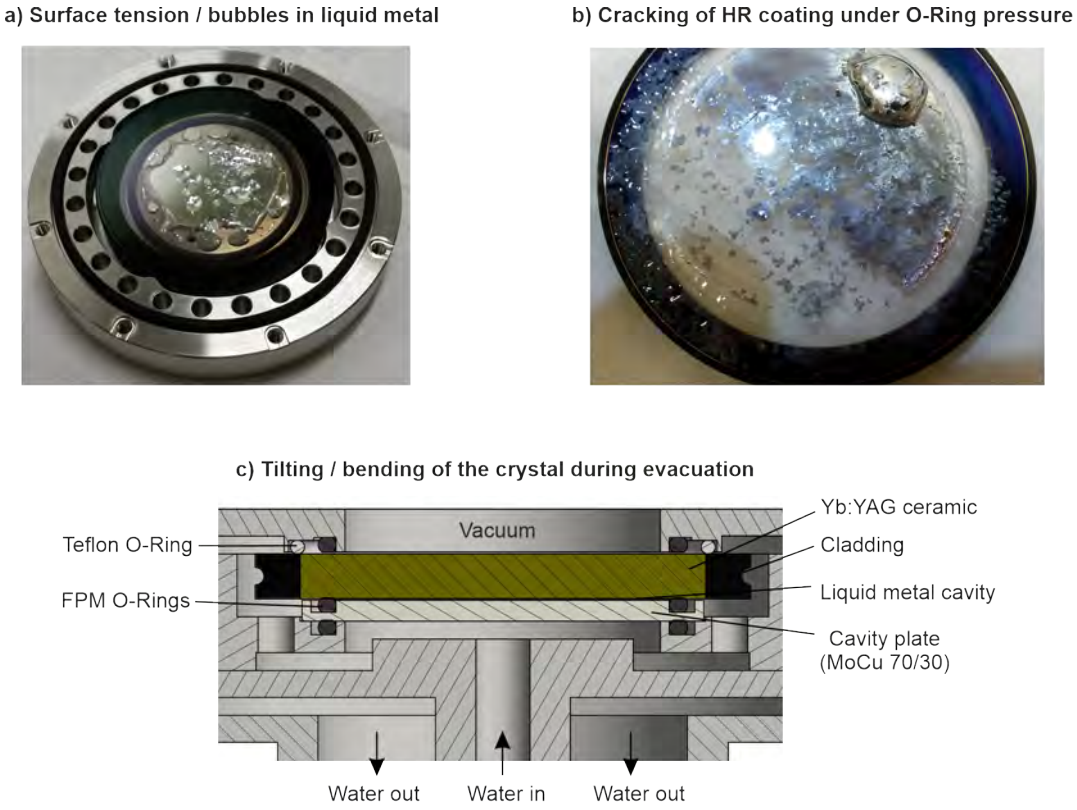

Figure 4.14: *Different challenges of using the AMKI heatsink with liquid metal. a) Air bubbles at the interface between a cladded ceramic and the liquid metal. b) Cracking of a brittle HR coating due to mechanical pressure of O-rings. c) Tilting of the crystal/ceramic during evacuation due to a lack of a rigid fixation in the O-ring based assembly.*

One of the distinctive properties of liquid metal is a significant surface tension. Although the material is as liquid as water, this surface tension increases the challenge of creating a homogeneous thermal interface layer. Often, bubbles or holes appear at the interface to the crystal or ceramic which drastically reduce the local heat transfer and therefore affect the beam profile. Due to the reversible assembly of the AMKI heatsink, this can be solved by trial and error but a more convenient heatsink design is desirable.

Two more issues in the AMKI design are of mechanical origin. In general, some batches of the Yb:YAG crystals and ceramics of PFS contain HR coatings which are rather brittle. The O-rings of the heatsink exert a force onto these coatings which caused them to occasionally crack. Although this is a manufacturing issue of the coating itself, the heatsink design further enhances it. The anti-reflective (AR) coatings proved to be more robust because of their thinner layer structure. A corrosive effect of the liquid metal can be excluded since the cracking issue happened also without any interface materials and it stopped entirely after switching to a new coating type.

Another issue arises from the lack of a fixation of the crystal or ceramic. Since they are mounted between O-rings, an external pressure or the thermal expansion under operation can cause a tilt

or bending. This is particularly pronounced when evacuating the amplifier. Furthermore, the direction of the tilt is typically not reproducible. The application of a Teflon O-ring decreases the tilting issue but it causes a noticeable degradation of the reflected wavefront.

As a conclusion, the liquid metal proves to solve all gluing related issues, but a mechanically more sophisticated heatsink design is required.

4.5 The seven golden rules for the perfect heatsink

Seven ”golden rules” for a high performing heatsink design for PFS were deduced from the performance and drawbacks of the MKIII and AMKI heatsinks:

1. The success rate of a crystal-to-heatsink assembly must be high to avoid wasting crystals and in particular ceramics. It requires:
   - Liquid metal as thermal interface for a reversible assembly in case of failures.
   - Glue as thermal interface in combination with a perfect heatsink surface.
   - Ideally a removable glue if it is applied as thermal interface material or as a fixation between the crystal and the heatsink.
2. The thermal interface between the crystal and the heatsink must be of high thermal conductivity and homogeneous over the full area. This allows for a high efficiency of the cooling and a high quality beam profile. It requires:
   - Glue or liquid metal as interface material between the heatsink and the crystal.
   - A homogenizing metal plate between the thermal interface and the water cooling.
3. Attaching the crystal to the heatsink must not influence the beam profile and wavefront. It requires:
   - In general a weak mounting of the crystal with a minimum force applied to it.
   - Ideally no fixation by O-rings, or if unavoidable only by O-rings as soft as possible, which also minimizes the chances of cracking a brittle coating.
   - If the crystal is glued, a perfectly flat and featureless surface and a minimum pressure to achieve a thin glue layer.
4. Any force that is exerted on the crystal and its coatings during operation must be minimized to prevent negative effects on the wavefront or even damages. It requires:
   - A thermal expansion matched material if the crystal is glued onto the heatsink.
   - A minimized pressure difference between the front side and back side of the crystal if the heatsink is used e.g. in vacuum.
5. The heatsink assembly must have a high mechanical stability and it must suppress vibrations. This is essential for low drifts, beam pointing and also timing jitter. It requires:
   - A massive metal body to dampen vibrations, e.g. from the water connections.
   - A not too turbulent water flow inside the heatsink, as it also generates vibrations.
   - A rigid fixation of the crystal, ideally over the full area.
6. The transverse ASE must be suppressed in order to increase the optical-to-optical efficiency and to lower the crystal temperature. It requires:
   - A chromium doped, ASE absorbing cladding in the case of ceramics.
   - An ASE absorber with index-matching liquid around the barrel of crystals.
7. The entire heatsink assembly must be vacuum compatible to operate it inside of an evacuated amplifier. It requires:
   - Materials with minimal outgassing.
   - As little influence on the heatsink as possible by evacuating the amplifier.

The gluing method is suitable for a rigid fixation of the crystal and therefore enables a high stability of the assembly. On the contrary, this method only has a moderate success rate, it is not reversible and it needs a perfect heatsink surface coupled with a sophisticated gluing process.

The liquid metal method enables a high thermal contact between the crystal and the heatsink, it has a negligible influence on the beam profile and wavefront, and it allows for a reversible assembly. However, the mechanical stability is limited since the crystal lacks a fixation along the entire back side.

4.6 One heatsink to rule them all – the hybrid MKX

The MKX heatsink was designed in accordance with the seven golden rules. It is a hybrid design that combines the high stability of the gluing method with the superb beam profile and wavefront properties of the liquid metal method. The MKX also allows for a reversible assembly and it can mount conventional crystals as well as cladded ceramics. It was mainly designed for the operation of the final 10 J amplifier.

4.6.1 Mechanical design of the MKX

The entire CAD model of the MKX heatsink is shown in figure 4.15, and a more detailed cross-section is shown in figure 4.16 in the next sub-section. The core part of the MKX is the front plate made of MoCu 70/30. The thermal contact to the crystal is achieved by a 500 µm thick cavity that is filled with liquid metal. The rather large thickness was chosen as a first prototype to easier fill in the liquid metal. It can potentially be reduced in future versions. The crystal itself is rigidly fixed onto the front plate by a circumferential fillet of glue around the barrel. Ideally, the glue is not in contact with the HR coating on the back side. This way, the following issues are solved:

- The liquid metal interface ensures a minimum influence on the beam profile and wavefront.
- The glue around the barrel fixes the crystal rigid enough without exerting a force on the crystal and its coatings.
- A rather soft and removable glue (e.g. a 1:1.5 mix of ”UHU Endfest”) grants the ability for the crystal to expand under heat load as well as to remove the crystal from the heatsink if necessary.
- The MoCu 70/30 material allows for an equal expansion of the crystal and the front plate if the working temperature is different to the temperature during assembly.

The diameter of the front plate is 65 mm which allows to mount cladded ceramics with a diameter of 55 mm as well as conventional crystals with a diameter of 38 mm. The effective thickness of the front plate is 7 mm, compared to 3 mm in the MKIII design. Although this increases the temperature of the crystal or ceramic by a few degrees, it further minimizes mechanical bending due to the water pressure and it reduces the sensitivity to water vibrations.

The cooling water circuit is an adapted version of the MKIII. Water channels on the back side of the front plate guide a central water stream towards the outer parts. An additional cone in the center helps to equally distribute the water and also prevents a dead zone of the water flow. A large reservoir at the water outlet homogenizes the flow and also increases the mass of the heatsink to around 1 kg. This mass effectively dampens any vibrations of the water connections. All parts are made from corrosion resistant and easy to manufacture 1.4305 steel except for the front plate and the inlet plate, which separates the water input from the output.

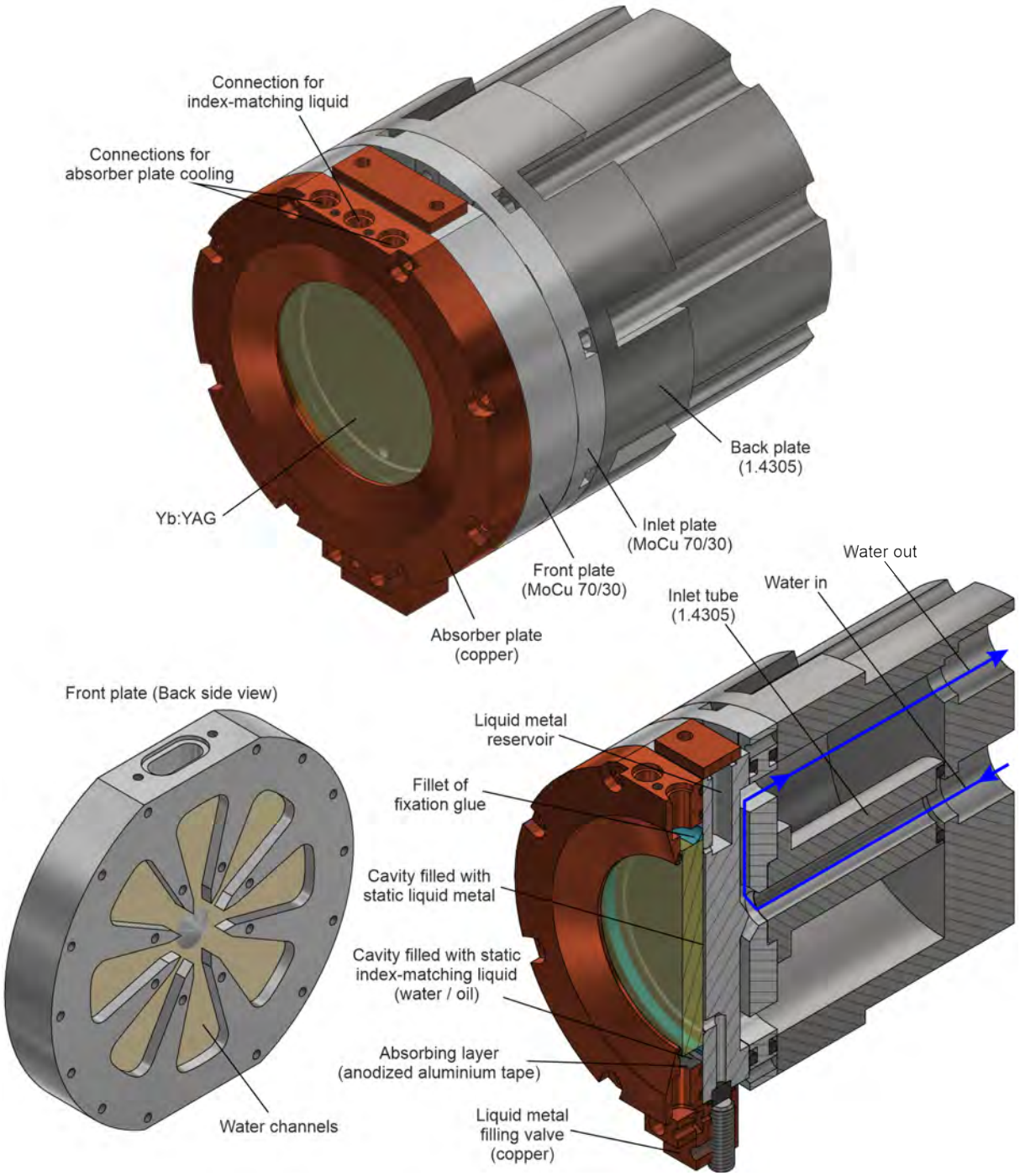

Figure 4.15: *The final heatsink design for active-mirror crystals or ceramics: the MKX. The crystal is glued only with its barrel to a thermal expansion matched MoCu 70/30 front plate. A ~500 µm thick gap between this plate and the crystal is filled with liquid metal. The front plate is cooled via a central stream of water and water channels that guide the stream equally to the outer areas. A large reservoir of water homogenizes the flow before it exits the heatsink. The liquid metal is filled in via a sealable valve after the crystal is glued to the front plate and the entire assembly is put in a vacuum environment. An additional reservoir of liquid metal acts as a piston to compress potential gaps in the liquid metal layer once the filling is finished and the heatsink is put to ambient pressure. An optional absorber plate can be attached to the front of the heatsink, with a cavity that is filled with a static index-matching liquid and an inner wall that absorbs ASE.*

An optional absorber plate can be attached to the front of the heatsink which absorbs transverse ASE. It is made of copper and consists of a separate water cooling circuit as well as a cavity that is filled with a static index-matching liquid, for example water or oil. The ASE that is coupled out of the crystal is then absorbed in a layer of anodized aluminum tape which is glued to the inner wall of the absorber plate. A flat chamfer on the front side of the absorber plate minimizes the turbulences of warm air in front of the crystal.

4.6.2 Vacuum injection of liquid metal

As stated in the troubleshooting of the AMKI heatsink in section 4.4, it is difficult to create a homogeneous layer of liquid metal without any inclusion of air bubbles due to its significant surface tension. To solve this issue, the MKX heatsink is fully assembled and afterwards the liquid metal cavity is filled under a vacuum environment. Therefore, no air exists which could potentially cause bubbles in the liquid metal layer. Besides modifications of the heatsink design, this solution also required a suitable filling process and the development of additional devices that allow for a remote injection of the liquid metal when the heatsink is in vacuum.

A detailed cross-section of the heatsink design and the features that are involved with the filling process are shown in figure 4.16. The heatsink is put in vacuum and the liquid metal is injected through a valve that is located at the bottom of the heatsink. The filling process is finished when an additional reservoir on the top is partially filled. The valve at the bottom is closed and the heatsink is put to ambient pressure. Due to the surface tension, gaps of the liquid metal layer can still occur, even in vacuum. However, once ambient pressure is applied, the liquid metal in the reservoir on the top acts as a piston and compresses any gap. As a result, a mirror-like layer of liquid metal is formed without any visible imperfection.

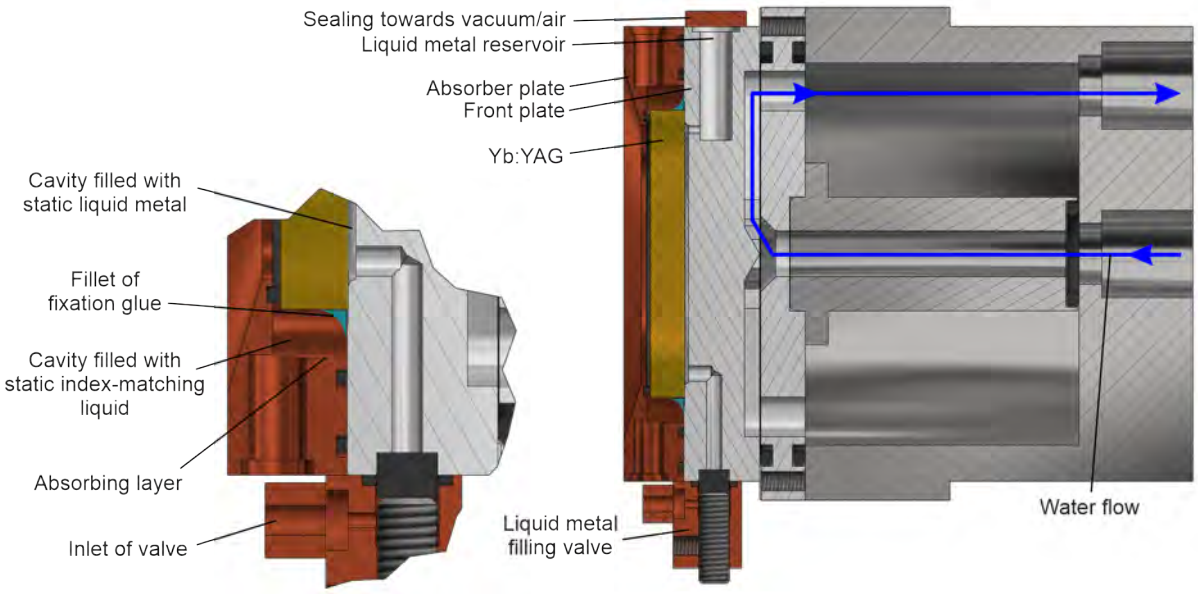

Figure 4.16: *Cross-section of the MKX heatsink with emphasis on the crystal assembly and the liquid metal cavity.*

The reservoir on the top can be sealed or left open afterwards. This enables the option to place the heatsink in a vacuum chamber of an amplifier and to connect the liquid metal to vacuum. If the sealing is left open, no pressure difference occurs between the front side of the crystal and the back side since both are connected to the vacuum pressure. Therefore, a bending of the crystal due to evacuation is avoided. It is important to note, however, that the outgassing behavior of liquid metal at pressures of less than 1×10^{-2} mbar was not investigated yet.

The setup of figure 4.17 was developed to inject the liquid metal into the heatsink in a vacuum environment. It consists of a vacuum chamber and several devices that can be remotely controlled via flexible shafts. The main component is a syringe-like "liquid metal injector" which stores the liquid metal. Once the chamber is evacuated, the injector is used to push the liquid metal through a Teflon tube into the heatsink.

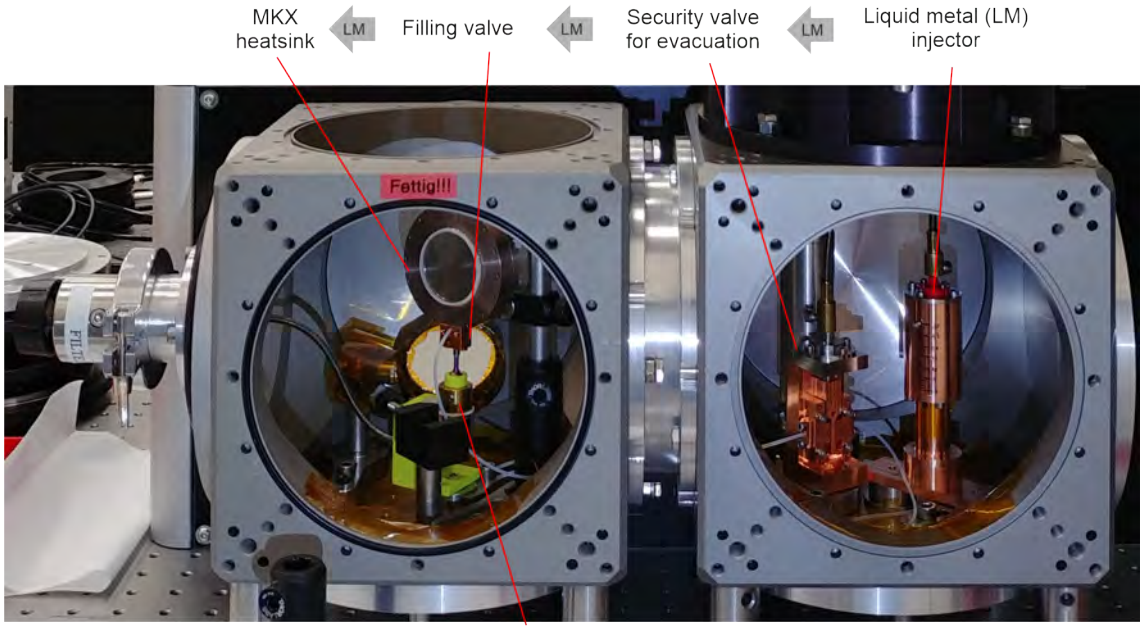

Figure 4.17: *Setup for injecting liquid metal into the MKX. The liquid metal is stored in an injector and it can be evacuated to remove air and moisture. The injector pushes the liquid metal through a Teflon tube into the heatsink. A security valve ensures that no liquid metal is pushed into the heatsink during evacuation because of different partial pressures. The filling valve seals the bottom of the MKX heatsink once the filling process is finished. All devices can be remotely controlled via flexible shafts.*

A CAD model of the injector is shown in figure 4.18. All parts are made of copper to prevent a corrosion by the liquid metal. The reservoir inside of the injector is connected to the ambient environment. This allows to evacuate the stored liquid metal and therefore, to remove any air or moisture from it before it is injected into the heatsink. This step proves to be crucial for a long-term operation of the MKX heatsink, as it prevents a crystallization of the liquid metal after several months of operation. More details on this are given in a following troubleshooting sub-section.

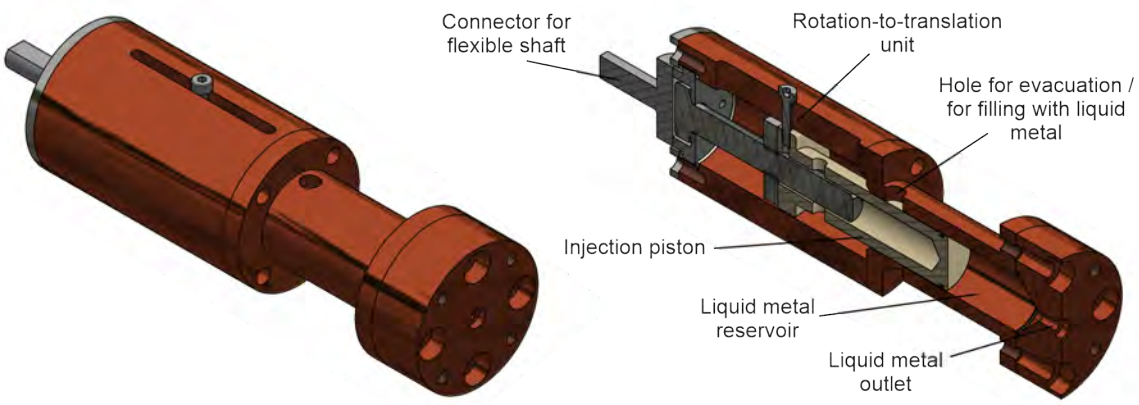

Figure 4.18: *Liquid metal injector which pushes the liquid metal into the heatsink. All parts that are potentially in contact with liquid metal are made of copper to prevent corrosion. The rotation from a flexible shaft is transformed into a translational movement of a piston, which pushes liquid metal through a nozzle into an attached Teflon tube. When pulled completely to the left, the piston clears an access hole which is used to fill in the liquid metal and to evacuate the liquid metal reservoir.*

4.6.3 Simulation of the thermal performance and fluid dynamics

The thermal properties of the MKX heatsink were thoroughly simulated and optimized, based on the data of the previous temperature measurements of section 4.2. In addition, the Autodesk CFD tool was used to optimize the water flow within the heatsink. The results for the final design are summarized in figure 4.19.

For the presented thermal simulation, the pump was set to 30 kW, 10 Hz, 1 ms and a diameter of 23 mm FWHM. These are the expected parameters which are required for an output energy of 10 J with two Ø38 × 3 mm, 2 % doped Yb:YAG crystals in the final 10 J amplifier. Within the pumped region of the crystal, the generated heat is set to 56 W or 18.5 % of the total absorbed pump and within the unpumped region to 50 W or 17 %. This corresponds to the values that were retrieved from the previous temperature measurements of section 4.2. The water cooling is set to 16 °C at a flow rate of 5 L/min, which are typical values of the water chillers of the PFS pump laser.

Without considering the ASE absorber, the simulated average temperature across the thickness of the crystal is 40 °C in the center. This is 4 °C higher than for a simulation of an MKIII heatsink with identical parameters and can be attributed to the thicker, but more stable front plate of the MKX. The absolute maximum temperature on the front side of the crystal is 49 °C and therefore still moderate. In case the ASE absorber is included in the simulation, no noticeable change of the crystal temperature is observed due to the separate water cooling. This is valid even if 50 % of the absorbed pump is converted to heat in the absorber.

The heatsink design generates an almost perfectly balanced distribution of the water flow across each water channel. Furthermore, an imprint of the channels into the temperature profile on the surface of the MKX front plate is not observed. The chosen thickness and the comparably high thermal conductivity of MoCu 70/30 is sufficient to spread and homogenize the transferred heat.

Extensive experiments, which are shown in chapter 8, proved the simulated performance of the MKX heatsink and the superior quality of the reflected beam profile and wavefront that can be achieved with it. The MKX heatsink eventually enabled a reliable operation and high performance of the final 10 J amplifier, with repetition rates of up to 10 Hz and output energies of up to 10 J, see also chapter 8.

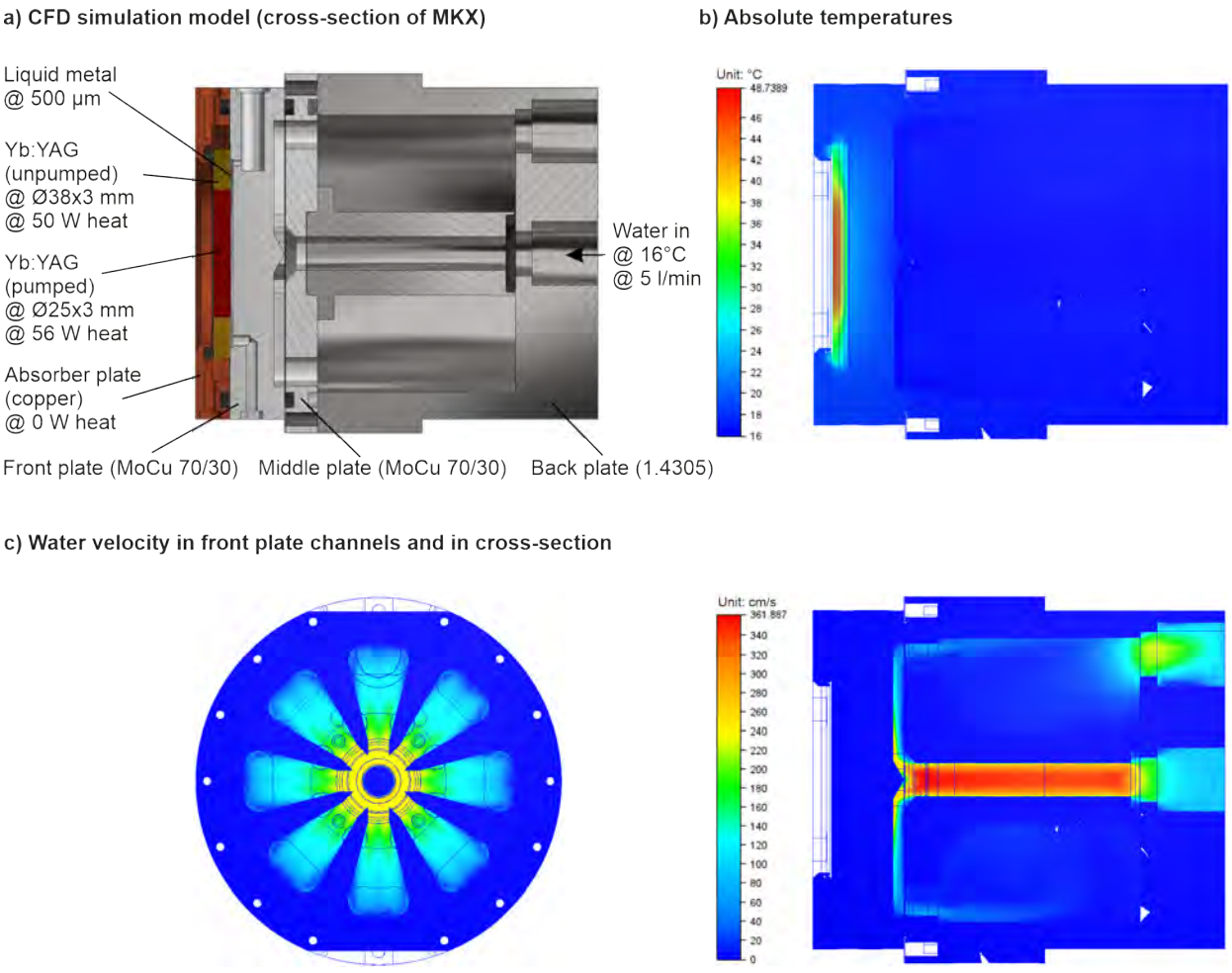

Figure 4.19: *Autodesk CFD simulation of the temperature distribution and water flow in an MKX heatsink with a Ø38 × 3 mm, 2 % doped Yb:YAG crystal . a) CAD Model and simulation parameters. The heat values correspond to a pump with* 30 kW, 10 Hz *and* 1 ms *within a diameter of* 23 mm *FWHM. The conversion factors for the generated heat are taken from the measurements of section 4.2. Additional heat that is generated in the ASE absorber is not considered. b) Temperature cross-section of the MKX heatsink. c) Water velocities along the water channels at the back side of the front plate as well as in a cross-section of the heatsink.*

4.7 The transmissive MKVII heatsink

The liquid metal method was also adapted to the MKVII heatsink of the new 100 mJ-class amplifier ”SuperBooster”. In earlier versions, the transmissive crystal was radially clamped between two copper blocks. An indium foil was used as the thermal interface material around the barrel of the crystal. This type of heatsink typically requires a considerable clamping force to create a sufficient thermal contact and as a consequence, a considerable mechanical stress is induced on the crystal. This in turn degrades the transmitted wavefront and potentially creates stress induced birefringence. There is a trade-off between a maximum thermal contact and a minimum influence on the crystal.

The new MKVII heatsink solves this issue entirely by incorporating liquid metal. The CAD model of the heatsink is shown in figure 4.20. A thermal contact between the crystal and the water cooled heatsink is created by a ring shaped, liquid metal filled cavity around the barrel of the crystal. To avoid gaps in the thermal interface, the liquid metal is injected under a vacuum environment, identical to the MKX heatsink.

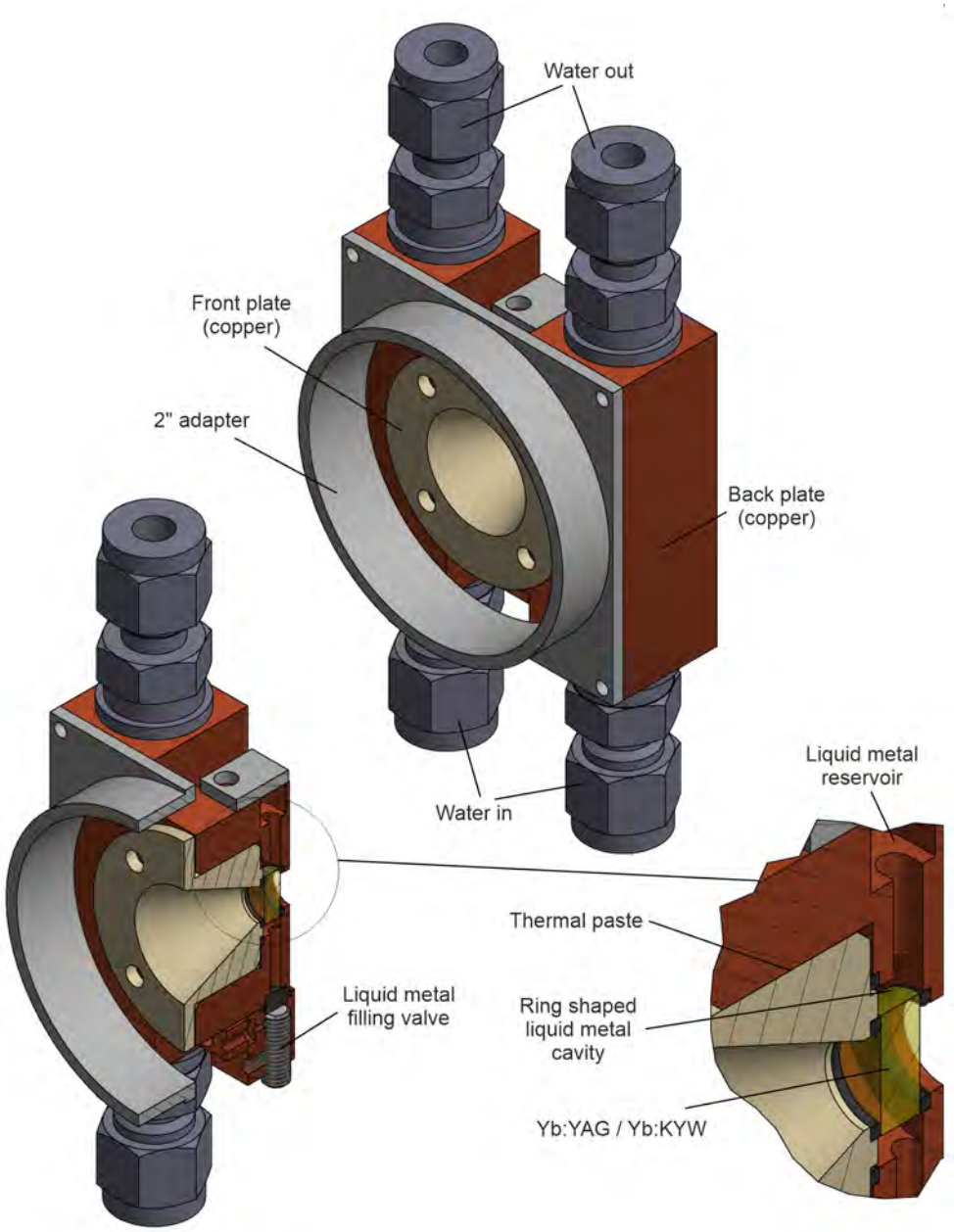

Figure 4.20: *MKVII heatsink for transmissive crystals. A ring shaped cavity around the crystal is filled with liquid metal under vacuum with the same procedure as for the MKX heatsink. All parts are made of copper to prevent corrosion by the liquid metal and to ensure an optimum thermal contact between the water cooling and the liquid metal.*

The advantage of the liquid metal method over the traditional clamping with an indium foil is the almost forceless mounting of the crystal between two soft O-rings. The issue of brittle coatings that potentially crack by the pressure of the O-rings can be neglected for AR coatings. Their significantly thinner layer structure is more robust than HR coatings. The lack of a rigid fixation can be neglected for the mechanical stability of transmissive crystals since the impact of any potential tilt is minimal due to the laws of refraction.

The geometry of the MKVII is designed larger in size than necessary. This enables the implementation of multiple crystal sizes, such as the Ø15 mm Yb:YAG crystals of the original Booster amplifier or the new Yb:KYW crystal with diameters as small as Ø6 mm.

Thermal measurements with the MKVII heatsink and the new Yb:KYW crystals were not conducted and are a topic of future investigations. Therefore, an accurate simulation of the crystal

temperatures cannot be performed. For reasons of completeness, only a rough estimation of the temperatures in the SuperBooster amplifier was conducted with Autodesk CFD. The estimation yields a temperature range in the center of a Ø8 × 3 mm Yb:KYW crystal of 45 to 75 °C, for a generated heat between 9 and 20 %.

A good thermal performance of the MKVII heatsink was proven in the laboratory. The design is highly successful and enables a 10 Hz operation at a maximum output energy of 140 mJ with the new Yb:KYW crystals, see also section 6.5.

4.8 Troubleshooting of the MKX/MKVII and liquid metal

The MKX heatsink solves all issues that are related to the first iteration of new heatsinks. During long-term operation in the 10 J amplifier, only two minor complications emerged.

One is the mechanical bending of the crystal under thermal load. This is a natural behavior since the front side of the crystal is hotter than the cooled back side. Both expand with a different amount and as a result, the crystal bends similar to a Bi-metal. In the MKX design, the crystal is only fixed around the barrel, hence the bending is not suppressed. For the 10 J amplifier, this bending corresponds to a radius of around 100 m and can be well compensated by the optical system.

The second complication is related to the long-term behavior of liquid metal. In the first assemblies of the MKX, several spots in the liquid metal interface appeared after a minimum of three months. They also showed up in the output beam profile but only when the crystal was pumped. The examination of the detached and cleaned Yb:YAG crystals with a microscope revealed a large number of small and sharp polygon structures that were stuck to the HR coating, see figure 4.21. Most of them are flat and only a few hundreds of nanometers thick, with sizes around 100 to 300 µm. Only a small number has a thickness in the range of a few micrometers. These are also the structures which cause features in the amplified beam profile.

A closer look to literature reveals that these structures are a crystallization of the liquid metal [101]. They are most probably Ga_2O_3 crystals which exhibit a lower thermal conductivity than the surrounding liquid metal. Hence, they only influence the beam profile when the Yb:YAG crystal is under thermal load from the pump. The crystallized structures can be removed with mechanical force and Q-tips. Another solution that has yet to be tested is the application of hydrochloric acid which potentially dissolves the Ga_2O_3 crystals. However, care must be taken that the underlying HR coating is not damaged.

A potential cause for the crystallization is the existence of local, gaseous oxygen in the interface layer that is contained either in the porous coating of the Yb:YAG crystal or in the liquid metal itself. The same oxidation behavior can be seen if the liquid metal is exposed to air before an application. The ambient pressure under which the liquid metal is filled into the heatsinks is around 1×10^{-2} mbar and therefore a fraction of oxygen still remains in the form of microbubbles in the interface.

A solution that proved to greatly delay the crystallization process is the evacuation of the vacuum injection chamber for at least 24 hours before injecting the liquid metal. An evacuation time of 12 hours for example showed only one crystallized spot after 5 months of application, another trial with 24 hours of evacuation showed no spots even after 9 months and more. A further decrease of the pressure by an additional turbo pump can potentially assist the delay, but it requires an investigation of the outgassing behavior of liquid metal at lower pressures than 1×10^{-2} mbar.

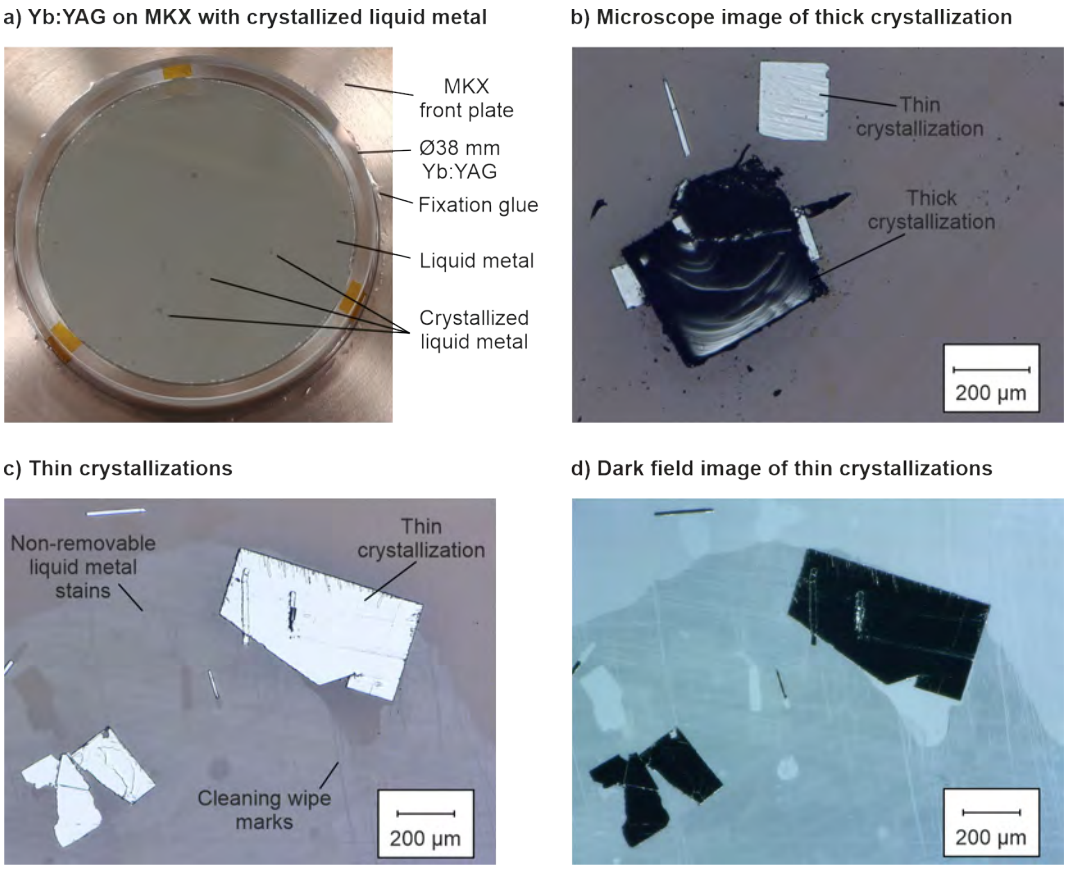

Figure 4.21: *Crystallization of liquid metal after several months of operation. a) Picture of an Yb:YAG crystal mounted on an MKX heatsink with dark, less reflective spots in the liquid metal layer. b) Picture of the spots on the cleaned back side of the Yb:YAG crystal under a microscope showing thick crystalline structures, probably made of Ga_2O_3. c) Thin crystalline structures under a microscope and d) dark field image of these structures.*

An etching process of the liquid metal which supplies the required oxygen from the crystal coating is considered improbable. Long-term measurements showed no degradation of the thermal interface or the coating once the delay of the vacuum injection was implemented.

For the MKVII the local crystallization of liquid metal has no noticeable effect on the beam profile or the thermal performance due to the cooling around the barrel and the resulting spatial separation of the amplification region.

Chapter 5

Optical systems of laser amplifiers

The gain medium sets the boundaries or limits to several fundamental parameters of a laser amplifier, such as the amplification bandwidth, the achievable pulse duration after compression, the central absorption and emission wavelengths, and the maximum feasible pulse energy or average power. In contrast to that, the optical system of a laser amplifier essentially determines how much of each parameter can be achieved. It also sets several key properties of the amplified laser beam such as the size, shape and wavefront. As a consequence, choosing a proper optical design is one of the key aspects in the successful development of any laser amplifier.

This chapter gives an overview of the fundamentals of optical systems and how they are implemented in the high energy amplifiers of the PFS pump laser.

Overview

5.1 Common optical systems:
Overview of the three most common types of optical systems of laser amplifiers, advantages and disadvantages of each for PFS.
5.2 Brief introduction to imaging and Fourier optics:
Brief description of Fourier optics and the most important properties of imaging optical systems.
5.3 Imaging multi-passes and their variants:
Overview of geometries for classical 4f-imaging systems and how they are applied for PFS, introduction of Type 2 imaging as a special case of 4f-imaging.
5.4 Case study of a reflective Type 2 imaging amplifier:
Detailed case study of the optical properties of an amplifier based on a reflective Type 2 imaging geometry, simulation of the impact of thermal lensing, positional alignment tolerances as well as astigmatism.
5.5 Conclusion:
Short summary of the most important insights, beneficial properties of the new Type 2 imaging for the amplifiers of PFS.

5.1 Common optical systems

The most common optical systems of a laser amplifier can be categorized in three main groups, based on the implemented optics and their arrangement: cavities, non-imaging systems and imaging systems. All three share the main purpose of relaying a laser beam multiple times onto an active gain medium to achieve an efficient energy extraction and therefore to maximize the amplification. Each optical system has its own advantages and disadvantages for certain applications, which is discussed briefly in the following section.

5.1.1 Cavities

Cavities "trap" a laser beam or pulse for up to hundreds of roundtrips inside a partially closed optical resonator that contains an active gain medium. In each roundtrip, the pulse passes through the medium and is amplified. To trap and eventually release the laser beam, either Q-switching or cavity dumping is used [44]. Both methods control the resonator losses, either by passive optical elements such as saturable absorbers or by active elements such as Pockels cells.

Q-Switching and cavity dumping
In classical Q-switching, the resonator losses are kept high during the pump process. This effectively keeps the amplifier below the lasing threshold and the inversion inside the gain medium can build up. Once the medium is saturated the Q-switch is activated and the resonator losses are reduced to a minimum. The seed pulse of the cavity is either coupled in externally prior to activating the Q-switch, or it is generated by the spontaneous emission inside of the cavity. The pulse gains energy with each roundtrip and is released from the cavity for example by a semi-transparent end mirror or output coupler.

Cavity dumping is a special case of Q-switching, where all end mirrors ideally have a 100 % reflectivity. The process of building up the inversion and trapping a pulse is similar to the aforementioned method. The major difference is the release of the amplified pulse. It is achieved by deactivating the Q-switch when the amplification reaches a sufficient saturation. Thus, the resonator losses are maximized and all of the trapped radiation is released at once from the cavity or "dumped". The Q-switching is commonly realized by a combination of a Pockels cell and a thin film polarizer (TFP).

Stable and unstable cavities
In stable cavities, the beam size and the wavefront are reproduced with each roundtrip. For the lowest resonator losses, the input beam must match the transverse resonator modes. Stable cavities are frequently employed for amplifiers up to a few hundred millijoules [89, 90].

They work particularly well for the amplification of gaussian TEM_{00}-mode beam profiles and typically maintain good M^2 values. This is the case for example for the regenerative amplifier of PFS. The nanojoule pulses of the stretcher output are amplified to more than 100 µJ, while maintaining the temporal pulse shape and a high quality, gaussian shaped beam profile. Stable cavities are, however, not suited for the joule-class energies and flat-top like beam profiles of the high energy amplifiers of PFS. For beams of this type, the resonator losses due to mode-mismatching are generally too high.

In unstable cavities, only the wavefront is reproduced with each roundtrip. The beam size typically increases until it exceeds the resonator optics, at which point the amplified beam is coupled out of the cavity. Unstable cavities could potentially reach the required, high energies of PFS because of their low losses for more complex transverse mode structures such as a flat-top beam profile. Currently, they are a new and hot research topic for Yb:YAG. Energies of

a few hundreds of millijoules from an unstable cavity based on Yb:YAG have been reported recently, with a nanosecond pulse duration and a flat-top like beam profile [91]. Compared to the goals of PFS, this is still several orders of magnitudes lower than the targeted energy of 10 J and the pulse duration of less than a picosecond. Hence, this method requires more extensive research before it can be applied for PFS.

The summarized key features of cavities are:

+ Ideal for low order TEM mode beam profiles because of minimum resonator losses
+ Output energy of several hundreds of millijoule for such beam profiles
+ Extremely high amplification factors of over 1×10^6 achievable, thus favorable for lower energy pre-amplifiers

− High resonator losses in stable cavities for more complex transverse modes, e.g. flat-top beam profiles
− Low resonator losses in unstable cavities for flat-top beam profiles, but output energies in the order of only a few hundreds of millijoules achieved so far with Yb:YAG

5.1.2 Non-imaging systems

The most attractive feature of amplifiers with non-imaging optical systems is the implementation of mostly flat optics without strong intermediate foci of the beam. This feature allows the propagation and amplification of highly energetic beams in air. A vacuum environment that prevents ionization is typically not necessary. Furthermore, without curved optics also their inherent introduction of optical aberrations is avoided, such as spherical aberration, astigmatism and coma. Altogether, these points make non-imaging systems an ideal choice for compact and cost-efficient amplifiers.

The most limiting feature is the underlying work principle: the beam is relayed through the amplifier only by free space propagation and plane mirrors. Any aberration that is introduced, such as a non-uniform wavefront of the beam or a thermal lens of a crystal will influence the amplified beam during propagation. Besides degrading the quality of the beam profile, this can cause a changing beam size and eventually a decreased beam overlap of each amplification pass with the pumped area of the gain medium. It is particularly pronounced for small beams with Rayleigh lengths that are comparable to the overall propagation distance. Larger beams generally show a lower impact of such aberrations and are favorable for the non-imaging concept.

Another point to consider for the propagation especially of flat-top beams is the fundamental diffraction. The steeper the edges of the beam profile are, the faster they will show diffraction effects during propagation. This typically manifests in the form of ripples around the edges with an increased, local intensity that can eventually lead to laser induced damages of optics. The strength of the diffraction effects mostly depends on the intensity gradient and is independent on the beam size. Therefore, the larger the beam is the less area of it is affected by diffraction from the edges.

Besides larger beams, the non-imaging concept works exceptionally well for beams with a gaussian TEM_{00} mode since they preserve their general beam shape during propagation. Only the beam size changes due to the fundamental diffraction, which can be neglected if the Rayleigh length is much longer than the total propagation distance inside the amplifier.

The original 140 mJ "Booster" amplifier of PFS is a special case of a non-imaging amplifier. It is seeded by a gaussian shaped beam that is relayed via free space propagation through a half bow-tie geometry, see section 2.2. Although the Rayleigh length is short compared to the total propagation distance inside the amplifier, it is partially compensated by exploiting the thermal

lens of the Yb:YAG crystal as an imaging optics. Together with a fine-tuned placement of all plane mirrors, a rather constant beam size at the position of the crystal is achieved for each amplification pass. The concept proved to be highly robust but a considerable degradation of the initial, gaussian beam profile was observed because of the limited compensation capability of the thermal lens. As a result, a subsequent spatial filtering with losses of up to 50 % was required to generate a high quality seed for the next amplification stage. Since the concept relies on the thermal lens of the crystal, it is also strictly fixed to one parameter set of the pump module. Any other set will introduce a different thermal lens and therefore requires a rearrangement of all optics to adapt for it.

In conclusion, the features of non-imaging amplifiers can be summarized to:

+ Compact and cost efficient, no vacuum necessary
+ Ideal for beams with gaussian TEM_{00} mode or large, smooth flat-top beams

− Degradation of the beam profile by diffraction effects or wavefront aberrations
− Not suitable for millimeter sized beams with steep edges
− Low flexibility to parameter changes, such as thermal load of the gain medium

5.1.3 Imaging systems

Amplifiers with imaging optical systems can overcome most of the aforementioned challenges. They share the main feature of stable cavities by reproducing the beam size and wavefront with each roundtrip. In fact, imaging systems are also considered as ”open cavities” that do not exhibit the mode filtering of closed, stable cavities.

Imaging amplifiers therefore have the great advantage that any kind of beam profile or wavefront can be relayed multiple times through them, while maintaining the beam quality and an optimum overlap with the pumped area of the gain medium. The only requirement is a proper re-imaging of the beam after each pass without the introduction of optical losses for example from a clipping on small, intermediate optics.

The greatest advantage of imaging systems is also one of its downsides. Without a mode filtering, also any imperfection or aberration is re-imaged. If for example a gain medium is placed in the image plane of an amplifier, any material or thermally induced wavefront aberration will be re-imaged. Thus, for an imaging multi-pass amplifier the overall impact is multiplied by the number of passes.

In terms of angular misalignment of the input beam, imaging systems are more robust than their non-imaging counterpart. If a gain medium is placed exactly in the image plane and the amplifier is optimized for it, a variation of the input beam angle will have no effect on the overlap of the beam with the pumped area of the gain medium. Furthermore, in order for the beam to walk off any optics, a much higher misalignment has to be applied, since the distance between imaging optics is typically much shorter than the overall propagation length in a non-imaging amplifier. This also causes imaging systems to have a higher flexibility for parameter changes like the thermal load of the gain medium.

Besides the introduction of optical aberrations like astigmatism, coma, spherical aberration etc., the biggest disadvantage of imaging systems is the occurrence of intermediate foci between the imaging optics. For high energy amplifiers this may require a vacuum environment since the intensities in the focus plane can be high enough to trigger ionization of the ambient gas. This also restricts the placement of folding mirrors, since potentially harmful beam sizes due to the intermediate foci must be avoided. Altogether this may considerably increase the overall size of an imaging amplifier compared to a non-imaging one.

To summarize, the key features of imaging amplifiers are:

+ Arbitrary beam shapes can be relayed through the system with minimum quality loss
+ Great flexibility to parameter changes, e.g. a varying thermal load
+ Lower sensitivity to input misalignment than non-imaging amplifiers

− Intermediate foci that can ionize gas or damage optics, which may requires vacuum
− Additional optical aberrations due to curved optics, such as spherical aberration, coma and especially for reflective geometries astigmatism due to off-axis placement of optics
− Beam profile is only maintained inside of image plane; outside strong modulations and hot spots can occur, depending on the wavefront

5.2 Brief introduction to imaging and Fourier optics

To fully understand the principles behind imaging it is necessary to know the fundamentals of Fourier optics. An excellent and comprehensive description is found in the book of J. W. Goodman [92]. Here, only a brief summary is given of the most important insights for the application of a laser amplifier.

5.2.1 Fourier optics

In signal processing, a periodical or non-periodical signal in time can be understood as a superposition of sinusoids with different phase offsets and frequencies. The more complex a signal is, the more sinusoids are required to resemble its shape. The composition of the fundamental sinusoids is retrieved by performing the Fourier transform on the time signal. The result is the complex-valued frequency spectrum of the fundamental sinusoids. As an example, a continuous sinusoidal signal naturally contains only a single frequency. Its Fourier transform in the frequency domain is made of two spikes, one for the negative and one for the positive frequency. In contrast to that, a signal with a rectangular amplitude in time has a Fourier transform that follows a sinc-function. Thus, the signal is composed of a wide range of different frequencies.

Optical signals in the spatial domain, such as a beam profile, obey the same fundamental laws and can be treated equally, hence the name Fourier optics. The only difference is a switch from time dependent signals to space dependent signals and the extension to two dimensions in space. In the scope of Fourier optics, an intensity distribution of light can be understood as a superposition of many fundamental beams of light. Each beam has a plane wavefront, a distinctive phase offset and a different angle of propagation in space. The description shares similarities with Huygen's principle, but it differs in the origin and type of the fundamental beams.

The Fourier transform of an intensity distribution of light yields the composition of fundamental beams, or in other words, the complex-valued spectrum of "spatial frequencies". In a rough approximation, these spatial frequencies can be considered as the corresponding angles of propagation of the fundamental beams.

An interesting feature of a classical lens is the natural Fourier transform that it performs: focusing a beam of light generates the Fourier transform of the beam profile in the focus plane of the lens. In this context, the focus plane is also commonly called "Fourier plane" and the lens a "Fourier lens". The focus plane is furthermore called "far field" since the Fourier transform is also the shape of the beam profile after an infinite propagation in space. Only the size of the shape in the focus is scaled compared to the actual far field.

As a result of the natural Fourier transform of a lens, the composition of spatial frequencies of a beam can be directly determined from the shape of its focus. Low spatial frequencies appear around the center, while high frequencies appear at an increasing distance. A more intuitive description to this is a simple lens that is hit by a beam under an angle. The higher the angle of incidence is, the larger is the lateral offset of the focus from the center.

Some examples for basic intensity distributions and their Fourier transform are:

- A beam with a uniform intensity, an infinite beam size (no edges) and a flat wavefront is composed of a single fundamental beam which points in the direction of propagation. The Fourier transform is a single spike, since only one fundamental beam is involved. In fact, if such a beam is focused, the shape of the focus will be a spot.
- An infinite sinusoidal intensity pattern is composed of two overlapping, fundamental beams. Each beam has a different angle of propagation. This is also similar to how the interference pattern in a Michelson interferometer is generated. The spatial frequency domain consists of two spikes, one corresponding to each angle of propagation. Thus, the focus consists of two spots.
- A square, flat-top shaped beam profile with sharp edges is composed of a continuous spectrum of fundamental beams that are aligned along the two principal axes of the square. The steeper the edges of the flat-top are, the higher are also the angles of propagation of the fundamental beams and the corresponding spatial frequencies. The Fourier transform is a cross, with an intensity along each axis that follows a sinc-function. Therefore, if a flat-top beam is focused, a cross appears in the focus plane.

If some of the higher spatial frequencies are cut-off, for example by an aperture in the focus plane, information of the optical signal is lost and sharp features cannot be fully resembled anymore. This is the basic concept of spatial filtering in a laser system, where high frequency modulations of the intensity or sharp edges of a beam are filtered out with a focusing telescope and a pinhole.

5.2.2 Walk off and imaging

As mentioned before, in a rough approximation the spatial frequencies and the angle of propagation of the fundamental beams can be considered equivalent. As a consequence, for any intensity distribution that contains a range of spatial frequencies, the fundamental beams walk off during propagation and their superposition decreases. This causes the intensity distribution to change and features to lose their sharpness – the intensity ”smears out”.

To compensate the walk off, imaging systems are used. The most prominent one of such systems is the human eye. The basic working principle of imaging is sketched in figure 5.1 on the basis of the widely used 4f-imaging system. In its simplest configuration only two lenses with equal focal lengths f are implemented. Both lenses are two focal lengths apart, with a known intensity distribution positioned in a plane one focal length before the first lens. In the field of classical optics, this plane is called the ”object plane”. Hence the intensity distribution in this plane is also called the ”object”.

All spatial frequencies that are emitted from the object will diverge or walk off during propagation according to Fourier optics. In the sketch, they are depicted by dashed lines. The 4f-imaging system collects the spatial frequencies and converges them again in a plane one focal length after the second lens. In this plane, a perfect reconstruction or ”image” of the object’s intensity distribution and wavefront is observed. This plane is also called the ”image plane”.

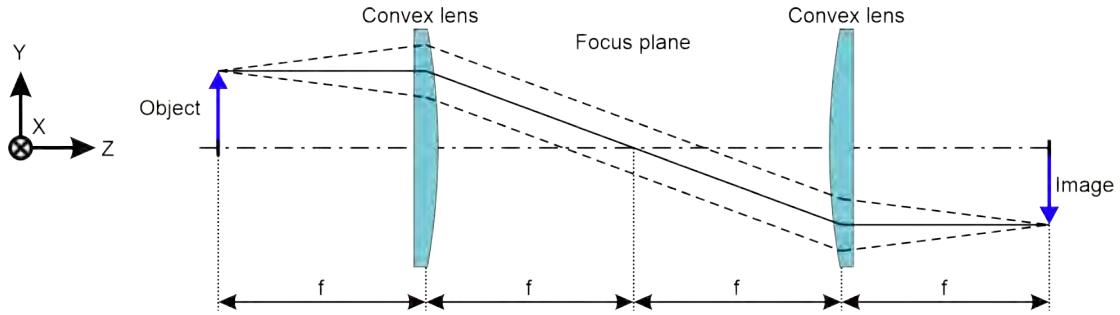

Figure 5.1: *Sketch of the fundamental concept of imaging on the basis of a 4f-imaging system that contains two lenses with equal focal lengths f. The intensity and wavefront information of an object is contained within spatial frequencies. In a rough approximation, these frequencies can be considered as the angle of propagation of the corresponding piece of information (dashed lines). During propagation, the spatial frequencies walk off and the information of the object "smears out". To compensate this, the object is positioned one focal length before the first lens. This way, all spatial frequencies are collected and perfectly re-imaged by the system to an image plane one focal length after the second lens. As a result, the object's original intensity distribution and wavefront are reconstructed.*

This work principle holds true for any object, as long as the imaging system has a large enough aperture and its acceptance angle or numerical aperture is bigger than the spatial frequencies that are emitted from the object. If not, spatial frequencies will be cut off at the apertures of the system and some of the object's information is lost. For a flat-top beam profile for example the edge steepness and homogeneity will degrade by this cut off.

5.3 Imaging multi-passes and their variants

Amplifiers with imaging optical systems are able to maintain the intensity distribution and the wavefront of a beam that passes through the system. Numerous variants exist that allow for multiple passes of the beam through the active gain medium, while re-imaging the beam after each pass. In the following, two of them are discussed which are particularly important for the PFS pump laser: multi-pass amplifiers based on the classical 4f-relay-imaging and amplifiers based on a special case of 4f-imaging, the "Type 2 imaging".

5.3.1 Multiple passes with 4f-relay-imaging systems

A straight-forward way to implement an imaging multi-pass geometry is cascading 4f-imaging systems as depicted in figure 5.2 a). A beam is imaged by the first 4f-system to the first image plane, which is imaged by the second 4f-system to the second image plane and so on. Since the beam is relayed from one imaging system to the other, this is also called "relay-imaging". This sequential arrangement does not allow for an efficient energy extraction in amplifiers since each image plane requires a separate crystal and thus, each crystal is only passed once. Instead this configuration is widely used to relay the beam from one amplifier to another.

The rotational symmetric arrangement of 4f-imaging systems in figure 5.2 b) provides a real multi-pass geometry. All 4f-systems, except the first one in the schematic, contain concave mirrors instead of lenses and are mounted on two fixed mirror wheels, one left and one right. In an amplifier, a gain medium with reflective coating on the back side replaces one or both of the plane mirrors in the image planes. The beam is imaged by the first 4f-system onto image plane 1, which is imaged by the following 4f-system onto image plane 2. During this, the plane of propagation is rotated around the Z-axis by 30° in order to realize multiple passes onto both

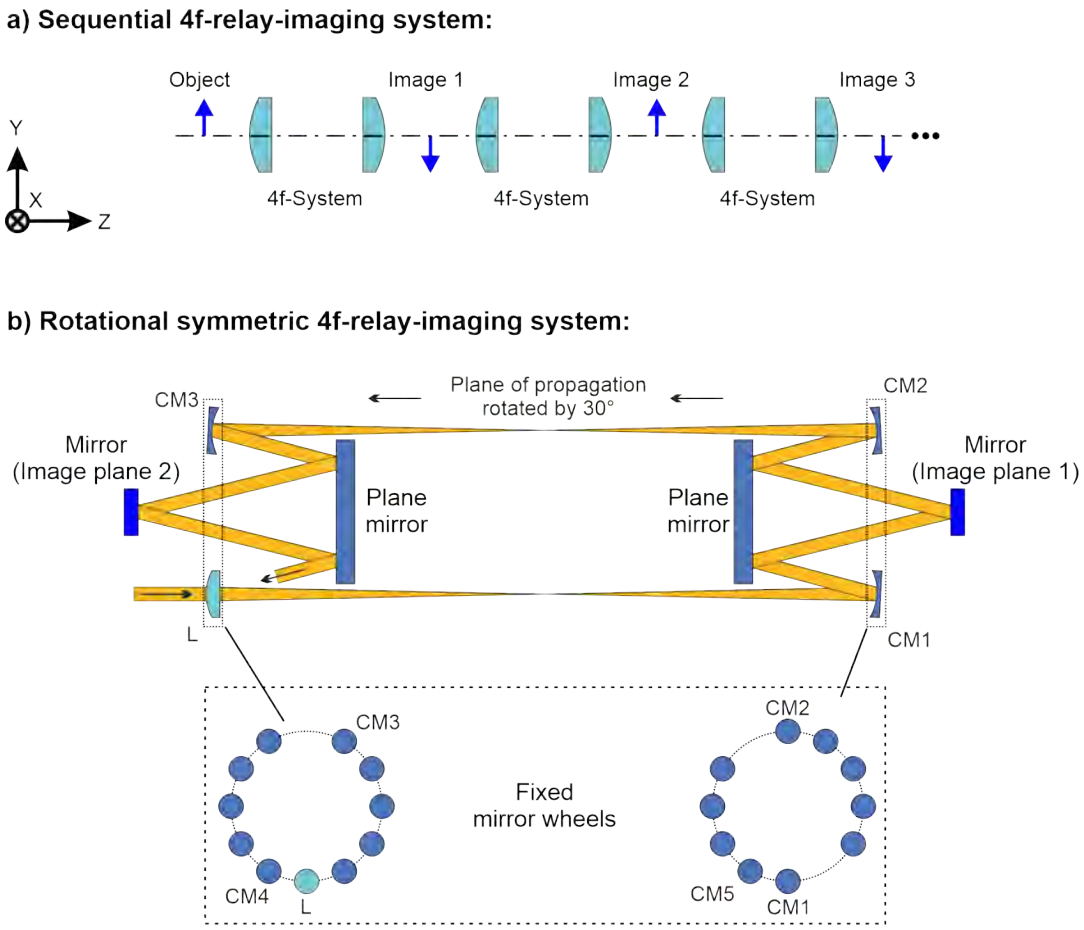

Figure 5.2: *Schematic of multiple imaging passes using a) sequential, transmissive 4f-imaging systems or b) reflective 4f-imaging systems arranged in a rotational symmetric geometry. The distances between all elements obey the rule for 4f-imaging: the distance between the curved optics and the image planes equals one focal length and the distance between two curved optical elements equals two focal lengths. CM: Concave mirror, L: Lens.*

image planes. Afterwards, a new roundtrip begins and the beam is imaged again onto image plane 1, then onto image plane 2 and so on.

An optical system like this allows for a rather compact implementation of multiple imaging passes. A beneficial feature of the rotational symmetry is the inherent compensation of astigmatism for a full propagation through the optical system. The rotational symmetric arrangement has been successfully used for the 1 J and 10 J amplification stages of PFS at the MPQ as well as in amplifiers of other groups [93, 94]. A comprehensive study of the optical properties and the aberrations of such an amplifier with an output energy of 1 J is given by C. Wandt [23].

Despite its benefits, the concept of rotational symmetric 4f-relay-imaging is not used for the final amplifiers of the PFS pump laser at the CALA facility. One of the main reasons is of mechanical nature: there is very limited space between the gain medium, the mirror wheels and the folding mirrors. This space constraint increases the challenge of implementing an efficient multi-pass geometry for the pump beam, for example one that is based on off-axis parabolas around the gain medium. Also, the lack of space and the mandatory vacuum chamber typically require the undesirable placement of the heat laden gain medium in a vacuum. This in turn is coupled with the challenges of a water cooling in vacuum, a probable increase of thermal drifts of the beam, lower damage thresholds of the coatings in vacuum and others. A placement of the gain medium outside of vacuum is therefore preferred.

Measures to relax the tight space constraint and to avoid a placement of the gain medium in vacuum are:

- **Long focal lengths and a consequently large amplifier.** For the 10 J amplification stage of PFS for example, this requires concave mirrors with focal lengths of at least 1250 mm which results in an overall amplifier length of roughly 4 m.
- **Non-monolithic folding mirrors.** Exchanging the monolithic folding mirrors with single mirrors that can be aligned separately allows to move the folding mirror closer to a mirror wheel. This shifts the gain medium further outside and creates more free space around it. However, this method greatly increases the complexity and maintenance effort of the amplifier.
- **Space efficient pump geometries.** Several pump geometries exist that only occupy a minimum of space around the gain medium and therefore allow to place a wall of the vacuum chamber between the gain medium and the mirror wheels. This includes for example coupling in the pump beam through the middle of the large folding mirror [93] or implementing dichroic mirrors. However, the space efficiency typically comes at the price of less pump passes that can be achieved and therefore, a lower energy storage efficiency of the pump.

Since the laboratory constraints at the CALA facility do not allow for large amplifiers of the PFS pump laser, and a maximum energy storage efficiency is necessary to achieve an output energy of 10 J in the main amplifier, a different optical system with a more relaxed space constraint was required. This eventually resulted in the implementation of the so-called "Type 2 imaging" optical system.

5.3.2 Multiple passes with a Type 2 imaging system

The name "Type 2 imaging" is defined by J. Körner as an imaging system with a fundamental geometry that is depicted in figure 5.3 [95]. In its simplest case, it can be understood as a special variant of a single 4f-imaging system where the distance between both lenses is reduced to zero. This arrangement is also identical to the classical example of imaging with a single lens.

In order to achieve a 1:1 imaging, the object is placed two focal lengths before the lens in figure 5.3 a). In the scope of Type 2 imaging, this lens is denoted L_1. The corresponding image appears two focal lengths after L_1. In contrast to classical 4f-imaging, only the intensity distribution of the object is reconstructed in the image plane. The wavefront will be spherical due to the focusing of L_1. An additional concave mirror, denoted L_2, is placed in the image plane and reflects the image back through the system. In order to maintain the imaging property, the radius of curvature of L_2 must be equal to the curvature of the wavefront in the image plane. This way, a 1:1 image is achieved in the position of the original object, two focal lengths before L_1. The intensity distribution and also the wavefront of the initial object are perfectly reconstructed.

A multi-pass geometry is created by placing a plane mirror in the object plane and tilting it. As a result, another roundtrip is initiated with a different path through the system. The path of each roundtrip is spatially separated on L_1 and overlaps in the object plane as well as the image plane on L_2. More passes are generated by adapting the tilting angle of the plane mirror. In an amplifier, the active gain medium replaces this plane mirror. A fully reflective Type 2 imaging geometry incorporates a concave mirror for L_1 instead of a lens, see figure 5.3 b).

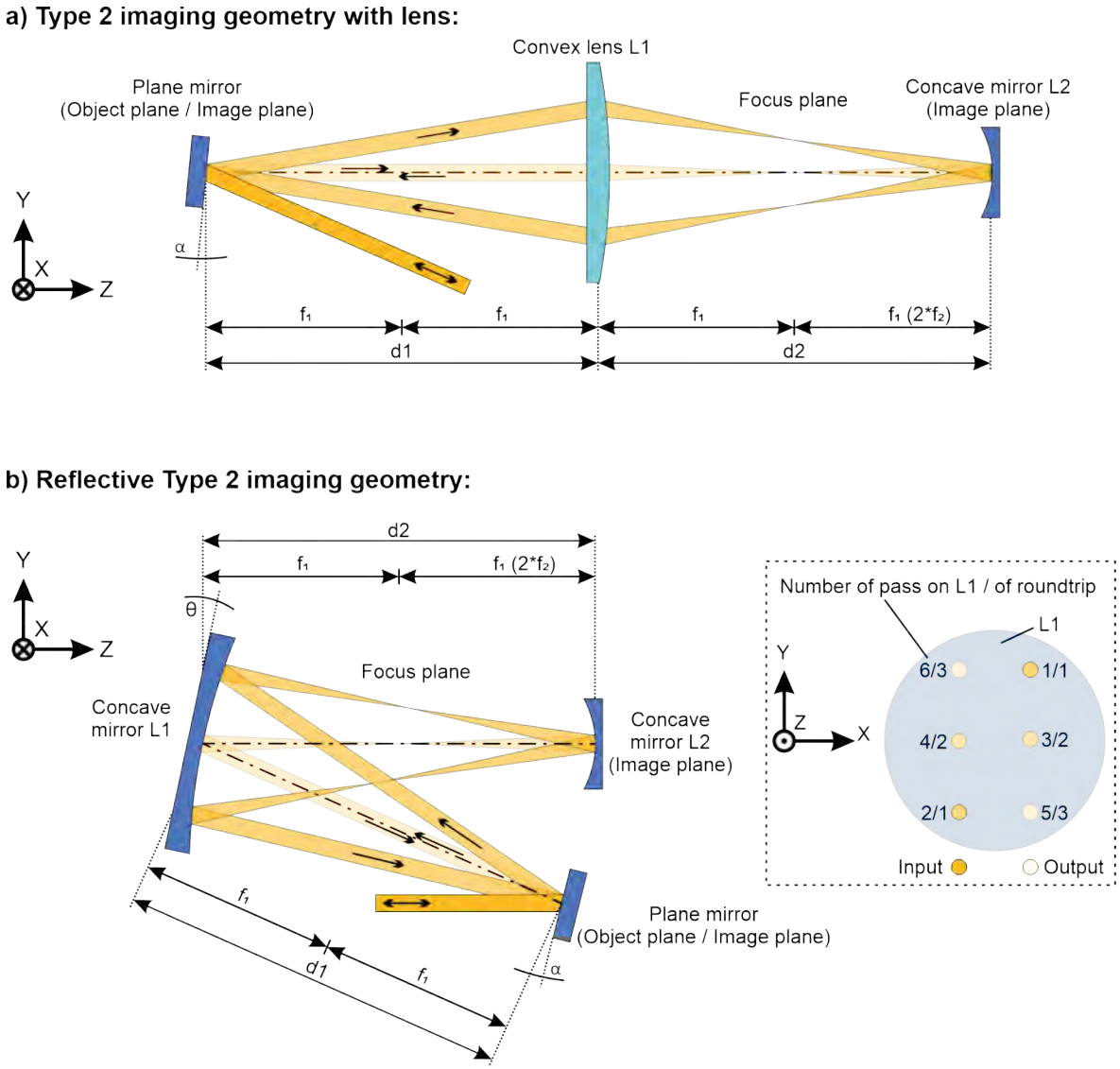

Figure 5.3: *Realization of multiple imaging passes using a Type 2 imaging geometry. For simplicity reasons, the focal length f_1 of the lens or concave mirror L_1 is two times the focal length f_2 of the concave mirror L_2. All optical elements are separated by two focal lengths f_1. Multiple passes are generated by tilting the plane mirror in the object plane around the X-axis. The spatial separation of each pass of a beam on L_1 is depicted in the inset. Note: the tilting angle θ is drawn in the Y-Z plane only for simplicity reasons. In the implementation of such a Type 2 imaging geometry θ usually tilts around the Y-axis.*

The ratio between the focal lengths f_1 and f_2 of both curved optics L_1 and L_2 respectively is not fixed and can be chosen freely. It directly determines the distances between the optics, with the distance d_1 from the plane mirror to L_1 [95]

$$d_1 = \frac{f_1^2 + 2f_1 f_2}{2f_2} \tag{5.1}$$

and the distance d_2 from L_1 to L_2

$$d_2 = f_1 + 2f_2 \tag{5.2}$$

This relationship between the focal lengths and the distances d_1 and d_2 proves to be particularly useful for designing a suitable vacuum chamber. By choosing a focal length of L_2 that is slightly smaller than half the focal length of L_1, the distance d_1 increases while d_2 decreases. Thus, both image planes become spatially separated along the optical axis and the plane mirror, or in case

of an amplifier the gain medium, moves further outside. This is a simple way to implement for example a vacuum chamber where all optics except the heat laden gain medium are placed inside vacuum.

Besides this, an optical system based on Type 2 imaging offers several other advantages over a rotational symmetric 4f-relay-imaging system:

- **Greatly reduced amount of optics.** The simplest multi-pass geometry with Type 2 imaging consists of only three optics. If the monolithic L_1 is instead made of separate concave mirrors, two of these mirrors are required for one roundtrip. In contrast, the rotation arrangement requires four concave mirrors per roundtrip, one or two large folding mirrors and two plane mirrors. Thus, the overall cost and maintenance effort of a Type 2 imaging amplifier is significantly lower.
- **Shorter length for reflective geometry.** For the same set of focal lengths, the reflective Type 2 imaging geometry theoretically requires an overall system length of only twice the focal length.
- **Increased distances between all optics.** Also for the same set of focal lengths, a Type 2 imaging system exhibits twice the distance between all optics along the optical axis. Thus, there is inherently more space for the placement of a suitable pump geometry for example.
- **Better placement of optics.** In a reflective Type 2 imaging system, all optics are placed at either end of the system with nothing in between. Together with the increased distances between optics this allows for an easier placement of the heat laden gain medium outside of the mandatory vacuum chamber.
- **Less optical aberrations.** A Type 2 imaging system introduces less optical aberrations [95]. Especially defocus, astigmatism and coma are reduced. Together with the improved positioning and distances of all optics, this allows for a reduction of the focal lengths while keeping optical aberrations acceptable. Thus, it also allows for an even further reduction of the overall footprint compared to a rotational 4f-arrangement.

All of these advantages together resulted in the decision to build the last two high energy amplifiers of the PFS pump laser in the reflective Type 2 imaging geometry.

5.4 Case study of a reflective Type 2 imaging amplifier

This section investigates the beam properties of an exemplary, reflective Type 2 imaging system. The case study is loosely based on the parameters of the 100 mJ "SuperBooster" amplifier of the PFS pump laser and allows to estimate the impact of thermal lensing, the alignment sensitivity and astigmatism.

The general parameters of the investigated reflective geometry are as follows:

- L_1 is a 3" mirror with a focal length of 300 mm
- L_2 is a 1" mirror with a focal length of 150 mm
- d_1 and d_2 are accordingly both 600 mm
- The beam is assumed to be a flat-top with 2 mm FWHM
- The plane mirror is assumed to be an active-mirror crystal with an HR coating on the back side. It is passed 10 times by the beam which corresponds to 20 amplification passes in an actual amplifier.

5.4.1 Fundamentals of the ABCD matrix analysis

An advanced calculation of all optical aberrations of the reflective Type 2 imaging system is beyond the scope of this thesis and has already been done for a comparable system in the extensive study of J. Körner [95]. The case study of this section focusses on beam properties such as:

- The beam pattern of all passes on the big concave mirror L_1
- The beam sizes and positions throughout the whole system with and without thermal lensing of the crystal
- The effects of misalignment
- The amount of accumulated astigmatism

A powerful and efficient simulation method to investigate these properties is the ABCD matrix analysis. It is a ray tracing method that is valid in the paraxial regime, where the angle α of any ray around the optical axis is small enough to allow for the following approximation:

$$\alpha \approx \tan(\alpha) \tag{5.3}$$

An optical element or propagation-operator is described as a 2×2 ray transfer matrix with real values. Since the Type 2 system only consists of curved and plane mirrors, two matrices are sufficient to describe it:

$$\text{Thin lens / Curved Mirror: } L = \begin{pmatrix} 1 & 0 \\ \frac{1}{-f} & 1 \end{pmatrix} \tag{5.4}$$

$$\text{Free space propagation: } FP = \begin{pmatrix} 1 & d \\ 0 & 1 \end{pmatrix} \tag{5.5}$$

with f being the respective focal length and d the distance of propagation. The optical system is calculated sequentially, such that no reflections occur that would reverse the direction of propagation along the optical axis. Due to this, a reflection from a plane mirror is simply considered as a unity matrix and therefore does not alter the beam size or the direction in the ray tracing simulation.

A ray in general is represented by a 2×1 vector with real values, where the first element x is the ray height relative to the optical axis and the second element α the tangent of the propagation angle:

$$\text{Ray: R} = \begin{pmatrix} x \\ \alpha \end{pmatrix} \tag{5.6}$$

One roundtrip through a reflective Type 2 imaging system is calculated by cascading the matrices of all optical elements:

$$RT = FP_1 * L_1 * FP_2 * L_2 * FP_2 * L_1 * FP_1 * Xt * R \tag{5.7}$$

with Xt being a unity matrix for the plane mirror or crystal, FP_1 and FP_2 the matrices for the free space propagation along d_1 and d_2 respectively, and the matrices L_1 and L_2 for both concave mirrors. R is the vector of the initial ray that hits the crystal and RT is the vector of the ray after one roundtrip.

To determine the beam size and divergence throughout the optical system, a ray tracing is required where the beam is assumed to propagate only along the optical axis for all passes, without the lateral offset from the separation of the passes. Thus, the tilt of the plane mirror or crystal

that is required in the actual optical system to separate the passes is omitted. In this case, the traced ray represents the outermost or enveloping ray of the beam with the vector

$$\text{Enveloping ray: } \mathrm{R_{Env}} = \begin{pmatrix} HWHM \\ Divergence \end{pmatrix} \tag{5.8}$$

The first element of the vector represents the Half-Width-at-Half-Maximum beam size and the second element the divergence angle of the beam relative to the optical axis.

A second ray tracing determines the center positions of the beam on all optical elements and takes the separation of the passes into account. The beam size and divergence is omitted in this case. Consequently, the traced ray changes to a representation of the center of the beam:

$$\text{Center ray: } \mathrm{R_{Cen}} = \begin{pmatrix} Beam\ height \\ Beam\ direction \end{pmatrix} \tag{5.9}$$

The first element is the beam height relative to the optical axis and the second element is the beam direction or angle of propagation relative to the optical axis. This ray tracing also includes the tilt of the crystal in order to account for the different propagation of each pass. The tilt is implemented by adding the double of the tilt angle to the beam direction upon each pass on the crystal.

Although this formalism allows to calculate most of the desired parameters with a sufficient precision, it assumes all optics to be ideal. Their actual thickness and curvature are neglected, as well as for example the impact of spherical aberration. In the implementation of such an optical system this is not the case which causes minor discrepancies of the propagation distance between the optics. As a result, the real beam positions and directions may deviate slightly from the simulated ones.

5.4.2 The ideal system

Figure 5.4 shows the results of a ray tracing for the ideal, reflective Type 2 imaging geometry. The results are categorized in four sub-figures: the positions of each pass of the beam on the 3" concave mirror L_1, the beam positions in the image planes of L_2 and the crystal, the beam sizes on all optics and the beam divergence after passing the crystal. The divergence is given as the change of the beam size per 1 m propagation distance, rather than the typical (half) divergence angle.

Several insights can be made from the figure:

- The imaging property of the system is clearly visible: each pass is perfectly imaged, neither the beam size and divergence nor the beam positions in the image planes change with the roundtrips.
- The beam pattern on L_1 follows two symmetric columns for an ideal alignment.
- A rotation of the crystal around the X-axis by $-0.3896°$ is sufficient to generate 9 passes plus the additional pass of the input beam on the crystal.
- The vertical distance between two adjacent beam positions on L_1 is 8.2 mm. Since the input and output beams pass by below L_1, this ideally leaves 3 mm of free space between the outermost beams and the edge of L_1. Typically, the uncoated area of a mirror is less than 1 mm thick which leaves an absolute maximum of 2 mm towards the edge for alignment-tolerances.
- More than 9+1 passes are not realistic for the given beam size of 2 mm FWHM and a 3" L_1 mirror since the free space towards the edge further reduces with additional passes.

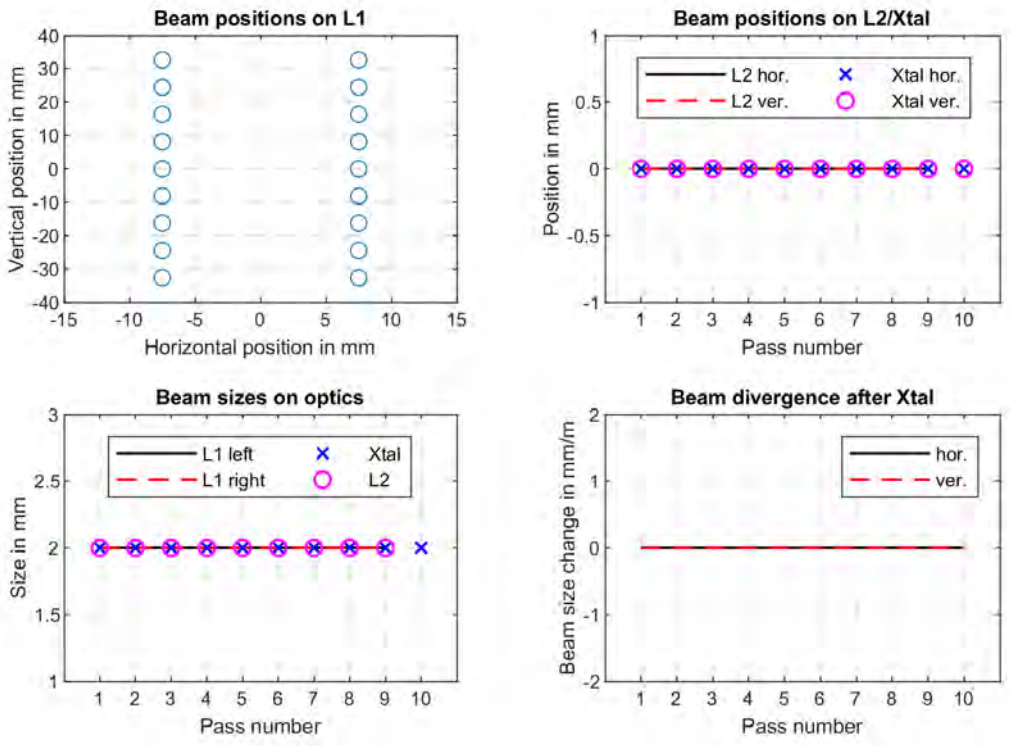

Figure 5.4: *Beam positions, sizes and divergence for an ideal, reflective Type 2 imaging geometry with* $f_1 = 300\,\text{mm}$, $f_2 = 150\,\text{mm}$ *and a FWHM beam size of* 2 mm. *The distances* d_1 *and* d_2 *are each* 600 mm. L_1 *is assumed to be a* 3" *mirror. The crystal (Xtal) is rotated by* $-0.3896°$ *around the X-axis to generate 9 passes through the system plus the additional pass of the input beam on the crystal. The beam divergence is given as the change of the beam size per* 1 m *propagation distance. Connecting lines are only drawn for better visualization.*

5.4.3 Influence of a thermal lens

A more detailed ray tracing also includes the effects of a thermal lens of the crystal. If the introduced wavefront is rather spherical, this can be done by exchanging the unity matrix of the reflective crystal with that of a lens in equation (5.7). In this case study, the focal length of the thermal lens corresponds to a ***double*** pass through the crystal. For the SuperBooster amplifier for example, this focal length is ~1500 mm in the worst case. Figure 5.5 shows the resulting changes to the beam parameters when such a thermal lens is introduced to the optical system and no compensation is applied.

The biggest impact can be seen for the beam sizes on the big L_1 mirror. With increasing passes, the beam sizes on the right column of beams drastically increase from 2 mm to almost 10 mm after nine passes, while on the left column a focus appears after already two passes. Furthermore, the beam divergence increases with each roundtrip and reaches a maximum change of the beam size of 27 mm per 1 m propagation distance. Besides this huge distortion of the system, the beam sizes and positions on L_2 and the crystal stay constant thanks to the imaging properties of the Type 2 geometry.

In order to also keep the beam sizes on L_1 constant and the corresponding energy fluence well below the laser induced damage threshold, the introduced thermal lens must be compensated. In a Type 2 geometry, this can be done rather easily by changing the distances d_1 and d_2 according to the following equations [95].

$$d_1 = f_1 + \frac{f_t}{2} \cdot (1 - LT) \tag{5.10}$$

$$d_2 = f_1 + f_2 \cdot (1 + LT) \tag{5.11}$$

$$LT = \sqrt{1 - \frac{2f_1^2}{f_2 f_t}} \tag{5.12}$$

f_1 and f_2 are the respective focal lengths of L_1 and L_2 and f_t is the focal length of the thermal lens for a ***single*** pass through the crystal. Consequently, f_t is set to 3000 mm for this case study. As a result of the compensation, the distances d_1 and d_2 change from 600 mm to 638.105 mm and 566.185 mm, respectively.

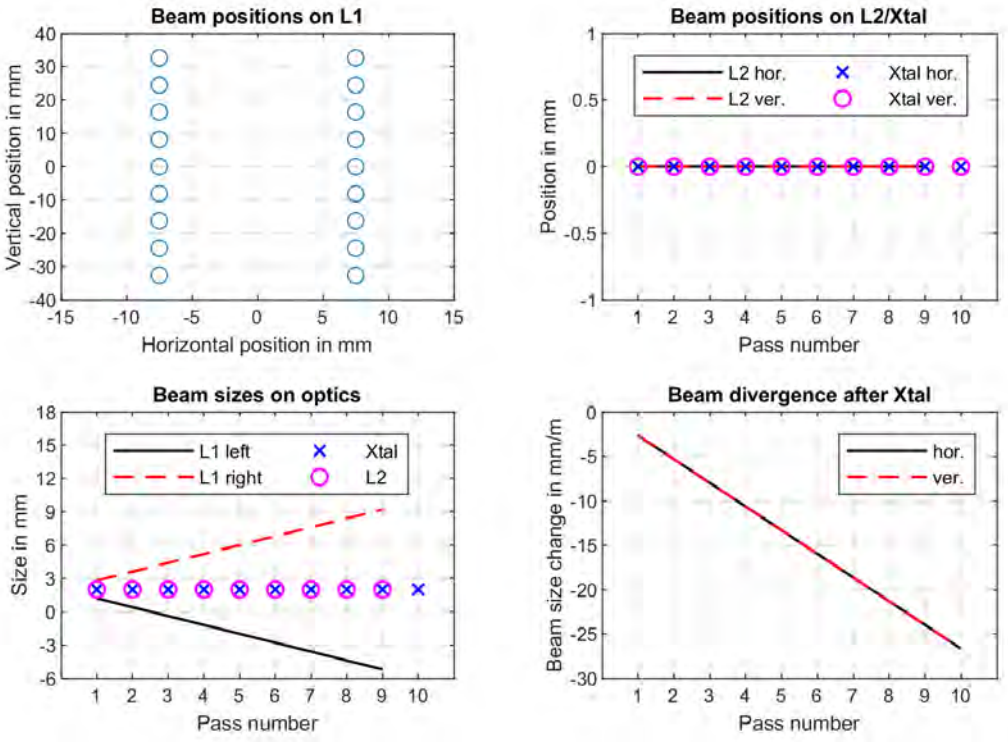

Figure 5.5: *Beam positions, sizes and divergence for the case of an uncompensated thermal lens with* 1500 mm *focal length that is introduced for a double pass through the crystal. Connecting lines are only drawn for better visualization.*

Figure 5.6 proves that this is enough to compensate the thermal lens for each roundtrip and to keep the beam sizes on L_1 as well as the divergence of the beam throughout the system constant. As a side-effect of this compensation, d_1 and d_2 are already spatially separated along the optical axis, which makes it easier to place the crystal outside of a vacuum chamber.

What remains is still a strong but constant decrease of the beam size from 2 mm down to 1.15 mm on the left column of beams on L_1. The corresponding fluence on L_1 increases by 300 % and potentially causes laser induced damages. Due to the shorter distance d_2, the beam size on L_2 is decreased from 2 mm down to 1.78 mm. The corresponding change in fluence is moderate with 26 %. In a more advanced Type 2 geometry, this can be prevented by choosing a slightly larger focal length f_2, which increases d_2 according to equation (5.11) and with it the beam size on L_2.

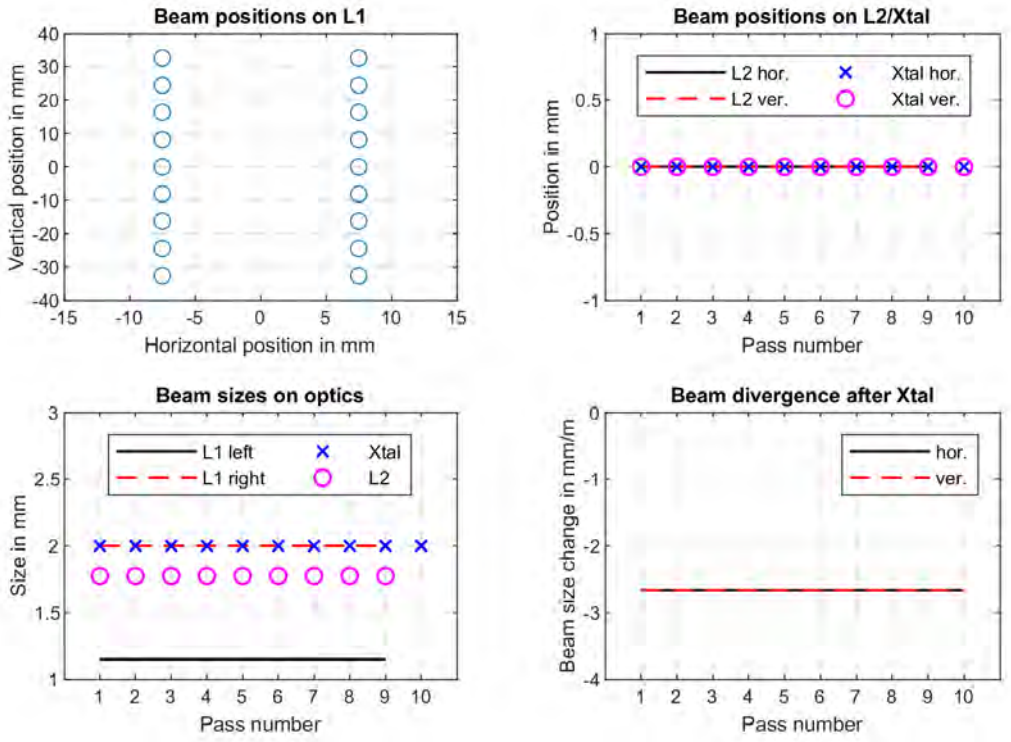

Figure 5.6: *Beam positions, sizes and divergence for the case of a thermal lens with* 1500 mm *focal length that is introduced for a double pass through the crystal and which is compensated by changing the distances* d_1 *and* d_2 *from* 600 mm *to* 638.105 mm *and* 566.185 mm *respectively. Connecting lines are only drawn for better visualization.*

The remaining decrease of the beam size on L_1 is caused by the uncompensated input pass of the beam on the crystal, which adds one additional thermal lens term to the system. This lens cannot be properly compensated by the roundtrips in a Type 2 geometry, where a collimated input beam hits the crystal first.

5.4.4 Thermal lens compensation with a focused input Type 2 geometry

An optimum compensation of the thermal lens can be achieved by focusing the input beam into the system and letting it hit the concave mirror L_2 first, rather than the crystal. This avoids the additional, uncompensated thermal lens term of before. To better distinguish this geometry, it is called "focused input" Type 2 imaging. Accordingly, the geometry used before with a collimated input beam that hits the crystal first is called "collimated input" Type 2 imaging. The resulting geometry after switching to a focusing input beam is sketched in figure 5.7.

All of the aforementioned equations for d_1 and d_2 are also valid for the focused input Type 2. Three points have to be considered for the implementation of such a geometry:

- The input beam must have a focus in the focus plane of the system.
- Since the input beam hits the concave mirror L_2 first, the overall number of passes on the crystal is reduced by one.
- Two additional concave mirrors are required: one to generate a focus for the input beam and another to collimate the output beam after the last focus. In the simplest case, these mirrors have the same focal length as L_1 and are placed directly below L_1 with the ***uncompensated*** distance d_2 towards L_2.

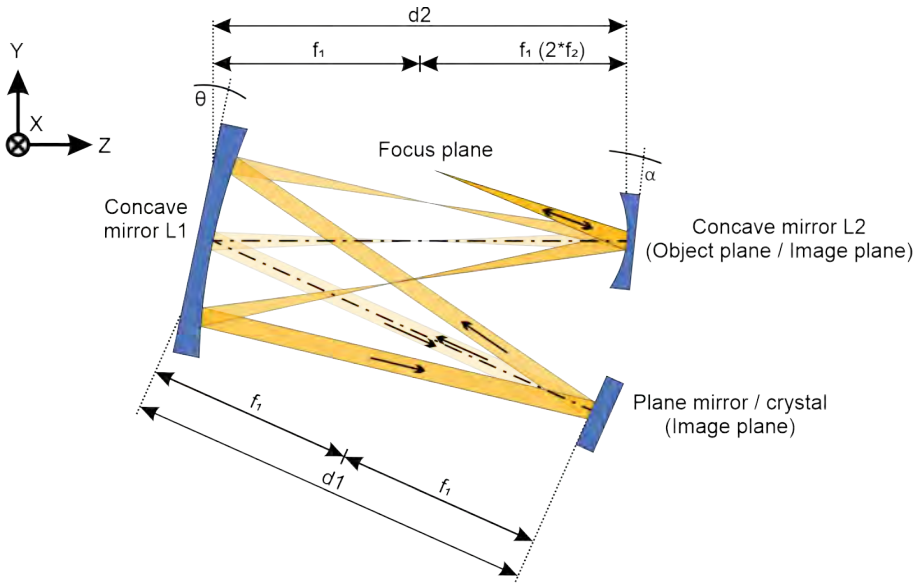

Figure 5.7: *"Focused input" reflective Type 2 imaging geometry. The input beam is focused into the system and hits the L_2 mirror first. This geometry allows for an optimum compensation of the thermal lens of a crystal. All distances are equal to the "collimated input" Type 2 imaging of figure 5.3. Note: Two additional concave mirrors are required, which focus the input beam and collimate the output beam. They are typically placed below L_1 but are not drawn here for clarity reasons. Also, the tilting angle θ is drawn in the Y-Z plane only for simplicity reasons. In the implementation of such a Type 2 geometry θ usually tilts around the Y-axis and not the X-axis.*

The results of the thermal lens compensation with a focused input Type 2 geometry are summarized in figure 5.8. Since all thermal lens terms are compensated, the beam size on L_1 only decreases from 2 mm to 1.6 mm for both columns of beams. This corresponds to an increased fluence of only 56 % compared to 300 % in the collimated input geometry.

Besides the better compensation of a thermal lens, the focused input Type 2 imaging geometry has two other advantages over a collimated input one:

- **Physically accessible image planes before and after the system.** The addition of two concave mirrors at the input and output of the optical system creates physically accessible image planes before and after the system. This greatly reduces the overall size and complexity of an amplifier based on such a geometry. In contrast, an amplifier based on the collimated input geometry requires additional telescopes to access the image plane of the crystal and relay it further, e.g. to the next amplifier.
- **The output beam can be perfectly collimated.** The additional concave mirror at the output of the system furthermore allows to easily correct any divergence or convergence that might remain after a non-perfect alignment of the optical system. Thus, for slight misalignments the time consuming re-alignment of all other optics can be avoided.

The only disadvantage of a focused input Type 2 imaging geometry is the reduction of the passes on the crystal by one.

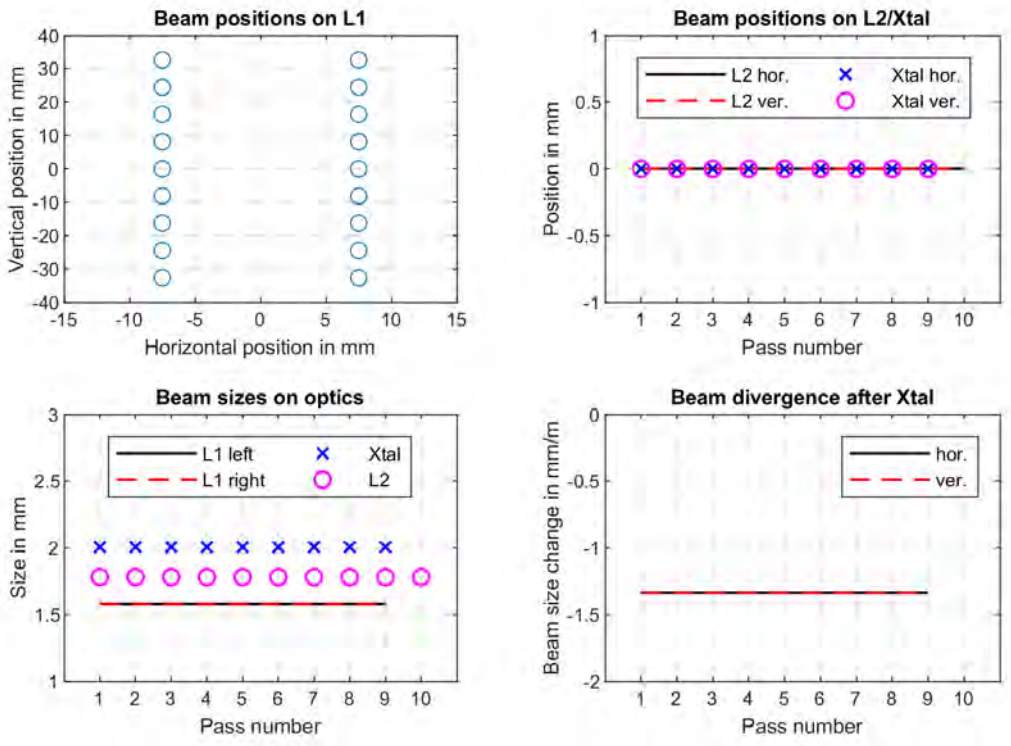

Figure 5.8: *Beam positions, sizes and divergence for a focused input Type 2 geometry with* $f_1 = 300\,\text{mm}$, $f_2 = 150\,\text{mm}$, *9 passes on a crystal (Xtal) and a FWHM input beam size of* 1.78 mm. L_1 *is assumed to be a* 3" *mirror. The system is compensated for a thermal lens with a focal length of* 1500 mm *by changing the distance* d_1 *to* 638.105 mm *and* d_2 *to* 566.185 mm. *The input beam is focused by a concave mirror with a focal length of* 300 mm *that is positioned below* L_1. *Connecting lines are only drawn for better visualization.*

5.4.5 Influence of positional misalignment

Another interesting case to study is the impact of a positional misalignment of the optics in an amplifier based on the focused input Type 2 imaging geometry. It can be challenging in the laboratory environment to precisely measure the proper distances d_1 and d_2. As a rule of thumb, the distances between curved optics can be measured with a precision of approximately ± 2 mm using a ruler. This issue is further enhanced by variations of the focal lengths of L_1 and L_2 since the typical manufacturing tolerance is around 1 %. Figure 5.9 shows the impact, when the distance d_1 is increased by 2 mm from the ideal value of the thermal lens compensated system.

The positional misalignment has mainly two impacts. First, the beam pattern on the L_1 mirror becomes deformed but stays well within the boundaries of the 3" mirror. Second, the beam positions in both image planes are shifted by up to 0.5 mm. While this poses no problem for the beam on L_2, it is particularly critical for the crystal since it degrades the overlap of the amplified beam with the pumped area of the crystal. For small beams as in the SuperBooster amplifier of PFS, this can cause a substantial loss of the beam quality and the extraction efficiency. An alignment stage is therefore necessary to optimize the distance d_1 with at least sub-millimeter precision until the beam position on the crystal stays constant for each pass.

The same positional misalignment also applies to the distance d_2. Therefore, another ray tracing was done where d_2 is reduced by 2 mm and d_1 is kept constant at the ideal value for the given thermal lens. The results are shown in figure 5.10.

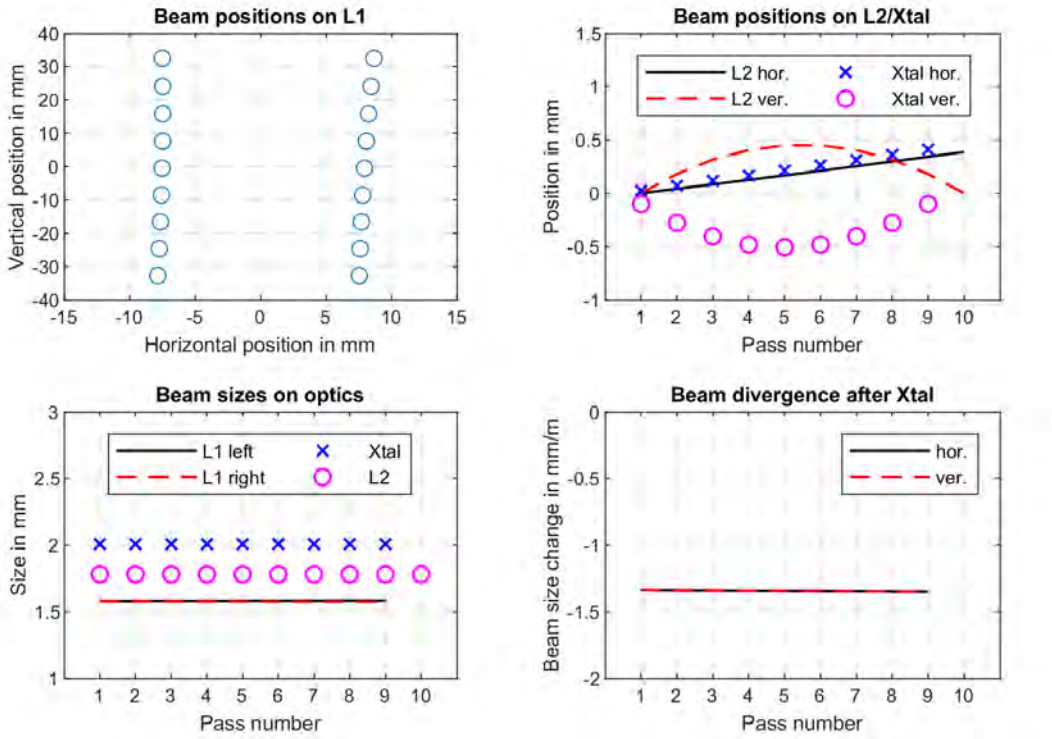

Figure 5.9: *Beam positions, sizes and divergence for a focused input Type 2 geometry with* $f_1 = 300\,\text{mm}$, $f_2 = 150\,\text{mm}$, *9 passes on a laser crystal (Xtal) and a FWHM input beam size of* $1.78\,\text{mm}$. L_1 *is assumed to be a 3" mirror. The system is compensated for a thermal lens with a focal length of* $1500\,\text{mm}$. *The distance* d_1 *is increased by* $2\,\text{mm}$ *from the ideal compensation value of* $638.105\,\text{mm}$, d_2 *is left unchanged at* $566.185\,\text{mm}$. *Connecting lines are only drawn for better visualization.*

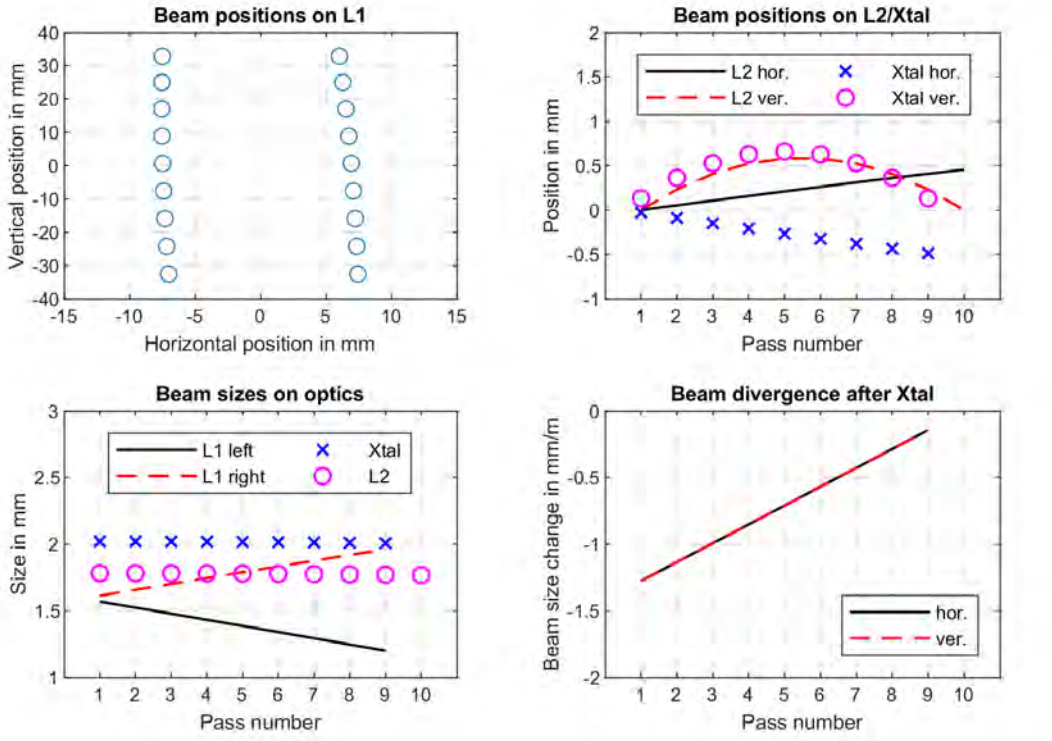

Figure 5.10: *Beam positions, sizes and divergence when the distance* d_1 *is left unchanged at the ideal compensation value of* $638.105\,\text{mm}$ *and* d_2 *is decreased by* $2\,\text{mm}$ *from* $566.185\,\text{mm}$. *Connecting lines are only drawn for better visualization.*

Similar to the change of d_1, the pattern on L_1 is deformed and the beam positions on L_2 as well as the crystal are shifted by up to 0.6 mm. A third effect is observed for the general divergence of the beam: it increases with each roundtrip through the system. This results in a considerable change of the beam size on L_1 and therefore causes potentially critical fluences. Also, the output beam is not collimated anymore. As a result, an additional alignment stage for L_2 is necessary to fine-align the distance d_2 until no changes of the beam positions occur and the beam divergence stays constant throughout the system.

Several conclusions can be drawn for the alignment of a Type 2 imaging amplifier:

- A non-ideal distance d_1 results in a shift of the beam positions on L_2 and the crystal.
- A non-ideal distance d_2 results in a change of the beam divergence throughout the system in addition to a shift of the beam positions on L_2 and the crystal.
- A good approximation is: d_2 mainly determines the divergence of the beam while d_1 sets the proper image plane and therefore the overlap of each pass of the amplified beam with the pumped area of the crystal.

5.4.6 Influence and compensation of astigmatism

A last important property to investigate is the impact of astigmatism in a reflective, focused input Type 2 geometry. Although the paraxial regime prevents the ABCD method from simulating optical aberrations, astigmatism can be implemented in a simplified model that is sufficient to characterize it.

Brief description of astigmatism

In general, astigmatism occurs when a curved mirror or lens is hit under an angle relative to its surface normal. This results in a change of the effective focal length and depends on the plane of propagation of the beam. For a beam that travels along the Z-axis and a curved optical element that is tilted around the X-axis by an angle α, the following definitions of astigmatism apply:

- The X-Z plane is defined as the sagittal plane. The component of the beam along this plane experiences a projection of the curved surfaces and thus, a longer focal length:

$$f_{XZ} = \frac{f}{\cos\alpha} \tag{5.13}$$

  The focus shape in this plane only suffers from the inherent spherical aberration from the curvature of the surface.
- The perpendicular Y-Z plane is defined as the tangential/meridional plane. Along this plane, the component of the beam experiences a shorter focal length:

$$f_{YZ} = f \cdot \cos\alpha \tag{5.14}$$

  This can also be understood as a curved surface that is hit off-center. The greater the offset of the beam on the surface is, or the greater the tilting angle of the optical element is, the stronger the spherical aberration becomes. Furthermore, coma is induced and the resulting focus in the tangential plane is smeared out. In general, the aberrations are considerably higher than in the sagittal plane.

As a consequence of astigmatism, a beam hitting a tilted lens or curved mirror experiences different focal lengths in the X-Z and Y-Z planes and therefore two focus planes appear along the optical axis.

Astigmatism in a reflective, focused input Type 2 geometry

There are two main sources of astigmatism in a Type 2 imaging system. In the horizontal X-Z plane astigmatism is caused by the folding angle of the big L_1 around the Y-axis, which is used to separates the two arms of the system. In the vertical Y-Z plane astigmatism is caused by the varying angles of incidence of each pass on L_2. Thus, the two main sources of astigmatism are decoupled from each other and furthermore, introduce astigmatism in perpendicular planes. Additional but typically negligible contributions to astigmatism come from the horizontal separation of the beams on L_1, which are not considered here. Overall, this allows for a convenient way to compensate astigmatism in a Type 2 system: a proper folding angle of L_1 compensates the astigmatism from the varying angles of incidence on L_2. However, this only works for a full propagation through the system. Each pass itself cannot be fully compensated because of the varying angles of incidence on L_2 and the fixed folding angle of L_1.

Figure 5.11 shows the results of a ray tracing, where the folding angle of L_1 is set to zero and therefore astigmatism is only caused by the unavoidable angles of incidence of the passes on L_2. For a better applicability of the results, the beam is hypothetically coupled out after each pass and the component in the horizontal X-Z plane is collimated by the concave output mirror. What remains is a converging beam component in the vertical Y-Z plane which can be calculated into a focal length, as shown in the lower right graph of figure 5.11.

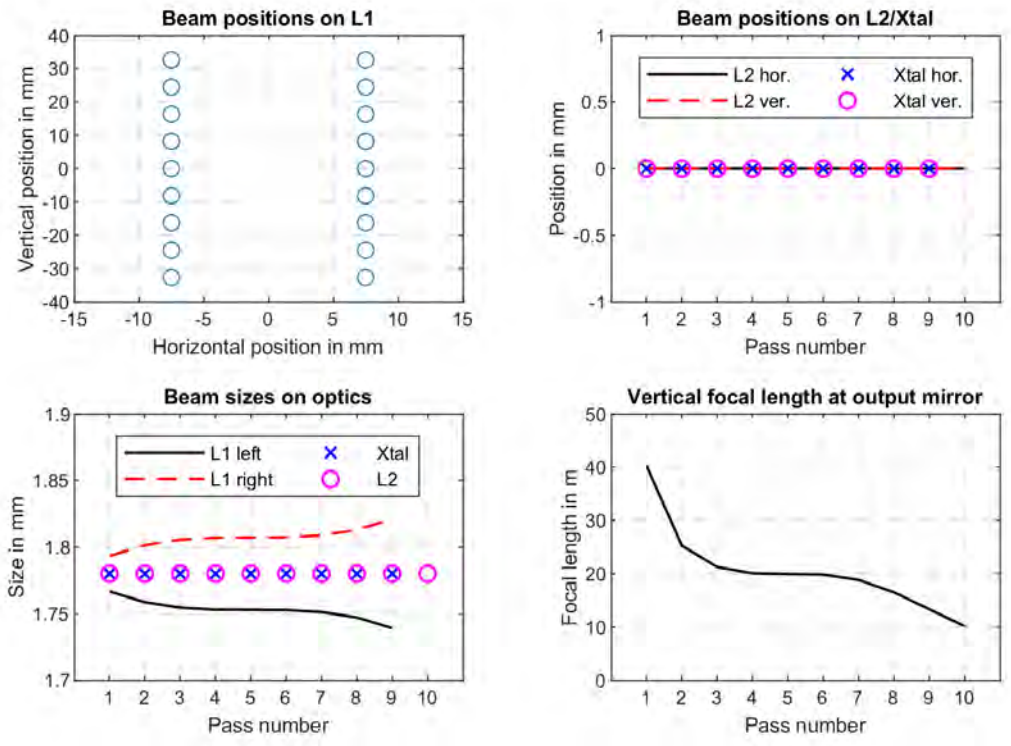

Figure 5.11: *Beam positions, sizes and influence of astigmatism for a focused input Type 2 geometry with $f_1 = 300\,\text{mm}$, $f_2 = 150\,\text{mm}$, 9 passes on the crystal (Xtal), a FWHM input beam size of 1.78 mm and without a thermal lens. Only the astigmatism caused by the varying angles of incidence on L_2 is included. L_1 is not tilted in this example and therefore does not contribute to astigmatism. For the lower right graph, the beam is hypothetically coupled out after each pass on L_2 and sent to the concave output mirror with a focal length of 300 mm. The horizontal X-Z plane is collimated, and the remaining focal length of the pass in the vertical Y-Z plane due to astigmatism is given. Connecting lines are only drawn for better visualization.*

The effects of astigmatism in the given Type 2 system are almost negligible, with slightly changing beam sizes on L_1 and a converging, astigmatic output beam. Because the first and last passes on L_2 exhibit the largest angles, they contribute the most to the overall astigmatism. Intermediate passes only show a minor impact. After the beam propagated through the entire system, a focal length of 10 m remains in the vertical Y-Z plane when the horizontal X-Z plane is collimated. The corresponding beam size on the output mirror is slightly elliptical with a ratio of 1.06.

Overall, the impact of astigmatism is minimal even without an additional compensation by L_1. If necessary, a 2.35° tilting angle of L_1 is sufficient to keep the beam sizes on L_1 almost constant, to collimate the output beam for both planes and thus, to compensate any astigmatic behavior. The only downside of this compensation method is a minor shift of the beam positions on L_2 and the crystal by up to 0.25 mm, see figure 5.12.

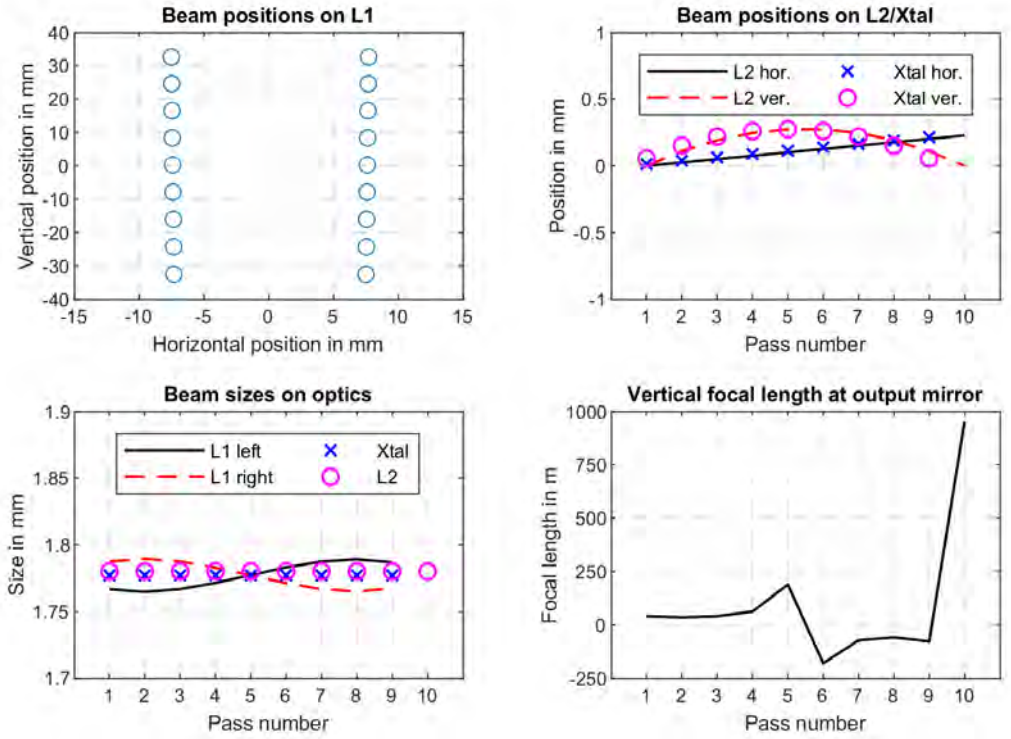

Figure 5.12: *Beam positions, sizes and influence of astigmatism for a focused input Type 2 geometry with $f_1 = 300\,\text{mm}$, $f_2 = 150\,\text{mm}$, 9 passes on a laser crystal (Xtal) without a thermal lens and a FWHM input beam size of 1.78 mm. The astigmatism caused by the vertical separation of the roundtrips is compensated with a tilt of L_1 around the (vertical) Y-axis by 2.35°. For the lower right graph the beam is hypothetically coupled out and collimated along the horizontal plane. The alternating sign of the remaining vertical focal length is caused by the alternating under- and overcompensation of astigmatism by the L_1 mirror for intermediate passes. The system is only compensated for a propagation through all 9 passes. Connecting lines are only drawn for better visualization.*

5.5 Conclusion

The high energy amplifiers of the PFS pump laser require an imaging optical system in order to maintain a flat-top shaped beam profile and in general, a high beam quality during amplification. An amplifier based on Type 2 imaging proves to be in particular beneficial, since it requires fewer optics and offers a smaller footprint compared to the previously used 4f-relay-imaging. The Type 2 imaging furthermore allows for a convenient placement of the heat laden gain medium outside of the mandatory vacuum chamber. Thus, any implication of a vacuum on the gain medium is avoided, such as thermal drifts of the alignment or a lower laser induced damage threshold of the coatings.

The conducted case study of such an optical system showed the feasibility to build the new 100 mJ-class amplifier "SuperBooster" in a reflective, focused input Type 2 geometry. The generally low aberrations allow to implement focal lengths as small as 300 mm and 150 mm for the two concave mirrors L_1 and L_2 respectively. A 3" diameter of L_1 is sufficient to generate up to 9 roundtrips through the amplifier, which corresponds to 18 amplification passes through the gain medium. The Type 2 geometry furthermore allows for an optimum compensation of a thermal lens as well as astigmatism, and it maintains a maximum overlap of the beam with the pumped area of the crystal for each roundtrip.

Because of these beneficial properties, also the 10 J amplifier "BigMama" was ultimately build in a reflective Type 2 imaging geometry. This allowed for a reduced amplifier length and therefore, to fit the amplifier in the tight space constraints of the new laboratory at CALA without sacrificing the beam quality or extraction efficiency. In addition, the convenient placement of the Yb:YAG crystals outside of the vacuum chamber avoids all kinds of thermal issues that emerge from the increased heat load of several hundreds of watts coupled with a vacuum environment.

Chapter 6

The SuperBooster

The ”SuperBooster” is a chirped pulse amplifier based on Yb:KYW as the gain medium. It was developed during this thesis and is used to directly seed the final 10 J amplifier of PFS. The maximum output energy of the amplifier is 140 mJ at a repetition rate of 10 Hz. To the best knowledge of the author, this is the highest energy ever reported for this gain material. The amplifier furthermore supports a spectrum with a bandwidth of 4.2 nm and it maintains a pre-shaped amplitude hole of the spectrum at 1030 nm which is used to compensate the gain narrowing in the subsequent 10 J amplifier.

The SuperBooster replaces the ”Booster” amplifier which was originally developed by Klingebiel et.al. [26] to seed the 1 J amplification stage of the PFS pump laser and later also the 10 J amplification stage, see also the overview of the PFS system in chapter 2. While the design of the original Booster proved to be highly reliable and stable, the limited amplification bandwidth of the implemented Yb:YAG crystal caused a considerable gain narrowing. As a result, the spectral bandwidth of the output beam decreased from 4.2 nm to below 3.5 nm and the pre-shaped amplitude hole around 1030 nm was almost filled up. Therefore, an efficient compensation of the gain narrowing in the subsequent Yb:YAG based 1 J and 10 J amplifiers was not possible and the spectral bandwidth further reduced. Since the chirped pulse duration depends directly on the spectral bandwidth, this translates into shorter nanosecond pulses and therefore a lower and potentially critical laser induced damage threshold of the amplifier optics.

The new SuperBooster solves the bandwidth issue by replacing the Yb:YAG crystal with the more broadband Yb:KYW, see chapter 3 for more details on this material. Also, with the new Type 2 imaging geometry of section 5.4 a significant improvement of the beam quality was achieved. Altogether, this paved the way to directly seed the final 10 J amplifier and to allow for a safe operation of it.

This chapter gives a detailed insight of how this was realized, and which performance is achieved in a day-to-day operation of the SuperBooster.

Overview

6.1 Target specifications:
The system and performance parameters of the SuperBooster that are required to seed the final 10 J amplifier.
6.2 Opto-mechanical design of the SuperBooster:
A full description of the optical system as it is set up in the laboratory, including diagnostics and ASE suppression methods.
6.3 New far-field pump homogenization:
Introduction of near-field and far-field homogenization techniques and the application of a custom-designed far-field homogenizer for the SuperBooster pump module.
6.4 Simulations for a suitable Yb:KYW crystal:
A theoretical case study to find optimum parameters for the application of an Yb:KYW crystal as the gain medium.
6.5 Laboratory performance:
Measured day-to-day performance parameters of the SuperBooster, including energy output dependencies, evolution of spectrum, stability, and beam profiles.
6.6 Conclusion:
Short summary of the SuperBooster's key aspects and achievements.

6.1 Target specifications

The following target specifications and requirements for a new 100 mJ-class pre-amplifier were made based on experiments with the original Booster pre-amplifier and the subsequent high energy amplifiers:

- **Size:** A footprint of $2000 \times 700\,\mathrm{mm}^2$ must not be exceeded because of laboratory space constraints.
- **Geometry:** In order to improve the beam quality and reduce the losses of spatial filtering, as well as to increase the flexibility of the system for e.g. varying pump powers, an imaging geometry is preferred.
- **Energy:** An output energy of 100 mJ at 10 Hz with a stability of ± 1 % Std. is sufficient to seed the 10 J amplifier.
- **Energy fluence:** Based on daily operations with the PFS amplifiers, a limit of $3\,\mathrm{J/cm}^2$ must not be exceeded for an operation under vacuum. In air, this can be increased to $6\,\mathrm{J/cm}^2$.
- **Spectral bandwidth:** The input bandwidth of 4.2 nm shall be maintained. Furthermore, the spectral amplitude hole at 1030 nm must be sustained to achieve an optimum gain narrowing compensation in the 10 J amplifier.
- **Beam shape:** A smooth, flat-top shaped output beam profile is preferred for an efficient seeding of the subsequent 10 J amplifier.
- **Mechanical stability:** A long-term stability of the beam drift coupled with a standard deviation of the beam pointing fluctuation below 30 µrad is required to ensure a stable operation of the 10 J amplifier. The values are taken from long-term experience with the original Booster amplifier.

6.2 Opto-mechanical design of the SuperBooster

In order to meet the specifications for overall size, amplifier geometry and beam shape, an imaging system based on the focused input Type 2 geometry was chosen for the design of the new SuperBooster. The full schematic of the optical system as it is set up in the laboratory is shown in figure 6.1.

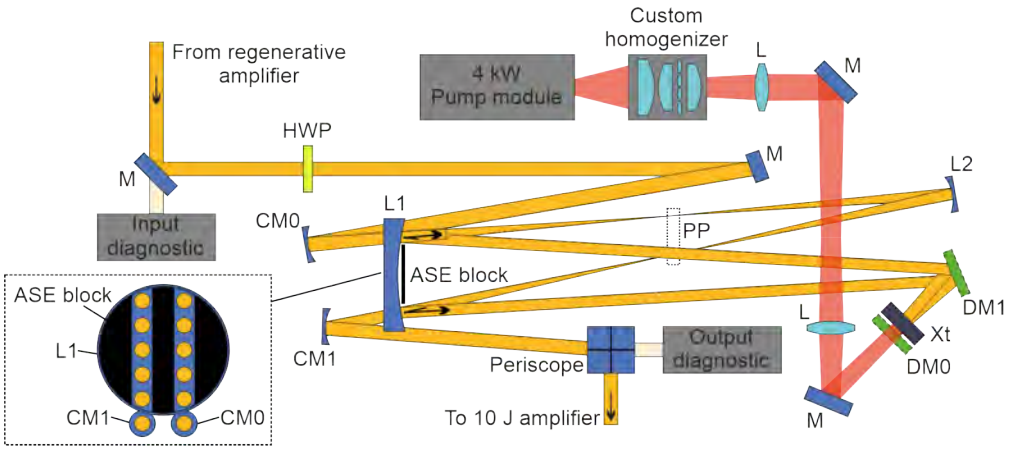

Figure 6.1: *Schematic of the SuperBooster's optical design. The fundamental geometry is the focused input Type 2 imaging with a single-pass pumped Yb:KYW crystal (Xt). The large L1 mirror is* 3" *in diameter with a focal length of* 300 mm*. The input and output concave mirrors (CM0, CM1) are* 1" *in diameter with the same focal length. The L2 mirror is* 1" *in diameter with a focal length of* 150 mm*. Up to 20 amplification passes can be achieved with the setup. The crystal is single-pass pumped through two* 940/1030 nm *dichroic mirrors (DM0* 0°*, DM1* 22.5°*). After homogenization, up to* 2.35 kW *of pump power at* 940 nm *and* 10 Hz *remains within a hexagonal shaped flat-top. The pump profile is imaged via two lenses (L) onto the crystal. A shade (ASE block) in front of L1 as well as a pinhole plate (PP) in the focus plane ensure a strong suppression of ASE feedback. A half-wave plate (HWP) selects the optimum beam polarization for the birefringent Yb:KYW crystal. The overall footprint of the amplifier is* $\sim 1000 \times 700\,\mathrm{mm}^2$*. M: Mirror.*

<u>*Fundamental design*</u>

The optical design is derived from the previous case study and is thoroughly described in section 5.4. Based on the specified limit for the energy fluence of $3\,\mathrm{J/cm}^2$ and the desired output energy of over 100 mJ, a FWHM beam size at the position of the crystal of at least ~2.5 mm is required. For such a beam it was experimentally proven that a focal length of 300 mm of the big concave mirror L1 is sufficient to safely prevent ionization in air. The safety margin is comparably large with a measured ionization threshold of ~350 mJ. As a consequence, the focal lengths of the two concave mirrors L1 and L2 are set to 300 mm and 150 mm respectively. This combination furthermore exhibits even lower optical aberrations than reported in the case study of a similar Type 2 amplifier by J. Körner et.al [95]. The diameter of the L1 mirror is set to 3" and allows for a maximum of 10 roundtrips through the system, which is equal to 20 amplification passes through the crystal.

Because there is no risk of ionization, the entire amplifier is built in air without the necessity of a vacuum chamber. This drastically simplifies the design and also relaxes the constraints for the maximum energy fluence, in particular of the beam on the L1 mirror. With the chosen focal length of 300 mm of L1 and a typical thermal lens of the crystal of ~2200 mm, the fluence on L1 is increased by 47 %. Despite this elevated fluence, no damage was observed for a long-term operation of over 2 years.

The overall footprint of the SuperBooster measures ~$1000 \times 700\,\mathrm{mm}^2$ and is dominated mainly by the pump module and the implemented pump beam homogenization. The compact Type 2 geometry itself only occupies ~$200 \times 700\,\mathrm{mm}^2$ of space.

Crystal and pump geometry
The pump beam is homogenized and shaped into a hexagon with a custom homogenizer, as will be shown in detail in the next section. A 4f-telescope images the beam onto the position of the crystal. The pump beam is coupled in and out of the Type 2 geometry with two dichroic mirrors that exhibit a maximum transmission for 940 nm and maximum reflection for 1030 nm. One dichroic mirror acts as the end mirror and is positioned in the image plane (DM0, 0°) and another (DM1, 22.5°) folds the beam path between the image plane and the L1 mirror.

A transmissive Yb:KYW crystal is placed directly in front of DM0 to maximize the overlap of each roundtrip of the amplified beam with the excited area of the crystal. The crystal is mounted in an MKVII heatsink. This transmissive setup is much less sensitive to vibrations of the water cooling than an active-mirror setup. The end mirror DM0 is mechanically decoupled from the crystal and therefore not affected by any vibrations. Also, with this geometry the necessary angular tuning of the birefringent Yb:KYW crystal has a significantly lower impact on the overall alignment of the amplifier.

ASE suppression
A 3D printed pinhole plate (PP) is placed in the focus plane of the amplifier to suppress the feedback of ASE. Rather large pinhole diameters between 1.5 to 4 mm are chosen to keep the alignment sensitivity of the system as low as possible while maintaining a sufficient suppression.

An additional 3D printed shade is mounted to the front of the 3" L1 mirror, as depicted in the inset of figure 6.1. It blocks up to 77 % of the otherwise unused surface area of L1 and adds a significant contribution to the overall suppression of ASE feedback.

Diagnostics
Diagnostics of the input and output beam continuously record the leakage through 45° mirrors. Each diagnostic consists of two cameras: one for the focus shape and position (far-field camera) and one for the beam profile and position in the image plane (near-field camera). In combination, these cameras create a robust alignment reference to check the alignment of the amplifier during operation and to precisely re-align it, should a misalignment occur.

6.3 New far-field pump homogenization

Most of the energy losses of the original Booster had their origin in a strongly inhomogeneous beam profile of the pump module. This in turn degraded the quality of the amplified beam profile and made a subsequent spatial filtering necessary, which caused an energy loss of up to 50 %.

The cause of the inhomogeneous pump profile is a vertical stacking of 24 diode bars inside the pump module without subsequent homogenization optics. Only the divergence and the overall shape of the emitted pump beam is modified by several cylindrical and aspherical optics. Since the same pump module is also used in the SuperBooster, an additional homogenizer based on microlens arrays (MLA) was implemented.

6.3.1 The concept of near-field homogenization

The fundamental working principle of such a homogenizer is shown in figure 6.2 by means of a ray tracing simulation. The simulation code was implemented in MATLAB using the ABCD-Matrix method. Three collimated input beams are traced, with different angles of incidence (dark green, blue, bright green). For simplicity reasons, each beam is reduced to three ray bundles: two for the boundaries of each beam and one for its center.

In its simplest case the homogenizer consists of either a monolithic, double-sided microlens array or two identical, air-spaced microlens arrays which are placed in the back-focal plane of a focusing lens. In the scope of homogenization, this lens is commonly termed a Fourier lens (FL).

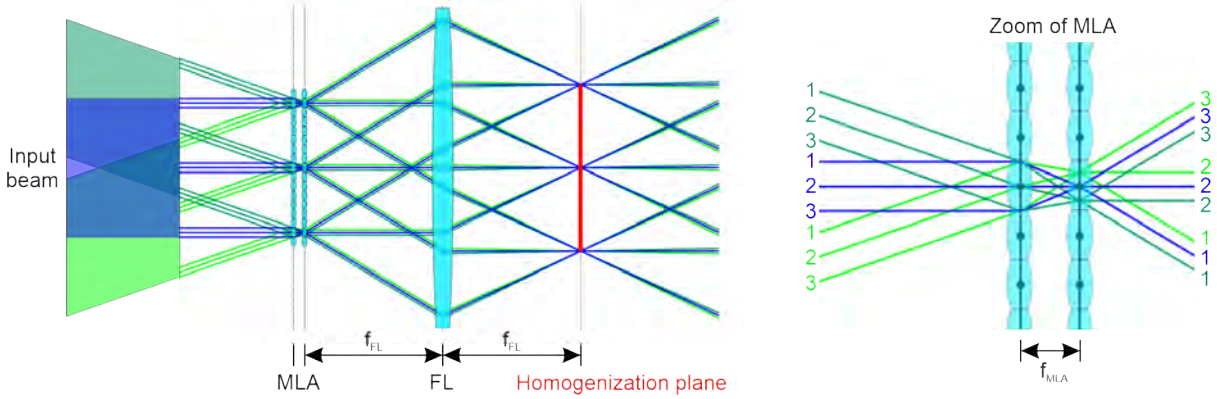

Figure 6.2: *Conceptual ray tracing for a "near-field" beam homogenization that is based on the combination of a microlens array (MLA) and a Fourier lens (FL). Three collimated input beams with different angles of incidence are traced through the system (dark green, blue, bright green). Three ray bundles are shown per angle: two for the boundaries of the beam and one for its center. Each ray bundle consists of 3 rays: two rays hitting the outer edges of a microlens and a center ray, see also the inset "Zoom of MLA". Note: All optical elements are assumed to be thin in the simulation. The drawings of bulk optics and the filled in input beams are artificial. Although the MLA is monolithic in the ray tracing simulation, the bulk drawing consists of two separate MLAs for a better understanding. f: Focal length.*

In a so-called "near-field" configuration, the first MLA samples the incoming, lateral intensity distribution of the beam and creates one beamlet per microlens. The second MLA in combination with the Fourier lens acts as an array of objective lenses. Each microlens or beamlet is imaged to the focal plane of the Fourier lens, thus creating a superposition of all sampled beamlets with a homogeneous intensity distribution. This plane is also called the homogenization or image plane.

Generated beam size and divergence

The shape of the homogenized image is identical to the shape of a microlens. The size D of the image can be calculated with the following equation [102]:

$$D = p_{LA}\frac{f_{FL}\,(f_{LA1}+f_{LA2}-a_{12})}{f_{LA1}\cdot f_{LA2}} \tag{6.1}$$

where p_{LA} is the center distance between two adjacent microlenses and also called the lens pitch, f_{FL} is the focal length of the Fourier lens, f_{LA1} and f_{LA2} the focal lengths of each MLA and a_{12} the distance between the MLAs. To further fulfill the imaging conditions a_{12} must be equal to f_{LA2} and both focal lengths f_{LA1} and f_{LA2} must be equal. As a result, equation (6.1) reduces to

$$D = p_{LA}\frac{f_{FL}}{f_{LA2}} \tag{6.2}$$

While this method generates beam profiles with a high homogeneity in the image plane, the divergence angle of the homogenized beam can increase compared to the input beam, as shown in figure 6.2. Here, the divergence angle is defined as the highest exit angle of all beamlets after the homogenization plane. This angle θ can be calculated as follows, with the input beam size d_{in} and the assumption that the Fourier lens is placed directly after the second MLA [102]:

$$\tan\theta = \frac{1}{2}\left(\frac{d_{in} - 2\cdot p_{LA} + D}{f_{FL}} + \frac{p_{LA}}{f_{FL}}\right) \tag{6.3}$$

The larger the input beam size or the more microlenses are illuminated, the higher the divergence of the homogenized beam will be. This behavior can be better understood with the example of a collimated beam hitting a focusing lens: the angle of incidence of the beam directly translates into the offset of its focus spot from the optical axis. The higher the angle, the higher the offset will be. The homogenizer is the inverted equivalent to this. Here, the focus spot (the microlens) is the source and the lens (the Fourier lens) creates the collimated beam. A higher offset of the focus (the microlens) from the optical axis therefore translates into a higher exit angle of the outgoing beam. Figure 6.2 further emphasizes this dependency with the three traced ray bundles per input beam: each has a different offset to the optical axis and thus a different exit angle.

In case of the SuperBooster, the achievable divergence of the homogenizer limits the useful length of the gain medium, where a sufficiently homogenized pump beam profile is maintained. Outside of this length, the decreasing superposition of the beamlets due to their different exit angles grows too strong.

The angle of incidence on the MLA only has a negligible influence on the overall divergence, as long as it stays below the acceptance angle of the MLA. If the acceptance angle is exceeded, cross-talk between microlenses occurs and ghost images form in the homogenization plane.

Limitation of the near-field homogenization

A distinctive feature of the near-field homogenization is the dependency on the intensity distribution of the input beam. A sufficient homogenization might not be accomplished if the input beam exhibits periodical intensity modulations or not enough microlenses are illuminated in case of a strongly inhomogeneous input beam. In both cases, the randomization of the intensity distribution by the superposition of each beamlet is not sufficient.

This feature is especially important for the homogenization of a beam emitted by stacked laser diode bars, as in the pump module of the SuperBooster. The emitted beam consists of 24 equidistant, horizontal lines. Without further modifications, this periodicity can interfere with the periodicity of the microlens array and periodical, "Moiré" patterns occur in the homogenization plane. In a worst case scenario, the line spacing of the input beam profile is equal to the pitch of the MLA. Each microlens then samples exactly the same intensity distribution and no homogenization occurs by the superposition of all beamlets. Thus, extra measures are required to shape the input beam in order to reduce these effects in a near-field homogenizer.

6.3.2 The concept of far-field homogenization

A way to mitigate the dependency on the input beam's intensity distribution is the lesser-known "far-field" homogenization. To achieve this, an additional lens is placed in front of the first MLA of a near-field homogenizer. This lens focusses the incoming beam onto the surface of the MLA or in other words, it creates the Fourier plane or far-field of the beam at the MLA. As a result, the angular spectrum of the incoming beam is sampled by the MLA rather than the original, lateral intensity distribution. Since the far-field typically has a much smoother, non-periodical shape, Moiré patterns are avoided.

The concept of far-field homogenization is depicted in figure 6.3 with the example of a divergent input beam. The beam consists of a wide angular distribution of its energy content, as is the case for a typical pump module with stacked laser diode bars. For simplicity reasons, this distribution is represented by only three sub-beams (bright green, blue, dark green), each with a different angle of incidence on the first lens. Furthermore, each sub-beam is divergent itself in order to generate a broad focus on a microlens rather than a narrow spot.

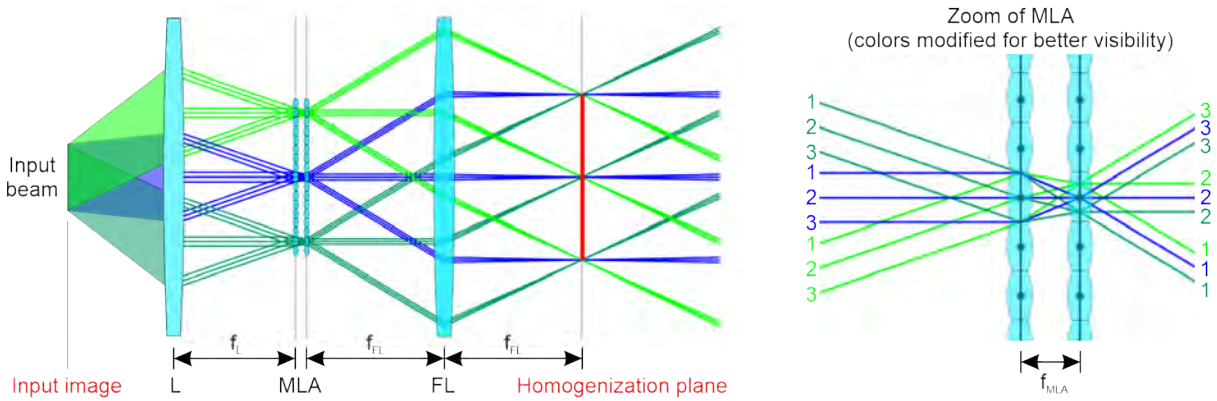

Figure 6.3: *Conceptual ray tracing for a "far-field" beam homogenization. A divergent input beam is focused by an additional lens (L) onto the first microlens array (MLA), after which the concept and depiction is similar to the near-field homogenization of figure 6.2. For simplicity reasons, the divergence of the input beam is represented by only three, non-collimated sub-beams (bright green, blue, dark green), each with a different angle of incidence on the lens. After the lens, three ray bundles are traced per sub-beam: two for the boundaries of the sub-beam and one for its center. Each of the ray bundle consists of two rays hitting the outer edges of a microlens and one ray hitting the center, see also the inset "Zoom of MLA". Note: All optical elements are assumed to be thin in the simulation. The drawings of bulk optics and the filled in input beams are artificial. Although the MLA is monolithic in the ray tracing simulation, the bulk drawing consists of two separate MLAs for a better understanding. FL: Fourier lens, f: focal length.*

Figure 6.3 shows another advantage of the far-field homogenization: the more "natural", direct dependency between the divergence of the input beam and the achievable divergence of the output beam. This is emphasized by the bright green and dark green sub-beams. The higher the angle of incidence of a sub-beam is, the higher the exit angle will be.

For the SuperBooster pump module, this direct dependency proves to be particularly beneficial. With increasing emission angle of the built-in laser diode stack, the energy content decreases. With a far-field homogenization, this transforms into an equivalent distribution of energy over the angular spectrum of the homogenized beam. Superimposed beamlets with higher exit angles therefore contain less energy and have a lower impact on the homogenized intensity distribution during propagation. Thus, the homogenized beam maintains its shape over a longer distance, in contrast to a near-field homogenization where each beamlet has approximately the same energy.

As a consequence, the maximum usable crystal thickness is potentially higher and the quality of the pump beam profile is better maintained throughout the crystal.

6.3.3 The custom far-field homogenizer of the SuperBooster

The far-field homogenization was originally implemented by Lastronics GmbH on another pump module of PFS. Due to the superior performance, this concept was then taken as a reference and an adapted version for the pump module of the SuperBooster was implemented. The new homogenizer consists of:

- several cylindric lenses to pre-shape the beam
- a focusing lens with a focal length of 65 mm
- a double-sided, hexagonal MLA with a lens pitch of 0.5 mm and a focal length of 2.78 mm (produced by aμs, Advanced Microoptic Systems GmbH)
- a Fourier lens with focal length 50 mm.

The pre-shaped beam in combination with the focusing lens creates a focus spot that illuminates a grid of $\sim 10 \times 10$ microlenses, while staying slightly below the 5° acceptance angle of the MLA. In accordance with equation (6.2), the homogenized pump profile size is ~9 mm FWHM.

An additional telescope with 400 mm and 125 mm focal lengths further reduces the size to ~2.7 mm FWHM at the position of the first surface of the Yb:KYW crystal. This size ensures a sufficient overlap of up to 20 amplification passes with the excited volume of the crystal and supports an amplified beam size with an energy fluence of less than $3\,\mathrm{J/cm^2}$ for the desired output energy of ~100 mJ.

Figure 6.4 shows the resulting, homogenized pump beam profile for four different positions along the optical axis, relative to the image plane where the first crystal surface is positioned. The intensity distribution for all four positions is exceptionally well homogenized and smooth, no ripples or features appear. The intensity stays above 80 % within a diameter of ~2.2 mm and above 50 % (FWHM) within a diameter of ~2.7 mm for a position of ± 1.5 mm relative to the image plane.

Owing to the superior properties of the far-field homogenization, only minor changes to the beam profile appear within a positional range of ± 4.5 mm around the image plane. The beam becomes slightly larger because of the inherent divergence and the edge steepness decreases. This behavior continues with increasing distance from the image plane and the degrading superposition of the microlens images becomes visible.

In conclusion, the homogenized pump beam grants an exceptionally smooth and flat beam profile within a total range of 3 mm around the image plane. This range can be extended up to a total of 9 mm with only minor changes to the beam shape.

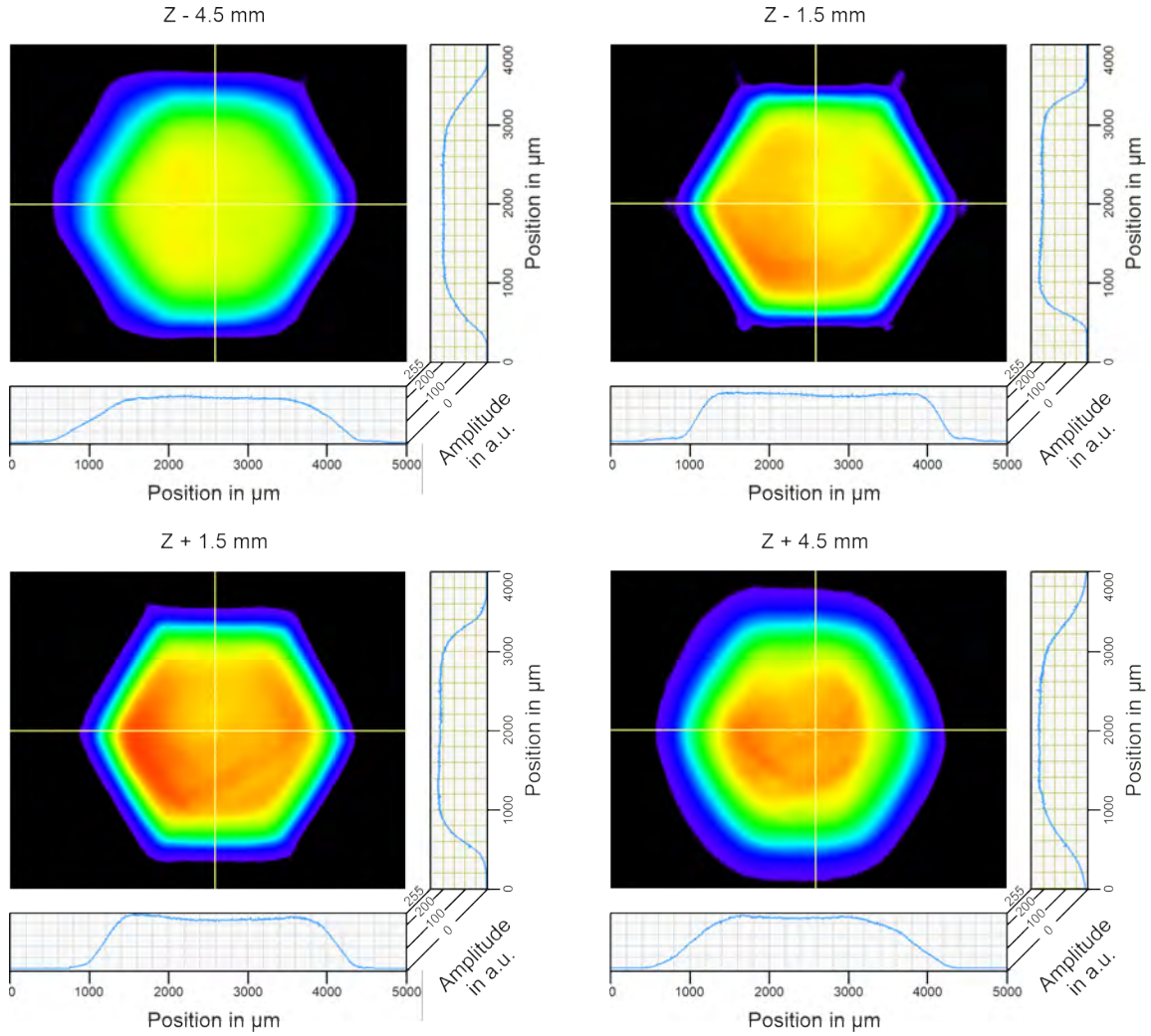

Figure 6.4: *Pump beam profile of the SuperBooster after far-field homogenization, recorded with a camera. The profile is recorded at different distances relative to the pump image plane ($Z = 0$ mm). The image plane coincides with the position of the first surface of the Yb:KYW crystal.*

6.4 Simulations for a suitable Yb:KYW crystal

Yb:KYW is the preferred gain medium for the new SuperBooster preamplifier. A detailed description of the material properties can be found in chapter 3. In contrast to the Yb:YAG used in the original Booster amplifier, the amplification bandwidth of Yb:KYW is sufficient to maintain the spectral bandwidth of 4.2 nm during amplification, even for an energy gain of more than 1000. Also, a filling up of the preshaped spectral amplitude hole around 1030 nm does not occur. As a result, the output spectrum can be used to efficiently compensate the gain narrowing in the subsequent 10 J main amplifier.

Yb:KYW can be furthermore efficiently pumped with the existing pump architecture of Yb:YAG. It exhibits an emission cross-section at 1030 nm similar to Yb:YAG and a considerably higher absorption cross-section between 934 and 941 nm, which partially compensates for the shorter lifetime. A brief comparison of the cross-sections is shown in table 6.1.

Table 6.1: *Absorption and emission cross-sections for each polarization axis of Yb:KYW at room temperature for typical Yb:YAG wavelengths. Yb:YAG values are added for comparison. Values taken from section 3.1.*

Polarization axis	σ_{abs} **at 934 nm in** 10^{-20}**cm**^{2}	σ_{abs} **at 941 nm in** 10^{-20}**cm**^{2}	σ_{em} **at 1030 nm in** 10^{-20}**cm**^{2}
N_g	0.4	0.4	0.4
N_p	1.1	1.0	1.1
N_m	3.3	1.9	2.5
Yb:YAG	0.4	0.8	2.2

This section is dedicated to finding an optimum combination of parameters for the Yb:KYW crystal and for the existing pump architecture. To achieve this, a comprehensive study was conducted with a MATLAB simulation tool called "V4" that was developed by J. Körner [47]. The tool is based on the fundamentals presented in section 3.2 and was benchmarked against several amplifiers of the POLARIS system [103]. It allows for a temporally and spatially resolved simulation of the pump as well as the amplification process inside arbitrary gain media. Further modifications were implemented in the scope of this thesis to also account for the birefringent nature of Yb:KYW with its three principal optical axes: N_g, N_p and N_m.

The V4 simulation tool also takes temperature dependent crystal properties into account. However, a precise calculation of the produced heat over a sequence of pulses cannot be done. Instead, the simulation is loaded with 3D temperature profiles generated with Autodesk CFD, similar to what was presented in section 4.2. Also the effects of ASE on the achievable output energy cannot be calculated with the V4 simulation. Thus, a safety margin of the simulated energy must always be considered.

6.4.1 Simulation parameters

In general, the pump and amplification processes inside a laser gain medium are complex with a large set of parameters. The most important ones are:

- crystal doping, thickness, and cut/orientation
- pump intensity, shape, size, spectrum, and duration
- seed energy, shape, size, duration, spectrum, and chirp
- number of amplification passes through the crystal
- cooling geometry and temperature.

Almost all of these parameters are cross-linked with each other in terms of the achievable output energy of an amplifier. In order to reduce the amount of possible combinations for the SuperBooster, several assumptions and boundaries are necessary.

First of all, an N_g-cut of the Yb:KYW crystal is the preferred choice since it allows direct access to the highest absorbing and emitting N_m axis. The N_g and N_p axes are not considered for the SuperBooster.

Second, the crystal doping is set at 5 % for which Yb:KYW is readily available on the market. Other doping concentrations such as 2 % and 3 % exist, but typically require the growth of custom boules and thus, are significantly more expensive.

Third, the following parameters are fixed by the available infrastructure of the PFS pump laser:

- The seed has a pulse duration of 3.8 ns with a spectral bandwidth of 4.2 nm and a spectral amplitude hole at the central wavelength of 1030 nm, see section 2.2. The seed is positively chirped, meaning the longer wavelengths arrive first at the crystal.
- The maximum seed energy is 100 µJ within a gaussian shaped beam profile.
- The pump module has a maximum power of 2350 W after homogenization. The central wavelength is 934 nm at 500 µs and shifts to 940 nm at 1500 µs due to heating up of the diodes.
- The pump profile presented in the previous section is directly loaded into the simulation. It is a hexagonal shaped flat top with 2.7 mm FWHM edge to edge.

Fourth, the following points have to be fulfilled to allow for a reliable and efficient operation of the SuperBooster:

- The amplified beam must have a flat-top profile with a FWHM diameter of at least 2.5 mm in order to stay below a fluence of $3\,\mathrm{J/cm^2}$ at 100 mJ output energy. This is the limit to avoid laser induced damages for a vacuum operation and ensures a safe operation in air, as mentioned in the target specifications of section 6.1.
- The 3" L1 mirror allows for up to 20 amplification passes. The angle of incidence of these passes decreases the overlap of each pass in the crystal. This in turn limits the effective crystal thickness to ~6 mm. Up to this value, each pass lies within the crystal area illuminated by the pump hexagon with 2.7 mm FWHM edge to edge.
- A crystal diameter of 8 mm allows for an easy mounting inside the liquid metal MKVII heatsink. The 1 mm thick sealing O-Ring leaves ~1.6 mm of clear aperture around the centered pump profile to fine align the overlap between the pump and the seed.
- The pump is set to a single pass through the crystal to reduce complexity and therefore to increase the robustness of the amplifier.
- A maximum pump duration of 700 µs is set. This is a factor of two higher than the fluorescence lifetime of Yb:KYW.
- The crystal is mounted in an MKVII heatsink and cooled via its circumference at a temperature of 15 °C to avoid condensation in the laboratory.

Fifth, the exact amount of optical losses per roundtrip through the amplifier geometry is unknown. Since the simulation is fed with ideal values, the losses are therefore set to zero first. Their impact on the simulated output energy is estimated afterwards as part of an error estimation that also includes variations of the generated heat of the crystal as well as tolerances of the pump beam size.

Sixth and last, a first iteration of simulations with all of the aforementioned parameters show an optimum $1/e^2$-diameter of ~2.1 mm for the gaussian input beam. This value is fixed for all following simulations.

6.4.2 Simulations and results

The V4 simulation tool does not allow for a precise calculation of the 3D temperature distribution within the crystal. Instead, a separate simulation is conducted in Autodesk CFD to retrieve this distribution. For this purpose, the remaining pump power as it travels through the Yb:KYW crystal is simulated with the V4 tool first. This allows to calculate the absorbed pump energy and with it the generated heat in the crystal. This heat is then used to simulate the 3D temperature distribution with Autodesk CFD.

The overall pump absorption only varies by a few percent within a temperature range of 0 to 100 °C, which has a negligible impact on the simulated output energy. Therefore, the crystal is set to the cooling temperature of 15 °C for the simulation of the pump absorption and only a single iteration step between the V4 tool and Autodesk CFD is conducted.

Pump absorption and material excitation

A summary of all simulation results is given in figure 6.5. The data of graph a) represents the remaining pump power as it travels through a 6 mm thick, 5 % doped Yb:KYW crystal, for the minimum and maximum simulated pump duration as well as for two pump wavelengths. The corresponding, relative excitation across the crystal is given in graph b).

Both graphs show the advantageous behavior of the pump module to shift the central wavelength from 940 nm towards 934 nm for short pump durations. The pump absorption is significantly stronger and causes a higher excitation of the crystal material. Furthermore, the effects of pump saturation are visible. The longer the pump duration is, the more saturated the material becomes, and the less absorption takes place. For example, at 934 nm and a pump duration of 200 µs, roughly 20 % of the initial pump power of 2350 W remains after traveling through the first 2 mm of the crystal. In contrast, at a pump duration of 700 µs this remaining power increases to ~35 % and thus, more of the subsequent crystal volume can be excited.

Most of the absorption takes place up to a thickness of 4 mm. After 6 mm, only a few percent of the initial pump power remains. Considering the equilibrium excitation β_{eq}, above which a gain is achieved, the maximum useable thickness of the crystal is 5 mm at the maximum pump duration of 700 µs. A thickness greater than this causes reabsorption during amplification. This thickness limit is further reduced if the actual temperature of the material is considered or shorter pump durations are applied.

Temperatures in crystal center

The remaining pump power at 934 nm shown in figure 6.5 a) was used to calculate a 3D map of the absorbed pump energy and with it the generated heat across the crystal. It is unknown, which percentage of the absorbed pump energy is actually converted into heat due to a lack of measurement data. Thus, two values are assumed: 10 %, which is close to the quantum defect, and 30 % which is a conservative guess based on the temperature measurements of Yb:YAG presented in section 4.2. The corresponding simulation of the temperature distribution inside of the crystal was conducted in Autodesk CFD for a pump duration between 200 and 700 µs as well as a crystal thickness between 2 and 6 mm.

Graphs c) and d) of figure 6.5 represent the retrieved temperatures along the center of the simulated crystals. While more pump durations were simulated, only the temperatures at the minimum and maximum durations are shown for better visibility. The temperatures for intermediate pump durations can be approximated from the presented data by a linear interpolation.

The maximum temperature is observed for a 2 mm thick crystal and ranges between ~70 °C and ~190 °C, depending on the generated heat. With increasing crystal thickness, the center temperature on the front side of the crystal decreases. This is mainly due to the improved heat dissipation of a larger volume and the larger cooling area of the circumferential cooling. A considerable drop of the temperature can be seen between the front and the back of each crystal. This is caused by the strong pump absorption in the first millimeters of the crystal. In addition, the comparably low thermal conductivity of $\sim 2.6\,\mathrm{W/(m\,K)}$ prevents an efficient heat dissipation from the hot areas on the front to the cold areas on the back.

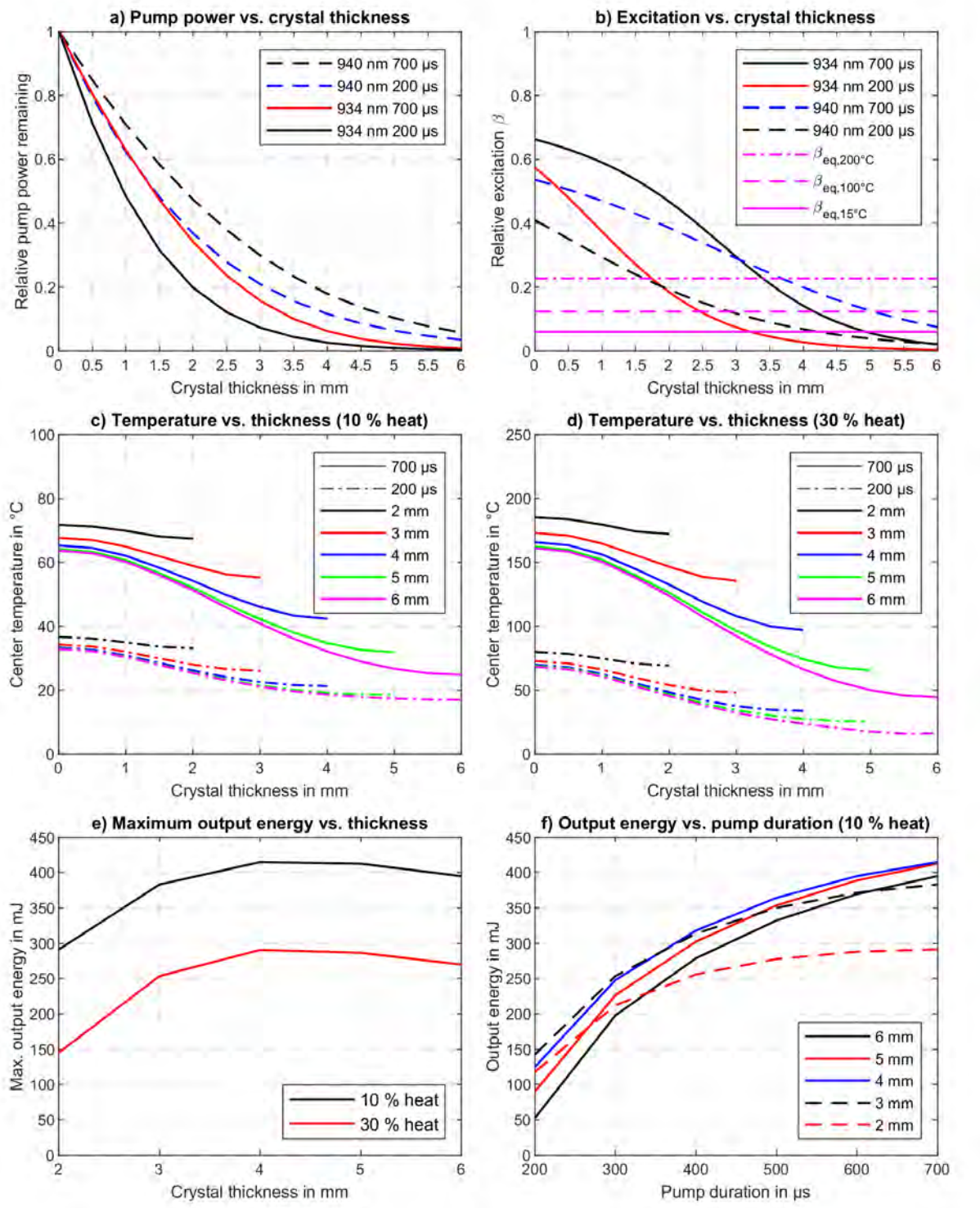

Figure 6.5: *Simulation results for Ø*8 mm, 5 % *doped Yb:KYW crystals, pumped with* 2350 W *in a hexagon with* 2.7 mm *FWHM edge to edge, seeded with a gaussian beam of* 2.1 mm *1/e²-diameter and* 100 µJ *input energy. The beam passes the crystal 20 times. A circumference cooling with* 15 °C *is assumed. a) Remaining pump power through a* 6 mm *thick crystal for two pump wavelengths and two pump durations. The crystal temperature is set to* 15 °C. *b) Corresponding, relative excitation of the crystal, with three different temperature values of the equilibrium excitation, above which a gain is achieved. c) and d) Center temperatures of* 2 *to* 6 mm *thick crystals. In c)* 10 % *of the absorbed pump energy is transformed to heat, in d)* 30 %. *e) The maximum energy that can be extracted per crystal thickness at* 700 µs *pump duration. f) Maximum output energy versus pump duration for* 2 *to* 6 mm *thick crystals and* 10 % *heat.*

It is important to note that all cross-sections and the thermal conductivity of Yb:KYW are only linear extrapolations for values above room temperature, as mentioned in the fundamentals of section 3.1. Thus, the simulation errors increase with higher percentages of the produced heat.

Achievable output energies

The retrieved 3D temperature distributions were loaded into the V4 tool and the maximum achievable output energies were simulated, see graph e) in figure 6.5. For all thicknesses, the maximum energy is reached at the maximum pump duration of 700 µs and at 20 amplification passes. Furthermore, each crystal thickness enables an energy of well above the desired 100 mJ.

Graph f) shows the dependency of the output energy on the chosen pump duration for each crystal thickness at a produced heat of 10 %. Increasing the heat to 30 % results in similar energy curves, but with an overall lower energy as depicted in graph e).

Conclusion

Several insights are gained for the choice of a suitable Yb:KYW crystal. First of all, the 100 mJ target specification for the output energy can be achieved for all crystal thicknesses, with rather large safety margins.

Second, the highest efficiency is obtained with a 4 mm thick crystal. It exhibits an optimum compromise between overall pump absorption and generated temperatures. Longer crystals operate at slightly lower temperatures but suffer from reabsorption at the end of the material, whereas shorter crystals suffer from increased temperatures and a lower pump absorption.

Third, for pump durations beyond 400 to 500 µs the generated heat grows considerably stronger than the output energy due to saturation effects. From 500 µs to 700 µs and a crystal thickness of 4 mm for example, the pump energy and with it the generated heat are increased by 40 %, whereas the output energy is only increased by an additional ~14 %. The resulting, higher temperatures translate directly into effects like thermal lensing and drifting. This makes the thermal management more demanding and potentially decreases the overall long term stability of the amplifier. Since the obtainable energy at 500 µs is already way above the targeted 100 mJ, longer pump durations are therefore not favorable.

Fourth, in terms of the achievable, maximum energy a 3 mm thick Yb:KYW crystal behaves similar to a 4 mm thick one up to a pump duration of 500 µs, with only minor energy differences. However, these differences grow with an increased heat of 30 % as will be shown in the subsequent paragraphs in more detail. While the slightly higher temperatures at 3 mm thickness might have a negative contribution to the thermal performance, the shorter bulk material potentially induces less aberrations to the amplified beam. This is in particular beneficial since the beam passes the crystal 20 times and therefore, any induced aberration is enhanced 20 times.

As a first conclusion, for the SuperBooster the optimum crystal thickness is between 3 and 4 mm and a maximum pump duration between 400 and 500 µs is favorable. In the following figure 6.6, more details are given for these combinations.

Dependency of the output energy on amplification passes and heat

The first two graphs of figure 6.6 represent the evolution of the output energy over the amplification passes for both crystal thicknesses and pump durations, and for 10 % as well as 30 % generated heat. At 10 % heat, a saturation of the amplification process is reached after ~14 passes. This shifts towards 16 to 18 passes with increased heat and shows the lower amplification efficiency at higher temperatures. The two pump durations show only a negligible influence on the saturation.

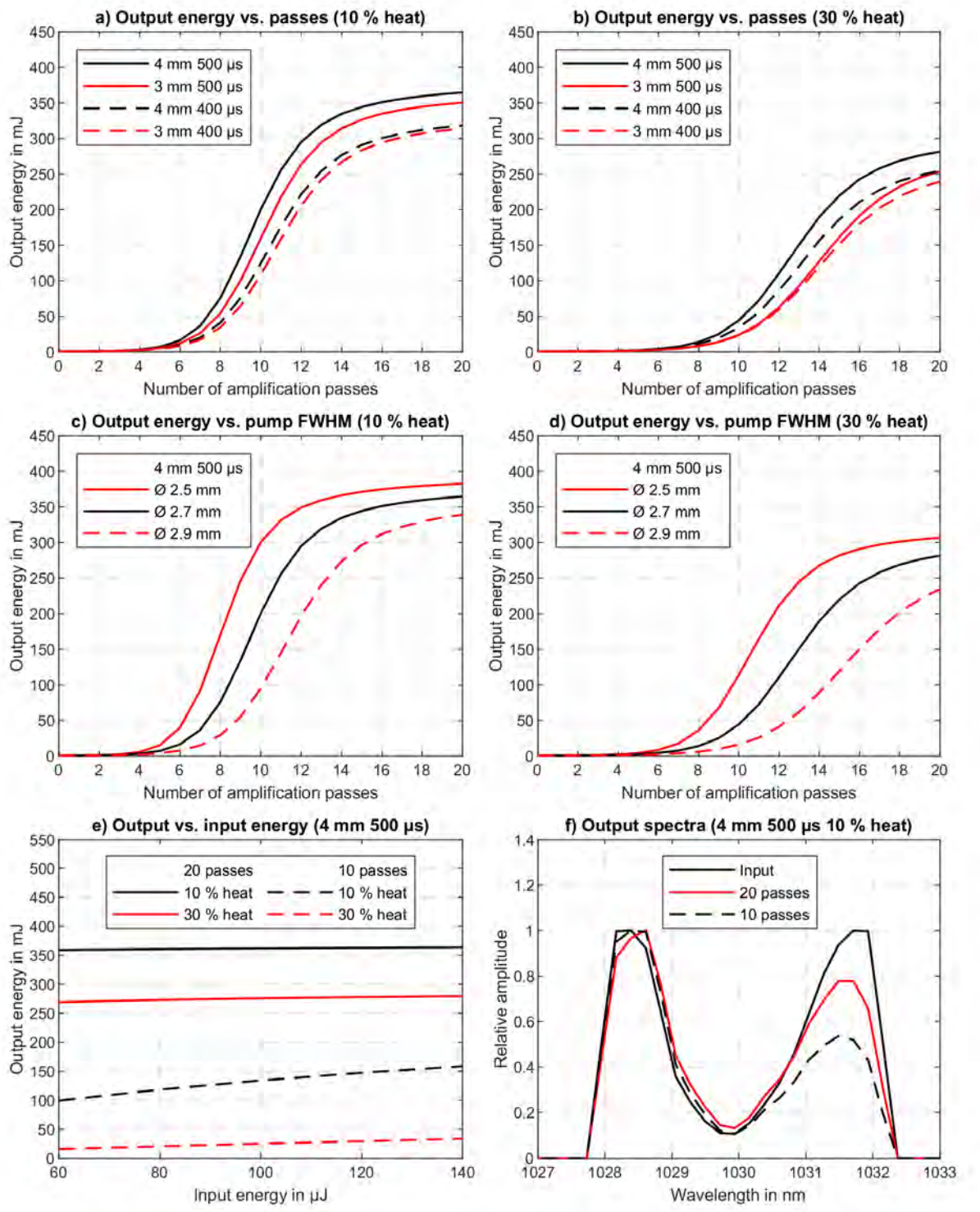

Figure 6.6: *Detailed simulation results for* 3 *and* 4 mm *thick, Ø*8 mm, 5 *% doped Yb:KYW crystals. a) and b) Output energy versus number of amplification passes, for* 400 µs *and* 500 µs *pump durations as well as* 10 *% and* 30 *% of absorbed pump energy that is converted to heat. c) and d) Output energy versus number of amplification passes for slightly different FWHM values of the hexagonal pump profile, for a* 4 mm *thick crystal and a pump duration of* 500 µs. *e) Influence of the input energy for the same crystal at 10 and 20 amplification passes as well as* 10 *% and* 30 *% produced heat. f) Evolution of an exemplary input beam spectrum over the amplification passes.*

In terms of the achievable output energy, both crystals exhibit a similar behavior at 10 % heat but show noticeable differences when the heat is increased. At 30 % heat, the pump and amplification processes are in favor for a 4 mm thick crystal due to the lower temperatures and the longer absorption length of the pump.

Dependency of the output energy on the pump beam size
Besides the generated heat, also the size of the pump beam profile has a substantial impact on the achievable output energy of the SuperBooster. This behavior is represented by graphs c) and d) for a 4 mm thick crystal at 500 µs pump duration and 10 % as well as 30 % heat.

Changing the 2.7 mm FWHM of the pump beam profile by ± 0.2 mm shifts the saturation along the amplification passes. At the maximum number of 20 passes, the impact on the obtainable output energy is moderate. However, below saturation energy differences of up to 50 % occur. This effect is particularly pronounced for higher heat values, where the saturation is already shifted due to the elevated temperatures.

Dependency of the output energy on the input energy
The input beam energy of 100 µJ proves to be a suitable value for the SuperBooster and a moderate change of it has almost no influence on the achievable output energy, as seen in graph e) of figure 6.6. A minor influence is observed only for an operation far below saturation, for example at half of the amplification passes.

Dependency of the output spectrum on amplification passes
The last graph of figure 6.6 shows the evolution of an exemplary beam spectrum over the amplification passes. It proves the initial intention of utilizing the broadband Yb:KYW instead of Yb:YAG to maintain a spectral bandwidth of 4.2 nm as well as the amplitude hole at 1030 nm.

The overall bandwidth stays identical at all times, as does the amplitude hole. Only the distribution of energy changes. This also shows a particular feature of Yb:KYW: the compensation of a positive chirp induced red shift with an emission cross-section induced blue shift. Before reaching saturation, represented by the graph for 10 passes, amplification is in favor of shorter wavelengths due to their slightly higher emission cross-sections. Upon reaching saturation, amplification is in favor of longer wavelengths since they arrive first at the crystal and therefore experience a higher gain.

Dependency of the output energy on optical losses
In the beginning of this sub-section the optical losses for a roundtrip were set to zero to keep the results as general as possible. The actual losses in the laboratory setup are estimated to be ~2 %. This value is based on the specified reflectivities: 99.7 % for L1, 99.8 % for the dichroic mirror DM1, 99.9 % for the dichroic mirror DM0 as well as L2 and 0.25 % for the remaining reflectivity of the AR coated crystal. The intrinsic losses of the crystal, caused for example by reabsorption, are already included in the simulation.

Additional simulations show that even at rather high optical losses of 5 % their impact is lower than the impact of the heat or the pump beam size. For a 4 mm thick crystal pumped at 500 µs, at a heat of 30 % and below saturation, such high losses only cause a ~25 % decreased output energy.

Parameters for a suitable Yb:KYW crystal
For the SuperBooster, the uncertainty of the generated heat as well as alignment tolerances of the pump beam size have to be considered for choosing a proper crystal and parameter set. From the aforementioned results, a safety margin with a factor of 2 to 2.5 between the simulated and the achievable output energy of the actual amplifier is reasonable. This factor ensures that the output energy meets the target specification of 100 mJ despite the uncertainties.

From the data of figure 6.6 this means either a 3 or a 4 mm thick, 5 % doped Yb:KYW crystal must be used with at least 14 to 16 amplification passes. The pump duration must be at least 400 µs at a pump power of 2350 W inside a hexagonal pump profile with 2.7 mm FWHM edge to edge. In terms of input energy, a value of 100 µJ is sufficient for a stable operation of the amplifier.

With this parameter set and the broadband emission bandwidth of Yb:KYW, the spectral shape of the input beam is maintained throughout the amplification process and thus, an efficient compensation of the gain narrowing in the subsequent 10 J amplifier can be achieved.

Also, this parameter set provides the best trade-off between optical-to-optical efficiency, requirements of the thermal management and beam quality. If necessary, a higher output energy can be achieved by thicker crystals or longer pump durations. However, this comes at the potential cost of a lower beam quality due to the risk of more material imperfections in case of a thicker crystal or unreasonably high thermal effects and a lower efficiency in case of longer pump durations.

6.5 Laboratory performance

During the assembly of the SuperBooster amplifier, only Ø8 × 3 mm, 5 % doped Yb:KYW crystals (from EKSMA Optics, UAB) were available for operation. The crystals are mounted inside the liquid metal MKVII heatsink. The following parameters prove to be the best for a day-to-day, maintenance free operation of the SuperBooster:

- Pump power: 2350 W @ 10 Hz
- Pump duration: 450 µs
- Pump pass number: 1
- Crystal cooling temperature: 15 °C
- Input energy: 100 µJ ±0.8 %
- Input bandwidth: 4.2 nm
- Amplification passes: 16

With these settings, a maximum output energy of over 100 mJ is achieved on a daily basis without the need for any realignment. The detailed performance parameters are presented in the following sub-sections.

6.5.1 Energy performance and spectrum

The implemented Yb:KYW crystal exhibits an absorption of 84 % of the overall pump. This value also matches closely the simulation for a 3 mm thickness. Thus, the application of only one pump pass is sufficient. A pump duration of 450 µs was chosen as a fix point for all measurements. This value exceeds the fluorescence lifetime of ~360 µs by 25 % but proves to be the best trade-off between a maximum output energy and a low thermal lensing. Qualitative experiments with longer pump durations showed a disproportional increase of the thermal lens while the additional output energy was moderate. This behavior was already seen in the simulations of figure 6.5, where the generated heat grows much stronger than the additional output energy after a pump duration of 400 to 500 µs.

Energy performance and dependencies

Up to a pump duration of 450 µs no noticeable contribution of ASE on the achievable output energy can be seen, as shown in figure 6.7 a). The graph represents the output energy for different time delays between the start of the pump pulse and the arrival of the seed pulse. The impact of ASE typically manifests itself in a strongly decreased slope of the energy curve, or in extreme cases as a roll-over of the curve, where no additional energy is gained despite a longer pump duration. Neither of both is observed for the Superbooster.

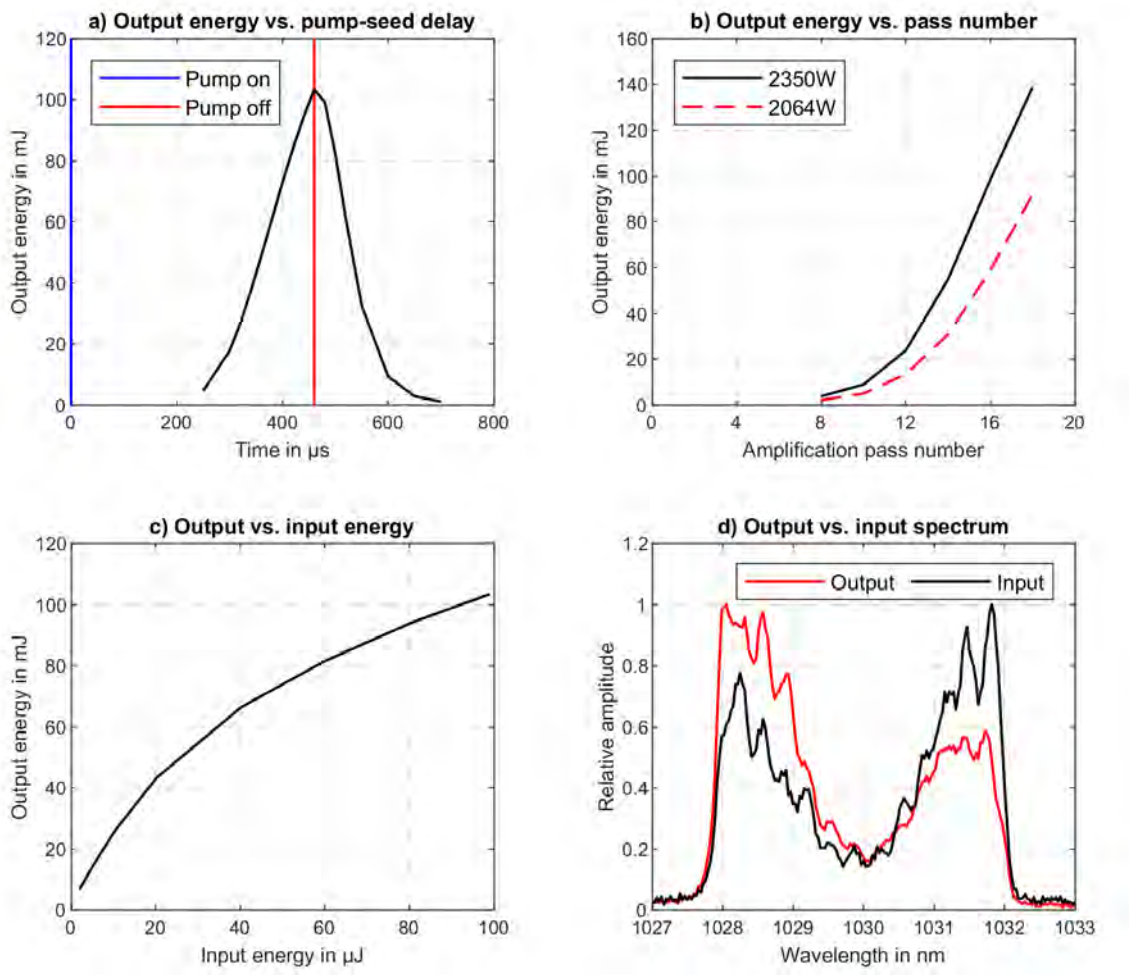

Figure 6.7: *Performance of the SuperBooster with day-to-day operation settings: The pump duration is set to* 450 µs *at* 10 Hz *for all graphs. The Ø*8 × 3 mm, 5 % *Yb:KYW crystal is water cooled at* 15 °C *and single-pass pumped in a hexagon with* 2.7 mm *FWHM. a) Output energy vs. arrival time of the seed after switching on the pump module, with a pump power of* 2350 W *and 16 amplification passes. b) Output energy vs. number of amplification passes for two different pump powers. c) Output vs. input energy at* 2350 W *pump power and 16 amplification passes. d) Output vs. input spectrum at the maximum output energy of c). Note: Oscillations in the spectrum are caused by the spectrometer fiber.*

A suitable working point of the amplifier that is balanced between overall alignment robustness and optical-to-optical efficiency was found at the maximum pump power of 2350 W in combination with 16 amplification passes, see figure 6.7 b). An output energy of up to 103 mJ is achieved with an optical-to-optical efficiency of ~10 %. The corresponding energy fluence is $2.8\,\mathrm{J/cm^2}$ and well below the specified limit of $6\,\mathrm{J/cm^2}$ of an operation in air. If required, the energy can be further boosted to 140 mJ with an optical-to-optical efficiency of 13 % by increasing the amplification passes to 18, and theoretically even further by increasing the passes to 20 which is the hard limit set by the 3” diameter of the L1 mirror.

During operation with 18 amplification passes a high sensitivity of the amplifier to misalignment was observed and clippings of the beam profile occured if the tight alignment tolerance were exceeded. This sensitivity typically required minor realignments each day before operating the amplifier at the maximum energy, depending on the day-to-day alignment of the overall pump laser. This extra step was avoided by switching to 16 amplification passes, which proved to be more robust. With it, no realignment of the amplifier was required for more than a year. Also, during this time no laser induced damages were observed, even at an output energy of 140 mJ.

The output energy could be further increased by a higher input energy, but the input is currently limited to the 100 µJ coming from the regenerative pre-amplifier, see graph c) in figure 6.7. A 20 µJ higher input energy is estimated to yield a ~10 mJ higher output energy. Nevertheless, the input energy of 100 µJ is high enough to reach the roughly linear region of the dependency between the input and output energy and thus, a sufficient energy stability can be achieved.

Comparison to simulation

The obtained output energy is a factor of two lower than the simulations. Also, a visible saturation of the energy over the amplification passes is not observed. This indicates that the generated heat is rather high. Another probable source of these deviations is the linear extrapolation of the cross-sections and of the thermal conductivities in the simulations, as described in section 3.1. Furthermore, only the thermal conductivity of undoped KYW is used since there is no suitable dataset for a doping with Yb^{3+}. As a consequence, the actual conductivity is expected to be lower and thus, the actual temperatures of the crystal will be higher. To investigate this further, temperature measurements with Yb:KYW are required similar to the ones presented in section 4.2.

More sources that may contribute to the energy difference could be a slightly off pump beam size, a crystal doping that varies from the specified 5 % or higher optical losses than ~2 % per roundtrip in the laboratory setup.

Spectrum

Figure 6.7 d) shows again the advantage of switching from the previously used Yb:YAG to Yb:KYW. Even at an energy gain of ~1000, the spectral bandwidth of the beam and especially the spectral amplitude hole around 1030 nm are kept constant. Only a slightly more pronounced amplification of the blue region compared to the red region of the spectrum is observed which falls in line with the previous simulations. Qualitative experiments also proved the compressibility of the spectrum to a pulse duration below 800 fs.

Energy stability

Figure 6.8 shows a typical recording of the energy stability over 10000 shots or ~17 minutes that was taken 30 minutes after switching on the full pump laser chain, including all chillers. The energy is set to ~80 mJ in the measurement. This value is sufficient to reach an output energy of ~10 J in the final 10 J amplifier on a daily basis.

The standard deviation of the average output energy is ±0.7 % over a sequence of 10000 shots. This value also includes the minor energy jumps around 9 minutes, 12 minutes and 14 minutes which were caused by the warm-up behavior of the regenerative pre-amplifier. The sudden energy drop at ~16 minutes was caused by an ionized dust particle in the focus plane of the SuperBooster. Without these energy jumps, the standard deviation e.g. within 1000 shots is remarkable with only ±0.46 %.

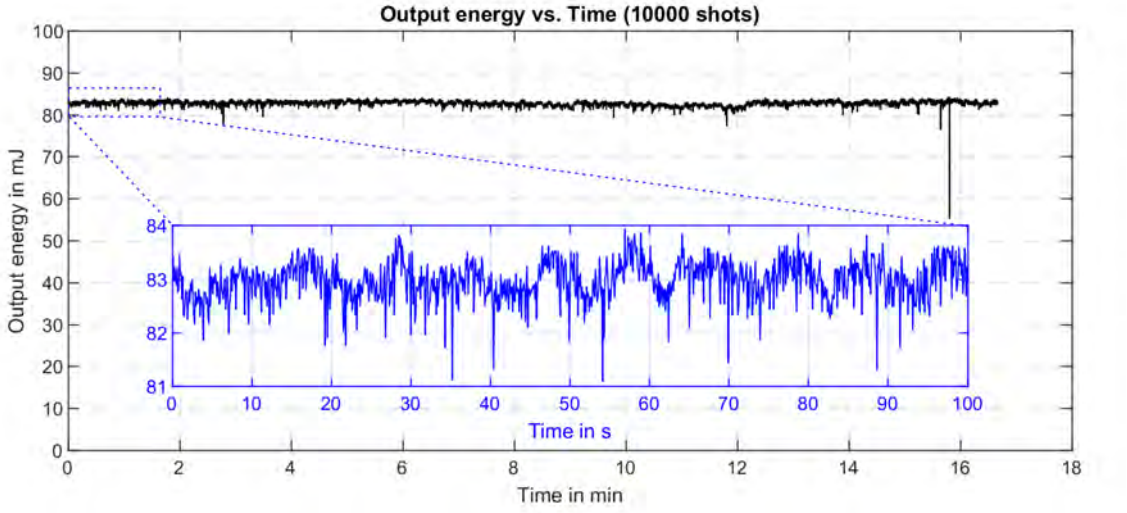

Figure 6.8: *Output energy stability over 10000 shots of the SuperBooster. The chosen energy corresponds to a typical setting that is required to reach an output energy of* 10 J *with the final* 10 J *amplifier. The measurement was started 30 minutes after switching on the full laser system. Inset: Detail view of the first 100 seconds or 1000 shots, with visible oscillations of the energy caused by the periodical cooling behavior of the crystal chiller. The mean energy over all 10000 shots is* 82.84 mJ ±0.7 %*, and over the first 1000 shots* 82.97 mJ ± 0.46 %*.*

Upon closer examination, the stability is dominated by periodical energy oscillations with a period of 5 to 10 seconds, as shown in the inset of figure 6.8. These oscillations are attributed to the cooling method of the water chiller, which periodically switches the cooling unit on and off. The typical oscillation of water temperature, as specified in the datasheet of the chiller, is within a range of ±0.1 to ±0.2 °C.

Overall, the achieved stability is sufficient to reliably seed the final 10 J amplifier. In case a better stability is desired, either a chiller with a linear cooling is required, or a large, intermediate water reservoir can be used that dampens temperature oscillations. Such a method is used for example for the 1 J amplifier The Cube, see section 7.5.

6.5.2 Beam profiles and pointing

The following three figures show the input beam profile, the output beam profile in the image plane and the shape of the focus. In each figure, two additional graphs are included, one for the horizontal and one for the vertical intensity cross-sections through the center of the beam profile. No artificial smoothing or fitting is applied to the data.

Figure 6.9 shows the input beam profile of the SuperBooster within the input image plane. The FWHM diameter is ~1.1 mm, which corresponds to a $1/e^2$-diameter of 1.9 mm. The gaussian beam shape together with the additional ~10 % magnification by the Type 2 system is sufficient to support an amplified output beam of the SuperBooster with a FWHM diameter of ~2.3 mm.

Figure 6.10 shows the hexagonal output beam profile at an energy of 100 mJ. The profile exhibits a high homogeneity and smoothness, owing to the exceptionally smooth and flat-top shaped pump beam profile of the homogenized pump module. 70 % of the output energy is contained within a central plateau of 2 mm diameter, with a standard deviation of the intensity of 11.5 %. The beam profile does not exhibit any high frequency modulations from the gain medium nor from the optical system, which makes a subsequent spatial filtering obsolete.

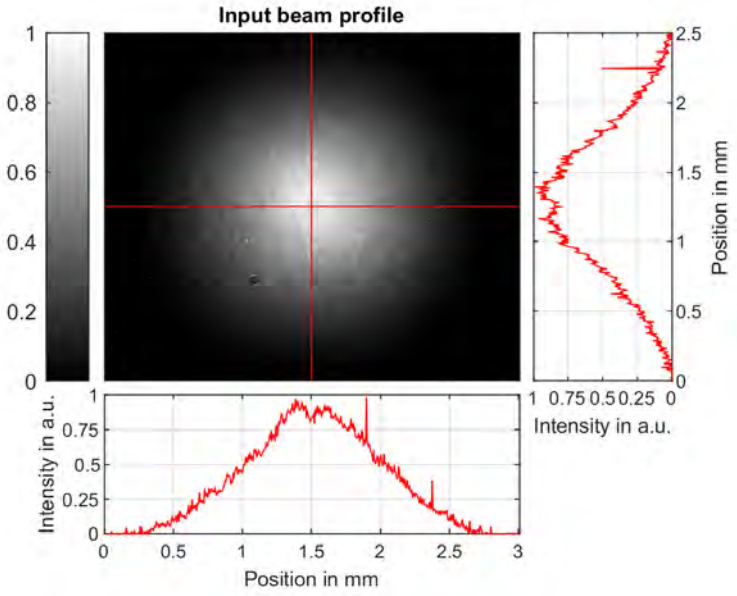

Figure 6.9: *Input beam profile of the SuperBooster with intensity cross-sections through the center, recorded with the diagnostics of the SuperBooster. Note: Black and white spots as well as diffraction rings are artifacts of the optics in the diagnostics.*

It was proven by separate measurements that this exceptional smoothness is not an effect of spatial frequencies that might be cut-off by the diagnostic system of the SuperBooster.

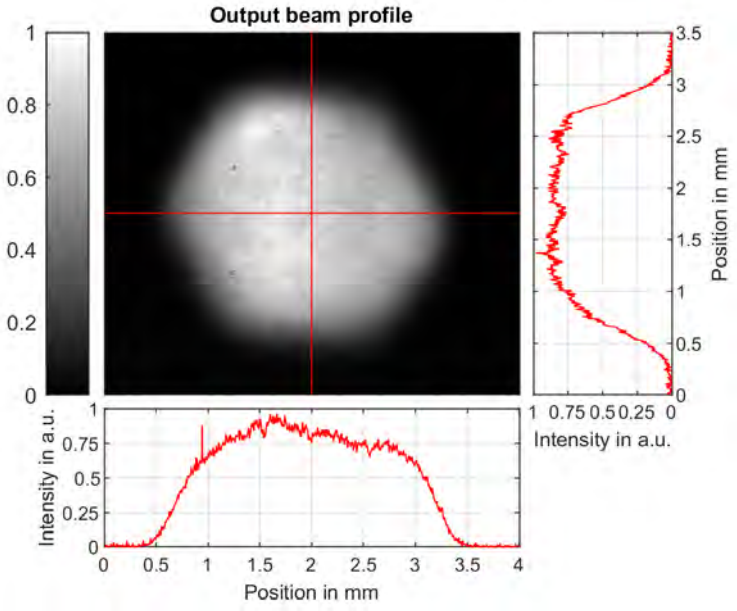

Figure 6.10: *Output beam profile in the output image plane of the SuperBooster with intensity cross-sections through the center, taken with the diagnostics of the SuperBooster at* 100 mJ. *The relative standard deviation of the intensity within a central diameter of* 2 mm *is* 11.5 %. *Note: Black and white spots as well as diffraction rings are artifacts of the diagnostic's optics.*

Figure 6.11 shows the shape of the focus after a lens with a focal length of 300 mm and at 100 mJ. Based on this, also the wavefront of the output beam is rather smooth without any substantial modulations or aberrations. 94 % of the overall energy is contained within the central peak of ~150 µm FWHM diameter and 5 % is contained within a side lobe on the right. This side lobe corresponds to a weak trail that appears during propagation of the collimated beam outside of the image plane and has its origin in the bulk material of the crystal.

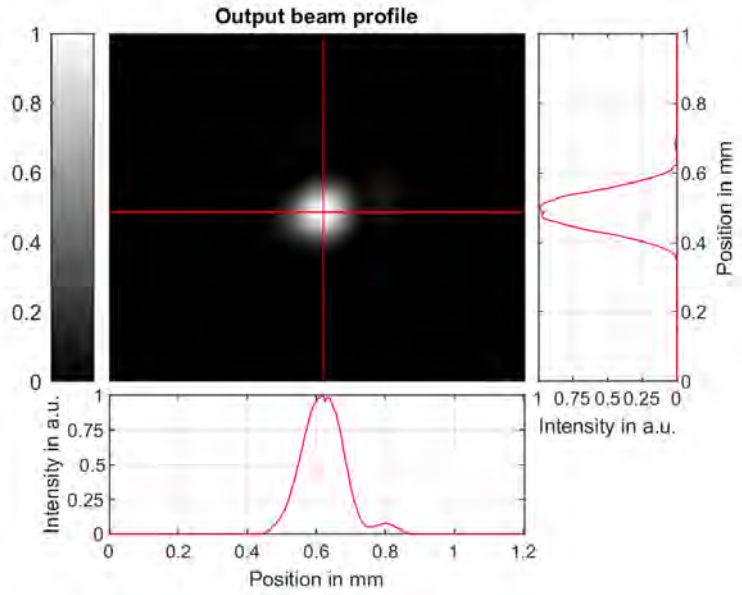

Figure 6.11: *Focus profile of the output beam of the SuperBooster with intensity cross-sections through the center, recorded at* 100 mJ *with a focal length of* 300 mm. *The main peak contains* 94 *% of the overall energy, the side lobe* 5 *%.*

The negligible effects of coma and astigmatism further prove the excellent optical quality of the Type 2 geometry. Considering the goal of the PFS pump laser chain to efficiently pump an OPCPA with a flat-top like beam profile rather than utilizing the focus, no corrections to the wavefront and the focus shape are required. Thus, the output beam of the SuperBooster is sufficient to seed the final 10 J amplifier.

Beam pointing and fluctuations

The SuperBooster proves to be a highly robust and stable amplifier, owing to the small amount of required optics in the Type 2 geometry, the compact footprint of ~$1000 \times 700\,\mathrm{mm}^2$ and especially the transmissive crystal setup. After all implemented water chillers are in thermal equilibrium and the pump module is switched on, the SuperBooster thermalizes within 15 seconds. Within this time, the thermal lens builds up and the direction of the output beam moves back to the alignment point for operation. After this, there is only a negligible drift that does not require an active realignment over the day.

Figure 6.12 shows the remaining beam pointing fluctuation for 10000 shots, which was taken during the energy stability measurement of figure 6.8. The measurement was started 30 minutes after switching on the full pump laser chain. The standard deviation of the horizontal beam pointing fluctuation is ±25 µrad and slightly lower in the vertical direction with ±17 µrad.

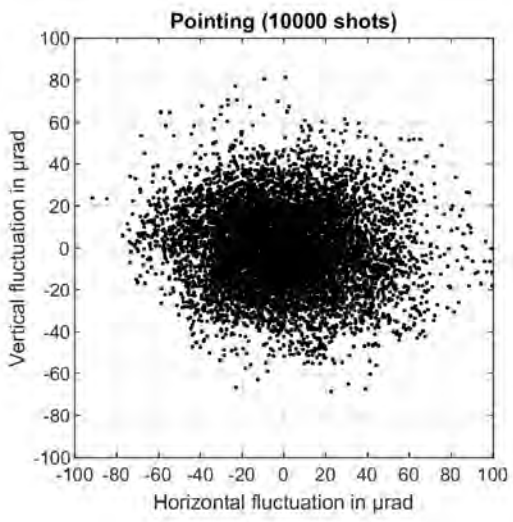

Figure 6.12: *Beam pointing fluctuation of the output beam over 10000 shots, taken with the focus diagnostic of the SuperBooster at* 100 mJ *and with a focal length of* 300 mm*, 30 minutes after switching on the full laser system. The horizontal fluctuation is* ±25 µrad *and the vertical* ±17 µrad*.*

The corresponding ratio between the lateral offset of the focus and the focus size calculates to 5.5 % and 4 % respectively. The absolute maximum value of the recorded beam pointing is 99 µrad. Altogether, these values lie well within the goal of the standard deviation of less than ±30 µrad that was specified in the beginning of this chapter.

6.6 Conclusion

The new SuperBooster fulfills all of the requirements that were specified in the introduction of this chapter for a successor to the original Booster amplifier. Table 6.2 shows a comparison of both amplifiers in terms of parameters and the measured laboratory performance.

Table 6.2: *Performance comparison between the original Booster amplifier and the new SuperBooster amplifier.*

	Original Booster	**SuperBooster**
Amplifier geometry	Non-imaging half-bowtie	Type 2 imaging
Footprint	$2500 \times 1000\,\text{mm}^2$	$1000 \times 700\,\text{mm}^2$
Crystal	Ø15 × 8 mm, 3 at.% Yb:YAG	Ø8 × 3 mm, 5 at.% Yb:KYW (N_g cut)
Pump	3000 W at 10 Hz, 1.5 ms, 940 nm, single pass	2350 W at 10 Hz, 0.45 ms, 934 nm, single pass
Input energy	Max. 180 µJ	Max. 100 µJ
Amplification passes	8	16 (18)
Output energy	137 mJ	103 mJ (140 mJ)
Energy stability	0.5 % Std.	<0.7 % Std.
Spectral input bandwidth	4.2 nm	4.2 nm
Spectral output bandwidth	<3.5 nm	4.2 nm
Beam pointing fluctuation	< 30 µrad Std.	25 µrad Std.

The new Type 2 imaging geometry and the custom homogenization of the pump beam profile caused a significant improvement of the output beam quality of the amplifier. This renders a subsequent spatial filtering and the resulting loss of energy obsolete and increases the overall efficiency of the amplifier.

Using a Ø8 $\times$ 3 mm, 5 % doped Yb:KYW crystal as the active gain medium proved to be highly successful. An output of over 100 mJ with a standard deviation of $\pm$0.7 % is achieved at a repetition rate of 10 Hz, with an option to increase the energy up to 140 mJ. Due to the broad amplification bandwidth of Yb:KYW, the spectral bandwidth of 4.2 nm and the spectral amplitude hole at 1030 nm are kept constant during amplification. This significantly counteracts the gain narrowing of the Yb:YAG based, final 10 J amplifier of PFS and makes the SuperBooster an ideal seed for it.

Long-term experiments show that the SuperBooster is highly robust in terms of mechanical stability, alignment-sensitivity, and maintenance. Over a period of one year, no realignment was required and no optical damages occurred despite extensive daily operations.

Compared to the simulations, the achieved output energy of the SuperBooster is by a factor of two lower and leaves room for further improvements. The cause for this can be a rather high heat load or discrepancies between the simulation parameters and the actual parameters of the laboratory setup. A potential option to improve the performance further is the application of a 4 mm thick, 5 % doped Yb:KYW crystal. Simulations show that the increased thickness allows for a higher output energy at the same heat load of the currently implemented crystal. Another option is a lower crystal doping combined with an even further increased thickness, for example 3 % and 6 mm.

Chapter 7

The Cube

”The Cube” is an amplifier for chirped pulses based on Yb:YAG, with an output energy of up to 2 J, a repetition rate of 10 Hz and an output spectrum that allows for a compression to a sub-picosecond pulse duration. It was the main amplifier of the PFS pump laser during its installation at MPQ and during the experiments of PFS published in [18–20]. It also served as an experimental platform for the development of the final 10 J amplifier.

The Cube was developed during this thesis as the replacement of the original 1 J main amplifier ”The Tube” [28]. It is based on the same optical design and incorporates several improvements, such as a pump module with significantly higher beam quality, the new AMKI and MKIII heatsinks presented in section 4.3, a modular vacuum chamber, and opto-mechanical components with higher stability. The development started during the design phase of the final 10 J amplifier, when several critical issues with The Tube emerged. Although the fundamental design of The Tube proved to be successful, these issues eventually prevented an efficient day-to-day operation of PFS. This includes a frequent breakdown of optics, instabilities of the beam and a maintenance effort of roughly one week per three weeks of operation. Due to the restrictive mechanical design of The Tube, modifications to solve these issues were not possible. Thus, the development of the 10 J amplifier was halted in favor of a replacement amplifier, The Cube.

The following sub-chapters give an in-depth overview of the experiences gained with The Tube, the conclusions that were drawn for the development of The Cube, its complete design, and its performance as the main amplifier of the PFS pump laser.

Overview

7.1 Experiences with The Tube:
Lessons learned from the original 1 J amplifier The Tube.
7.2 Target specifications:
System and performance requirements of the pump laser for a stable OPCPA and reproducible SHHG experiments.
7.3 Opto-mechanical design of The Cube:
In-depth description of the optical system and detailed schematic of the laboratory setup including the new modular vacuum chamber.
7.4 Simulations for 3 mm crystals and 5 mm ceramics:
Theoretical study of the performance with 3 mm thick Yb:YAG crystals or 5 mm thick Yb:YAG ceramics with ASE absorbing cladding.
7.5 Laboratory performance:
Detailed summary of all measured performance parameters.
7.6 Issues with The Cube:
Common issues that emerged during operation.
7.7 Conclusion:
Short summary of The Cube's key aspects and achievements, comparison of the performance with The Tube.

7.1 Experiences with The Tube

Despite the issues that emerged with The Tube, it granted valuable insights into the daily challenges of joule-class Yb:YAG amplifiers. These insights paved the way to develop The Cube and the final 10 J amplifier. The most important ones are summarized within this section.

Summary of The Tube
The basic characteristics of The Tube amplifier in its final configuration are as follows:

- Geometry: 20-pass rotational symmetric 4f-relay-imaging
- Footprint: ~$2500 \times 500\,\mathrm{mm}^2$
- Crystal: Active-mirror, $40 \times 40 \times 6\,\mathrm{mm}^3$, 2 % doped Yb:YAG
- Pump: 10.5 kW at 1.25 ms, 938 nm and 2 Hz
- Energies: Input of up to 90 mJ, output of up to ~1 J
- Spectrum: <3.2 nm bandwidth, centered at 1030 nm
- Compressibility: <800 fs.

More background information can be found in the dissertation of C. Wandt [23].

Successful design features
The fundamental optical design of The Tube and its equivalent version at the POLARIS system [94] showed the superb properties of the 20-pass rotational symmetric 4f-relay-imaging concept, see also section 5.3 for an overview of the concept. The design exhibits an intrinsic compensation of astigmatism and allows for the generation of high quality beams. It also keeps the required footprint comparably small despite the high number of amplification passes.

Furthermore, experiments with The Tube showed that a 6 mm thick, 2 % doped Yb:YAG crystal is sufficient to reach an output energy of 1 J at a pump intensity of $10.5\,\mathrm{kW/cm}^2$, a pump duration of 1.25 ms and an input energy of 90 mJ. Together with an input spectrum that exhibits an amplitude hole around 1030 nm to counteract gain narrowing, a spectral bandwidth of up to 3.2 nm can be achieved, which supports a compression of the pulses to below 800 fs.

Fundamental shortcomings

The most limiting feature of The Tube turned out to be its vacuum chamber. A sequence of flange-mounted DN320 vacuum tubes was chosen to enclose the amplifier due to the rotational symmetric imaging system. All optics and sub-assemblies are mounted on rings, which are interconnected by thick, carbon-reinforced rods. This design choice resulted in severe drawbacks for daily operations:

- **The design leaves no room for modifications.** There is little to no space for a more sophisticated cooling of all components, a modification of the pump optics or for the implementation of improved crystal heatsinks and mounts.
- **There is no quick access to the amplifier.** In case of maintenance or realignment, the DN320 tubes have to be disassembled and eventually reassembled. This process also causes a misalignment of the optical system and thus, increases the overall maintenance effort. The issue is further enhanced by the short, 60 mm working distance of the pump module which requires a shift in position and a subsequent realignment in case the chamber needs to be opened. Altogether, this typically requires a full working day for any alignment step.
- **The optical system is prone to vibrations and bending.** Only two mounting rings are directly connected to the DN320 tubes via counter screws. All other rings are connected only to the rods. Due to the limited bending stiffness of the rods, these rings are prone to vibrations and oscillations. Furthermore, the rod assembly has a low torsional stiffness and only the two fixed rings partially counter any rotation. This causes the whole opto-mechanical setup to twist and misalign when it is put into or out of the vacuum chamber for maintenance.
- **The optical system is mechanically coupled to the vacuum chamber.** Because of this, evacuating and venting the vacuum chamber and the corresponding movement of the chamber results in a misalignment of the optical system. Although this is partially compensated by motorized optics, it severely limits the alignment tolerance of the amplifier and causes a frequent beam clipping.
- **The optical system is prone to thermal drifts.** Spontaneous emission of the crystal and stray light of the pump module heat up the vacuum chamber and also the internal sub-assemblies. Together with the mechanical coupling between the optical system and the vacuum chamber, this results in severe thermal drifts of the amplified beam. Up to a repetition rate of 2 Hz this can be compensated by motorized optics. Above that, the limited alignment tolerance of the system is exceeded and the beam walks off the optics. In addition, modifications to the cooling concept to reduce thermal drifts are limited by the tight space constraints of the DN320 tubes.

Other drawbacks that are not directly related to the vacuum chamber are:

- **Optics frequently break down.** The measured energy fluence within the output image plane at an energy of 1 J is on average $\sim 2.4\,\mathrm{J/cm^2}$, with several features in the beam exceeding this value. These features either emerge from the crystal material itself or from imperfections and dust on optics. Together with the in general high energy fluence in vacuum, these features are considered as the main driver for the frequent breakdown of optics. This breakdown is further enhanced by the frequent beam clipping.
- **No depolarization is considered.** Neither the crystal orientation nor the polarization state of the seed beam is optimized to keep the depolarization losses at minimum. This causes the beam to change the state of polarization across the beam profile, see also section 3.5. As a result, a considerable amount of energy is sent towards the pre-amplifier after separating the input and output beams with a TFP. This undetected energy poses little risk to the pre-amplifier due to a spatial filter and an optical isolator. However, it causes

an increased but undetected energy fluence within The Tube since the aforementioned value of $2.4\,\mathrm{J/cm^2}$ is measured after the TFP.

- **The wavefront of the output beam is deteriorated by the crystal heatsink.** The concept of gluing an active-mirror crystal to a water cooled metal heatsink works well in terms of the cooling performance. In contrast, the concept shows drawbacks of the achievable beam quality. The strong mismatch between the thermal expansion coefficient of the copper heatsink and the glued Yb:YAG crystal induces considerable wavefront distortions to the beam. For more details see section 4.1. This effect further increases with higher repetition rates or longer pump durations, since also the temperatures rise.
- **Any aberration in the image plane is enhanced by a factor of 10 or 20.** The multi-pass geometry re-images the beam 10 times onto the crystal, which translates to 20 passes through the bulk material of the crystal. Therefore, the effect of any aberration of the surface or the bulk material is enhanced by a factor of 10 to 20. As a consequence, an extraordinarily high quality is required for a crystal or mirror that is placed in one of the amplifier's image planes.

All of these drawbacks limit the day-to-day operation and the quality of the PFS pump laser, and thus, also the operation of the OPCPA stages and the experiments of PFS.

7.2 Target specifications

In order to reliably pump the OPCPA stages of PFS the following target specifications were set for the redevelopment of the 1 J amplifier:

- **Size:** A footprint of $3000 \times 750\,\mathrm{mm^2}$ must not be exceeded because of laboratory space constraints.
- **Geometry:** The fundamental 20-pass 4f-relay-imaging geometry of the previous The Tube amplifier shall be applied with some modifications to keep wavefront aberrations under control.
- **Vacuum chamber:** A vacuum chamber with quick and easy access to all optics is required to drastically shorten maintenance downtimes.
- **Mechanical stability:** The optical system must be decoupled from the vacuum chamber. Furthermore, the beam pointing fluctuation should stay below a standard deviation of 50 to 100 µrad, based on OPCPA experiments that were performed with The Tube.
- **Energy:** An output energy of >1 J at 10 Hz with a stability of $\pm 0.6\,\%$ is required to reliably pump the OPCPA stages of PFS.
- **Energy fluence:** Based on the breakdown of optics in The Tube, a fluence limit of $3\,\mathrm{J/cm^2}$ must not be exceeded for an operation under vacuum. If possible, the fluence should be kept far below this limit to ensure a maintenance free long-term operation.
- **Spectrum and bandwidth:** The output spectrum must have a bandwidth of at least 3 nm FWHM to minimize LIDT issues and without an amplitude hole at 1030 nm for an optimal compression.
- **Compression:** The bandwidth of the output pulses must support a compression in time to below one picosecond.
- **Beam shape:** A flat-top shaped output beam profile without features is preferred for an efficient SHG process and pumping of the OPCPA stages.

7.3 Opto-mechanical design of The Cube

The Cube shares the almost identical optical design of The Tube to meet the aforementioned target specifications and to minimize the required development time. The mechanical design was drastically modified. The concept of DN320 tubes was scrapped and instead a modular, cuboid vacuum chamber was implemented with more sophisticated opto-mechanics.

Another major change to the design is the implementation of a new 33 kW pump module (PM48 from Lastronics GmbH), which was initially bought as the pump source of the final 10 J amplifier. The new pump module offers a significantly higher quality of the pump beam and a more than two times longer working distance than the pump module of The Tube.

7.3.1 Schematic of the opto-mechanical design

The detailed optical assembly of The Cube, as it is set up in the laboratory, is illustrated in figure 7.1.

Seed and pump beam paths
A total of 10 4f-imaging telescopes based on concave mirrors (CM) are arranged in a rotational symmetric geometry. All mirrors are mounted on fixed rings, so called ”mirror wheels”. The concave mirrors are 1” in diameter and have a focal length of 1000 mm. Together with the active-mirror Yb:YAG crystal (Xtal), 20 amplification passes are achieved.

The pump beam is imaged onto the crystal via a telescope made from two bi-convex lenses (L). Due to the more advanced technology of the pump module, a 2” lens is sufficient for a focal length of 125 mm, which doubles the working distance compared to The Tube.

The seed and pump beams are separated by a dichroic mirror (DM) which transmits the pump at 940 nm and reflects the seed at 1030 nm. Owing to the significantly greater space of the new vacuum chamber and the longer working distance, the tilting angle of the dichroic mirror could be optimized for a maximum reflectivity at 1030 nm. At the optimum angle of 43°, the remaining leakage of the seed is on average ~0.8 % per hit.

Control of ASE and stray light
Additional water cooled shades separate the crystal area from the rest of the amplifier. This way, stray light from the pump and spontaneous emission from the crystal are blocked and the heat load to the opto-mechanical assembly is reduced. In contrast, this was not the case in The Tube which resulted in a thermal drift of the amplified beam.

The generally higher alignment stability of The Cube allowed for the implementation of a pinhole plate in the focus plane of the amplifier which blocks all light except the amplified beam. Thus, parasitic reflections and a feedback of ASE are efficiently suppressed. For this task, a Ø4 mm aperture of each pinhole proved to be sufficient and it also keeps the alignment sensitivity of the system on a reasonable level.

A central shade in front of the big folding mirror FM1 prevents oscillations of the ASE between the mirror and the crystal. Without this shade, the plane FM1 mirror and the thermal lens of the crystal form a high quality cavity that amplifies the ASE to potentially harmful energy levels.

The issue of oscillations never occurred within The Tube, since the general misalignment from closing the DN320 tubes prevented a precise angular alignment between the FM1 mirror and the crystal. Thus, multiple reflections of the ASE quickly walked off the crystal. The cavity issue became particularly pronounced within The Cube due to the highly stable opto-mechanical system and a new, high precision alignment method. This method comprises attachable alignment marks on each optics and IR cameras to observe them. It enables an angular alignment preci-

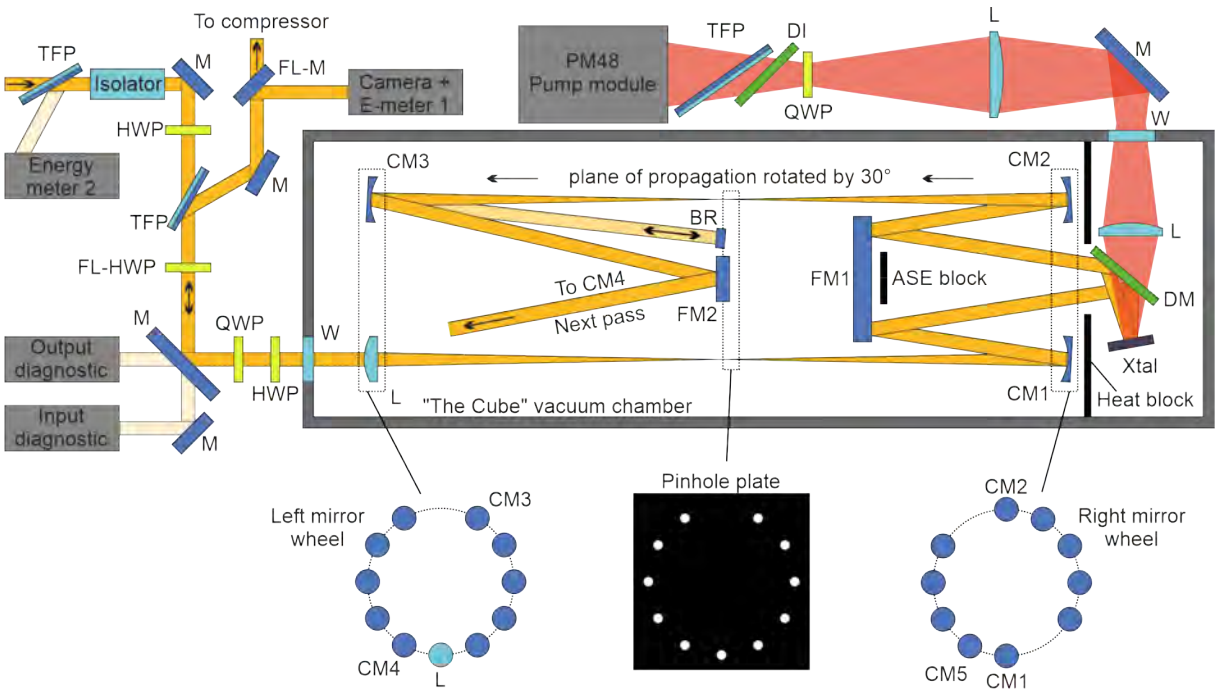

Figure 7.1: *Schematic of The Cube's optical assembly. The fundamental geometry is the 20 pass 4f-relay-imaging of the previous amplifier The Tube. The input and output beams are divided by a* 65° *thin film polarizer (TFP). A quarter-wave plate (QWP) and a half-wave plate (HWP) generate an elliptical input polarization that counteracts depolarization inside the amplifier. They also cause a* 90° *rotated, linear polarization of the output beam on its way back. Inside the vacuum chamber, all concave mirrors (CM) as well as the input lens (L) are* 1" *in diameter with a focal length of* 1000 mm. *They are mounted on two fixed wheels, separated by a pinhole plate that filters out unwanted parasitic reflections and ASE. The active-mirror Yb:YAG crystal (Xtal) is pumped through a* 45° *dichroic mirror (DM) that is set under an angle of* 43° *to optimize reflectivity at* 1030 nm. *The pump is imaged by a telescope onto the crystal. A TFP and a dichroic mirror (DI) filter out backreflections of the pump and parasitic leakages of the seed. The seed beam propagates for 5 roundtrips and is reflected back by a mirror (BR) for another 5 roundtrips. The plane of propagation is tilted by* 30° *after each roundtrip. Input and output diagnostics record the beam profiles through leakages of* 45° *mirrors (M). A removable half-wave plate (FL-HWP) optimizes the leakage for either the input or the output beam. FL-M: Flip (removable) mirror, E-Meter: Energy meter, W: Window, FM: Folding mirror.*

sion of less than 100 µrad for all mirrors, which for example corresponds to a positioning error of 0.2 mm of the ~Ø12 mm beam on a concave mirror. As a result, the FM1 mirror is aligned almost perfectly parallel to the crystal, if the beam path is projected through the dichroic mirror.

Input and output beam manipulation and detection

The quarter-wave plate in The Tube which rotates the linear polarization of the beam by 90° after hitting the backreflector (BR) was removed from the optical system. Instead, a polarization state generator based on a quarter-wave plate (QWP) and a half-wave plate (HWP) is positioned in front of the vacuum chamber. With it, a state of polarization can be generated that efficiently compensates the depolarization that is induced by the crystal and the slightly polarization-dependent dichroic mirror.

Furthermore, upon exiting the vacuum chamber, a linear polarization is generated that is rotated by 90° with respect to the input beam. The remaining depolarization losses are transmitted through the TFP and reflected out of the beam path by an optical isolator. An energy detection of this beam is used to fine adjust the polarization state generator.

A dedicated diagnostic system enables the permanent observation of the input and output beams. In addition to the common near-field/image plane camera and the far-field/focus camera, also the beam profile on the last concave mirror CM1 is recorded by a third camera. This way, a sufficient evaluation can be conducted whether a feature in the beam profile potentially causes a laser induced damage or not.

7.3.2 Mechanical implementation of The Cube

Most of the changes to the optical system were possible due to the new vacuum chamber and its significantly larger inner volume. A 3D render of the vacuum chamber including the complete opto-mechanical assembly can be found in figure 7.2.

Modular vacuum chamber design

In order to keep the price and manufacturing time as low as possible, a vacuum chamber was developed that could be manufactured completely in-house. The result is a design based on four modular, cuboid chambers with a size of $400 \times 400 \times 500\,\mathrm{mm}^3$ each. Hence also the name "The Cube". The chambers are bolted together with a custom O-ring interconnection to create a tight vacuum sealing. With this configuration, the fully assembled and operating amplifier achieves pressures down to 1×10^{-7} mbar. The size of the assembled vacuum chamber is $\sim 450 \times 450 \times 2500\,\mathrm{mm}^3$ at a total material cost of less than 6000 €.

Stable mounting of optics

Each modular chamber contains a breadboard which is screwed directly to the optical table by additional metal posts which are connected to the vacuum chamber via bellows. Such posts are also called "decoupled feet" since they mechanically decouple the breadboard from the surrounding vacuum chamber. Thus, evacuating and venting the vacuum chamber has only negligible influence on the overall alignment of optics that are mounted on the breadboards, in contrast to The Tube. Additional guide rails in the center of each breadboard minimize the angular misalignment if any sub-assembly needs to be shifted. This is particularly beneficial for the mirror wheels, whose center distance is adapted to compensate the thermal lens of the crystal.

Owing to the larger inner volume of the vacuum chamber, all sub-assembly mounts are made of thick aluminum plates that are reinforced with additional struts. The fixed crystal mount of The Tube was exchanged with an XY linear stage and a custom-developed, metal-joint kinematic mirror holder that allows to mount and align the heavy AMKI and MKIII heatsinks. Furthermore, an active cooling is applied to the dichroic mirror mount as well as the last pump lens.

Altogether, this greatly enhances the mechanical and thermal stability of the amplifier setup and reduces beam pointing fluctuations and thermally induced beam drifts. Due to this superior stability, only the FM2 mirror in the second image plane of the amplifier is motorized to compensate slight angular tilts of the crystal under full thermal load.

Beam delivery to The Cube

Besides the amplifier assembly, also the spatial filter between the original Booster pre-amplifier and The Cube was redesigned. New optics and a better filtering with a pinhole increased the maximum available input energy of The Cube from 90 mJ to 137 mJ. Furthermore, a combination of waveplates and an optical isolator enables a precise filtering of backreflected depolarization losses from The Cube, which would otherwise damage the pinhole over time.

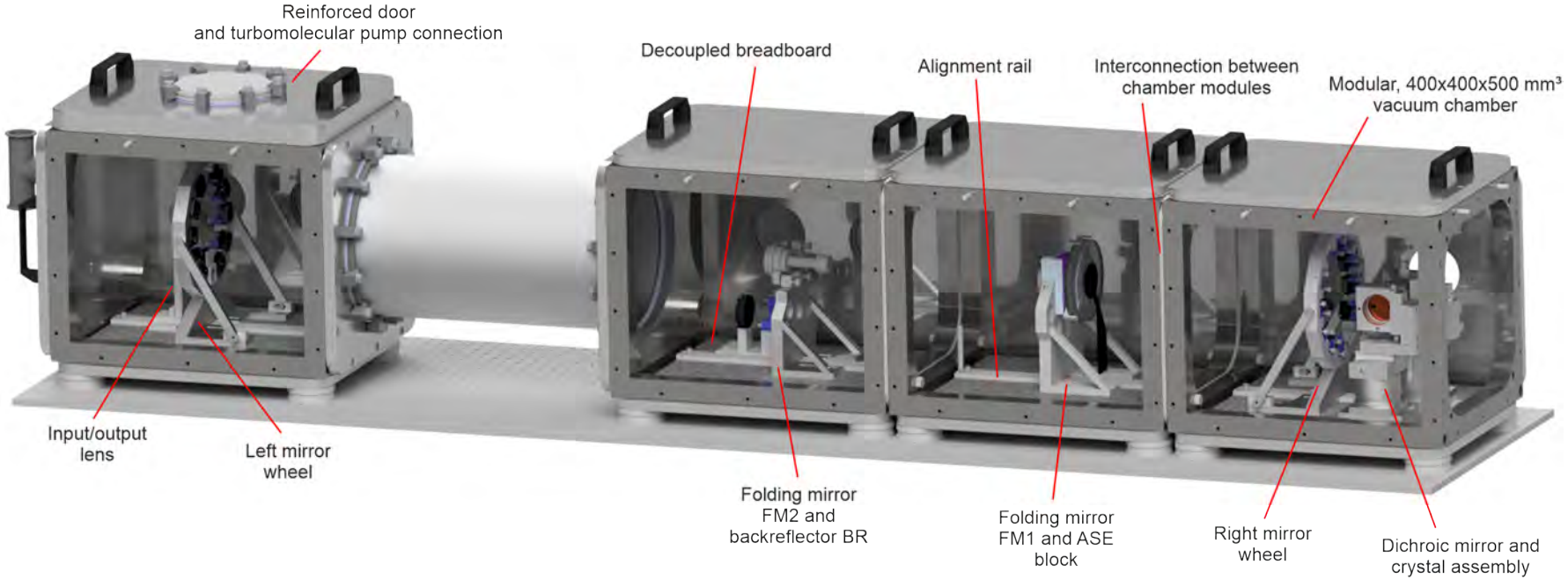

Figure 7.2: *Rendered image of the vacuum chamber and complete opto-mechanical assembly of The Cube, generated with Autodesk Inventor. The vacuum chamber is made out of four modular chambers that are combined via custom O-ring interconnections. The overall size is* $\sim 450 \times 450 \times 2500\,\mathrm{mm}^3$*. Each modular chamber contains a breadboard that is mechanically decoupled from the chamber and screwed directly to the optical table. All optics are mounted on solid, reinforced aluminum mounts that can be shifted along guide rails without losing the angular alignment.*

7.4 Simulations for 3 mm crystals and 5 mm ceramics

To further increase the performance of The Cube, new Yb:YAG crystals, or alternatively ceramics, are implemented as the gain medium. First estimations for a suitable parameter set of the crystal and the pump were based on the operational parameters of The Tube, which are:

- **Crystal material:** 2 % doped Yb:YAG, random lattice orientation.
- **Crystal geometry:** Squared $40 \times 40\,\mathrm{mm}^2$, 6 mm thick.
- **Crystal cooling:** Active-mirror, glued on top of a water cooled CO_2-laser mirror, 20 °C.
- **Pump:** Double-pass, 10.5 kW at 938 nm, 2 Hz and 1.25 ms within an area of $10 \times 10\,\mathrm{mm}^2$.
- **Seed:** Up to 90 mJ, gaussian shaped beam profile, 3.5 nm FWHM bandwidth, 20 amplification passes.
- **Output:** Up to ~1 J at 2 Hz, bandwidth <3.2 nm FWHM.

7.4.1 Estimations for the crystal and pump parameters

First, The Cube only requires a reduced pump duration of ~400 µs to achieve the same pump energy as The Tube. This is made possible by the new 33 kW pump module. Due to the shorter pump duration, effects of ASE are expected to be significantly lower and therefore an output energy of more than 1 J is reasonable. Another side effect of this is a decreased reabsorption of ASE within the crystal and thus, lower operating temperatures. This in turn allows for a higher repetition rate and a more relaxed thermal management.

Second, another expected boost to the optical-to-optical efficiency comes from the higher pump intensity of the new pump module. At a pump peak power of 33 kW, the pump intensity within an area of $10 \times 10\,\mathrm{mm}^2$ calculates to 33 kW/cm², which is three times higher than in The Tube.

Third, the higher pump intensity enables the option to efficiently pump the crystal in a larger area. This way, the amplifier can be operated at a lower energy fluence of the amplified beam and thus, issues with the laser induced damage threshold (LIDT) are more relaxed. Because of this, a new pump area of $13 \times 13\,\mathrm{mm}^2$ is defined for The Cube. This calculates to a ~70 % larger pump area compared to The Tube and a ~40% decreased energy fluence of the amplified beam.

Fourth and last, two new gain media are of particular interest: An Yb:YAG crystal with 3 mm thickness, 2 % doping and [111] lattice cut as well as an Yb:YAG ceramic with 5 mm thickness, 2 % doping and an ASE absorbing, chromium-doped YAG cladding. Both were originally intended to be used in the final 10 J amplifier, but their parameters are also suited for The Cube. Furthermore, their application within The Cube allows to evaluate their performance for the 10 J amplifier.

7.4.2 Simulation of the optimum crystal and pump parameters

Original simulations to find a suitable parameter set for the 10 J amplifier were conducted in a custom written MATLAB code that is based on the work of C. Wandt [23]. As a result, an Yb:YAG crystal with a thickness of 3 mm, a doping concentration of 2 % and a diameter of 38 mm was chosen and a batch of such crystals was purchased.

In the meantime, the more accurate V4 simulation tool of J. Körner was developed, see section 6.4, and temperature measurements of the 3 mm crystals were conducted, see section 4.2. Since this allows for more accurate simulation results and better insights, a second simulation campaign was conducted with the V4 tool to show the feasibility of the 10 J amplifier crystals for The Cube.

In comparison to the simulations of the SuperBooster, most of the system parameters of The Cube are already fixed either by the amplifier design or by the existing crystals and ceramics. Thus, the only two parameters remaining are the pump duration and the choice between a 3 mm thick crystal or a 5 mm thick ceramic. Since ceramics and crystals behave almost identical, both gain media are considered as Yb:YAG crystals in the simulation.

The parameter for the simulation campaign with the V4 tool are:

- **Pump:** 33 kW, 10 Hz, 4th order supergaussian with square shape of $13 \times 13\,\mathrm{mm}^2$, 933 nm center wavelength at 400 µs pump duration, double-pass (active-mirror)
- **Seed:** Gaussian beam shape with 1/e²-diameter of 10 mm, maximum energy of 137 mJ, 3.5 nm FWHM bandwidth with shallow spectral amplitude hole at 1030 nm, 20 passes
- **Gain medium:** 2 at.% Yb^{3+}, 3 mm or 5 mm thickness, active-mirror, average temperature of ~35 °C at 400 µs pump duration (based on the measurements of section 4.2).
- **Losses:** ~3.5 % per roundtrip/double-pass, considering a measured, average loss of 0.8 % per hit of the dichroic mirror, a specified reflectivity of 99.7 % for the concave mirrors, 99.95 % for FM1 and FM2, an AR-coating of the crystal with 0.25 % remaining reflectivity and an HR coating with 99.9 % reflectivity. Losses are applied after a double-pass through the gain medium.

The temperature dependent emission and absorption cross-sections of Yb:YAG are taken from the measurement data of J. Körner et.al [37]. All simulation results are generated without the impact of ASE, since the V4 tool does not include this process. Furthermore, ASE effects are expected to be negligible in The Cube because of the short pump duration. In contrast, ASE strongly affects The Tube due to the long pump duration of 1.25 ms [23]. Therefore, no comparison graphs of The Tube will be shown.

Pump absorption within the crystal

Figure 7.3 summarizes the results of the simulation campaign with the V4 tool. The remaining pump power as it travels into and out of the 3 and 5 mm thick Yb:YAG crystals is represented by graph a). The pump duration is set to 400 µs, which corresponds to a pump energy that is similar to The Tube. The data shows that for both thicknesses only a fraction of the pump is used. For 3 mm a total of 45 % of the pump is absorbed and for 5 mm 65 %. This indicates that the energy output of the amplifier can be further increased by adding more pump passes, if necessary. Also, the comparably large amount of unused pump power that exits the crystal must be considered for the thermal management since it potentially heats up surrounding components.

Material excitation

The overall absorbed pump energy is almost constant along the penetration depth of the crystal due to the double-pass of the pump and the generally moderate absorption. As a result, the excitation of the material shown in graph b) is almost independent of the penetration depth. Furthermore, it stays well above the equilibrium excitation β_{eq}, above which an energy gain is achieved.

Output energy vs. pump duration

Graph c) illustrates the dependence of the achievable output energy on the pump duration in a range between 200 and 500 µs. The seed energy is set to the maximum of 137 mJ. The results clearly indicate the benefit of a thicker crystal due to the higher overall pump absorption. This also underlines the results found by C. Wandt for The Tube, where a 6 mm thick Yb:YAG crystal with a doping concentration of 2 % showed an optimum working point of the amplifier.

In terms of the targeted output energy of 1 J both simulated thicknesses are sufficient. For a thickness of 3 mm a pump duration of at least 340 µs is required to reach 1 J which reduces to 300 µs for a thickness of 5 mm.

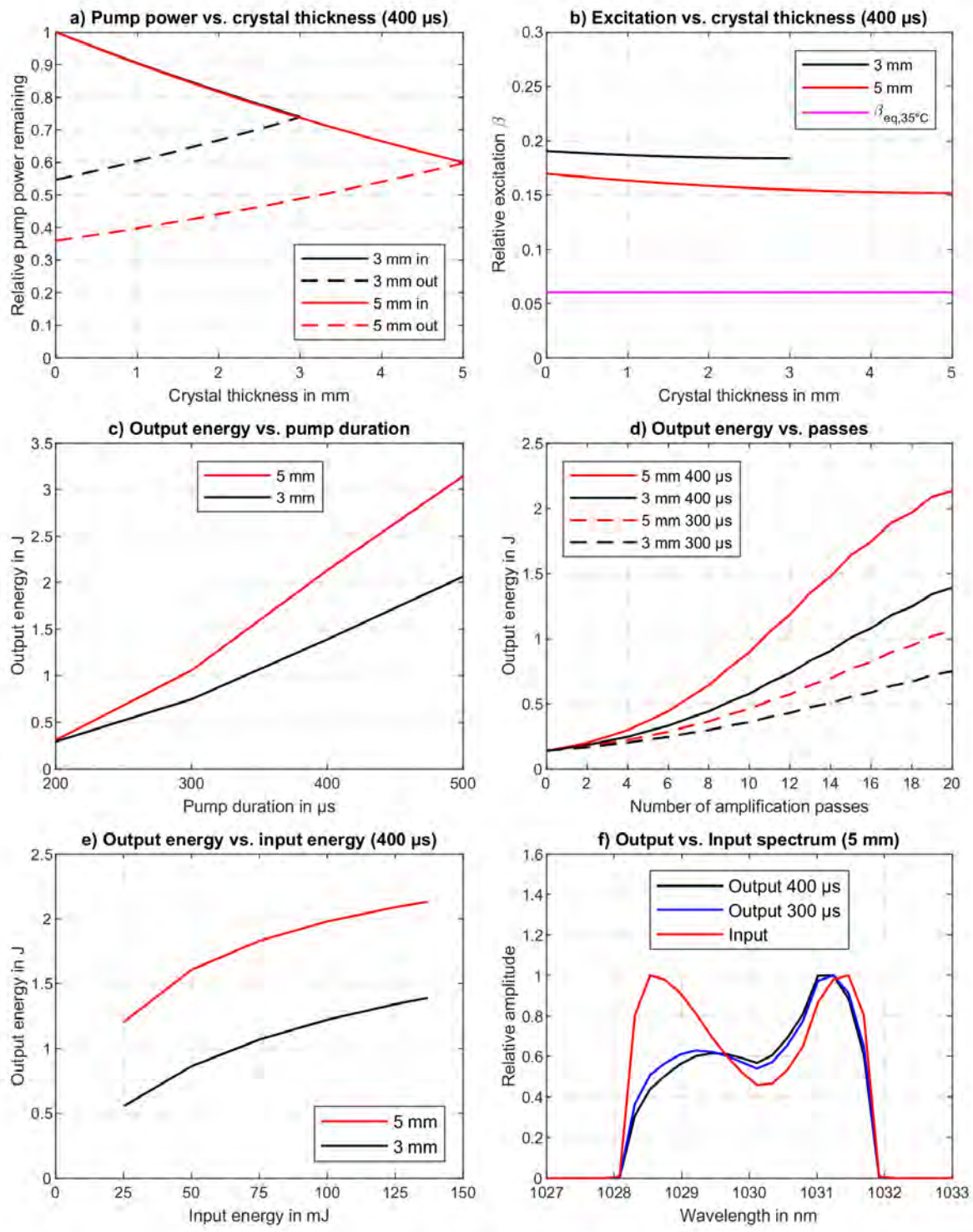

Figure 7.3: *Simulations for* 3 mm *and* 5 mm *thick,* 2 % *doped Yb:YAG crystals implemented in The Cube. The system parameters are:* 33 kW *pump peak power at* 933 nm *and* 10 Hz*, in a flat-top square with* 13 mm *FWHM; double-pass pump; gaussian shaped seed beam with* 10 mm *1/e²-diameter; maximum seed energy of* 137 mJ*; 20 amplification passes with* 3.5 % *losses every other pass. The active-mirror crystals have an average temperature of* 35 °C*. a) Remaining pump power as it travels into and out of the crystal at a pump duration of* 400 µs*. b) Corresponding relative excitation and equilibrium excitation, above which a gain is achieved. c) Maximum achievable output energy versus pump duration. d) Energy build-up over each amplification pass for* 300 *and* 400 µs *pump duration. The wiggling lines are caused by the applied losses. e) Impact of the input energy on the achievable output energy. f) Evolution of an exemplary input spectrum for a* 5 mm *thick crystal.*

Saturation effects of the amplification
Although the number of amplification passes is fixed by the design of The Cube, the evolution of the output energy over each pass is investigated in graph d). The line wobbles are caused by the application of the aforementioned optical losses after each double-pass through the crystal. The curves show that a strong saturation of the output energy over the amplification passes does not occur for any of the given combinations of the crystal thickness and the pump duration.

A moderate saturation effect can be seen in graph e) for the dependence of the output energy on the input energy. As a consequence of the decreasing slope of the curves, a moderate improvement of the energy stability of the output beam compared to the input beam is expected. Nonetheless, a sufficiently stable input beam is still required to meet the target specification of the energy stability of 0.6 %.

Evolution of the output spectrum
The output spectrum shows only a moderate gain narrowing due to the lack of a strong saturation. The data in graph f) shows the evolution of an exemplary input spectrum for a 5 mm thick crystal pumped at 300 and 400 µs. The amplitude hole at 1030 nm is filled up and the amplification process is in favor of the longer wavelengths, which arrive first at the crystal. The bandwidth loss due to gain narrowing is only 0.2 to 0.4 nm.

Conclusion
In conclusion, crystals with a thickness of 3 or 5 mm, the new 33 kW pump module and pump durations of 300 to 400 µs are sufficient to achieve the required energy output of more than 1 J. Since the amplifier only shows a moderate saturation, the maximum available input energy must be used to achieve the highest energy stability of the output beam. The simulations also show that gain narrowing is moderate for The Cube. Thus, as spectral input bandwidth of ~3.5 nm FWHM in combination with a comparably shallow spectral amplitude hole around 1030 nm is enough to reach the targeted output bandwidth of ~3 nm FWHM.

All in all, the crystals and ceramics bought for the 10 J amplifier can also be used with The Cube and together with the new pump module the output energies can be pushed beyond 1 J, if necessary.

7.5 Laboratory performance

Over the course of two years, The Cube proved to be a reliable and stable main amplifier of the PFS pump laser, which enabled a series of successful OPCPA and SHHG experiments with PFS. The changes and improvements over The Tube amplifier are shortly summarized as follows:

- A new modular vacuum chamber is implemented with increased space, a better accessibility, and mechanically decoupled breadboards for all optics.
- A new 33 kW pump module is installed with a higher power and better beam quality.
- Either a Ø38 × 3 mm Yb:YAG crystal is used as gain medium or a Ø55 × 5 mm Yb:YAG ceramic with ASE absorbing cladding, both with a doping concentration of 2 %.
- Two new heatsinks are used: the liquid metal interfaced AMKI for the ceramic, and the glue interfaced MKIII for the crystal, see also section 4.3.
- Sophisticated opto-mechanics are implemented, such as high stability, metal-joint mirror mounts, reinforcements of each optical sub-assembly and blocking shades for stray pump light and ASE.
- A new spatial filter increases the available input energy by 50 %.

Altogether, this results in a performance superior to The Tube, with a 10 Hz operation at a maximum output energy of 2 J and the ability to compress the pulses to ~800 fs. Furthermore,

the beam quality is significantly improved and the mechanical stability allows for a reliable day-to-day operation without the need for daily realignments.

The following sub-sections give a closer look to the performance of The Cube, with measurements that were mostly taken during the daily check-up routines before starting experiments at PFS.

7.5.1 Energy output and stability

First experiments with The Cube were conducted with an Yb:YAG crystal from the same batch as the one in The Tube. The crystal had a 2 % doping concentration, a size of $40 \times 40 \times 6\,\text{mm}^3$ and a random lattice cut. Later, the aforementioned 3 mm thick, 2 % doped crystals with [111] cut as well as the 5 mm thick, 2 % doped ceramic with ASE absorbing cladding were used for the majority of experiments with The Cube. The energy performance with each of these gain media is compared in figure 7.4 for an operation at 10 Hz.

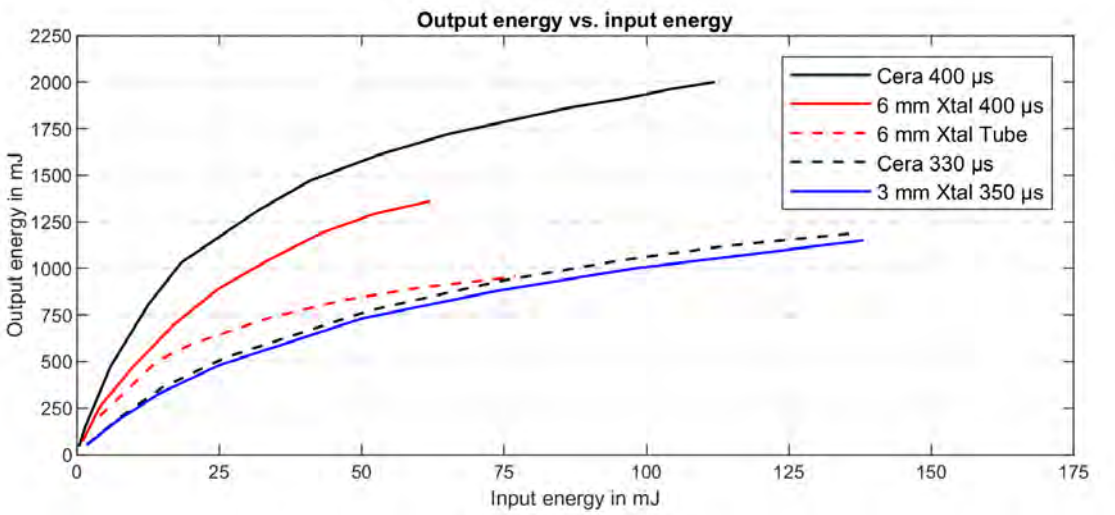

Figure 7.4: *Energy performance of The Cube for* 3 *and* 6 mm *thick,* 2 *% doped Yb:YAG crystals (Xtal) as well as a* 5 mm *thick,* 2 *% doped Yb:YAG ceramic with ASE absorbing cladding (Cera). The* 6 mm *crystal is from the same batch as the one in The Tube amplifier and exhibits similar properties. The graph "*6 mm *Xtal Tube" shows the day-to-day performance of this crystal inside The Tube at* 2 Hz *and* 10.5 kW *pump power within an area of* $10 \times 10\,\text{mm}^2$ *and at a pump duration of* 1250 µs*. All other measurements were carried out with The Cube at* 10 Hz *and* 33 kW *pump power within an area of* $13 \times 13\,\text{mm}^2$ *and at different pump durations:* 400 µs *corresponds to a similar pump energy as The Tube,* 350 µs *as well as* 330 µs *correspond to an energy output of* ~1.2 J *which is sufficient for daily operations of the OPCPA stages of PFS. All measurements were taken within a time frame of one year. The available input energy of each measurement varied due to continuous improvements of the beam transport system.*

Performance of a 5 mm ceramic and a 3 mm *crystal*

The highest output energy was achieved with the ceramic. On record, an energy of 2 J was measured after the reflection on the TFP and with a pump duration of 400 µs (see curve "Cera 400 µs"). The depolarization losses of 7.5 % caused an additional energy of ~150 mJ that was transmitted through the TFP and subsequently filtered out with the optical isolator. This translates into an optical-to-optical efficiency of ~14 %. The bandwidth of the output spectrum was 3.2 nm FWHM.

The output energy was limited by the LIDT of the HR coating on the back side of the ceramic. After ~1000 shots with an energy of 2 J a laser induced damage occurred. The corresponding maximum energy fluence was $2\,\mathrm{J/cm^2}$. This comparably low damage threshold is mainly attributed to the brittle HR coating, which suffered from severe internal stress, as mentioned in section 4.4. Operating at 1.7 J for several 10000 shots on the same spot did not show any sign of damages.

The output energy was typically set to 1.2 J for a daily operation of the OPCPA stages by reducing the pump duration to 330 µs (see curve "Cera 330 µs"). To achieve the same energy performance with a 3 mm thick crystal required a slightly longer pump duration of 350 µs to account for the shorter thickness (see curve "3 mm Xtal 350 µs"). An advantage of the thinner crystal and the optimized [111] cut is an almost negligible depolarization loss of 1.8 %.

Comparison with simulations

The laboratory results closely match the simulated performance of the previous section, with a maximum deviation of ~200 mJ. Also, there is no fundamental change of the performance when a crystal is used instead of a ceramic with ASE absorbing cladding. As a conclusion, the impact of ASE is negligible for such short pump durations and a cladded ceramic poses no advantage over conventional crystals for The Cube.

Comparison with The Tube

With a crystal of The Tube, an output energy of 1.35 J was achieved with The Cube at an input energy of 62 mJ and a pump duration of 400 µs, which corresponds to the same pump energy as in The Tube (see curve "6 mm Xtal 400 µs"). Due to the random lattice cut of the crystal, an additional 12.6 % of the energy was lost by depolarization. In comparison, the Tube only reached an output energy of ~0.9 J with the same type of crystal at a slightly increased input energy of ~80 mJ and for the same pump energy (see curve "6 mm Xtal Tube").

This shows the advantage of the higher pump intensity of The Cube and also the three times shorter pump duration. Both contribute to an increased optical-to-optical efficiency of more than 9 % in contrast to the typical ~6 % of The Tube. Also, the values with The Cube were achieved at a repetition rate of 10 Hz whereas The Tube was limited to 2 Hz.

Energy stability

The Cube also provided a remarkable energy stability during all measurements. To benchmark it, a measurement was conducted over seven consecutive hours at an output energy of 1.4 J. This energy was defined as the upper limit for a daily operation to not risk laser induced damages. To achieve 1.4 J, the ceramic was used with a pump duration of 350 µs. The results of this long-term measurement are shown in figure 7.5.

The standard deviation over roughly seven hours or 240000 shots is ±0.6 % at an average energy of 1.41 J. Only a negligible beam drift was observed during the measurement and no damages occurred. Besides typical shot-to-shot fluctuations, the main contribution to the measured stability are energy jumps that are connected to the cooling behavior of the implemented water chillers. This type of chillers periodically switches on and off the refrigerator unit to cool down the water, which in turn affects the temperature of the ceramic. The resulting temperature fluctuations are in the range of 0.1 to 0.2 °C. Because of this, periodical and abrupt jumps of the output energy of The Cube occur. The maximum amplitude of these jumps in the presented graph is ±30 mJ, which corresponds to a maximum fluctuation of 2 % around the average energy.

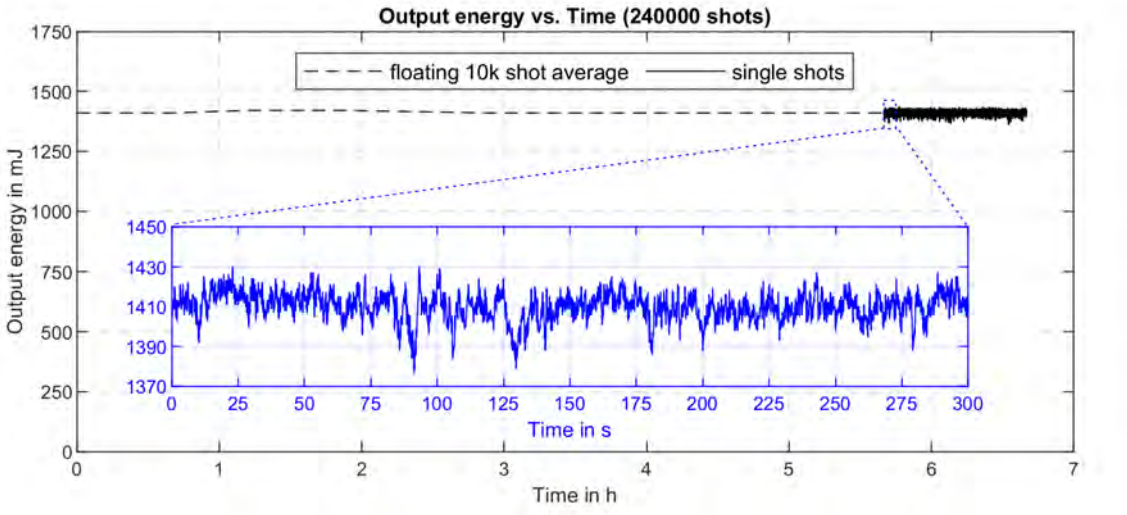

Figure 7.5: *Long-term energy stability measurement of The Cube with a* 2 % *doped,* 5 mm *thick Yb:YAG ceramic. The pump duration is set to* 350 µs *which results in an output energy of* 1.4 J*. The first* ~5.7 *hours represent the continuously measured average over 10000 shots since the energy meter could not store enough samples. The energy of each single shot is only shown for the last 36000 shots, see also the blue inset. The standard deviation of the energy over almost seven hours or 240000 shots is* ±0.6 %*.*

Evolution of spectrum

The evolution of the spectrum in figure 7.6 shows a moderate extent of gain narrowing within The Cube, due to the comparably low overall gain of roughly 10 to 15. In contrast, most of the gain narrowing takes place already in the Booster pre-amplifier. There, the ~180 µJ pulses of the regenerative amplifier are boosted to 137 mJ which corresponds to a gain of ~850.

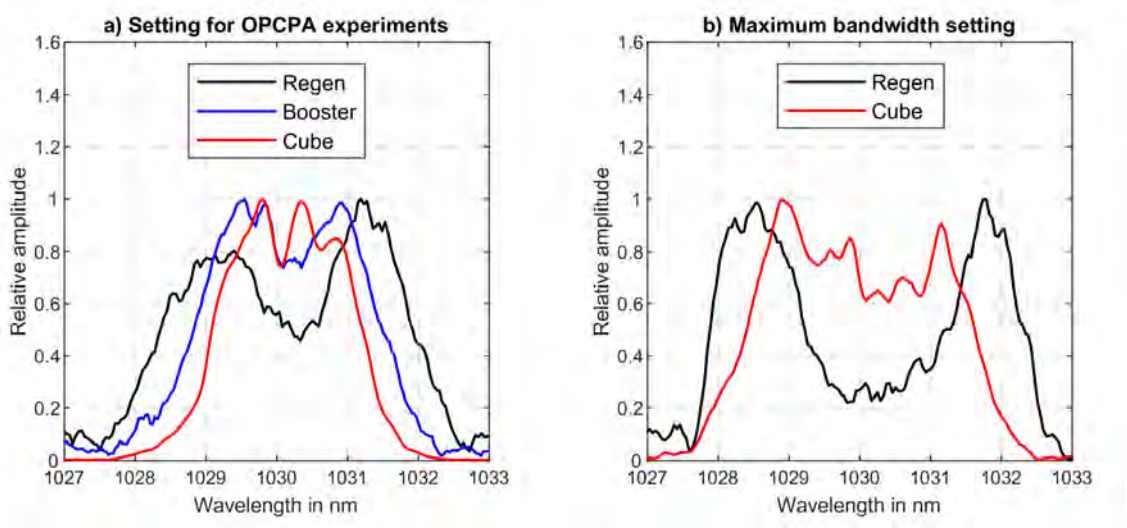

Figure 7.6: *Measured evolution of the beam spectrum throughout the PFS pump laser for two settings: a) narrow bandwidth operation for OPCPA experiments and b) maximum bandwidth operation. The graphs show the initial spectrum at the output of the regenerative pre-amplifier at* ~180 µJ*, the corresponding spectrum after the Booster amplifier at* 137 mJ *and the final spectrum after amplification within The Cube to* 1.2 J*. Note: for the broadband setting, no separate measurement of the Booster amplifier was conducted.*

For graph a) The Cube output was optimized for a daily operation of OPCPA and SHHG experiments. This typically required an output energy of 1.2 J and a narrow output spectrum. At this

setting, the spectrum narrowed down from an initial FWHM of 3.6 nm after the regenerative amplifier, to 2.6 nm after the Booster pre-amplifier and finally to 2.1 nm after The Cube. The spectral amplitude hole around 1030 nm was mostly filled up by the Booster already. Although this also shortened the pulse duration, a safe operation of the amplifier was still achieved due to the reduced output energy.

In graph b) The Cube output was optimized for a maximum bandwidth at 1.2 J. The corresponding spectrum of the Booster was not measured for this setting since only the spectrum of the regenerative amplifier was typically used as reference for daily operations. In this measurement, the spectrum of the beam narrowed down from the initial 4.4 nm FWHM after the regenerative amplifier to the final 3.2 nm after The Cube.

7.5.2 Beam profiles

By far the most impressive achievement of The Cube is the outstanding quality of the output beam. Modulations of the intensity as well as the wavefront are minimized by the flawless bulk material of the crystals or ceramic and the new MKIII and AMKI heatsinks. Together with the smooth, flat-top shaped beam profile of the new pump module an almost flawless profile of the amplified beam is achieved in the image plane of the amplifier.

Figure 7.7 shows an exemplary beam profile that was recorded during the energy stability measurement of figure 7.5 at an energy of 1.4 J. The beam size is 11.7 mm FWHM in the horizontal direction and 10.7 mm FWHM in the vertical direction. Within this FWHM area, 77 % of the total energy is contained. The average amplitude is 72 % of the maximum, at a standard deviation of ± 12 %. This deviation also includes the supergaussian curvature of the intensity profile. Without this curvature, only a slight intensity noise is left, which is mostly caused by the bulk of the Yb:YAG ceramic. No noticeable modulations or features occur. Only the top left corner shows some diffraction rings, which were caused by a wavelength filter (Thorlabs FEL1000) in front of the recording camera.

Since the OPCPA process favors a flat-top shaped pump beam profile, the output of The Cube is well-suited for this purpose. The lack of features and the smooth shape also improve the efficiency and quality of the subsequent second harmonic generation process, which will be shown in a later figure.

Besides the beam profile in the output image plane, also the input beam profile, the output focus as well as the beam profile on the last concave mirror CM1 were recorded. The three profiles are summarized in figure 7.8.

Focus profile

Although the rotational symmetric imaging system minimizes astigmatism, a strongly astigmatic focus was recorded after a lens with a focal length of 100 mm. This contradicting behavior was mostly caused by the crystal or ceramic and typically varied between each heatsink assembly. One contribution is the back side polish which is typically not perfectly flat. The overall flatness of all purchased crystals and ceramics is measured to be within the specification of better than $\lambda/10$. However, after 10 re-imaged roundtrips the remaining flatness error sums up and becomes visible in the output wavefront. Another contribution to the astigmatic behavior is the contacting of the gain medium with the heatsink. This occasionally causes a slight spherical or cylindrical bending which becomes visible in the focus due to the 10 re-imaged roundtrips.

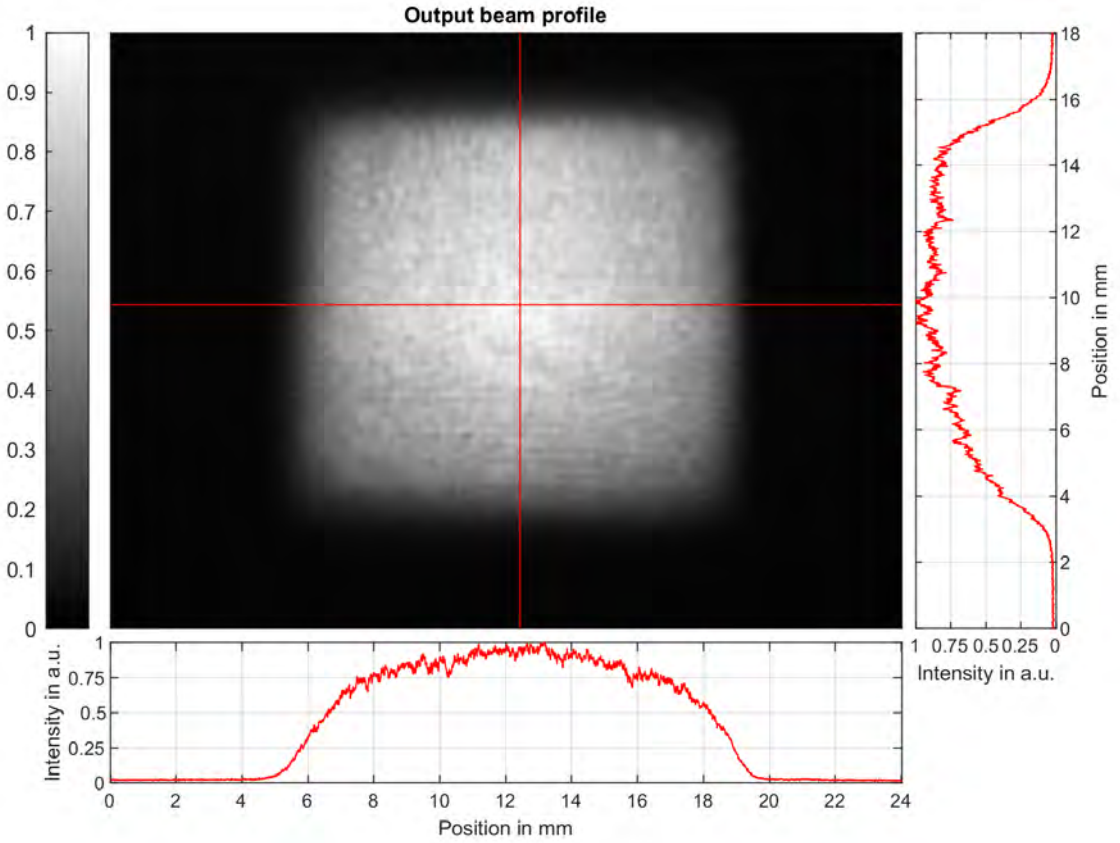

Figure 7.7: *Beam profile in the output image plane of The Cube, at an energy of* 1.4 J *and with the* 5 mm *thick Yb:YAG ceramic.* 77 % *of the total energy is contained within the boundaries of the horizontal FWHM of* 11.7 mm *and the vertical FWHM of* 10.7 mm. *Inside this area, the average intensity is* 72 %, *with a relative standard deviation of* ±12 %. *Note: the feature of the beam profile on the top left corner originates from a filter in front of the recording camera.*

As a consequence, special care must be taken in case the shape of the focus spot is of interest. Since for The Cube only the beam profile in the image plane is of interest, the quality of the focus is considered acceptable. The astigmatism is compensated afterwards with a tilted lens of the telescope between The Cube and the compressor.

Wavefront of the output beam

A separate measurement of the output beam wavefront was not conducted. Instead, the quality is benchmarked with the general shape of the focus as well as with the beam profile on the last concave mirror CM1. This beam profile corresponds to a free space propagation of 1 m relative to the image plane. Therefore, strong aberrations of the wavefront become visible in the form of intensity modulations. This detection method is sufficient since the main interest in the wavefront is the occurrence of strong modulations that could potentially damage optics of the amplifier or the subsequent beam-delivery system.

The presented CM1 image in figure 7.8 proves the high quality of the bulk material of the ceramic and the entire amplifier, with a relative standard deviation of ±9 % of the intensity. This wavefront quality is sufficient to let an expanded beam of 40 mm size propagate over 24 m through the subsequent compressor with only minor quality losses of the beam profile.

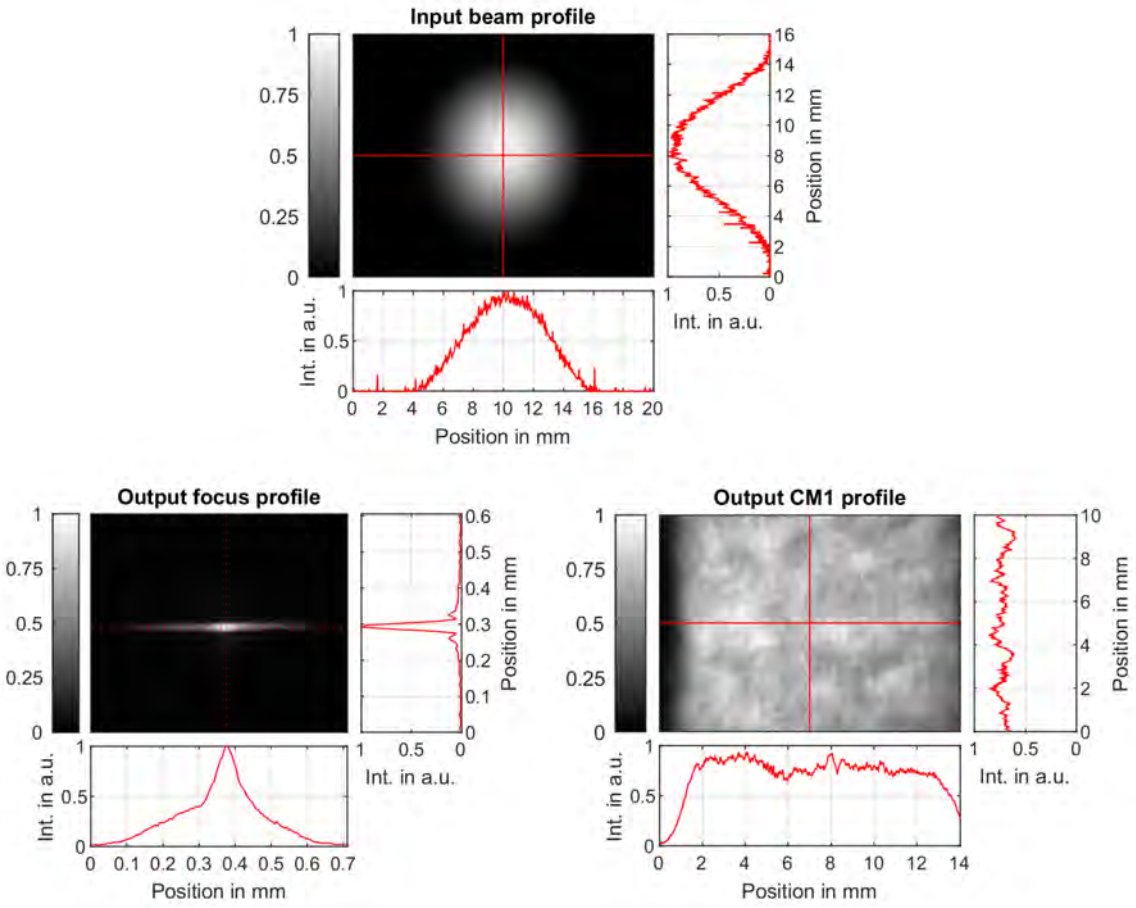

Figure 7.8: *Input beam profile, output focus profile and the beam profile on the CM1 mirror of The Cube, recorded with the internal diagnostics during the measurement of figure 7.7. The 1/e²-diameter of the input is* 9.8 mm *in horizontal direction and* 10.7 mm *in vertical direction. The output focus suffers from strong astigmatism, with a 1/e²-diameter of* 420 µm *in horizontal direction and* 40 µm *in vertical direction, measured with a focal length of* 100 mm. *The picture of the beam on the last CM1 mirror is cut by the limited demagnification of the camera objective. The recorded profile corresponds to the central part of the output beam. The intensity within this profile is on average* 70 % *of the maximum, at a standard deviation of* ±9 %.

7.5.3 Beam pointing fluctuation

One of the weak points of The Cube is the beam pointing fluctuation of the output beam which is presented in figure 7.9. Without further modifications, a standard deviation of ±76 µrad occurs in the horizontal direction and ±114 µrad in the vertical direction. This calculates to ~25 % of the focus size. In comparison, the input fluctuates with less than 30 µrad or ~5 %.

The origin of this issue is mainly the cooling method of the dichroic mirror. This mirror is hit twice per roundtrip, which sums up to 20 reflections. Therefore, any angular deviation is amplified by a factor of 20 and therefore causes a noticeable change of the beam pointing. The main source for such a deviation is a mechanical vibration caused by the cooling water due to turbulences and in particular pressure fluctuations. These fluctuations originate from the water chillers and are synchronized with the periodical energy jumps that are observed in figure 7.5.

In order to damp the pressure fluctuations, water filled 10 L beer kegs with already built-in tube connectors (OPTIKEG by BLEFA GmbH) were installed at the outlet of all chillers. This

measure reduces the pointing fluctuation of The Cube by up to 40 %. As a side-effect, the added water capacity of 10 L acts as a low pass filter for the outlet temperature of the chiller and therefore improves the temperature stability of the cooling water.

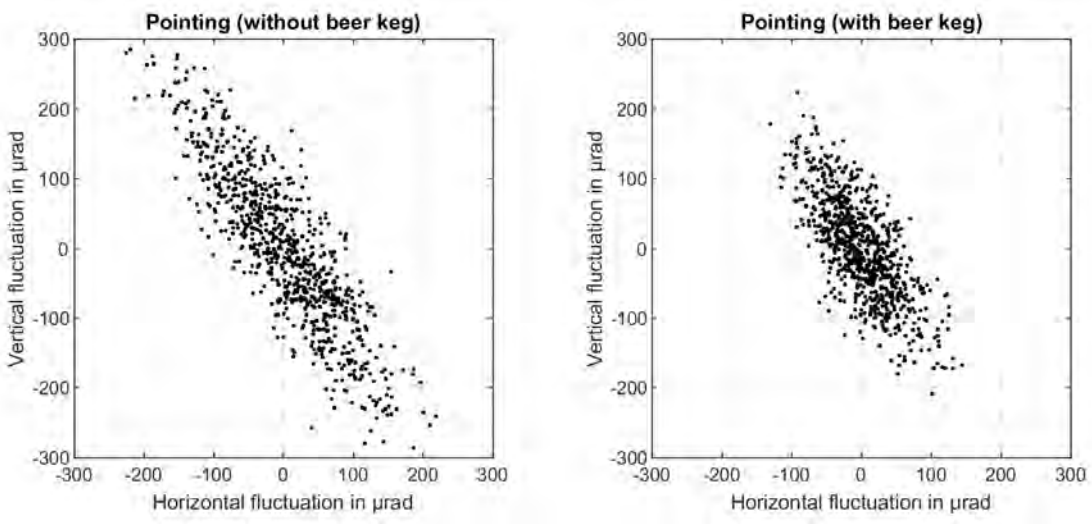

Figure 7.9: *Beam pointing fluctuation of the output beam of The Cube, recorded after a lens with* 300 mm *focal length. a) Raw output without modifications to the amplifier. The standard deviation in horizontal direction is* ±76 µrad *and in vertical direction* ±114 µrad*, which corresponds to* ~25 *% of the focus size in vertical direction. b)* 40 *% reduced fluctuations after the implementation of a vibration damping, water filled* 10 L *beer keg to the cooling circuits of the crystal and dichroic mirror chillers.*

7.5.4 Compression

The compression performance of The Cube is similar to The Tube. For OPCPA experiments, pulses with an energy of 1.2 J and a bandwidth of 2.1 nm were compressed to 820 fs on a daily basis. After compression, 0.86 J remained which translates into an efficiency of 73 % and a peak power of ~1 TW.

An exemplary FROG measurement (frequency-resolved optical gating) and FROG retrieval was conducted for figure 7.10 with the original second-order single shot FROG of The Tube [104]. As retrieval software, the tool developed by V. E. Leshchenko was used [105], which delivers more accurate results for non-gaussian shaped spectra. The retrieval achieved a good G error of 0.0027 (0.3 %) with a close match of the measured fundamental spectrum and the retrieved spectrum. The retrieved phase suffers from a third order dispersion (TOD) which prevents a compression to the Fourier transform limit of 766 fs. If required, the TOD can be further optimized with the angle of the compressor grating. However, OPCPA experiments showed that a pulse duration of 820 fs is sufficient and an improvement is not necessary.

Additional contrast measurements were conducted by A. Kessel and V. E. Leshchenko which revealed an energy content of 92 % within the main peak of the compressed pulse. The remaining energy is contained within a 4.6 % post-pulse caused by the regenerative amplifier and an ASE pedestal of 3.4 %. Without the fast Pockels cell after the cascaded fiber amplifier of the pump laser (see the system overview in section 2.2), up to 18 % of energy is contained within this pedestal. A more detailed description of the measurements can be found in [22].

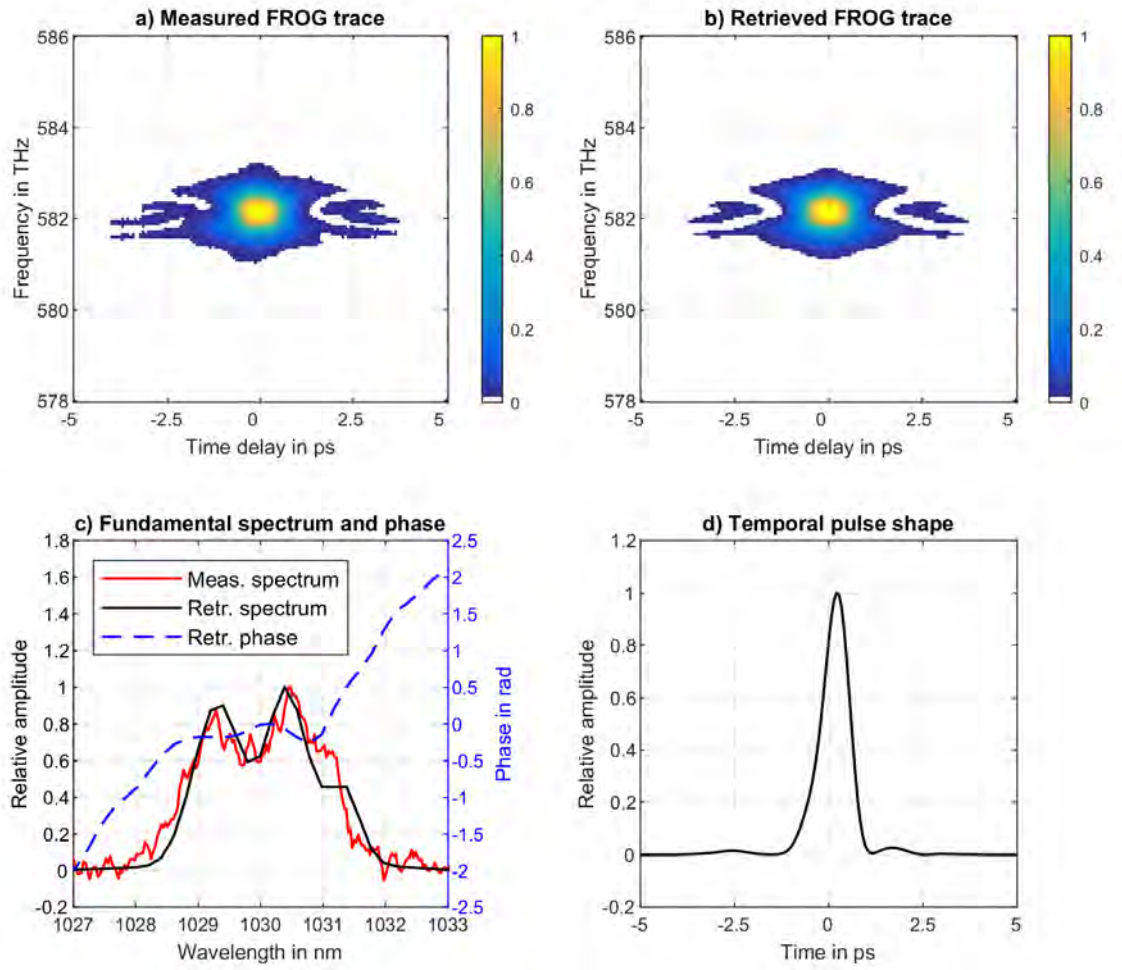

Figure 7.10: *Measured and retrieved FROG trace of the PFS pump laser. For the measurement, The Cube was set to an output energy of* 1.2 J *and a narrow bandwidth of* 2.1 nm *that is optimized for daily OPCPA and SHHG experiments. A* 3 mm *thick,* 2 % *doped Yb:YAG crystal was used as gain medium. After compression,* 73 % *of the energy was left. a) FROG trace measured with a second-order single-shot FROG. b) FROG trace retrieved with the software developed by V.E. Leshchenko [105]. c) Measured (red) and retrieved (black) fundamental spectrum as well as the retrieved phase (blue) of the compressed pulse. d) Temporal shape of the retrieved pulse. The algorithm retrieved a compressed pulse duration of* 820 fs *FWHM with a Fourier transform limit of* 766 fs. *The corresponding G error is 0.0027 (*0.3 %*).*

7.5.5 Second harmonic generation (SHG)

SHG experiments by A. Kessel and V. E. Leshchenko showed a generally high quality of the compressed pulses. For this purpose, the compressed pulses with up to 0.86 J were sent to a 4 mm thick Type II DKDP crystal. As a result, up to 475 mJ of energy with a shot-to-shot stability of 1.5 % was converted to the second harmonic at 515 nm, which translates into an SHG efficiency of 55 %. The dependence between the fundamental energy and the second harmonic energy is illustrated in figure 7.11. The efficiency of 55 % also matches well with theoretical predictions made by A. Kessel. More details of the measurement and the theory are given in [22].

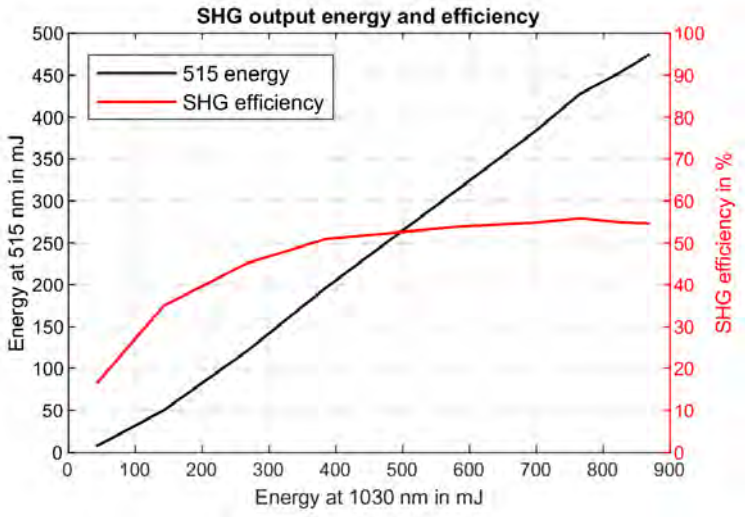

Figure 7.11: *Measurement of the SHG efficiency with the compressed pulses of the PFS pump laser and a* 4 mm *thick, Type II DKDP crystal. Data by the courtesy of A. Kessel.*

The high quality of the output beam of The Cube is maintained after compression and also SHG. Only minor diffraction effects on the edges of the beam emerge and several line features are imprinted by the compressor grating, see figure 7.12. The beam profile is still rather smooth and thus, also the frequency-doubled beam exhibits a good quality with a standard deviation of the intensity of ~20 %.

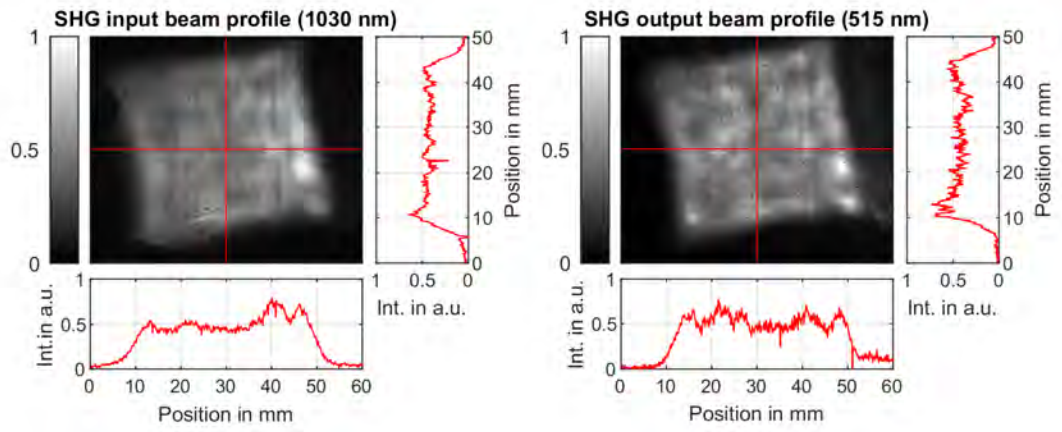

Figure 7.12: *Beam profiles of the compressed pulses: a) of the fundamental beam at* 1030 nm *and b) of the second harmonic beam at* 515 nm. *Both are measured at the position of the SHG crystal with an energy of* 0.86 J *of the fundamental beam and* 0.48 J *of the second harmonic. Data by the courtesy of A. Kessel.*

Altogether this significantly pushed the available pump energy of the OPCPA stages and increased their overall efficiency, which paved the way for the high energy SHHG experiments presented in [19].

7.6 Issues with The Cube

Despite all of the aforementioned improvements, also a few issues emerged with The Cube over an operation time of two years.

7.6.1 Vacuum lensing

One of the most prominent effects that occurred is the so-called ”vacuum lensing”. The name originates from a growing focusing behavior of the output beam when The Cube is being evacuated, which can be treated as an additional lens. Several measurements were conducted to investigate this effect further. Figure 7.13 shows one of these measurements.

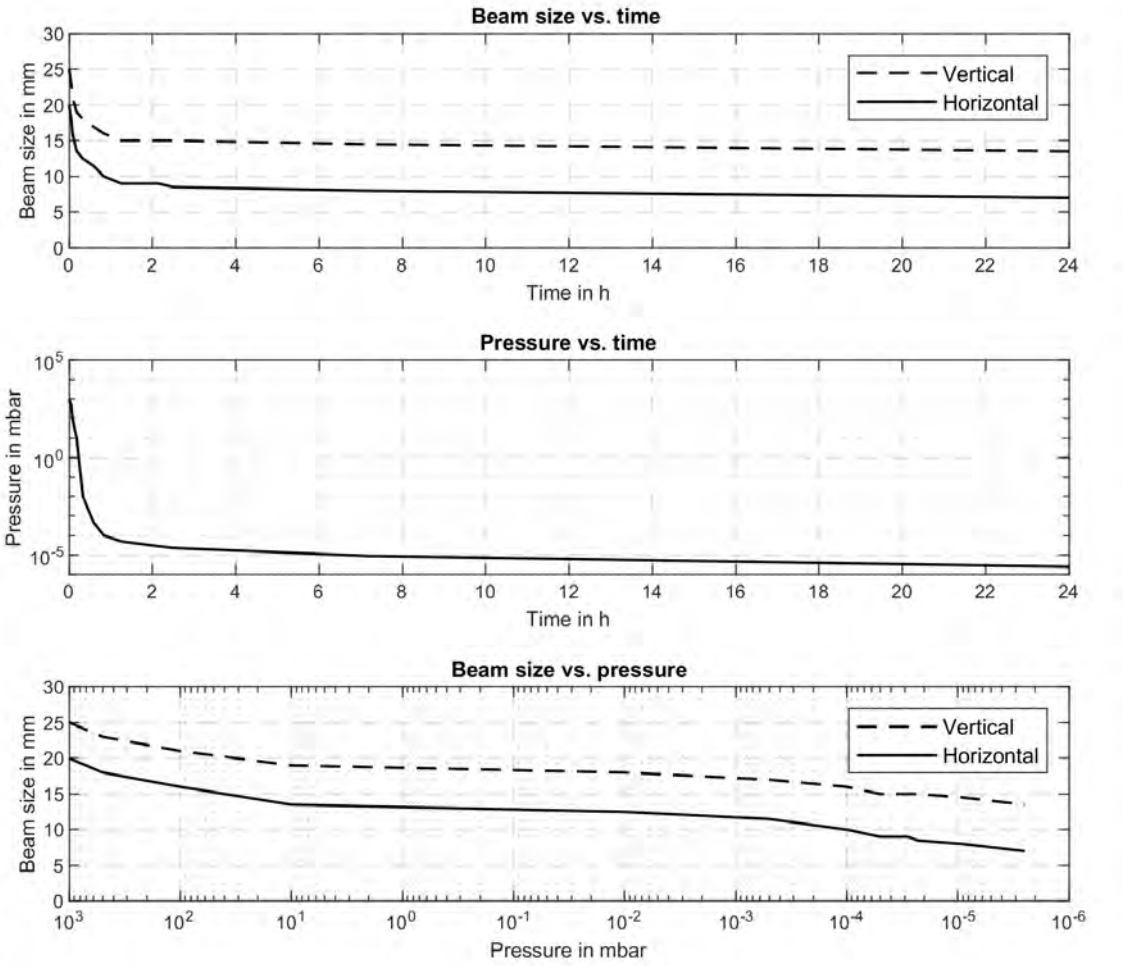

Figure 7.13: *Vacuum lens effect of The Cube. During evacuation of the vacuum chamber, the output beam becomes more focusing. This effect continues over time and reaches an equilibrium after roughly 24 to 48 hours. The beam size was measured in a distance of* 8 m *after the output image plane.*

The beam size was recorded in a distance of 8 m after the output image plane of The Cube over the course of 24 hours after evacuating the chamber. Within 24 hours, the beam size decreased from 25 mm in the vertical direction to only 14 mm, whereas in the horizontal direction it decreased from 20 mm to 7 mm. The strongest change is observed within the first hour, where also the pressure drops the most. Although the measurement indicates a correlation between the strength of the vacuum lens and the pressure, this is a fallacy. The same behavior over time also occurred when the pressure was kept constant at 1×10^{-2} mbar by switching off the turbomolecular pump.

Although not finally proven, the most promising explanation is an outgassing of the 20 concave mirrors inside of The Cube. Their E-beam coating is prone to absorb water from the ambient air. During evacuation, this water evaporates and changes the mechanical stress inside the coating. As a consequence, the mirrors bend more and thus, an additional focusing behavior is observed. ABCD-matrix simulations show that a change of 0.4 % of the radius of curvature of each mirror is enough to result in the recorded change of the beam size.

The focusing behavior can be easily pre-compensated by a proper distance between the two mirror wheels where the concave mirrors are mounted on, similar to how the thermal lens of the crystal is compensated. However, the vacuum lensing effect slows down the maintenance time of The Cube since a stable beam size is achieved only after one to two days.

The vacuum lensing effect was also present in The Tube amplifier but the impact was covered by other, more severe effects after evacuating the amplifier. Therefore, a comparable investigation was never conducted.

7.6.2 Extraordinarily high quality requirements of optics

Another prominent issue with the 20-pass imaging geometry in general is the extraordinarily high quality requirement of the optics that are placed close to or within the image plane. Since the beam passes the exact same spot on these optics ten times, any existing aberration will be accumulated and the resulting effect on the beam profile or the wavefront is ten times as strong. In case of the bulk material of the crystal, this translate into a 20 times stronger effect since the material is passed twice per roundtrip.

From experiences with The Cube, the absolute minimum specification of the flatness of an optics in the image plane is $\lambda/10$. It is advisable though to purchase optics with a flatness far better than $\lambda/20$ to avoid any visible effect on the beam quality. While this can be achieved for the FM2 mirror in the second image plane with rather standard optics, this is a substantial issue for purchasing proper Yb:YAG crystals or ceramics. At the required size of Ø38 mm, manufacturers typically do not guarantee a transmitted wavefront better than $\lambda/8$ for the bulk material. Above this value, only a best effort is guaranteed.

Furthermore, the supplied interferograms of the measured wavefront typically do not exhibit a resolution that is sufficient for the sensitivity of The Cube. Thus, crystals or ceramics that appear to be good at first glance can cause noticeable intensity and wavefront modulations once they are implemented in the amplifier. As a consequence, the most applicable way to ensure a high performance of The Cube is to order several crystals or ceramics at once, ideally from different growth boules, and to select them by measuring their quality within the amplifier.

7.7 Conclusion

The Cube proved to be a highly reliable and stable amplifier that outperforms its predecessor The Tube in every aspect. The implementation of The Cube as the main amplifier of the PFS pump laser eventually paved the way for plenty of OPCPA and SHHG experiments with PFS. The key numbers of The Tube and The Cube are summarized in the following table 7.1.

Table 7.1: *Comparison of the key numbers of The Tube and The Cube.*

	The Tube	**The Cube**
Amplifier geometry	20-pass relay-imaging	20-pass relay-imaging
Footprint	$2500 \times 500\,\mathrm{mm}^2$	$2500 \times 700\,\mathrm{mm}^2$
Gain medium	$40 \times 40 \times 6\,\mathrm{mm}^3$, 2 at.% Yb:YAG	Ø38×3 mm, 2 at.% Yb:YAG crystal Ø55×5 mm, 2 at.% Yb:YAG ceramic
Gain medium cooling	Active-mirror, glue interface	Active-mirror, glue/liquid metal interface
Pump	10.5 kW at 2 Hz, 1.25 ms, 938 nm, $10 \times 10\,\mathrm{mm}^2$, double-pass	33 kW at 10 Hz, 0.4 ms, 933 nm, $13 \times 13\,\mathrm{mm}^2$, double-pass
Input energy	Max. 90 mJ	Max. 137 mJ
Amplification passes	20	20
Output energy	~1 J	Max. 2 J, safe operation till 1.4 J
Energy stability	0.6 % Std.	0.6 % Std.
Spectral output bandwidth	<3.2 nm	<3.2 nm
Compression	740 fs	820 fs
Beam pointing fluctuation	<70 µrad Std.	45 to 70 µrad Std.

The maximum output energy of The Cube is 2 J with a safe day-to-day operation for energies of up to 1.4 J. The repetition rate is 10 Hz and the output bandwidth allows for a compression of the stretched pulses to 820 fs. This performance was achieved by adapting the fundamental optical design of The Tube amplifier and implementing numerous improvements, such as:

- A new, modular vacuum chamber with relaxed space constraints and mechanically decoupled optical assemblies
- A new 33 kW pump module with a high quality pump beam (PM48 by Lastronics GmbH)
- The implementation of either a 3 mm thick, 2 % doped Yb:YAG crystal together with the thermal expansion matched MKIII heatsink or a 5 mm thick, 2 % doped Yb:YAG ceramic with ASE absorbing cladding together with the liquid metal interfaced AMKI heatsink
- Sophisticated, high stability optical mounts and an extensive thermal management, including water filled beer kegs to increase the stability of the cooling system
- A higher throughput spatial filter between the Booster pre-amplifier and The Cube.

The Cube was also used as an experimental platform for the technology of the final 10 J amplifier. This opened up the opportunity to evaluate the performance of several opto-mechanical designs, new gain media as well as several iterations of heatsinks which drastically reduced the development time of the 10 J amplifier.

Chapter 8

The BigMama

The ”BigMama” is the 10 J main amplifier of the PFS pump laser. It is based on Yb:YAG as the gain medium and allows for output energies of up to ~10 J at a repetition rate of 2.5 Hz, with an optical-to-optical efficiency of ~20 % for an operation at room temperature. At the desired repetition rate of 10 Hz an output energy of up to 5 J can be achieved currently. The amplified pulses can be compressed to a pulse duration of 672 fs with a peak power of ~11 TW. To the best knowledge of the author, these are by far the most powerful and energetic sub-picosecond pulses ever created with an Yb:YAG based CPA laser.

The BigMama largely incorporates the technology that was developed for the SuperBooster and for The Cube. This drastically reduced the required development time and allowed for the first high energy experiments shortly after the finishing of The Cube. The final version of the BigMama is built in the Type 2 imaging geometry and allows for the implementation of either one or two Yb:YAG crystals. Furthermore, the amplifier utilizes the latest MKX heatsink design with vacuum injected liquid metal for a superior cooling and beam quality.

The following sub-chapters give an in-depth overview of the implemented technology, the experimental results that were achieved with one or two crystals in the amplifier setup, the limitations of the BigMama and how to overcome them for the targeted operation at 10 J and 10 Hz.

Overview

8.1 Target specifications:
The system and performance parameters of the BigMama that are required for a stable driver of the PFS OPCPA stages.
8.2 Simulation of setups with one or two crystals:
Simulations of the achievable output energy for setups with one or two Yb:YAG crystals, optimum choice of crystals and ceramics.
8.3 Opto-mechanical design of the BigMama:
Opto-mechanical design and mechanical implementation of the BigMama.
8.4 Low energy experiments:
Evaluation of the new 8-pass pump geometry, measurements of ASE influence.
8.5 High energy experiments with one crystal:
Performance and ASE limitations for an operation with a single Yb:YAG crystal at a repetition rate of 2.5 Hz.
8.6 High energy experiments with two crystals:
Performance, limits, the first compression at full energy and contrast measurements for an operation with two crystals at 2.5 Hz.
8.7 Latest experiments with 10 Hz and amplifier limits:
Latest measurements at a repetition rate of 10 Hz, including limitations by depolarization and strong thermal lensing.
8.8 Conclusion and future measures:
Summary of the achieved record parameters, outlook for future improvements and activities.

8.1 Target specifications

The target specifications of the BigMama are based on the design specifications of the PFS system and are modified by the experiences that were gained with The Tube and The Cube amplifiers:

- **Size:** A maximum footprint of $3000 \times 1500\,\mathrm{mm}^2$ is required because of laboratory constraints.
- **Geometry:** An imaging geometry with at least 20 amplification passes is required.
- **Vacuum chamber:** A vacuum chamber with quick and easy access to all optics is required to minimize development and maintenance time.
- **Mechanical stability:** The optical system must be mechanically decoupled from the vacuum chamber. Furthermore, the beam pointing fluctuation should stay below a standard deviation of 50 to 100 µrad, based on experiments with the PFS OPCPA stages.
- **Energy:** An output energy of >10 J at 10 Hz with a stability of $\pm 0.5\,\%$ is required to reliably pump the OPCPA stages.
- **Energy fluence:** Based on the breakdown of optics in The Tube and The Cube, a limit of $3\,\mathrm{J/cm}^2$ must not be exceeded for an operation under vacuum.
- **Spectrum and bandwidth:** The output spectrum must have a bandwidth of at least 3 nm FWHM to minimize LIDT issues and must be without an amplitude hole at 1030 nm for an optimal compression.
- **Compression:** The spectral bandwidth of the output pulses must support a compression in time to below one picosecond.
- **Beam shape:** A smooth, flat-top shaped output beam profile is preferred for an efficient SHG process and pumping of the OPCPA stages.

8.2 Simulation of setups with one or two crystals

The original design of the PFS pump laser incorporated four 10 J amplifiers in parallel which were seeded by two 1 J amplifiers [13, 14]. Thus, first simulations for the BigMama assumed a seeding with an input energy of ~500 mJ. During the progress of PFS it became clear that much less input energy in the range of only ~100 mJ is required to reach an output energy of 10 J. Furthermore, the PFS design was revised with only a single 10 J amplifier at the CALA facility. This rendered the seeding by The Cube and thus, the whole 1 J amplification stage obsolete. Instead, the 100 mJ-class SuperBooster amplifier is used to directly seed the BigMama.

The following simulation campaign of the achievable output energy of the BigMama only takes this case into account. The campaign shows the feasibility of an amplifier setup that contains either one or two Yb:YAG crystals as the gain medium.

8.2.1 Simulation parameters

The combination of the V4 tool and Autodesk CFD from sections 6.4 and 7.4 was also used to determine the performance of different parameter combinations of the BigMama. Of particular interest are an optimum crystal thickness and pump duration for a working point at an output energy of 10 J. The basis for all simulations is:

- **Crystals:** Yb:YAG; [111] cut or ceramic; preferably 2 % doping due to the common availability of this doping concentration for large diameters and the experiences with The Tube and The Cube.
- **Pump:** Two pump modules (”PM48” Lastronics GmbH) with 27 kW pump; a maximum pump duration of 1500 µs and a center wavelength between 934 nm and 938 nm at 10 Hz, depending on the chosen pump duration; a round, 16th order supergaussian beam profile with 24.5 mm FWHM; 8 pump passes.
- **Input:** Up to 100 mJ energy; 4.2 nm bandwidth with spectral amplitude hole around 1030 nm; a round, second order gaussian beam profile with 24.5 mm 1/e²-diameter.
- **Amplification:** 20 passes per crystal / 10 roundtrips through the system as in The Cube; 2 % optical losses per roundtrip.

The dimension of the input beam and the pump beam profile are chosen such that the operation at an output energy of 10 J stays below the specified energy fluence limit of $3\,\mathrm{J/cm^2}$. The optical losses of 2 % are based on measurements with The Cube and are adapted for a setup without a dichroic mirror in the beam path.

The wavelength shift of the pump modules is implemented in the simulation in accordance with measurements. A constant center wavelength of 934 nm is observed up to a pump duration of 500 µs with a bandwidth of 5 nm. For higher pump durations the wavelength shifts almost linearly to a maximum of 938 nm at 1500 µs.

8.2.2 Simulation of a 20-pass amplifier with one crystal

The first simulation examines the performance of the amplifier with a single Yb:YAG crystal that is pumped with two of the available pump modules or 54 kW. A crystal thickness in the range between 2 mm and 6 mm is chosen together with a 2 % doping concentration. Lower thicknesses are difficult to manufacture in a sufficient optical quality for the required crystal diameters of 38 mm and higher thicknesses suffer from excessive thermal issues.

Without considering the impact of ASE, other doping concentrations behave similar to the presented results, if the product of thickness times doping concentration is equal to the presented combinations. For example, without ASE a 3 mm thick crystal with a 2 % doping concentration has a similar amplification performance as a 6 mm thick crystal with 1 % doping. The only difference is an increased temperature for the thicker crystal.

The results of the single crystal simulation are summarized in figure 8.1.

Average crystal temperature
The first graph a) depicts the average center temperature of each simulated crystal for pump durations between 200 and 1500 µs. The temperature is averaged along the thickness of the bulk material. The simulation assumes an absorption of 100 % of the pump energy and a conversion of the absorbed pump energy to heat of 18.5 %, in accordance with the measurements of section 4.2. At the maximum pump duration of 1500 µs the average temperature lies between ~70° and ~130° for a thickness of 2 mm and 6 mm, respectively.

Remaining pump power
Graph b) shows the relative pump power that remains upon exiting the crystal after eight passes. Different slopes of the curves are mainly caused by the wavelength shift of the pump beam for longer pump durations as well as saturation effects.

The results show that eight pump passes are too little for a thickness of 2 mm, as up to ~25 % of the pump power exits the crystal. Thus, a significant amount of pump energy is not absorbed. This in turn also means that the real temperature of the 2 mm thick crystal is ~5 °C lower than the presented values in graph a). The same holds true for a thickness of 3 mm, but to a much lesser extent with only ~10 % remaining pump power. For thicker crystals, almost 100 % of the pump is absorbed after eight passes.

Material excitation
The corresponding material excitation is represented in graph c) by the relative excitation of Yb^{3+} ions. The given excitation is averaged over each crystal thickness. The actual difference of the excitation between the front and the back of the crystal is only a few percent because of the comparably low absorption per pump pass and saturation effects.

For a single crystal setup, the applied pump power is enough to already invert the material at the minimum possible pump duration of 200 µs. For a better evaluation of this, also the values of the equilibrium excitation are shown. That is ~5 % at 20 °C and ~11 % at 130 °C. Above these values, a gain is achieved. The highest excitation is observed at a thickness of 2 mm and a pump duration of 1500 µs with an average of 53 % across the bulk material. This is reduced to 26 % at 6 mm and 1500 µs. The data also shows the onset of pump saturation as the slopes decrease for all thicknesses towards longer pump durations.

Maximum achievable output energy
Graph d) shows the maximum output energy which can be achieved with 20 amplification passes and an input energy of 100 mJ. The maximum output energy is 22 J at a pump duration of 1500 µs and a crystal thickness between 3 and 4 mm for a doping concentration of 2 %. This corresponds to an optical-to-optical efficiency of ~26 %. Although a 2 mm thick crystal provides a higher material excitation, the achievable output energy is lower with 18 J due to the total pump absorption of only ~75 %. For crystals thicker than 4 mm the lower output energy is caused by increased temperatures and a lower material excitation.

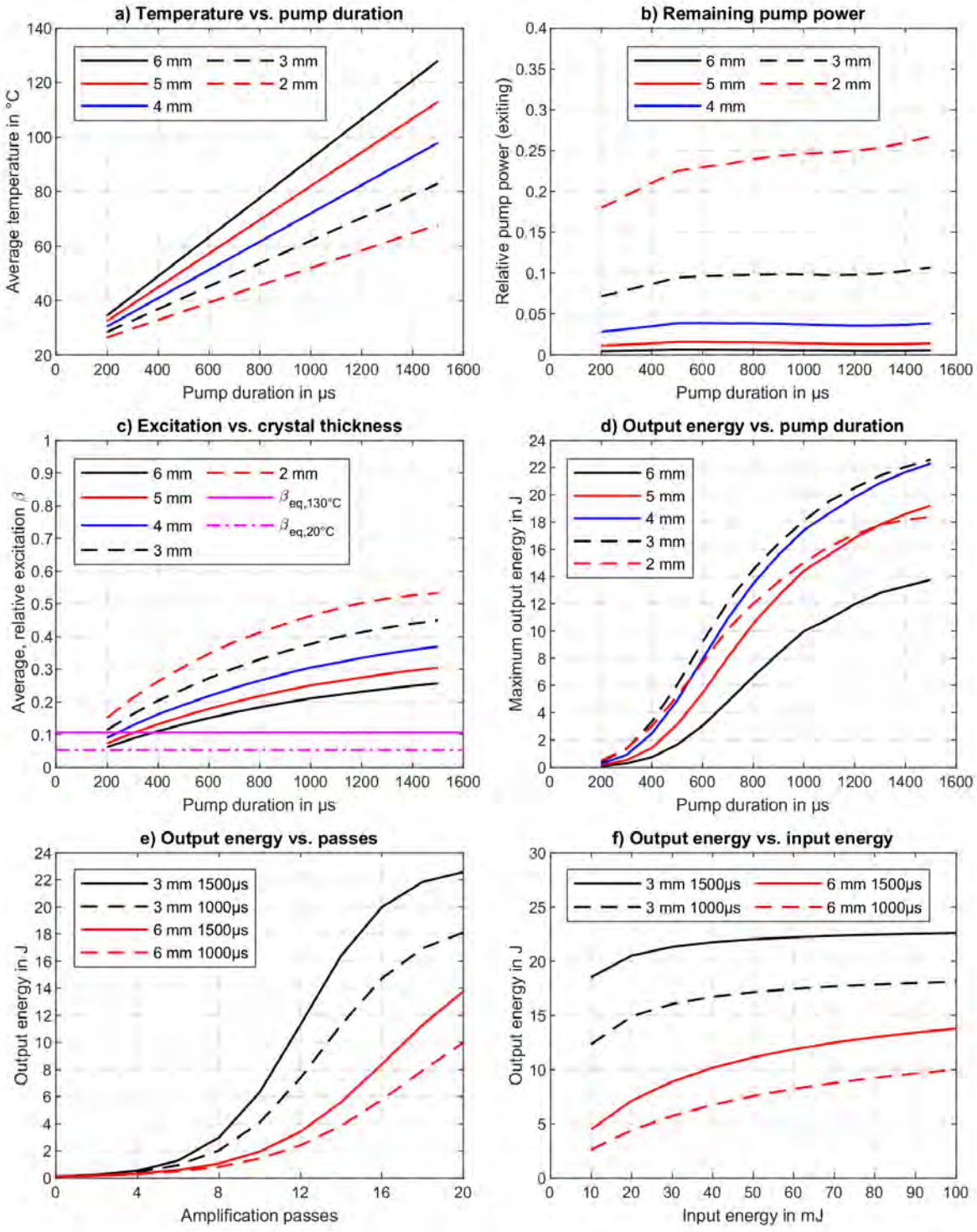

Figure 8.1: *Simulations for a single crystal setup of the BigMama. The system parameters are:* 2 % *doped, active-mirror Yb:YAG crystals; an 8-pass pump with* 54 kW *pump peak power at* 934 *to* 938 nm, *depending on the pump duration,* 10 Hz *repetition rate, a round, 16th order supergaussian beam profile of Ø*24.5 mm *FWHM; a 2nd order supergaussian seed beam with* 24.5 mm *1/e²-diameter, a maximum seed energy of* 100 mJ *and 20 amplification passes with* 2 % *losses every other pass. a) Crystal center temperatures averaged over the thickness, with* 18.5 % *of pump energy converted to heat. b) Remaining pump power after eight passes through the crystal. c) Average, relative excitation in the crystals with values for equilibrium excitation. d) Maximum achievable output energy. e) Energy build-up over amplification passes. Other parameter combinations with equal output energies (see graph d) behave similar. f) Dependency between input and output energy.*

In general, the simulation shows that theoretically all thicknesses are sufficient to achieve the targeted output energy of 10 J. However, the simulation does not consider any effect of ASE and therefore the actual output energy may differ significantly from the presented values. A first estimation on this is done in a later sub-section.

Evolution of the output energy over 20 amplification passes
The evolution of the output energy over 20 amplification passes is examined in graph e) of figure 8.1. Only four parameter combinations were chosen, two for the optimum crystal thickness of 3 mm and two for the least favorable thickness of 6 mm. As long as the output energy is similar to the four combinations, other parameter combinations of graph d) behave similar to the depicted curves of graph e). For example, a thickness of 3 mm at a pump duration of ~650 µs has a similar evolution over the passes as the depicted thickness of 6 mm at 1000 µs. Both allow for an output energy of 10 J.

Overall, the data shows that a strong saturation is achieved for parameter combinations with an output energy above 18 J. More amplification passes would therefore cause no notable increase of the output energy. Contrary to that, saturation effects are only minor for the more interesting region around 10 J. This proves to be beneficial in terms of the temporal contrast of the output beam. Besides the energetic main pulse, the pulse train typically contains an ASE background and pre- or post-pulses which originate from the pre-amplifiers. If the amplifier is operated without saturation, the relative gain of these parasitic pulses is similar to the main pulse. On the contrary, in the saturated regime the amplification of the main pulse is suppressed compared to the weaker pre- and post-pulses or ASE. Thus, the temporal contrast of the main pulse decreases.

Influence of the input energy
The influence of the input energy on the achievable output energy is plotted in graph f). Parameter combinations with an output energy above 18 J show an onset of saturation already for input energies above 10 to 20 mJ.

To emphasize the temporal contrast issues caused by this, a pre-pulse with an energy of only 0.25 % of the maximum input energy of 100 mJ is assumed. This pre-pulse can originate for example from a reflection of the pre-amplifier crystal or a leakage of a regenerative pre-amplifier. As a result of the saturation of the main peak, the pre-pulse is disproportionally amplified and reaches ~11 % of the total output energy. This is a factor of ~40 higher than initially. To mitigate this, a much lower input energy is required which in turn can cause contrast issues related to the ASE background.

Contrary to that, a working point around an output energy of 10 J shows only a weak saturation at the maximum input energy of 100 mJ. Thus, an initial pre-pulse of 0.25 % only contains ~1 % of the total energy after amplification. However, the input beam must have a high energy stability in order to reach a sufficient output energy stability of the amplifier since no significant improvement is expected due to the lack of saturation.

Evolution of spectrum
The previous chapters already mentioned that gain narrowing in Yb:YAG limits the achievable bandwidth of the amplified pulses. To compensate the gain narrowing in the BigMama, a strong pre-shaping of the input spectrum is required. The resulting evolution of the output spectrum is shown in figure 8.2 for a 3 mm thick crystal that is pumped with different pump durations.

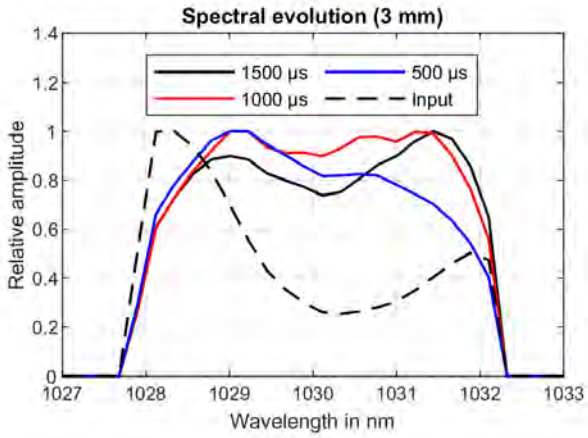

Figure 8.2: *Simulated evolution of the output spectrum for a single* 3 mm *thick,* 2 *% doped Yb:YAG crystal that is pumped with three different pump durations. The input spectrum is pre-shaped to counteract gain narrowing.*

Interestingly, the pre-shaped amplitude hole of the spectrum is already filled up for a pump duration of 500 µs which corresponds to an output energy of 6 J. For longer pump durations the red part of the spectrum is amplified more than the blue part because of saturation effects and the positive chirp of the pulses. This is in accordance with the results of the SuperBooster and The Cube. The overall reduction of the bandwidth is negligible due to the sufficient compensation of gain narrowing with the pre-shaped input spectrum.

Influence of varying parameters

Figure 8.3 shows the simulated sensitivity of the amplifier to parameter tolerances that occur by typical measurement errors. For this purpose, a 3 mm thick crystal is assumed with a pump duration of ~650 µs which enables an output energy of ~10 J.

The biggest influence on the achievable output energy is observed for the pump profile size. A variation of ±5 % causes an output energy difference of ±20 %. The influence of the pump power and the optical losses are slightly lower. The least influence can be seen for temperature variations. As a reference, 5 % of 47 °C is roughly the measurement accuracy of the setup used in section 4.2. Although the actual energy in the laboratory can differ considerably from the simulated values due to these tolerances, this can be easily compensated by longer pump durations.

Conclusion for a single crystal setup

The simulations show that, in the absence of ASE, a single Yb:YAG crystal pumped at 54 kW with a thickness of 2 to 6 mm and a doping concentration of 2 % is sufficient to achieve the targeted output energy of >10 J.

The highest optical-to-optical efficiency is reached with a crystal thickness between 3 to 4 mm. The required pump duration for an output energy of ~10 J with this thickness is ~650 µs. At this working point, the amplification process only shows minor saturation. Thus, a good temporal contrast can be achieved but a high energy stability of the input beam is required. Furthermore, a strong pre-shaping of the input spectrum is required to achieve a flat-top or supergaussian output spectrum with a FWHM of at least 3 nm.

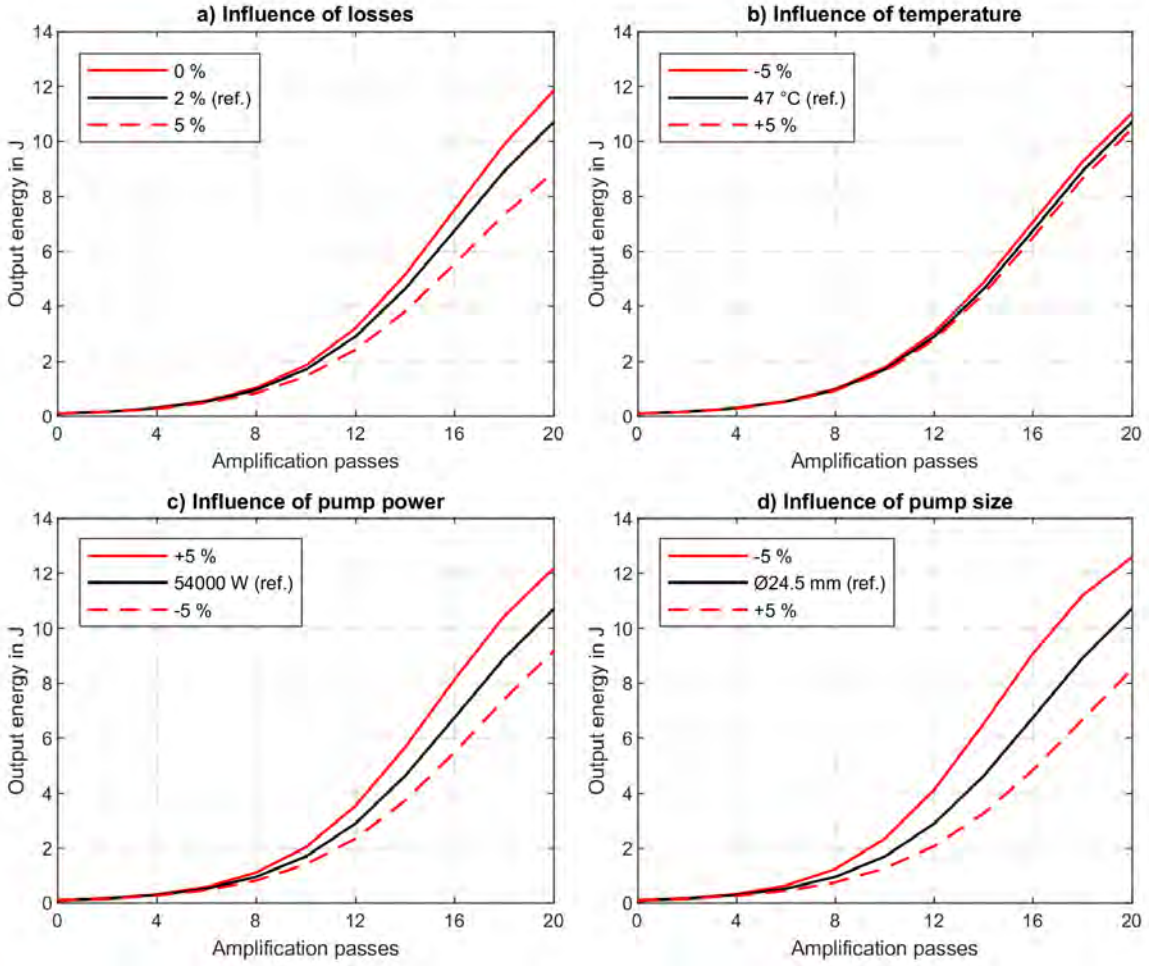

Figure 8.3: *Simulated impact of parameter tolerances at an output of ~10 J, shown for a single 3 mm thick, 2 % doped Yb:YAG crystal pumped at ~650 µs. a) Variation of optical losses that are applied every other pass. b) Impact of the average crystal temperature, c) impact of the pump power and d) impact of a different pump profile size, all within a tolerance margin of ±5 % to the reference values used for figure 8.1.*

8.2.3 Simulation of a 40-pass amplifier with two crystals

Although the previous simulations already show the feasibility of an amplifier setup with one Yb:YAG crystal, a setup with two crystals has some advantages despite the higher complexity. First, by pumping each crystal with only 27 kW the heat load per crystal is lower and thus, the thermal management is more relaxed. Second, a lower impact of ASE is expected by the lower excitation of each crystal, as will be shown in a following sub-section.

The previous simulation is extended by a second Yb:YAG crystal, also with a doping concentration of 2 % and a thickness between 2 to 6 mm. Each crystal is pumped by only one pump module with 27 kW and passed 20 times by the amplified beam. This calculates to overall 40 amplification passes. All other parameters are identical to the single crystal case. Figure 8.4 shows the results of the simulation with two crystals.

Average crystal temperatures

By distributing the heat load to two crystals, lower temperatures are achieved, see graph a) of figure 8.4. At the maximum pump duration of 1500 µs the average temperature of the bulk material lies between ~45 °C and ~75 °C for a thickness of 2 mm and 6 mm respectively. As a comparison, the single crystal setup results in 70 to 130 °C.

Remaining pump power
The lower temperatures in the two crystal setup increase the efficiency of the pump as well as the amplification process due to the higher absorption and emission cross-sections at lower temperatures. As a result, a stronger absorption of the pump is observed in graph b). This is further enhanced by the decreased pump power of 27 kW which causes a lower pump intensity and therefore also a lower pump saturation. An average of ~16 % of the pump power remains after passing a 2 mm thick crystal eight times. For a thickness of 3 mm this reduces to ~5 %. This compares to 25 % and 10 % in a single crystal setup. For thicker crystals, almost all of the pump is absorbed.

Material excitation
The bulk material experiences less excitation than in a single crystal setup due to the lower pump power. In graph c) this also manifests in a higher minimum pump duration that is required to exceed the equilibrium excitation. With an average of ~33 %, the highest, relative excitation is still achieved for a 2 mm thick crystal at a pump duration of 1500 µs. This reduces to ~13 % for a 6 mm thick crystal, which is only slightly higher than the required equilibrium excitation of ~8 % at the expected temperatures of ~75°.

Maximum achievable output energy
As a result of the overall lower excitation, the amplification process is in favor of thinner crystals than in a single crystal setup, as depicted in graph d). The optimum thickness is between 2 and 3 mm with a maximum output energy of 20 J at a pump duration of 1500 µs. The 4 mm thick crystal manages an output energy of ~17 J. Thicker crystals are not suitable for a two crystal setup due to their low excitation. Although a thickness of 5 mm still shows a maximum energy of 12 J, this could be already too little if also tolerances and ASE are considered.

Evolution of the output energy over 40 amplification passes
The evolution of the output energy over 40 amplification passes is similar to the single crystal setup, if the increased number of passes and the lower output energy are taken into account. The four parameter combinations in graph e) were chosen to represent the full range of output energies. As mentioned for the single crystal setup, other parameter combinations with the same output energies behave similar. A strong saturation can be seen for combinations with an output energy greater than ~14 J in comparison to ~18 J in a single crystal setup. At the targeted energy of 10 J, saturation effects are minor.

Influence of the input energy
The similarity to a single crystal setup also manifests itself in the influence of the input energy on the output energy, see graph f). Thus, the same conclusions can be drawn for the two crystal setup: an input beam with either a low energy or a high contrast is required for output energies beyond 14 J or a high energy stability of the input beam is required for an operation around 10 J.

Evolution of spectrum and influence of varying parameters
As a consequence of the similar behavior between a one and a two crystal setup, the spectral evolution of figure 8.2 and the tolerances of figure 8.3 are also valid for a two crystal setup. Therefore, separate figures are not shown.

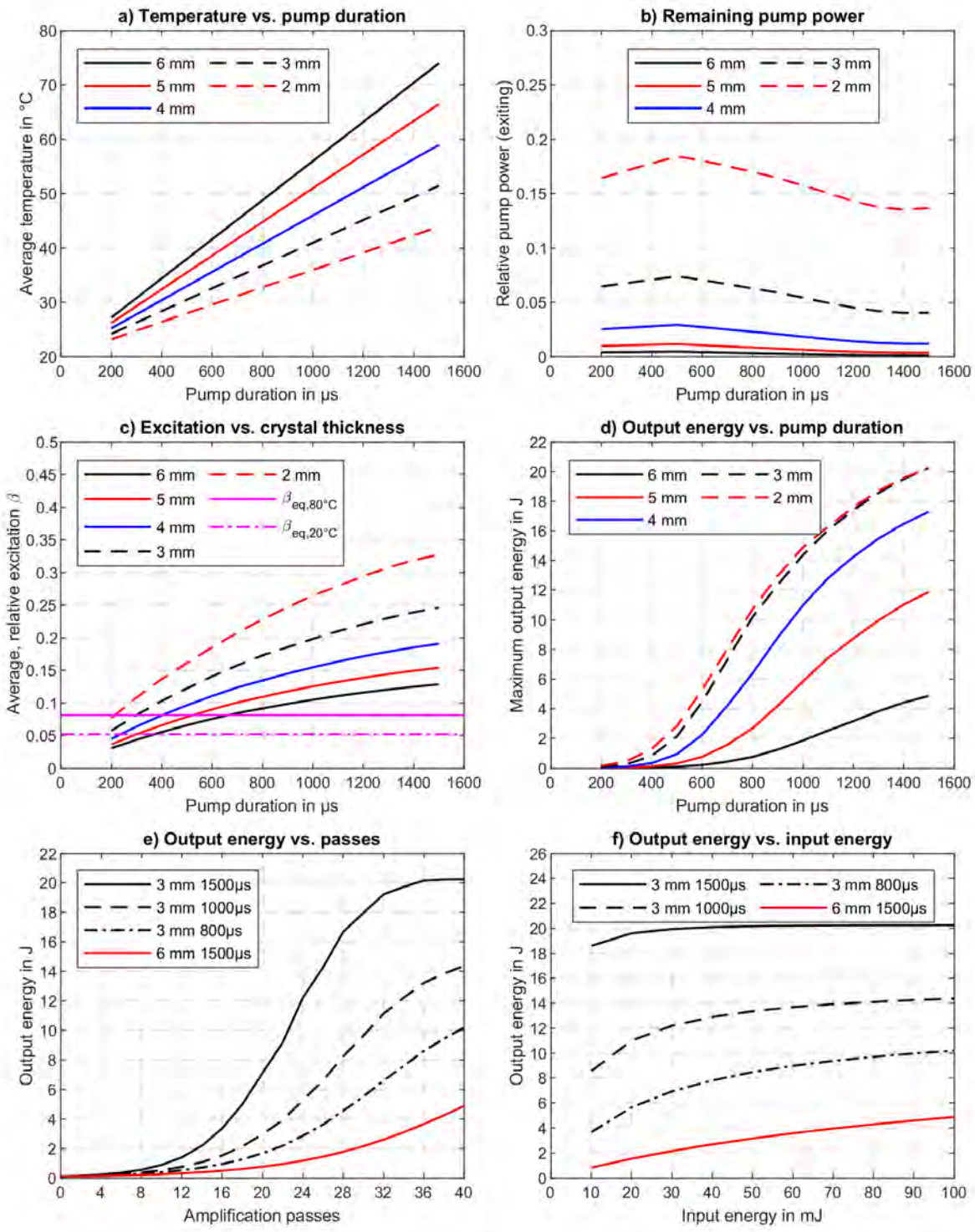

Figure 8.4: *Simulations for a two crystal setup of the BigMama. The system parameters are: 2 % doped, active-mirror Yb:YAG crystals; an 8-pass pump per crystal with 27 kW pump power at 934 to 938 nm (depending on the pump duration), 10 Hz repetition rate, a round, 16th order supergaussian beam profile with Ø24.5 mm FWHM; a 2nd order supergaussian seed beam with 24.5 mm 1/e²-diameter, a maximum seed energy of 100 mJ and 40 amplification passes with 2 % losses every other pass. a) Simulated average crystal temperatures, with 18.5 % of pump energy converted to heat. b) Remaining pump power after eight passes through the crystal. c) Average excitation in the crystals, with values for equilibrium excitation. d) Maximum achievable output energy. e) Energy build-up over amplification passes. Other parameter combinations with equal output energies (see graph d)) behave similar. f) Dependency between input and output energy.*

Conclusion for a two crystal setup
The simulation shows that also a two crystal setup is feasible for an operation at output energies above 10 J. At a doping concentration of 2 % and a pump power of 27 kW per Yb:YAG crystal the optimum crystal thickness is between 2 and 3 mm. For both, an output energy of ~10 J is achieved at a pump duration of ~800 µs in the absence of ASE. Another potential thickness is 4 mm, which requires an increased pump duration of ~950 µs.

Similar to a single crystal setup, the working point around 10 J shows no significant saturation of the amplification process. Thus, a good temporal contrast of the amplified pulses can be achieved but a high energy stability of the input beam is required for a suitable energy stability of the output beam.

8.2.4 Estimation of ASE impact

The previous simulations show that in the absence of ASE a similar performance is achieved with one or two crystals in the amplifier setup. If ASE is taken into account this may drastically change. Therefore, it is important to determine the influence of ASE on the achievable output energy before a decision is made in favor of one of the two setups. As described in section 3.3, a quick way to estimate whether the impact of ASE is critical or not is to estimate the transverse gain. If it is too large, the amplification of ASE reaches saturation and significantly depopulates the bulk material before the arrival of the seed pulse.

The impact of ASE can be roughly approximated by including the M_{ASE} factor into the previous simulations. The factor is approximated with [51]

$$M_{ASE} \approx e^{\{\sigma_e \hat{n} L\}} \tag{8.1}$$

where σ_e is the emission cross-section, $\hat{n}$ the material inversion and L the characteristic length of the gain medium. For the partially pumped, disc shaped crystals of the BigMama this length is the diameter of the pump profile. The M_{ASE} factor acts as a reduction of the fluorescence life time τ_f according to the equation

$$\tau_{f,\,\mathrm{corr}} = \frac{\tau_f}{M_{ASE}} \tag{8.2}$$

This reduction must be calculated in the simulation of the V4 tool for every time step of the pump process and every position of the pumped crystal region.

A further increase of the depopulation by ASE occurs if the transverse gain exceeds the losses at the barrel of the disc shaped crystal and the ASE starts to oscillate. A figure of merit for this oscillation threshold is the product $g_0 L$ of the small signal gain g_0 and the characteristic length L. The small signal gain is calculated by

$$g_0 = N_{dop} \cdot [\sigma_e \beta - \sigma_a (1 - \beta)] \tag{8.3}$$

where N_{dop} is the density of Yb^{3+} ions, σ_a and σ_e the absorption and emission cross-sections and β the relative excitation. The product of $g_0 L$ must stay below 3.7 for water as index-matching liquid around the barrel of the crystals. A higher $g_0 L$ exceeds the losses from the remaining reflection of 2.5 % at the barrel and therefore causes an oscillation of the transverse ASE. If the barrel is surrounded by air, oscillations occur for $g_0 L$ values above 2.4. In general, an acceptable operation of any amplifier is expected for a product of $g_0 L$ below ~4 [51].

Table 8.1 shows a summary of the $g_0 L$ values for the previous simulations. To increase the precision, also the unpumped and therefore absorbing area of the crystal is considered in the factor. The table furthermore shows the reduction of the achievable output energy when the M_{ASE} factor is included in the previous V4 simulations.

Table 8.1: *Rough approximation of the ASE impact on the simulated output energies. Parameter combinations are chosen such that an output energy of ideally* 11 *to* 12 J *is achieved. g_0L is the product of the small signal gain with the pump diameter plus the respective product in the unpumped area of the crystal. ASE losses are estimated by incorporating the M_{ASE} factor into the V4 simulation. The maximum allowed pump duration is* 1500 µs.

Number of crystals	Thickness in mm	Doping in %	Pump duration in µs	Energy out (no ASE) in J	g_0L	Energy out (with M_{ASE}) in J
One	3	2	800	14.5	3.0	11.4
	4.5	2	1000	16.1	2.0	12
	5	2	1200	16.9	1.7	11.7
	5	1.1	900	13.8	1.7	11
Two	3	2	1000	14.6	1.6	11.6
	4.5	2	1500	15.2	1.0	10.5
	5	2	1500	12.4	0.8	8
	5	1.1	1000	13.6	0.9	11.4

Four crystal combinations were chosen for the table, with pump durations that support an output energy of ideally 11 to 12 J after taking ASE into account:

- A 2 % doping concentration with 3 mm thickness, which provides the highest efficiency in the absence of ASE for a setup with one or two crystals.
- A 2 % doping concentration with an intermediate thickness of 4.5 mm. Together with the 3 mm thickness and the 6 mm thick crystals of The Tube, this allows for a wide range of parameters to validate the simulation results in the laboratory.
- A thickness of 5 mm with either 2 % or 1.1 % doping concentration. These two combinations are typically available for Yb:YAG ceramics with an ASE absorbing cladding from Baikowski Japan Co., Ltd.

ASE consideration for a setup with one crystal

As expected, the higher material excitation in the single crystal setup causes higher values of g_0L than in a two crystal setup. Therefore, a greater impact of ASE is expected. A maximum g_0L of 3 is observed for a 3 mm thick crystal that is pumped at 800 µs. To achieve an efficient operation with this thickness an index-matching liquid with ASE absorber is required. Thicker crystals show a lower g_0L and thus, potentially provide a more reasonable working point.

Interestingly, the 1.1 % doping concentration with 5 mm thickness proves to be the most promising combination for a single crystal setup, even without the ASE absorbing cladding of a ceramic. It provides almost the same efficient operation as a 3 mm thick crystal due to the similar product of doping concentration and thickness but it exhibits a lower g_0L due to the increased thickness. The only disadvantage is the higher temperature of the thicker material.

ASE consideration for a setup with two crystals

The two crystal setup exhibits the lowest values of g_0L. As a consequence, the achievable output energy in the laboratory is expected to be closer to the simulated energies than with a single crystal setup. The highest g_0L is still achieved at a thickness of 3 mm but with a value of only 1.6. A thickness of 4.5 mm or above at a doping concentration of 2 % shows a considerably lower feasibility. The required, longer pump durations far beyond the fluorescence lifetime of Yb:YAG cause the ASE to strongly increase which significantly lowers the storage efficiency of the pump process.

The 1.1 % doping concentration with a thickness of 5 mm is also the most promising combination for a two crystal setup, with a g_0L of only 0.9.

Limitation of ASE considerations
Although all of these considerations grant a first insight into the behavior and impact of ASE, they are only rough approximations. For example, the total internal reflection of ASE inside the crystal increases the overall amplification length and therefore can cause higher g_0L values than presented. Furthermore, saturation effects of ASE are not properly accounted for. A method to also include these is for example the HASEonGPU tool [61], which calculates the ASE flux via a ray tracing simulation and includes the total internal reflection between the front side and the back side of the crystal. Since the calculated g_0L values of table 8.1 indicate a manageable impact of ASE in the BigMama with a rather large safety margin, further investigations with this tool were not conducted.

Also the actual geometry of the heatsink around the crystal and possible reflections of ASE from the heatsink material can cause a considerable discrepancy of the achievable output energy. Therefore, it is advisable to choose a range of crystal combinations to evaluate their performance in an actual laboratory setup.

8.2.5 Conclusion and choice of crystals and ceramics for the BigMama

The simulations show that an amplifier setup with one or two Yb:YAG crystals, 20 amplification passes per crystal and two 27 kW pump modules is sufficient to achieve the targeted output energy of 10 J. In the absence of ASE, an optimum performance is achieved with one or two 3 mm thick, 2 % doped Yb:YAG crystals. If ASE is taken into account, a lower doping concentration of 1.1 % with an increased thickness of 5 mm proves to be beneficial since the expected impact of ASE is lower.

Although the theoretical performance of a setup with one or two crystals is similar, there are a few advantages of incorporating two crystals into the first prototype of the BigMama. The thermal load in each crystal is lower and therefore relaxes the thermal management of the amplifier as well as the heatsink development. Besides this, the impact of ASE is generally lower than in a single crystal setup due to the lower material excitation per crystal. As a consequence, the two crystal setup is expected to reach the desired output energy without the need of ceramics with ASE absorbing cladding or a sophisticated ASE suppression scheme for conventional crystals.

On the contrary, a single crystal setup exhibits a greatly reduced complexity of the amplifier which is advantageous for a robust and low-maintenance operation. Therefore, if the higher thermal load and the greater impact of ASE can be sufficiently managed, a setup with only one crystal is the preferred choice of the BigMama.

As a result, from these insights, the two crystal setup was chosen for the first prototype of the BigMama with the future goal of implementing only one crystal in the amplifier. Therefore, crystals were purchased that are suitable for both setups. Based on the results of the simulations, these are:

- 3 and 4.5 mm thick, 2 % doped Yb:YAG crystals with [111] cut and a diameter of Ø38 mm, purchased from Northrop Grumman SYNOPTICS
- 5 mm thick, 2 % and 1.1 % doped Yb:YAG ceramics with ASE absorbing, chromium doped cladding and a diameter of Ø55 mm, purchased from Baikowski Japan Co., Ltd.

These crystals and ceramics allow for a wide range of parameters than can be tested together with the developed heatsinks for an optimum working point of the BigMama. Furthermore, the purchase of cladded ceramics ensures an output energy of more than 10 J in a worst-case scenario for the ASE.

8.3 Opto-mechanical design of the BigMama

The first prototype of the BigMama was set up at the MPQ and largely adapted the opto-mechanical design of The Cube. It was based on the same rotational symmetric, 20-pass 4f-relay-imaging concept but with ~1.5 times larger optics to account for the increased output energy. Furthermore, two crystals were implemented instead of only one. A thorough description of the setup can be found in appendix B.

The prototype allowed for the first amplification to an output energy of 10 J but was limited to a single-shot operation. It proved that with two 3 mm thick, 2 % doped Yb:YAG crystals the impact of ASE is manageable also without a sophisticated ASE suppression scheme. However, during the operation several drawbacks of the amplifier design and particularly of the developed MKIII and AMKI heatsinks emerged which ultimately resulted in a redesign of the entire amplifier. These drawbacks are shortly summarized as follows:

- By implementing two crystals into the amplifier all heatsink or crystal related issues are doubled. This includes the frequent degradation of the wavefront and beam profile with the gluing method of the MKIII heatsink and in particular the mechanical instability of the AMKI heatsink during evacuation. As a result, the amplifier suffered either from a low quality beam profile or from strong drifts of the beam. While this was manageable with only one crystal in The Cube, it required a redevelopment of the heatsinks for the BigMama.
- Even with the highly stable MKIII heatsinks, the increased challenge of placing and aligning two independent, heat laden crystals inside vacuum remains. Therefore, a placement outside of vacuum is desired which allows for a separation of the heat source from the vacuum and an easier realignment in case of e.g. thermal drifts. Due to the inherent lack of free space in the developed 4f-relay-imaging concept, this placement outside of vacuum was not possible.

A further drawback emerged when the PFS system was moved to the CALA facility. The new laboratory required a shorter amplifier length, which was not possible with the 4f-relay-imaging concept of the prototype. As a result, the entire amplifier was redesigned based on the reflective Type 2 imaging concept of the SuperBooster. This allowed for an overall shorter amplifier length and especially for a comparably easy placement of the crystals outside of the vacuum chamber. Furthermore, the MKX heatsink was developed which enables a maximum mechanical stability and a superior quality of the beam profile even with two crystals in the setup.

8.3.1 Opto-mechanical design of the final BigMama

The opto-mechanical design of the final version of the BigMama is presented in figure 8.5. The design is largely based on the Type 2 imaging geometry of the SuperBooster and is modified for an implementation of two crystals.

Path of the amplified beam

The entire optical setup is mirrored along the concave L2 mirror to generate an additional image plane in which the second crystal (Xt) is placed. This results in a W-shaped geometry and two L1 mirrors. The L1 mirrors are furthermore non-monolithic and contain a grid of 1.5" concave mirrors (CM). By choosing a focal length combination of 1000 mm and 450 mm for the L1 and L2 mirrors respectively, a separation along the optical axis between the crystals and the L2 mirror is achieved. This provides enough space to place the crystals outside of the vacuum chamber while all other optics of the multi-pass geometry stay inside. Two Ø80 × 10 mm high grade windows (W) separate the crystal side from the vacuum side of the amplifier.

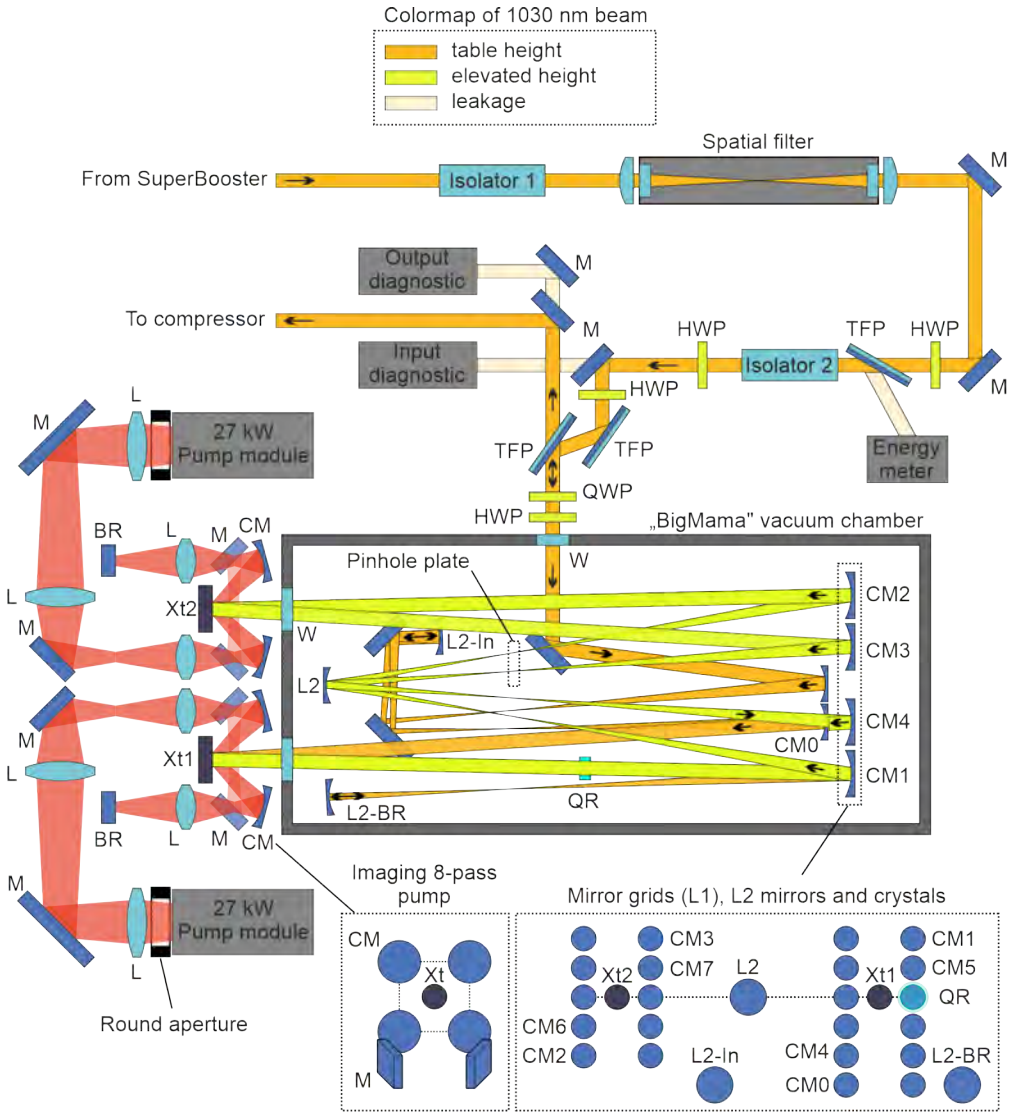

Figure 8.5: *Schematic of the optical design of the final BigMama. The fundamental geometry is based on the Type 2 imaging of the SuperBooster amplifier. The geometry is mirrored along the concave L2 mirror to implement two crystals. Each active-mirror Yb:YAG crystal is placed in an image plane of the amplifier, outside of the vacuum chamber. The input beam passes a sequence of two isolators and a spatial filter to maximize the suppression of back reflections. The input and output beams are divided by a* 55° *thin film polarizer (TFP). A quarter-wave plate (QWP) and a half-wave plate (HWP) generate an elliptical input polarization that counteracts depolarization inside the amplifier. They also cause a* 90° *rotated, linear polarization of the output beam. A folded Type 2 telescope inside the vacuum chamber (L2-in) images the input beam onto the first crystal. The two L1 mirrors are made of mirror grids which contain* 1.5" *concave mirrors (CM), each with a focal length of* 1000 mm. *The focal lengths of the concave mirrors L2 and L2-in are* 450 mm *and* 550 mm *respectively. A pinhole plate between L1 and L2 filters out unwanted parasitic reflections and ASE. Both crystals are pumped under* 15° *by an 8-pass 4f-relay-imaging geometry that incorporates four* 3" *concave mirrors with a focal length of* 150 mm. *The amplified beam propagates for 5 roundtrips and is reflected back for another 5 roundtrips by a concave mirror (L2-BR) with a focal length of* 450 mm. *A quartz rotator (QR) is placed after 3 roundtrips towards the L2-BR to compensate depolarization effects. Input and output diagnostics record the beam profiles through leakages of* 45° *mirrors (M). W: Window, BR: Backreflector, L: Lens.*

An additional Type 2 telescope (L2-in) images the input beam onto the first crystal. Together with the multi-pass geometry this results in 24 amplification passes through the first crystal and 20 passes through the second.

Path of the pump beam
The pump beam is imaged four times onto each crystal by a new 4f-relay-imaging pump geometry which replaces the dichroic mirror arrangement of The Cube. The geometry is based on four 3" concave mirrors with a focal length of 150 mm that are hit under an angle of 7.5°.

Each pump beam is cut from a square profile to a round one by an aperture in front of the pump modules. This greatly relaxes the required size of optics inside and outside of the amplifier. A total pump power of 27 kW remains per pump module after the aperture.

More details on the new pump geometry are given in the following sub-section.

Control of stray light and ASE
Since the entire crystal and pump assembly is placed outside of the vacuum chamber, the thermal management is more relaxed and additional water cooled shades as in The Cube are not required. A pinhole plate in the focus plane of the amplifier blocks any parasitic reflection and suppresses most of the ASE. The typical diameter of each pinhole is 4 to 6 mm.

Input and output beam manipulation and detection
The input and output beams of the amplifier are separated by a 55° thin film polarizer (TFP). An arbitrary polarization state of the input beam can be created with the combination of a quarter-wave plate (QWP) and a half-wave plate (HWP). Together with an additional quartz rotator (QR) inside of the amplifier this enables a sufficient compensation of depolarization losses in the BigMama. More details on this compensation method are given later in section 8.7.

The waveplates are furthermore used to convert the output beam of the amplifier to a linear polarization that is rotated by 90° relative to that of the input beam. The output beam is transmitted through the TFP while the remaining depolarization losses are reflected towards the pre-amplifier and eventually filtered out by an optical isolator. Due to the size of the implemented Ø35 mm isolator, the isolation ratio is limited to a measured value of only 1×10^{-2} to 1×10^{-3}. Since the BigMama is seeded directly by the SuperBooster pre-amplifier, this ratio is not sufficient to suppress all back reflections at an output energy of 10 J. To further improve the suppression, a second isolator with a diameter of only Ø15 mm and a higher isolation ratio is added before the spatial filter, in the path of the non-expanded input beam.

Several diagnostics allow the permanent monitoring of the back reflections, the input beam, and the output beam. This includes the recording of the near-field and far-field beam profiles as well as the beam profile on the last concave mirror (CM0) inside the amplifier. These measurements are sufficient to evaluate whether a feature in the beam profile may cause laser induced damages or not.

8.3.2 Mechanical implementation

The mechanical implementation of the BigMama is shown in figure 8.6. The footprint of the entire amplifier is $\sim 2800 \times 1000\,\mathrm{mm}^2$. The setup largely utilizes the technology that was developed for The Cube and for the prototype of the BigMama. The vacuum chamber consists of three connected sub-chambers, each with a mechanically decoupled breadboard inside. All L2 mirrors, the pinhole plate as well as the L1 mirror grids are placed inside of the chambers. The entire pump assembly as well as the two crystal assemblies are placed outside of the vacuum chamber on the left. The crystals and their heatsinks are mounted in custom-developed, solid metal-joint kinematic mounts to account for the high weight of the MKX heatsinks.

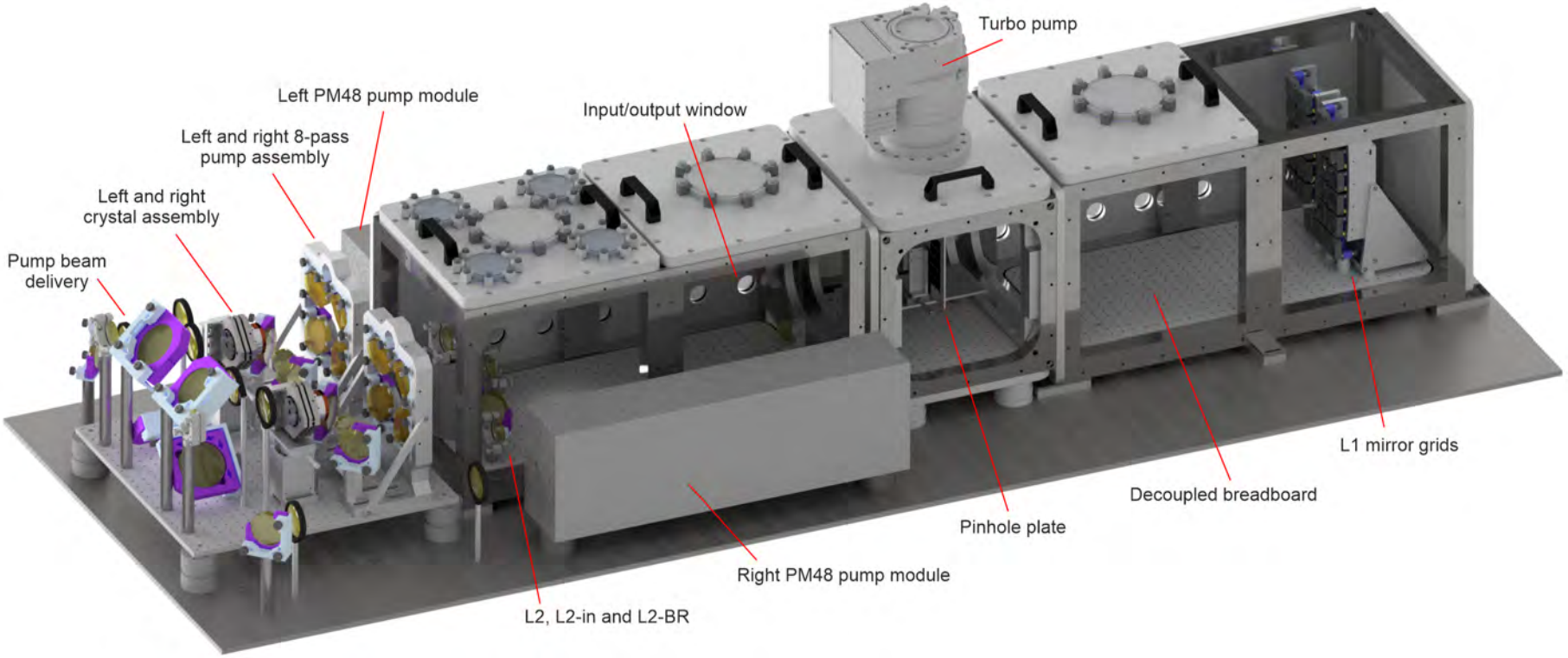

Figure 8.6: *Rendered image of the vacuum chamber and complete opto-mechanical assembly of the final BigMama, generated with Autodesk Inventor. The overall size including the pump beam delivery is* $\sim 2800 \times 1000 \times 500\,\mathrm{mm}^3$. *The vacuum chamber consists of three connected sub-chambers, each with a mechanically decoupled breadboard inside.*

Pump geometry

A detail view of the new 8-pass imaging pump geometry is given in figure 8.7. The picture was originally rendered for the prototype of the BigMama but it allows for a clearer view of the optical arrangement. Furthermore, it emphasizes the tight space constraints of the original, rotational symmetric 4f-relay-imaging geometry which prevented the placement of the crystals outside of the vacuum chamber.

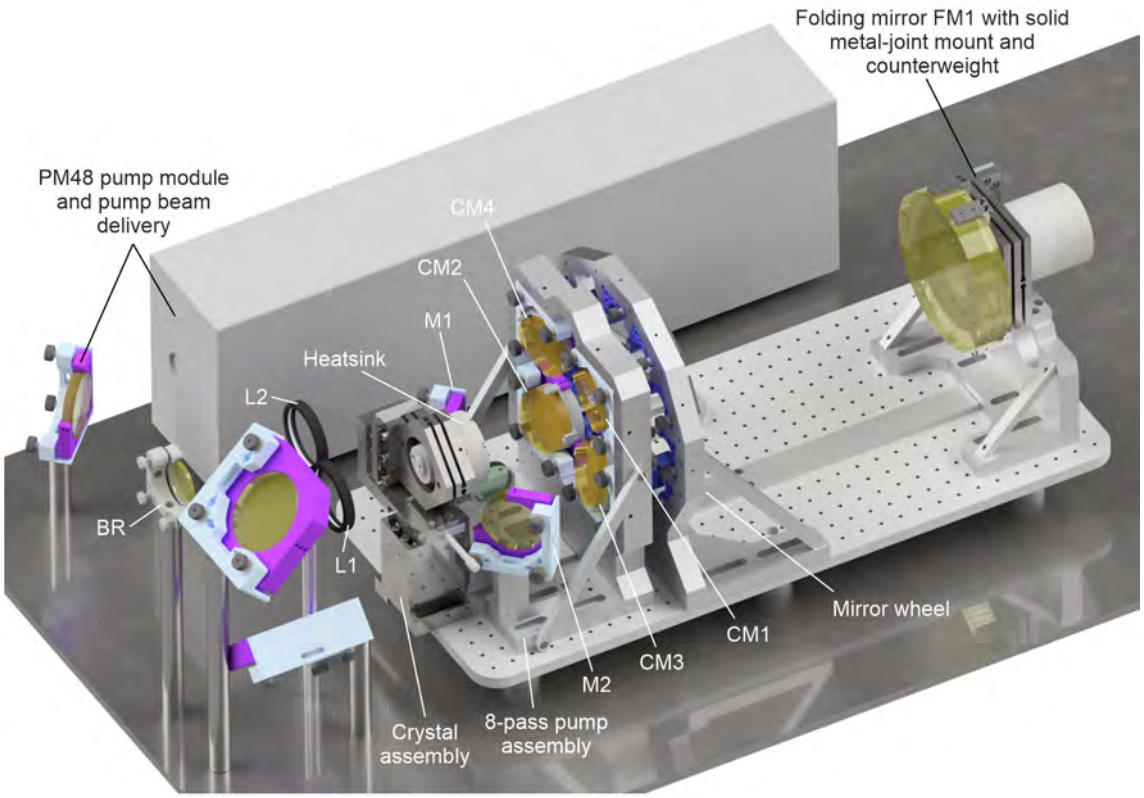

Figure 8.7: *A detail view of the 8-pass imaging pump geometry. The image was rendered for the prototype of the BigMama with a rotational symmetric 4f-relay-imaging system but it allows for a clearer view of the optical arrangement of the pump geometry. Accordingly, the mirror wheel and the folding mirror FM1 can be neglected in the image. The pump beam is imaged four times onto the crystal by four concave mirrors (CM) which are arranged in a 4f-imaging geometry. Each mirror has a diameter of* 3”*, a focal length of* 150 mm *and is hit under an angle of* 7.5°*. The order of optics which the pump beam passes is as follows: lens L1, concave mirror CM1, crystal/heatsink, CM2,* 45° *mirror M1, an optional cylindrical lens, M2, CM3, crystal, CM4, L2 and the backreflector BR. The focal length is* 175 mm *for L1 and* 150 mm *for L2. The angle of incidence of the pump beam on the crystal is* 15°*.*

The pump geometry is based on four concave mirrors which form two 4f-imaging telescopes. Each mirror has a diameter of 3” and a focal length of 150 mm. The mirrors are arranged such that the amplified beam can pass through the center of the pump geometry. Together with a back reflecting mirror the geometry enables four re-imaged roundtrips or eight passes through the crystal.

Each concave mirror is hit under an angle of 7.5°, which results in an angle of incidence on the crystal of 15°. The size of the pump beam on the mirrors is ~35 mm and thus, strong astigmatism is expected. To compensate it, three optional cylindrical lenses can be implemented into the pump beam path. However, experiments showed that a sufficient quality of the pumped crystal area is also achieved without these optional lenses.

Another effect of the angle of incidence is a lower spatial overlap of the incident and reflected pump beams inside the crystal. For a crystal thickness of 5 mm for example, a separation of ~1.4 mm occurs between both beams at the front side of the crystal. The separation causes an overall lower excitation of the crystal at the border region of the pumped area. This proves to be particularly beneficial for the amplifier since it also causes a lower amplification in this region and therefore smoother edges of the amplified beam profile. This smoothing compensates the sharp edges of the pump beam profile which are introduced by cutting a circle out of the original square shape. Without the smoothing effect, these sharp edges would imprint into the amplified beam profile and cause severe diffraction effects during propagation.

8.3.3 Comparison between 4f-relay-imaging and Type 2 imaging

The Type 2 imaging geometry of the final BigMama has several, fundamentally different features than the rotational symmetric 4f-relay-imaging geometry of the prototype or The Cube.

Increased number of amplification passes
For a single crystal setup, the maximum number of amplification passes is increased from 20 to 24 and for a setup with two crystals from 40 to 44. According to the previously shown simulations in figure 8.1 and figure 8.4 slightly higher energies can be achieved by this which is beneficial to compensate the impact of ASE.

Setup with one crystal
In a Type 2 geometry with one crystal, only half of the optics is required. This reduces the number of reflections from optical surfaces to a total of 4 per roundtrip. This compares to 8 reflections for the prototype of the BigMama or The Cube. Since the number of reflections has a significant impact on the wavefront of the amplified beam, the Type 2 geometry is expected to perform better than the 4f-relay-imaging geometry. Furthermore, a single crystal setup provides a sufficient compensation of astigmatism, as proven in section 5.4 and the SuperBooster.

Setup with two crystals
For a Type 2 geometry of the BigMama with two crystals, the number of reflections increases to 8, compared to 10 in the prototype. The greatest disadvantage of the setup with two crystals is the lack of a proper compensation of astigmatism. In a V-shaped Type 2 geometry with only one crystal, the folding angle of the L1 mirror in the horizontal direction compensates the astigmatism of the L2 mirror in the vertical direction. By creating a W-shaped geometry as in figure 8.5 an additional folding angle is introduced along the horizontal direction of the L2 mirror which causes additional astigmatism and coma. As a reference, L2 is hit under an average angle of ~2.7° at a focal length of 450 mm and a beam size of ~22 mm. This cannot be easily compensated by the geometry only.

Experiments showed that the astigmatism can be sufficiently compensated after the amplifier by tilted lenses, since the overall goal is a suitable pump beam profile for an OPCPA system rather than a perfect focus. This goal also relaxes the requirements on the coma.

On the negative side, the additional aberrations reduce the alignment tolerance of the amplifier in combination with the indispensable pinhole plate in the focus plane. In order to suppress any feedback of ASE, the pinholes must have a sufficiently small diameter. The diameter is typically chosen several times larger than the focus size to also allow for a certain tolerance against any misalignment of the amplifier. The additional astigmatism and coma of the two crystal setup considerably increase the focus size and as a result, the free aperture of the pinholes to tolerate any misalignment is reduced.

Optical quality of windows
Another feature to consider for the BigMama in a Type 2 geometry is the implementation of two Ø80 × 10 mm windows which separate the vacuum part of the amplifier from the crystals in air. Each window is passed twice per roundtrip through the amplifier. This calculates to a total number of 44 passes through the windows in a two crystal setup. Therefore, a considerable amount of bulk material is added to the beam path which potentially degrades the wavefront of the output beam.

To avoid this, high grade windows were purchased from Manx Precision Optics Ltd. with an extraordinarily high bulk quality. Interferometric measurements show a transmitted wavefront of better $\lambda/50$ per pass of a 633 nm beam. As a result, no visible changes to the output beam wavefront could be measured with the diagnostics of the BigMama.

8.4 Low energy experiments

The prototype of the BigMama at the MPQ was used to thoroughly characterize the new pump geometry as well as the impact of ASE for different crystals. A short summary of the most important results is given in this section since they are also valid for the final version of the BigMama with a Type 2 geometry.

8.4.1 Characterization of the new pump geometry

The measurement of the pump beam profile at the position of the crystal proved to be challenging due to the high peak power, the rather large beam size of ~24.5 mm FWHM and the necessity to record the profile after overlapping eight passes in the crystal. As a trade-off, an evaluation of the pump profile quality was done by recording the emitted fluorescence light of the crystal with a camera and an objective during the pump process. Although this does not provide the actual pump beam profile, it enables the observation of the overall shape of the pumped crystal area.

A single, 3 mm thick Yb:YAG crystal was pumped with one pump module at 27 kW for the measurement of figure 8.8. The recorded fluorescence light in figure 8.8 a) is rather symmetric and homogeneous. The overall shape resembles the round pump beam profile with a close match of the size. Only a minor influence of the steep angle of incidence of the pump beam can be seen on the upper and lower left corners of the pumped area. This influence manifests itself in the form of lobes which originate from the oval shape of the pump profile when it hits the crystal under 15°. Within these lobes the pump beam does not properly overlap for all eight passes.

A low energy, gaussian shaped seed beam was sent through the prototype amplifier to further evaluate the quality of the pump geometry. After 20 amplification passes an output energy of ~1.6 J was achieved with an astonishingly smooth and round beam profile, see figure 8.8 b). Together with the recorded fluorescence light this proves the uniform excitation of the crystal that is achieved with the new 8-pass pump geometry.

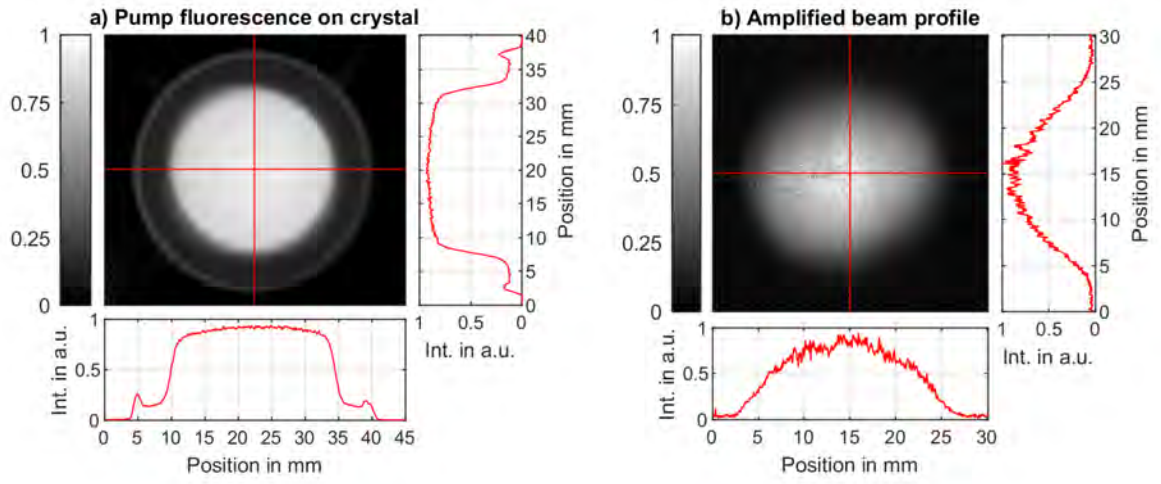

Figure 8.8: *Evaluation of the quality of the 8-pass pump geometry. a) Fluorescence light of a* 3 mm *thick Yb:YAG crystal that is pumped with one pump module at* 27 kW*. The fluorescence light is recorded with a camera and an objective in front of the crystal. The FWHM diameter of the pumped area is* 24.5 mm*. b) First amplification experiment with an output energy of* 1.6 J *after 20 amplification passes of a gaussian shaped input beam.*

8.4.2 Characterization of ASE

The same setup of the prototype amplifier was also used to examine the ASE behavior of the purchased Yb:YAG crystals. A separate measurement for the cladded ceramics was not done. Only one crystal was implemented at a time in the prototype and one pump module was used with 27 kW. A seed beam with a small input energy of only 0.8 mJ was sent into the amplifier to minimize saturation effects and the resulting output energy was measured. For the measurement of figure 8.9 a) all crystals were mounted in an adapted AMKI heatsink with water surrounding the crystal barrel and an additional ASE absorber. Therefore, ASE was already partially suppressed. The measurement shows the dependency between the achievable output energy and the applied pump duration.

The influence of ASE manifests itself in two features. First, for longer pump durations the slope of each curve decreases more than theoretically expected since the ASE depopulates the crystal during the pump process. Second, at some point the depopulation by ASE overpowers the pump process and the curve shows a peak after which no additional output energy is gained despite the ongoing pump process.

The observed impact of ASE is strongest for the 3 mm thick crystal, as already expected by the simulations in section 8.2. With water as index-matching liquid a maximum pump duration of 1400 µs is possible. The 4.5 mm thick crystal shows a lower influence of ASE and therefore provides a higher output energy for pump durations beyond ~1200 µs. The 6 mm thick crystal shows no clear indication of ASE effects. The deviation of the curve is mostly caused by thermal issues of the thick material.

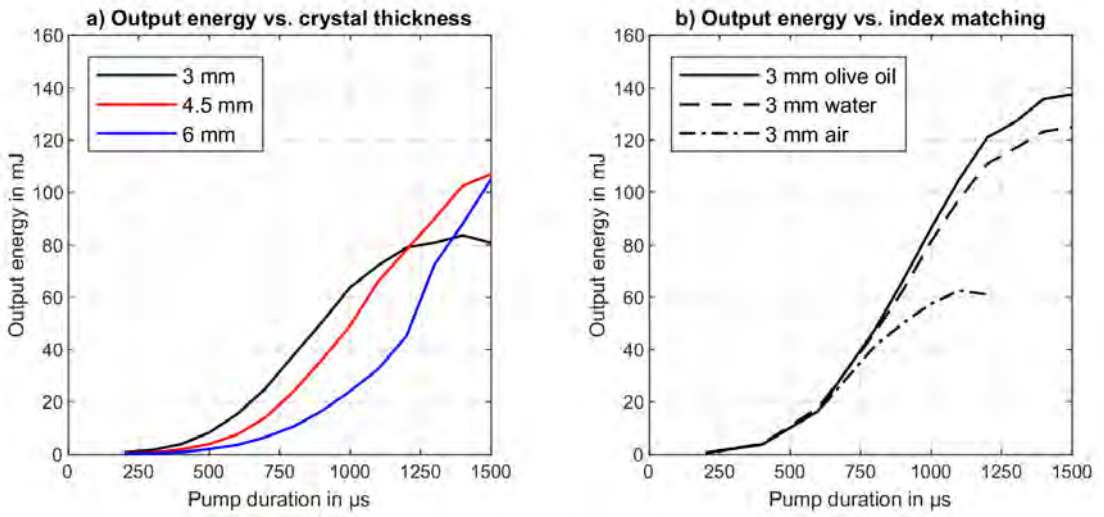

Figure 8.9: *Influence of ASE on the energy gain in the prototype BigMama. The setup consists of a single* 2 % *doped Yb:YAG crystal, pumped at* 27 kW *within a diameter of* 24.5 mm *and seeded with a low energy of* 0.8 mJ *to minimize saturation effects. a) Achievable output energy for three different crystal thicknesses with decreasing slopes of the curves due to ASE. All crystals are mounted in an adapted AMKI heatsink, with water surrounding the crystal barrel. b) Suppression of ASE by different index-matching materials around the barrel of a* 3 mm *thick crystal. Note: measurements for a) and b) were taken with slightly different settings on different days. Thus, the absolute energy values are not comparable.*

In figure 8.9 b) the influence of different index-matching materials around the barrel of a 3 mm thick Yb:YAG crystal is shown. In accordance with the fundamentals of ASE in section 3.3, a significant increase of the energy gain is observed when applying water or olive oil. Also, the maximum possible pump duration is increased. The corresponding reflection of the crystal barrel is reduced from ~8.6 % in air to ~2.4 % in water (refractive index 1.33) and to 0.9 % in olive oil (refractive index ~1.5). Further experiments with liquids that match closer the refractive index of ~1.82 of YAG were not conducted.

Since the measurements operate far below saturation with a small input energy, the saturated gain for high output energies will only increase by a fraction of the measured values. Based on the simulations of section 8.2, an increase of the output energy of 1 to 3 J is expected for a working point at 10 J if water or olive oil is applied around the crystal barrel instead of air.

An interesting observation over the course of the measurements is an inconsistent impact of the ASE for theoretically identical crystal-heatsink assemblies. The maximum, ASE limited pump duration varied by roughly ± 100 µs for the same combination of crystals, heatsinks and operational parameters. This can be attributed to slight variations of the crystal surface topology, the crystal parameters or the manufacturing/assembly tolerances of the heatsink. All of these points influence how the ASE is reflected inside the assembly and therefore cause a lower or higher impact of ASE on the achievable output energy.

8.5 High energy experiments with one crystal

The first high energy campaign of the BigMama in the new Type 2 geometry was conducted with a single crystal setup since it only requires half of the amplifier assembly. The BigMama was seeded by the SuperBooster pre-amplifier with 56 mJ which was the maximum at that time.

A 4.5 mm thick, 2 % doped Yb:YAG crystal was chosen for all measurements due to the more relaxed impact of ASE. The crystal was mounted in the new MKX heatsink with the option to attach an additional ASE absorber. The 8-pass pump geometry was adapted to pump the crystal either with one or two pump modules at 27 kW or 54 kW respectively, in a FWHM diameter of ~24.5 mm. The pump modules were operated at 2.5 Hz to characterize the achievable output energy in the absence of thermal issues.

8.5.1 Energy performance with a pump power of 27 kW or 54 kW

The measured output energies with the single crystal setup are plotted in figure 8.10 for both pump powers. The first column of graphs represents the achievable output energy for different arrival times of the seed pulse relative to the pump pulse. The ASE absorber was not implemented for these measurements. The second column of graphs represents the dependency of the output energy on the input energy. This measurement was also used to characterize the improvement with the additional ASE absorber and water as index-matching liquid.

The operation at 27 kW shows an ASE induced saturation of the pump process for pump durations longer than 1250 µs. Without countermeasures for ASE a maximum energy of 3.4 J can be extracted from the crystal after 24 amplification passes. The application of the ASE absorber shifts the saturation point beyond a pump duration of 1500 µs and increases the output energy to a maximum of 4.7 J.

As expected, the operation at 54 kW shows a much earlier saturation of the pump process at already 650 µs. A strong roll-over of the curve is observed for longer pump durations if no countermeasures for ASE are applied. The pump duration can be pushed to a maximum of 950 µs with the ASE absorber. For this setting an output energy of 7.1 J is achieved with additional depolarization losses of 5.6 %.

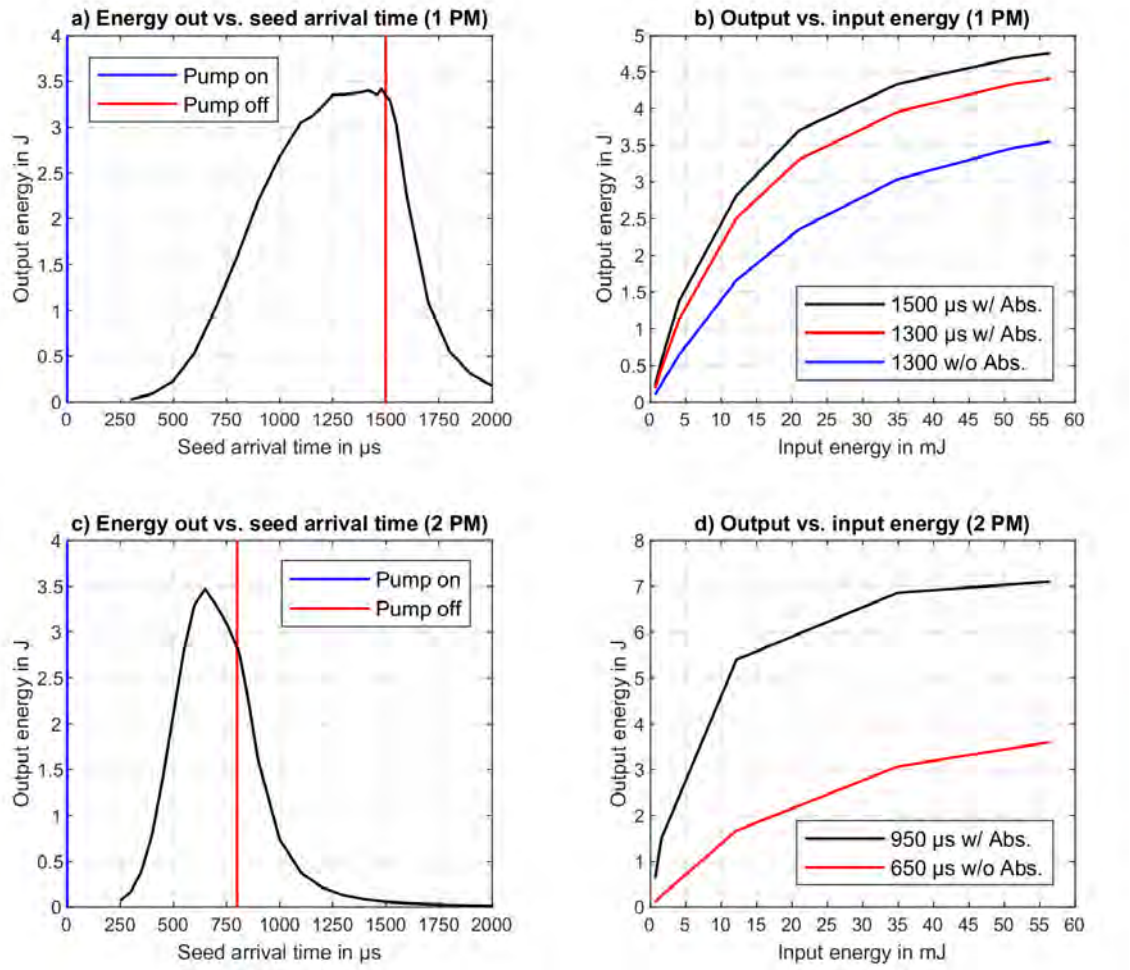

Figure 8.10: *Energy performance of the 24-pass single crystal setup in a Type 2 geometry. A* 4.5 mm *thick,* 2 % *doped Yb:YAG crystal is mounted in an MKX heatsink and pumped at* 2.5 Hz *within a diameter of* 24.5 mm *by either one or two pump modules (PM), each with a pump power of* 27 kW*. a) Maximum achievable output energy for an operation with one pump module. Each plotted energy value is recorded at a different arrival time of the seed pulse during the* 1500 µs *long pump pulse. b) Dependency between the output energy and the input energy for different pump durations, with (w/) and without (w/o) an additional ASE absorber and water as index-matching liquid around the crystal barrel. c) Time delay scan for an operation with two pump modules at a pump duration of* 800 µs*. The strong roll-over of the curve is induced by ASE. d) Corresponding dependency between the output energy and the input energy.*

8.5.2 Evolution of spectrum with Yb:YAG and Yb:KYW pre-amplifier

The single crystal setup was also used to evaluate the performance of the broadband Yb:KYW SuperBooster as a pre-amplifier. In figure 8.11 the output spectrum of the BigMama at an energy of 4.5 J is shown. For the measurement of a) the BigMama was seeded by an Yb:YAG-based SuperBooster and for b) by an Yb:KYW-based SuperBooster. As expected, with the more broadband SuperBooster a spectral bandwidth of more than 3 nm is maintained during amplification in the BigMama which allows for a safer operation and a compression to well below one picosecond even at the multi-joule level.

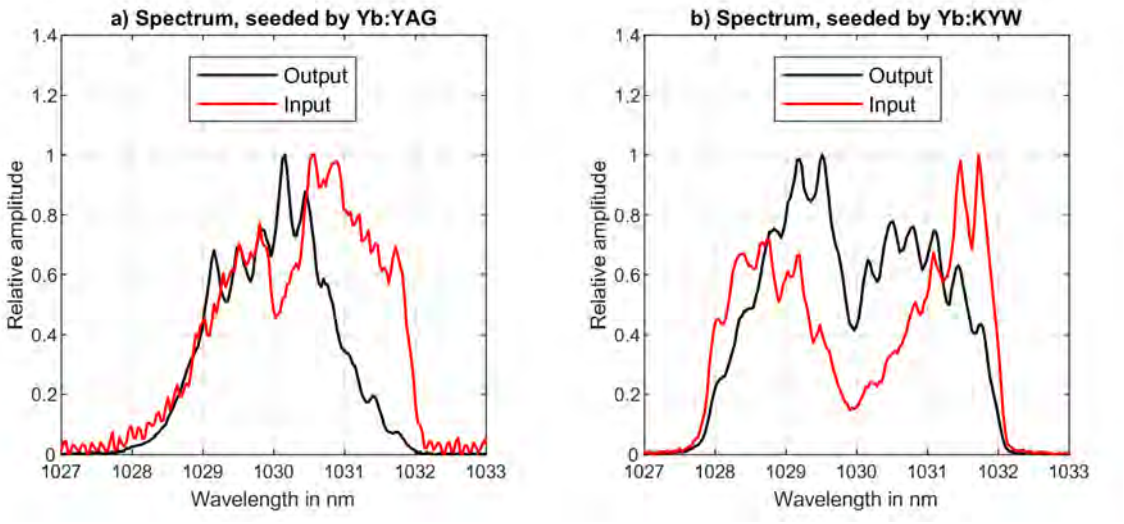

Figure 8.11: *Evolution of the spectrum for the single crystal setup. The output energy was set to* 4.5 J *for both measurements. a) BigMama seeded by the Yb:YAG based SuperBooster. The initial bandwidth of* 2.7 nm *is reduced to* 1.8 nm. *b) BigMama seeded by the Yb:KYW based SuperBooster. The initial bandwidth of* 3.7 nm *is reduced to* 3 nm.

8.5.3 Input and output beam profiles

The implemented Yb:YAG crystal is from the same high quality batch as the crystals used in The Cube. Because of this, an outstanding quality of the amplified beam profile is achieved at the maximum energy of 7.1 J, see figure 8.12. The FWHM diameter of the profile is 23.5 mm. Within this diameter, 90 % of the total energy is contained, at an average intensity of 73 % and a relative standard deviation of ±12 %. The maximum fluence of the beam profile is 2.1 J/cm^2. The overall beam profile is exceptionally smooth. Only weak, horizontal growth lines of the

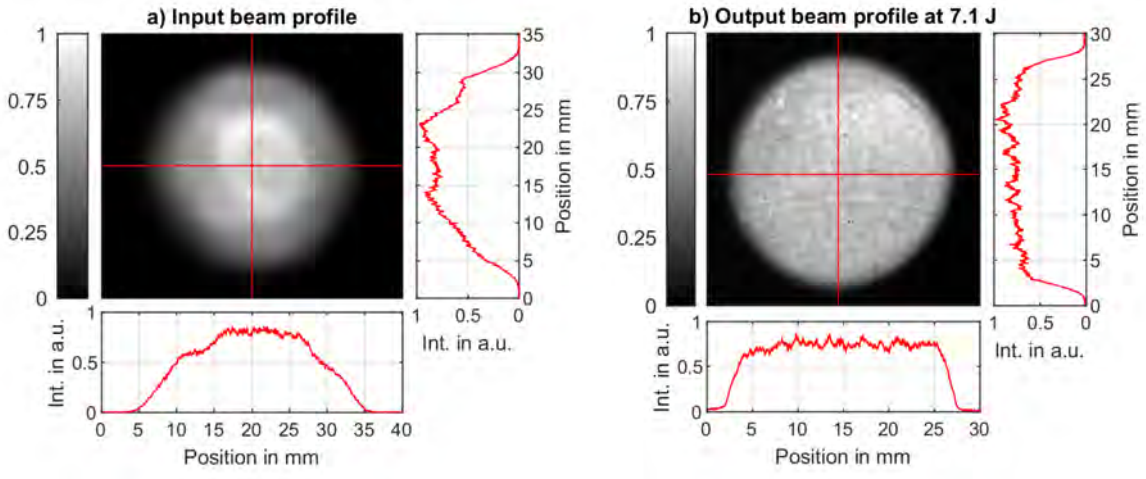

Figure 8.12: *a) Input beam profile with a 1/e²-diameter of* ~28 mm. *b) Output beam profile at* 7.1 J *with a* 4.5 mm *thick,* 2 % *doped Yb:YAG crystal. The FWHM diameter of the profile is* 23.5 mm. *Within this diameter,* 90 % *of the overall energy is contained. The average intensity is* 73 % *with a relative standard deviation of* ±12 %.

crystal material can be seen in the lower part. Taking the high number of 12 imaging passes into account further proves the excellent quality of the crystal material. Other features in the beam profile are attributed to the diagnostic optics.

8.5.4 Conclusions from the single crystal experiments

The Type 2 geometry of the BigMama with one crystal allows for a maximum output energy of 7.1 J which is currently limited by ASE effects. This performance is achieved with a single 4.5 mm thick, 2 % doped Yb:YAG crystal that is pumped at 54 kW, a pump duration of 950 µs and 2.5 Hz. A spectral bandwidth of more than 3 nm FWHM is maintained by a strong pre-shaping of the input spectrum and the broadband Yb:KYW-based SuperBooster as the pre-amplifier. The excellent performance of the less complex Type 2 geometry together with the high material quality of the implemented crystal results in a remarkable quality of the amplified beam profile.

Limitations and further improvements

The operation of the single crystal setup was mostly limited by the applied ASE absorber. First, the geometry of the absorber created strong turbulences of the warm air in front of the crystal and therefore caused a severe instability of the amplified beam. As a consequence, the operation was limited to only a few measurements to not damage any optics. Second, the onset of transverse ASE oscillations was observed for pump durations beyond 950 µs despite the application of the ASE absorber with water as index-matching liquid. As a result, a further increase of the output energy can be achieved with a more sophisticated design of the ASE absorber and an index-matching liquid that matches closer the refractive index of Yb:YAG.

Another limitation was found in the form of a strong ASE lasing in the direction of the amplified beam that occurred for longer pump durations. This lasing manifested itself in a sudden jump of the output energy and sharp peaks of the output spectrum at either 1024 nm or 1030 nm. The peak at 1030 nm was attributed to a non-sufficient suppression of ASE feedback by the pinhole plate in the focus plane of the amplifier. The instability of the beam that was caused by the ASE absorber required rather large pinhole diameters to not cut the amplified beam. Therefore, an improved ASE suppression by smaller pinhole diameters was not possible with the first design of the ASE absorber.

The origin of the peak at 1024 nm is more complex. It is a ”super resonator” that was created between the regenerative amplifier, the SuperBooster pre-amplifier and the BigMama. This resonator caused an oscillation of ASE between the three amplifiers for several roundtrips. The source of the oscillating ASE was the Yb:KYW crystal of the SuperBooster. In fact, the maximum emission-cross section of the N_m-axis of Yb:KYW is at 1024 nm, see section 3.1. All optical isolators and TFPs of the PFS pump laser are optimized for 1030 nm and therefore exhibit a lower isolation ratio for the 1024 nm peak. The oscillation at 1024 nm further benefits from the broad amplification bandwidth of the regenerative amplifier and the high amount of stored energy in the Yb:YAG crystal of the BigMama. This causes a small signal gain of more than 1000 in the BigMama, even at a wavelength of 1024 nm.

The oscillation of ASE was eventually suppressed by the addition of a second optical isolator in the beam path between the SuperBooster and the BigMama and by a careful optimization of the involved isolators and TFPs.

8.6 High energy experiments with two crystals

More high energy experiments of the BigMama were conducted with the two crystal setup in order to achieve the targeted output energy of 10 J. For this purpose, the amplifier was changed from the previous V-shaped Type 2 geometry to the W-shape of figure 8.5 and a second crystal was implemented. Each crystal is pumped with only one pump module at 27 kW and 2.5 Hz. The decreased pump power per crystal results in an overall lower excitation of the bulk material. Therefore, the impact of ASE is lower than in the previous single crystal setup and a higher output energy can be achieved.

Two crystal thicknesses were examined for the campaign: a thickness of 3 mm which already allowed for an output energy of 10 J in a single-shot operation of the prototype BigMama, and a thickness of 4.5 mm which allowed for 7.1 J in the single crystal setup of the Type 2 BigMama. All crystals were mounted in MKX heatsinks but no additional ASE absorber was attached due to the induced instabilities on the amplified beam.

The results of high energy experiments with two crystals are summarized in the following subsections.

8.6.1 Energy performance with 3 mm and 4.5 mm crystals

The achieved output energies are plotted in figure 8.13 a). For the measurements, the input energy was fixed to 44 mJ at all times and the output energy was instead regulated by reducing the arrival time of the seed pulse after the end of the pump pulse. This approach avoids the generation of high output energies during the pump process, where the crystal still heats up and the thermal lens potentially changes. Thus, a safer operation of the amplifier is ensured.

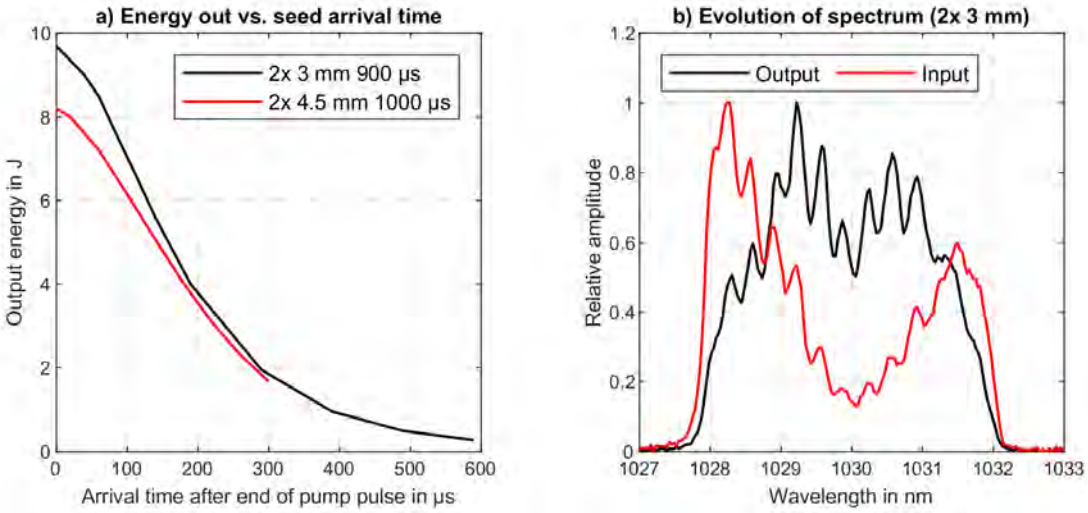

Figure 8.13: *Measurements with the 44-pass two crystal setup in a Type 2 geometry. Either two* 3 mm *thick or two* 4.5 mm *thick,* 2 % *doped Yb:YAG crystals are implemented in the amplifier. All crystals are mounted in MKX heatsinks without an additional ASE absorber. Each crystal is pumped at* 27 kW *and* 2.5 Hz *within a FWHM diameter of* 24.5 mm*. The input energy is set to* ~44 mJ*. a) Output energy for different arrival times of the seed after the end of the pump pulse. The applied pump durations of* 900 µs *and* 1000 µs *respectively are the maximum before transverse oscillations of ASE start. b) Evolution of the output spectrum for the case of two* 3 mm *thick crystals. The initial bandwidth of* 3.7 nm *is reduced to* 3.2 nm *at an output energy of* 9.7 J*.*

An output energy of up to 9.7 J is achieved with an additional 3.4 % of depolarization losses for the setup with two 3 mm thick, 2 % doped Yb:YAG crystals and a pump duration of 900 µs. The corresponding optical-to-optical efficiency is ~20 % which is an extraordinarily high value considering the operation at room temperature and the broadband output spectrum. The standard deviation of the output energy over 1000 shots is less than 0.5 %. The two 4.5 mm thick crystals allow for a slightly longer pump duration of 1000 µs. However, in accordance with the simulations this thickness is less efficient and therefore an output energy of only ~8 J is achieved. The maximum pump duration for both setups is limited by the onset of transverse oscillations of ASE. With a proper ASE absorber attached to the heatsink an output energy of at least 10 J is expected for the 4.5 mm thick crystals and 11 to 12 J for the 3 mm thick crystals.

Similar to the single crystal setup, a broadband output spectrum is achieved when the amplifier is seeded with the Yb:KYW-based SuperBooster. An exemplary spectrum is shown in figure 8.13 b) for the case of two 3 mm thick crystals. The measured FWHM of the spectrum is 3.2 nm at the maximum output energy of 9.7 J. The output spectrum with two 4.5 mm thick crystals is almost identical. Therefore, a separate figure is not presented.

8.6.2 Output beam profiles and focus

The overall quality of the output beam profiles of the setup with two crystals is comparable to the single crystal setup. For both crystal thicknesses, a rather smooth, flat-top like beam profile is achieved with a FWHM of ~23.5 mm, as shown in figure 8.14.

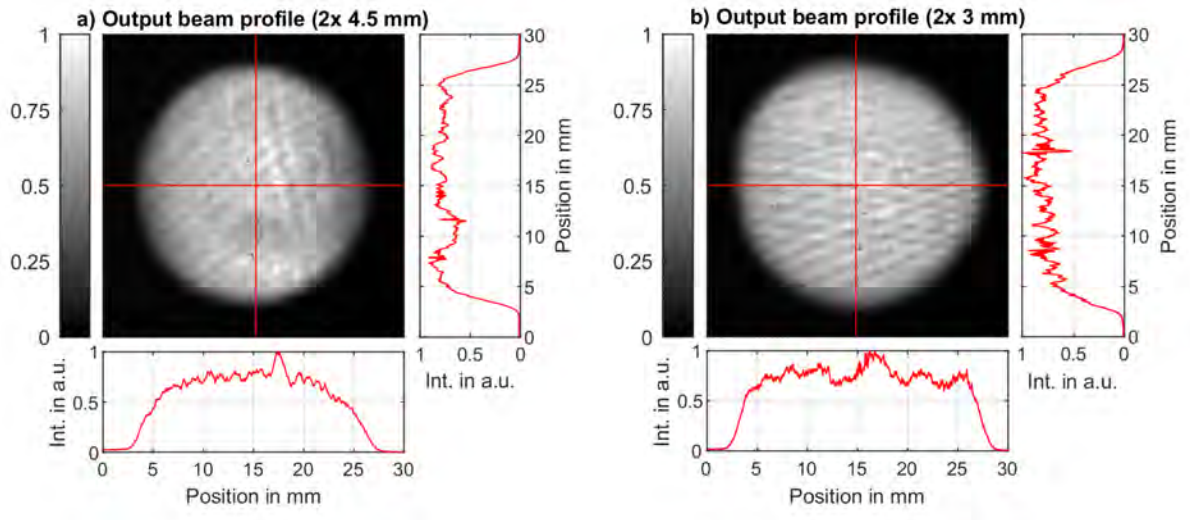

Figure 8.14: *Output beam profiles of the two crystal setup. a) Beam profile with two* 4.5 mm *thick crystals and b) with two* 3 mm *thick crystals. The profiles are recorded at an output energy of* 8 J *and* 9.7 J *respectively. In b) the stronger modulations are caused by growth lines of the* 3 mm *crystals. Within the FWHM* ~23.5 mm, 89 % *of the total energy is contained, with an average intensity of* 72 % *and a relative standard deviation* ±12 %*. The maximum measured fluence within the beam profile is* $3\,\mathrm{J/cm^2}$ *at an output energy of* 9.7 J.

The setup with two crystals exhibits more noticeable growth lines of the crystal material, since a new batch of crystals was implemented. Even though the new batch matches the initial specifications of the previous, higher quality batch, a lower ”best effort” quality beyond these specifications was achieved. Due to the 44 amplification passes this becomes visible in the beam profiles and shows again the extraordinary sensitivity of the amplifier design.

The resulting intensity modulations are already mitigated in the recorded profiles by shifting the spatial overlap of each pass of the amplified beam on the crystals randomly by ~0.5 mm. Furthermore, an orientation of the two crystals is chosen which generates a grid like pattern of the growth lines instead of overlapping them to long, strongly modulated lines. With it, the modulations of the beam profiles are reduced to less than $\pm 10\,\%$. A maximum energy fluence of $3\,\mathrm{J/cm^2}$ is measured within the beam profile of the two 3 mm thick crystals at an output energy of 9.7 J.

Focus profile

The evolution of the focus profile was examined with three measurements presented in figure 8.15. Since the Type 2 geometry with two crystals lacks a sufficient compensation of astigmatism, a strong impact can be seen.

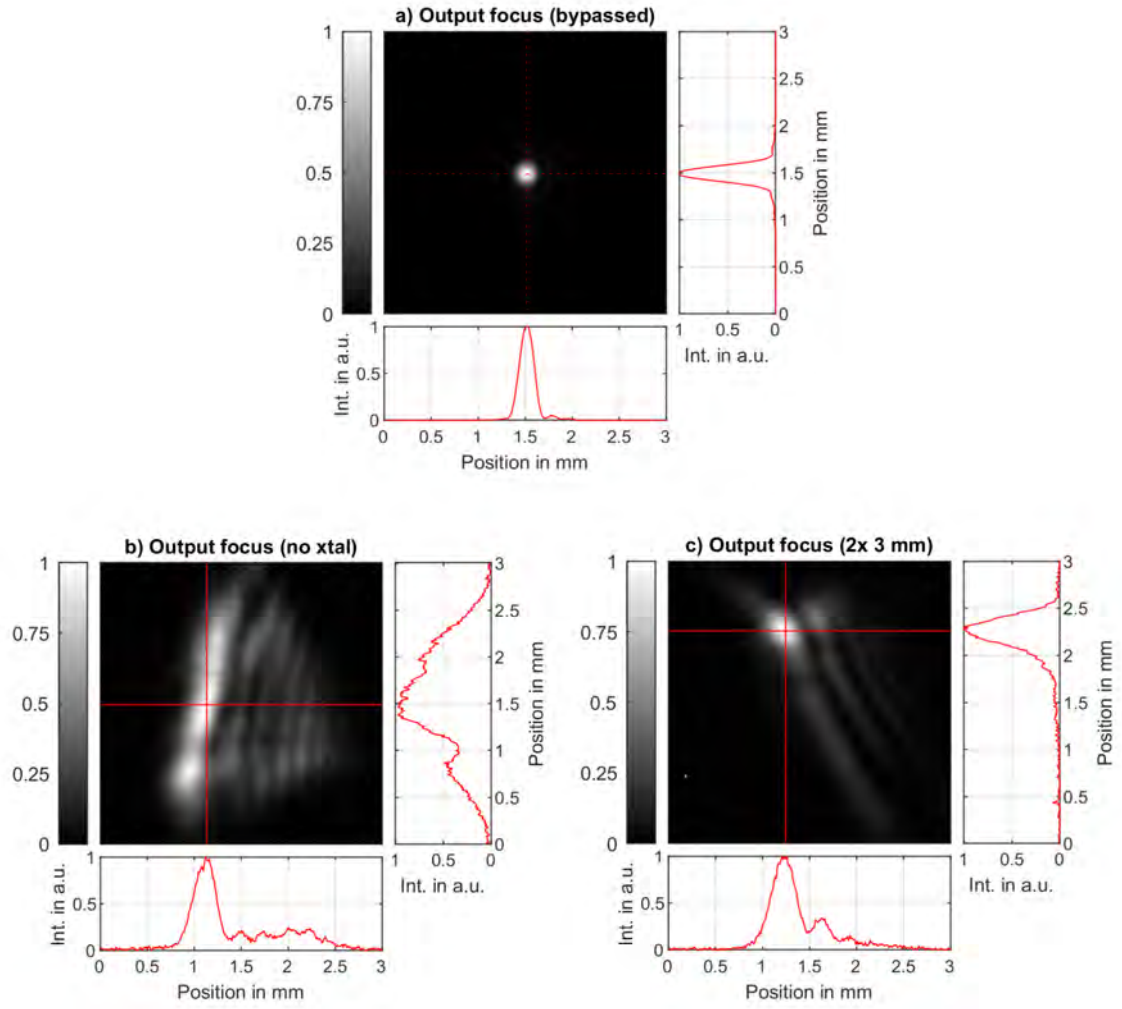

Figure 8.15: *Evolution of the output focus profile for a setup with two* 3 mm *thick Yb:YAG crystals (xtal), mounted in MKX heatsinks. a) Output focus when the BigMama is bypassed, b) profile suffering from strong astigmatism and coma after passing through the full amplifier without any crystal and c) with both crystals implemented. All foci are measured with a focal length of* 1566 mm.

For a) the BigMama was bypassed and thus, the focus quality corresponds to the output of the SuperBooster. For b) the seed beam was sent through the entire amplifier while no crystal was implemented. A strong influence of astigmatism and coma is observed, which greatly enlarges the size of the focus. For c) an improvement can be seen by implementing both crystals. This

was achieved by exploiting a slightly cylindrical wavefront of the crystals that is caused by either the polishing or the heatsink assembly. With the right orientation of both crystals, more energy is concentrated within the focus. However, the overall size stays almost the same.

Since the goal of the PFS pump laser is a homogeneous pump profile for the OPCPA stages and not a perfect focus, the induced astigmatism is sufficiently compensated by a tilted lens after the amplifier. However, inside of the amplifier the increased focus size due to astigmatism and coma severely limits the tolerance against any misalignment. The suppression of ASE by the pinholes in the focus plane sets an upper limit to the allowed pinhole diameters. Therefore, a greater focus size reduces the free aperture of the pinholes which is used to avoid a clipping of the amplified beam in case of minor misalignments. For an operation at 2.5 Hz the decreased alignment tolerance of the two crystal setup is still manageable. It proves to be particularly challenging for the final operation at 10 Hz, where a strongly non-spherical thermal lens introduces additional aberrations to the focus.

8.6.3 Compression performance

The setup with two 3 mm thick crystals was used to evaluate the compressibility of the high energy pulses. For this purpose, the full energy was sent through the compressor with an overall compression efficiency of 86 % and a FROG trace was recorded with a custom-developed, second-order single shot FROG. In order to couple the beam out of the vacuum chamber of the compressor without causing non-linear effects, most of the energy was dumped by reflecting the beam off a pair of uncoated wedges inside the compressor. Up to 300 mJ remained afterwards, of which ~6 mJ was used to record the FROG trace. The FROG setup is the same one as for The Tube and The Cube. The tool developed by V. E. Leshchenko [105] was used to retrieve the FROG trace. The measurements as well as the retrieval results are plotted in figure 8.16.

The pulses are compressed to a duration of 672 fs, which is close to the theoretical Fourier transform limit of 652 fs. The G error of the retrieval is 0.006. The measured and retrieved fundamental spectra at 1030 nm match almost perfectly. The modulations in the measured spectrum are artifacts of the fiber coupled spectrometer. The spectral phase shows a remaining third-order dispersion which mostly originates from the compressor grating angle.

Preliminary SHG measurements indicate a quality of the compressed pulses that is similar to the one achieved with The Cube. For this purpose, the beam for the FROG setup was used with ~6 mJ and focused into a 4 mm thick LBO crystal. The measurement showed a conversion efficiency of ~50 % which is close to the results of The Cube. Further, quantitative measurements must be conducted to validate the SHG results for the full energy of the compressed pulses.

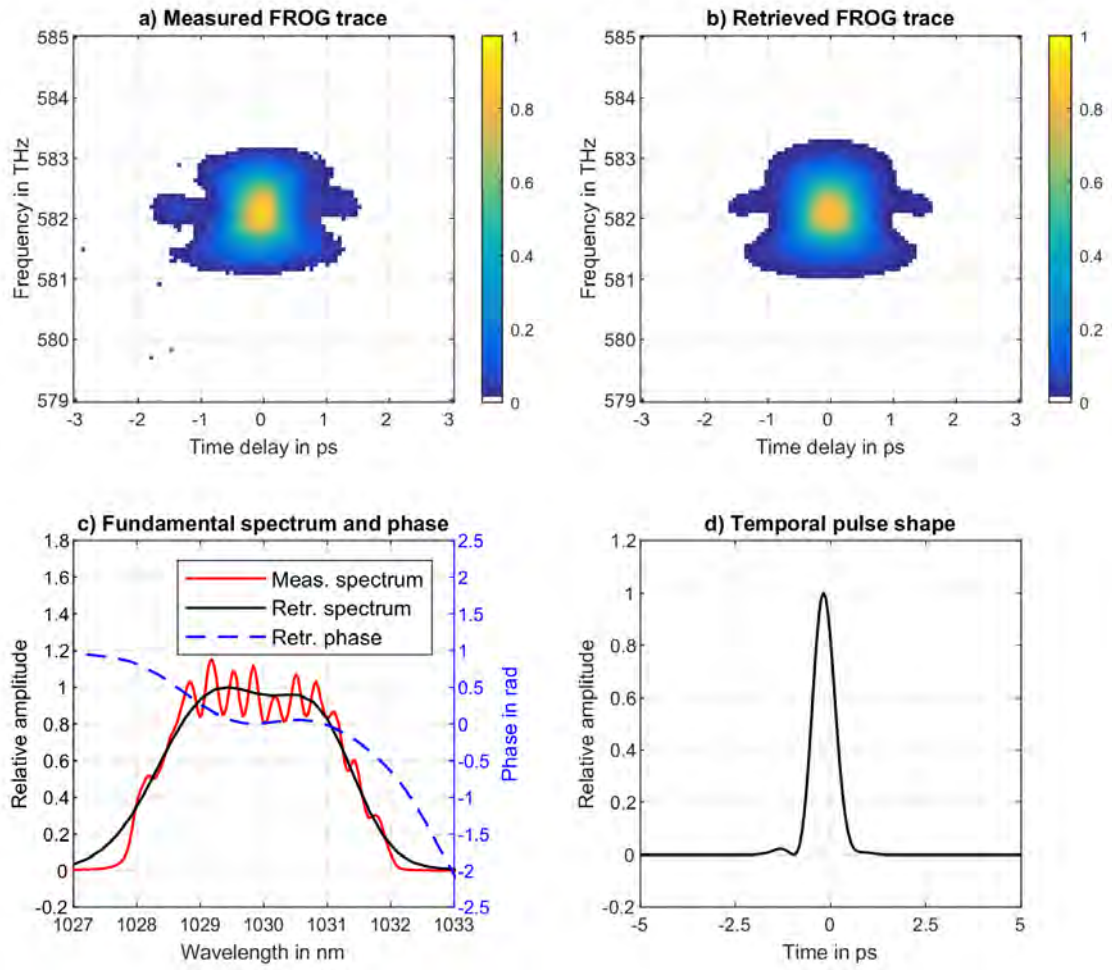

Figure 8.16: *Compression results of the BigMama with a Type 2 geometry and two* 3 mm *thick,* 2 % *doped Yb:YAG crystals. The FROG was measured with a custom-developed, second-order single-shot FROG after compressing* 9.7 J *with an efficiency of* 86 %*. a) Measured FROG trace, b) retrieved FROG trace, c) measured and retrieved fundamental spectrum as well as retrieved spectral phase (blue) and d) retrieved temporal shape of the compressed pulse. The retrieval algorithm shows a compressed pulse duration of* 672 fs *that is close to the Fourier transform limit of* 652 fs*. The G error of the retrieval is 0.006. The spectrum has a FWHM bandwidth of* 3.2 nm *and suffers from oscillations due to the fiber coupled spectrometer.*

8.6.4 Contrast measurements

The compression of the pulses enabled the investigation of the temporal contrast of the PFS pump laser with the BigMama as the main amplifier. A measurement of the contrast with a photodiode is shown in figure 8.17. The plotted data is stitched together from two separate, calibrated measurements to increase the dynamic range.

Several features are present in the pulse train. Before the arrival of the main pulse, a train of pre-pulses is seen with a time spacing of 10 ns that matches exactly the roundtrip time of the regenerative amplifier. A total of 66 pre-pulses is measured, which accounts for an estimated maximum of ~6 % of the total pulse energy. The main pulse contains at least 91 % of the total energy. A series of three post-pulses is seen afterwards. Only one of the three is considered to be properly scaled, since the other two exhibit a significantly lower amplitude in measurements with higher resolution. An estimated 1 to 3 % of the total energy is contained within the highest post-pulse, and less than 0.2 % within the other two.

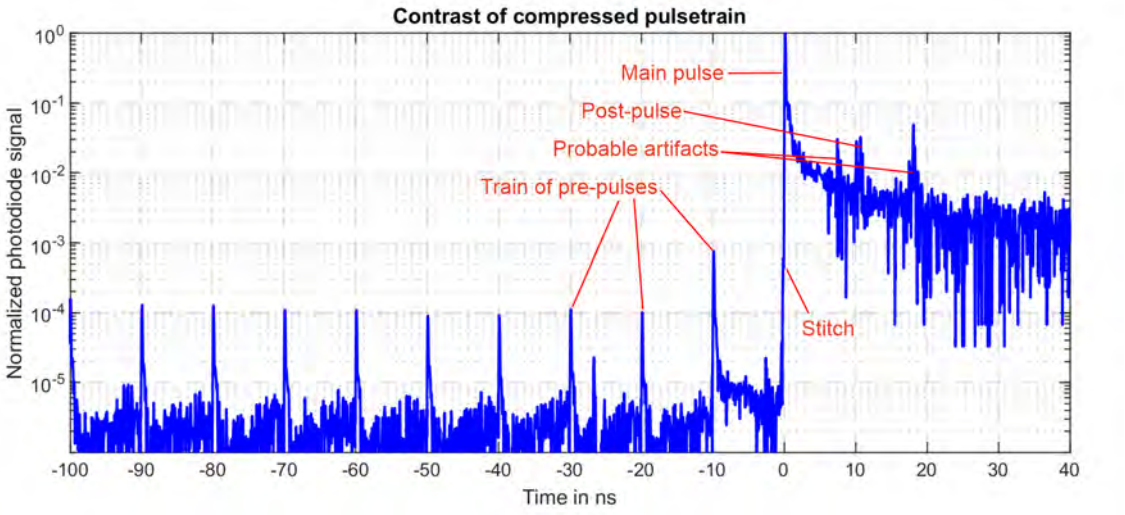

Figure 8.17: *Temporal contrast of the compressed pulse train, measured with a photodiode. The data is stitched together from two measurements to maximize the dynamic range: from* -100 ns *to* 0 ns *with a high voltage gain of the photodiode and from* 0 ns *to* 40 ns *with a low voltage gain. The energy content in each pre-pulse is estimated to be* ~0.09 % *with a total of 66 pre-pulses (not shown). The post-pulse is estimated to contain* 1 *to* 3 % *of the total energy and the main pulse at least* ~91 %*. Other peaks are assumed to be measurement artifacts, as they do not show up or only with a much lower amplitude in higher resolved measurements.*

Interestingly, a strong ASE pedestal as in the contrast measurement of The Cube does not occur. This cannot be attributed to the fast Pockels cell that cuts out ASE from the fiber amplifiers since it was also present for the measurement with The Cube. A more reasonable explanation is the significantly higher pulse energy of the new oscillator and the three times higher throughput of the overhauled stretcher. This causes higher input energies of the fiber amplifiers as well as the regenerative amplifier and therefore a more suitable working point regarding the ASE contrast.

Contrast with third-order autocorrelator

Further contrast measurements were conducted with a third-order autocorrelator ("TUNDRA", UltraFast Innovations GmbH). The contrast is plotted for two time windows in figure 8.18.

A calibration of the noise level in figure 8.18 a) reveals a device detection limit of 1×10^{-13}. The trace shows an ASE floor at 1×10^{-7} as well as several pre- and post-pulses around the main peak. The pre-pulses match the time delay and roughly the amplitude of the post-pulses. Thus, according to [106] they are most probably generated by post-pulses during amplification, either by saturation effects or the non-linear refractive index.

The pre- and post-pulses around ~250 ps and ~500 ps are assumed to be double or quadruple reflections of the Pockels cell inside the regenerative amplifier or of the fast Pockels cell that cuts out the ASE of the fiber amplifiers. In the shorter time window of figure 8.18 b) the time delay of ~10 ps corresponds to a material thickness of ~1 mm and indicates a reflection of a waveplate. The pre- and post-pulses with a delay of ~20 ps are also present in the contrast measurement of the standalone oscillator.

It is important to emphasize again the main purpose of the PFS pump laser to evaluate the results. The high energy pulses centered at 1030 nm will be frequency-doubled to 515 nm which further improves the temporal contrast. The pulses are eventually used to pump several OPCPA stages of PFS on the picosecond timescale. Earlier OPCPA experiments were conducted with The Cube as the main amplifier of the PFS pump laser and with a similar contrast performance

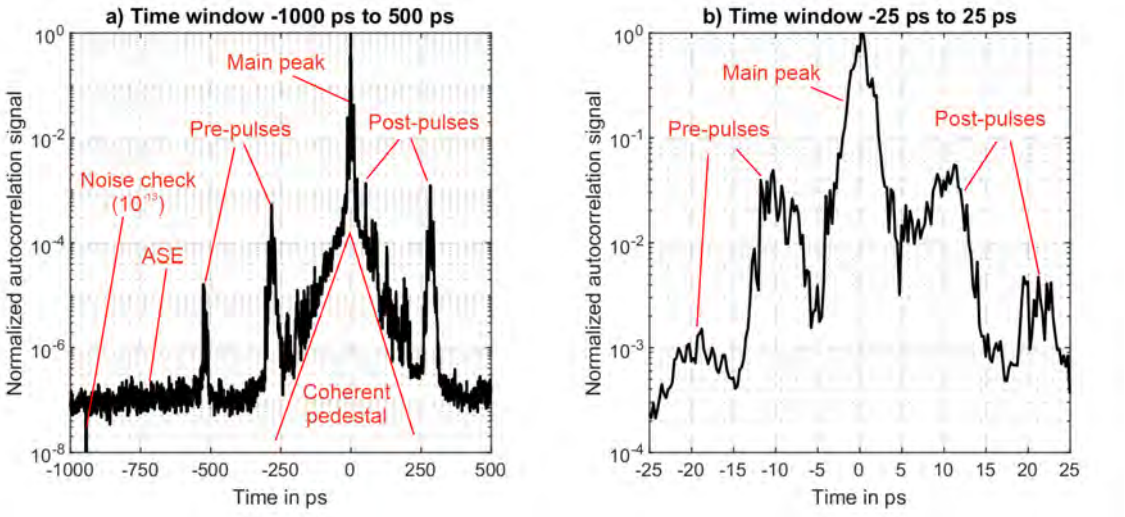

Figure 8.18: *Temporal contrast of the compressed pulse train, measured with a third-order autocorrelator for two time windows. In a) one of the two beam paths in the autocorrelator was blocked at the beginning to calibrate the noise level of* 1×10^{-13}*. Visible pre-pulses are most probably generated by post-pulses during amplification in one of the amplifiers.*

of the pump pulses. As a result, a temporal contrast of more than 1×10^{11} was achieved for the amplified, few-cycle pulses of the OPCPA stages [18]. Therefore, the measured contrast of the PFS pump laser with the BigMama as the main amplifier lies well within the requirements of the PFS system.

8.6.5 Conclusions from the experiments with two crystals

The BigMama in a Type 2 geometry with two crystals enables an amplification to the targeted output energy of ~10 J. This performance is achieved with two 3 mm thick, 2 % doped Yb:YAG crystals which are mounted in MKX heatsinks. Each crystal is pumped at 27 kW, 900 µs and 2.5 Hz. Two 4.5 mm thick crystals achieve a slightly lower output energy of ~8 J. If a suitable ASE absorber is attached to the heatsinks, an output energy of ~10 J is expected for the 4.5 mm thick crystals and 11 to 12 J for the 3 mm thick crystals.

The campaign with two 3 mm thick crystals further showed the excellent properties of the output pulses, which can be compressed to 672 fs at an efficiency of 86 %. Contrast measurements show that at least 91 % of the compressed energy is contained within the main pulse, which results in a peak power of ~11 TW.

A drawback of the Type 2 geometry with two crystals are the significantly higher optical aberrations in the form of astigmatism and coma. For the purpose of the PFS pump laser, this is still manageable at a repetition rate of at least 2.5 Hz.

8.7 Latest experiments with 10 Hz and amplifier limits

For all previous measurements, the BigMama was operated at a repetition rate of 2.5 Hz. This enabled the evaluation of the overall performance in the absence of thermal issues, such as depolarization, strong thermal lensing, or thermal drifts of the beam. In hindsight, the switch to a repetition rate of 10 Hz justified this decision, as several issues prevented a safe operation at 10 J and 10 Hz. As will be discussed in this section, the maximum output energy with two 3 mm thick crystals is limited to ~5 J at a repetition rate of 10 Hz so far.

The following sub-sections discuss the various challenges of an operation at 10 Hz with the Type 2 geometry and two 3 mm thick crystals.

8.7.1 Depolarization losses

A significant increase of the depolarization losses is observed due to the four-fold increase of the average pump power at 10 Hz and the corresponding, higher thermal load in the crystals. This in turn causes stronger temperature gradients across the pumped area of each crystal. In accordance with section 3.5 these gradients result in an increased mechanical stress of the bulk material and therefore in a stronger, stress induced birefringence.

Without additional countermeasures up to 40 % of the total output energy is contained within the wrong state of polarization due to the stronger birefringence. This energy is eventually reflected towards the pre-amplifier by the TFP in front of the BigMama and subsequently filtered out. In comparison, the depolarization losses are only around 5 % for an operation at 2.5 Hz. The losses are particularly high at the borders of the pumped crystal area since the steepest temperature gradients occur there. Such a behavior was already expected by the temperature measurements of section 4.2. The impact on the beam profile is recorded for three different cases in figure 8.19.

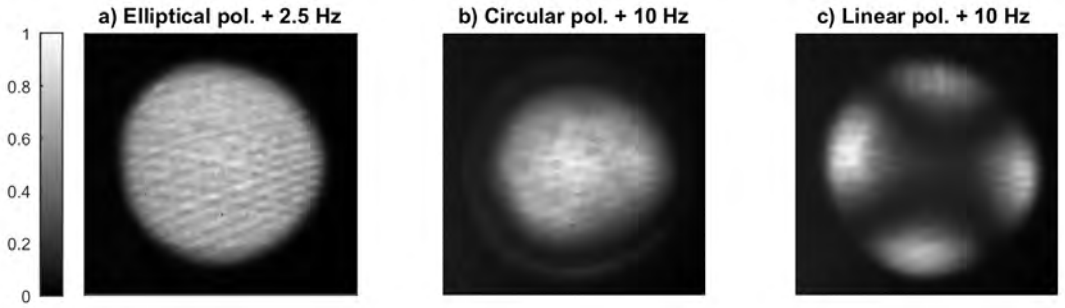

Figure 8.19: *Effects of severe depolarization losses at a repetition rate of* 10 Hz *with two* 3 mm *thick crystals. a) Output beam profile after the TFP in front of the BigMama, recorded at a repetition rate of the pump modules of* 2.5 Hz*. No effects of depolarization are visible due to an efficient compensation by an elliptical state of polarization of the input beam. b) Output beam profile after the TFP at* 10 Hz *with a circular and c) with a linear state of polarization of the input beam. In both cases significant depolarization losses occur which cannot be sufficiently compensated by the polarization state of the input beam.*

Each beam profile is recorded with the diagnostic of the BigMama after the output beam passes the TFP and the depolarization losses are separated. As a reference, the beam profile at a repetition rate of 2.5 Hz is given in figure 8.19 a). For this repetition rate, a compensation of depolarization losses by the waveplates in front of the vacuum chamber is enough to reach the typical losses of around 5 %.

For an operation at 10 Hz this compensation is not sufficient anymore and the beam profile suffers from strong depolarization losses, as seen in figure 8.19 b) and c). In b) a circular state of polarization was chosen for the input beam. As a result, the effects of the depolarization are rotational symmetric and more energy is lost for regions closer to the borders of the pump profile. In these regions, steeper temperature gradients occur and therefore a stronger birefringence is induced.

For c) a linear state of polarization was chosen. Two perpendicular axes of the crystal exist where the induced birefringence aligns with the linear polarization of the input beam. As a consequence, no changes occur to the state of polarization for these axes and the output beam resembles a bright cross. For the presented measurement, the waveplates were aligned such that the actual beam is sent towards the pre-amplifier and only the depolarization losses are sent forward to the diagnostic. Thus, the recorded image shows the inverted shape of the amplified beam.

The solution to this issue is the implementation of a 90° quartz rotator inside of the BigMama, see also section 3.5. The rotator is placed after half of the roundtrips towards the backreflector, as shown in figure 8.20. This way, the state of polarization of the amplified beam is rotated by 90° for the second half of the roundtrips towards the backreflector. As a result, the horizontal and vertical axes of the beam accumulate approximately the same phase from the birefringent crystal upon arrival at the backreflector. Thus, the initial state of polarization is maintained. The same is also valid for the propagation back through the amplifier. Since the rotatory power of the quartz rotator is independent on the state of polarization, this compensation is valid for any location in the beam profile and for any strength of the stress induced birefringence.

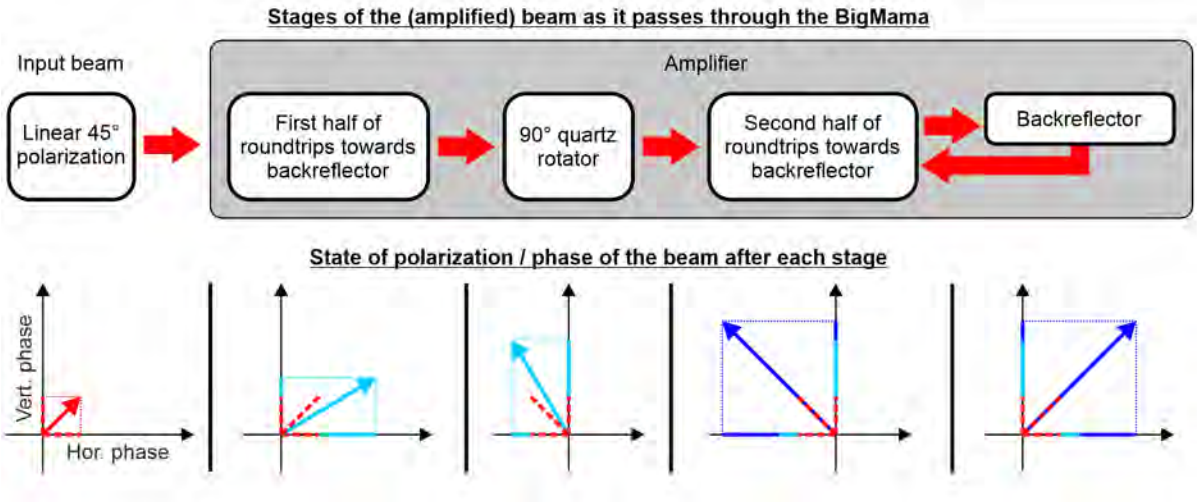

Figure 8.20: *Sketch of the compensation of depolarization losses by an additional quartz rotator inside of the BigMama. The rotator is place after half of the roundtrips towards the backreflector. This way, the horizontal and vertical axes of the amplified beam accumulate an equal amount of phase from the birefringent crystal and therefore, no change of the state of polarization occurs.*

A rotator thickness of 13.2 mm was chosen in accordance to the rotatory power given by [87] and [88]. A diameter of Ø32 mm proved to be sufficient for the amplified beam size. By implementing such a quartz rotator, a reduction of the depolarization losses to ~5 % is achieved for a repetition rate of 10 Hz. The resulting output beam profile is identical to the 2.5 Hz operation shown in figure 8.19 a).

8.7.2 Non-spherical thermal lens

Another issue that is related to the elevated thermal load at 10 Hz is a strongly non-spherical thermal lens at 10 Hz. It is directly connected to the aforementioned, steep temperature gradients that occur across the crystal. This issue ultimately prevented an output energy of 10 J at 10 Hz.

Figure 8.21 a) shows a simulation of the temperature cross-section of the implemented 3 mm thick crystal when it is pumped at a repetition rate of 10 Hz. The simulation is based on the data of the temperature measurements from section 4.2.

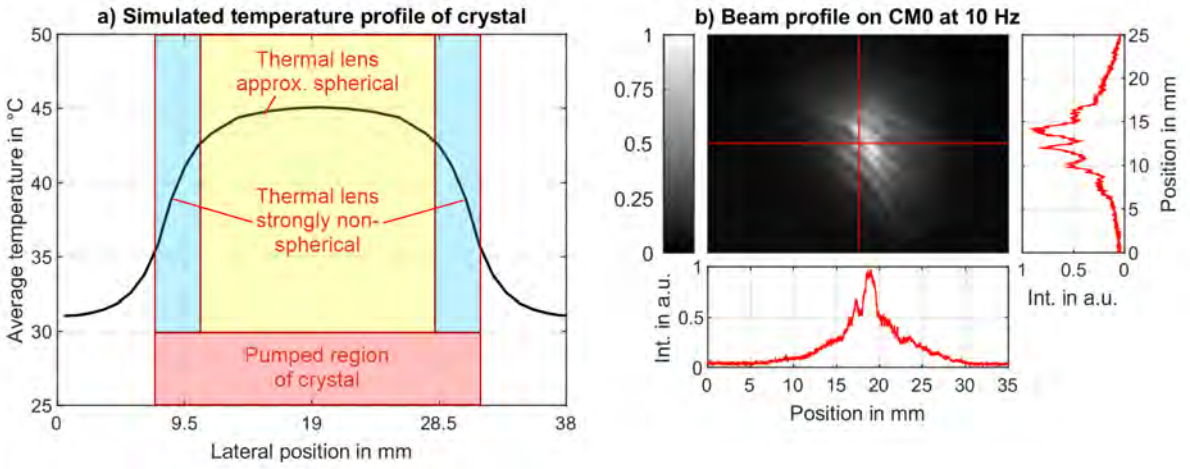

Figure 8.21: *Effects of a strongly non-spherical thermal lens in the BigMama with two* 3 mm *thick Yb:YAG crystals pumped at* 10 Hz*. a) Simulated temperature profile across one crystal, taken from section 4.2. Red region: overall area of the crystal that is pumped. Yellow region: pumped area with approximately spherical temperature profile, causing a thermal lens that can be compensated by the Type 2 geometry. Blue region: area with steep temperature gradients, causing a non-spherical thermal lens that cannot be efficiently compensated by the amplifier geometry. b) Beam profile on the last concave mirror (CM0) in the system when the thermal lens of the yellow region in a) is compensated. The overall size of the beam is similar to the size on the crystal due to the compensation, but the blue region in a) causes a focusing of energy towards the center of the beam profile.*

The temperature cross-section of the crystal can be divided into two regions: a yellow region with low temperature gradients which causes an approximately spherical thermal lens and a blue region with steep temperature gradients which causes a strongly non-spherical thermal lens. The thermal lens of the yellow region can be easily compensated by shifting the L2 mirror of the Type 2 geometry. This introduces a spherical deformation to the wavefront of the amplified beam in the opposite direction of the thermal lens. For the blue region, the compensation cannot be done by the amplifier geometry only. As a consequence, the amplified beam cannot be perfectly collimated. This poses a problem in particular to the amplifier optics since it changes the beam size on the concave mirrors.

An exemplary impact of the strongly non-spherical thermal lens is shown in figure 8.21 b). The recorded beam profile corresponds to the intensity distribution of the amplified beam at the last concave mirror CM0 of the BigMama. The amplifier is compensated for the yellow region of the crystal and thus, the overall beam size is roughly that on the crystals. However, the uncompensated blue region causes energy to converge towards the center of the beam which induces a sharp peak. The issue is further exacerbated by a wavefront defect of one crystal that induces a sharp line in the lower left of the beam profile. The measured fluence in the center

of the beam on CM0 is between 10 to 20 J/cm^2 due to the only partially compensated thermal lens. This compares to a fluence of ~3 J/cm^2 on the crystals in the image plane. Due to the imaging property, the opposite concave mirror CM1 shows an inverted behavior of the beam profile with a concentration of the energy around the edges of the beam.

For the operation at 10 Hz a suitable compromise between the compensation of the yellow and the blue region was not found by only shifting the L2 mirror. Laser induced damages occurred either in the center of CM0 or at the borders of CM1 at energies below 10 J. Another approach to compensate the strongly non-spherical thermal lens is to mitigate the temperature gradients across the crystal by smoothing the edges of the pump beam profile. At the time of this thesis, this was not realizable. Instead, the pump beam size was increased, which effectively shifts the region of steep gradients out of the amplified beam profile. However, this comes with the drawback of a lower optical-to-optical efficiency.

8.7.3 LIDT limited operation at 10 Hz

The latest high energy experiments at a repetition rate of 10 Hz were conducted with two 3 mm thick crystals and an increased diameter of the pump beam profiles. One crystal was pumped within a FWHM diameter of 26 mm and the other within 29 mm. The size was limited by the available ASE absorbers which were implemented to compensate for the lower optical-to-optical efficiency of the larger pump profiles. Each absorber was filled with olive oil as index-matching liquid to suppress the transverse ASE. The pump durations were set to 1000 µs and 1100 µs for each crystal, respectively. The measurement results at a repetition rate of 10 Hz are summarized in figure 8.22.

The larger pump beam profiles allow for a safe operation of the BigMama at ~5 J and 10 Hz. According to the energy curve in figure 8.22 a) and simulations, an output energy of at least 11 J is expected when the seed arrives exactly at the end of the pump pulse. For the given configuration it was not possible to reach this timing as laser induced damages occurred for output energies beyond 7 to 8 J. The measured spectrum at the maximum recorded output energy of 8.6 J in graph b) is similar to the broadband spectra of the previous experiments with 2.5 Hz. The achieved FWHM of the spectrum is 3.1 nm.

At the time of the 10 Hz experiments, only one redesigned ASE absorber was available. Therefore, also the old model had to be implemented which suffered from turbulences of the warm air in front of the crystal. As a consequence, an increased beam pointing fluctuation is observed in graph c) with a standard deviation of 84 µrad in the horizontal direction and 25 µrad in the vertical one. A conversion of the beam pointing values to multiples of the focus diameter is not done due to the strong aberrations of the focus profile.

The amplified beam profile in graph d) exhibits a high quality with an extraordinarily smooth intensity distribution. The FWHM diameter of the profile is slightly increased to 25 mm due to the larger pump beam profiles. Only a few line shaped features can be seen in the upper right corner which are caused by a defect of the bulk material of one crystal. This defect strongly affects the wavefront and is also responsible for the visible edge in the previous figure 8.21 b).

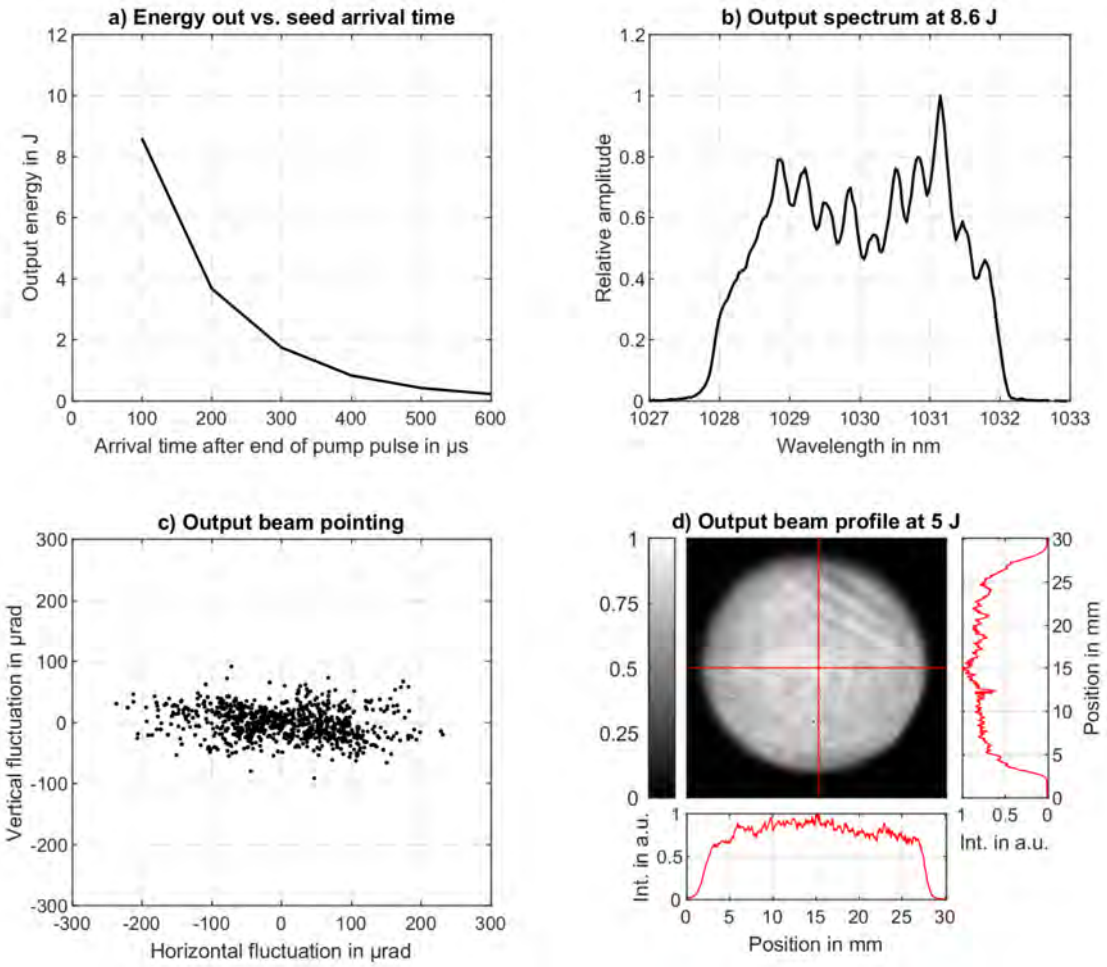

Figure 8.22: *Latest results of the BigMama at a repetition rate of* 10 Hz *with two* 3 mm *thick,* 2 % *doped Yb:YAG crystals. Both crystals are mounted in MKX heatsinks with ASE absorbers and olive oil as index-matching liquid. Each crystal is pumped at* 27 kW, *one within a FWHM of* 26 mm *and at a pump duration of* 1000 µs *and the other within* 29 mm *at* 1100 µs. *The seed energy is set to* 60 mJ. *a) Output energy for different arrival times of the seed after the end of the pump pulse. The operation is limited to* 8.6 J *at* 100 µs *delay due to LIDT issues. b) Output spectrum at* 8.6 J *with a FWHM of* 3.1 nm. *c) Beam pointing fluctuation of the output beam recorded with a focal length of* 90 mm. *The horizontal standard deviation is* 84 µrad *and the vertical* 25 µrad. *d) Output beam profile taken at* 5 J, *which is the maximum output energy without a risk of laser induced damages. The FWHM of the profile is* ~25 mm.

8.8 Conclusion and future measures

Overall, the experiments conducted with the BigMama prove the feasibility of the developed concepts, such as the new, broadband Yb:KYW SuperBooster, the Type 2 geometry of the BigMama and the hybrid MKX heatsinks.

8.8.1 Summary of results

Several experiments were conducted with one or two crystals implemented in the BigMama in order to find an optimum working point. A short comparison of the results is done in table 8.2.

Table 8.2: *Comparison of the one and two crystal Type 2 setups with the highest output energy. For both, the crystals were mounted inside liquid metal interfaced MKX heatsinks and the amplifier was seeded by the broadband Yb:KYW SuperBooster. The* 10 Hz *operation and the first prototype of the BigMama with 4f-imaging are not included since both did not allow for a suitable operation at the intended energies.*

	One crystal	**Two crystals**
Amplifier geometry	24-pass Type 2 imaging	20+24-pass Type 2 imaging
Gain medium	1x Ø38 × 4.5 mm 2 at.% Yb:YAG	2x Ø38 × 3 mm 2 at.% Yb:YAG
Pump	54 kW at 2.5 Hz, 0.95 ms, 8-pass, 24.5 mm FWHM	2x 27 kW at 2.5 Hz, 0.9 ms, 8-pass, 24.5 mm FWHM
Output energy	7.1 J with ASE absorber	9.7 J without ASE absorber
Energy stability	<0.5 % Std.	<0.5 % Std.
Spectral output bandwidth	<3.2 nm	<3.2 nm
Compression	not measured	672 fs
Contrast	not measured	ASE: $\sim 1 \times 10^{-7}$, Side peaks: $\sim 1 \times 10^{-3}$
Beam pointing fluctuation	not measured	25 to 84 µrad Std.

At a repetition rate of 2.5 Hz an output energy of up to 7.1 J was achieved with one 4.5 mm thick, 2 % doped Yb:YAG crystal and a record of 9.7 J was achieved with two 3 mm thick crystals. The output energies were mostly limited by ASE. Therefore, further improvements are expected with improved ASE absorbers attached to the MKX heatsinks. In general, an exceptional quality of the amplified beam profiles was achieved.

The setup with two 3 mm thick crystals was further used for compression experiments with the amplified pulses at full energy. Measurements with a second-order single shot FROG show a compressed pulse duration of 672 fs at a Fourier transform limit of 652 fs. With a compression efficiency of 86 % and an energy content within the main pulse of at least 91 % this calculates to a peak power of ~11 TW.

The same two crystal setup was also used to evaluate an operation at the desired repetition rate of 10 Hz. Although a potential energy output above 10 J is expected, the operation is currently limited to ~5 J in order to avoid laser induced damages. The main origin for these damages is the stronger, non-spherical thermal lens at the increased heat load which could not be sufficiently compensated in the current state of the amplifier. First trials with larger pump beam profiles showed improvements, but failed to safely reach the required output energy of 10 J.

8.8.2 Future measures for an operation at 10 J and 10 Hz

The last, yet unmatched target specification of the BigMama is an output energy above 10 J at the increased repetition rate of 10 Hz. As mentioned before, the main limiting factor is the stronger, non-spherical thermal lens. In order to achieve a safe operation at 10 J, several options are considered. The options are as follows, in descending order of their ease of application.

1. A further increase of the pump beam size
In the latest experiments one crystal is pumped within a FWHM diameter of 29 mm and the other within 26 mm. The first crystal already incorporates a new ASE absorber prototype with a larger aperture and reduced air turbulences, see also the schematic of the MKX heatsink in section 4.6. In contrast, the second crystal still relies on an older version of the ASE absorber which limits the allowable pump profile size. Both absorbers are strictly required to suppress transverse oscillations of ASE. Implementing the new ASE absorber also for the second crystal allows for a larger pump size. This shifts the crystal region with a strongly non-spherical thermal lens further away from the area that is hit by the amplified beam. This in turn reduces the impact of the thermal lens and lowers the peak energy fluence on the amplifier optics.

2. The reactivation of the single crystal setup
The single crystal setup poses a significant advantage regarding the mitigation of the thermal lens. Choosing a different size for both overlapping pump beam profiles generates smoother temperature gradients inside of the crystal. As a result, the non-spherical behavior of the thermal lens is reduced and a better compensation with the amplifier geometry can be achieved. In addition, the single crystal setup also exhibits a significantly better focus profile due to a proper compensation of astigmatism and it only contains half of the optics.

Since the output energy of 7.1 J with the single crystal setup was mostly limited by the onset of transverse oscillations of ASE, a further increase of the energy towards the targeted 10 J is expected with the newly designed ASE absorber. First experiments with this absorber showed promising results. Furthermore, the simulations in the beginning of this chapter show that, if ASE is sufficiently suppressed, a further increase of the output energy can be achieved with a 3 mm thick, 2 % doped Yb:YAG crystal instead of the implemented 4.5 mm thick one. Altogether, this potentially allows for a maximum output energy of above 10 J at 10 Hz.

In a worst-case scenario of ASE, the purchased ceramics with ASE absorbing cladding can be implemented. This option was originally put on hold due to the risk of laser induced damages of the expensive ceramics. However, the amplifier is now better understood and a damage of the ceramic can be excluded for a proper working point of the amplifier.

3. Reshaping of the pump beam profile
A pump beam profile with inherently smooth edges can mitigate the strongly non-spherical shape of the thermal lens. In the current amplifier, this cannot be done easily with a single pump module. Two future options exist to smoothen the edges: the first one is a new and optimized beam homogenization system for each pump module, which requires the exchange of the entire optical assembly of each module. The second option is the modification of the cutting apertures in front of the pump modules to a serrated-like shape. This allows to gradually reduce the average pump density for the outer regions of the pump profile.

4. The implementation of an adaptive mirror
The issue of a strongly non-spherical thermal lens is also observed for thin disk setups [107, 108]. To compensate the step-like wavefront of the induced thermal lens, adaptive mirrors are implemented into the system. These mirrors introduce a step-like wavefront which resembles the inverted shape of the temperature profile of the crystal.

In the BigMama, the L2 mirror can be exchanged with such an adaptive mirror. In the given Type 2 geometry, this is a complex task and the last option to be considered because of several reasons:

- The adaptive mirror has to be placed in the tight space of the vacuum chamber.
- It also has to introduce the required focal length of 450 mm of the L2 mirror.
- For a sufficient compensation in the setup with two crystals, all passes on the L2 have to precisely overlap with the sharply defined, step-like shape of the mirror surface.
- This in turn removes the alignment freedom of the position of each beam pass on the crystals, which is currently exploited to mitigate the effects of crystal growth lines in the amplified beam profile.

Preferred option

The single crystal setup of point 2 is the most promising option for solving the thermal lens issue and for future activities in general. Besides a potential operation at 10 J and 10 Hz, the setup also drastically reduces the complexity of the amplifier by halving the number of optics. This in turn relaxes the maintenance effort and costs. Since all optics were purchased for a setup with two crystals, the reduced number of required optics also means there are twice as many replacement parts, including crystals and ceramics.

Furthermore, the quality of the amplified focus profile is significantly better by the intrinsical compensation of astigmatism. This greatly relaxes the alignment tolerances in combination with the pinhole plate. It also enables the PFS pump laser to be used as a driver for focusing applications rather than just exploiting the beam profile for pumping OPCPA stages.

Chapter 9

Conclusion and outlook

This thesis has given an in depth description of the most recent development of an all diode-pumped, Ytterbium-based CPA laser chain - the pump laser of the Petawatt-Field-Synthesizer (PFS). A total of three new amplifiers based on Yb:KYW or Yb:YAG as the gain medium was developed. These amplifiers allowed to push the output energy of the pump laser to the targeted 10 J at a repetition rate of 2.5 Hz, or alternatively to 5 J at the targeted 10 Hz. For both settings an energy stability of ~0.5 % is achieved. The amplified pulses are centered at 1030 nm and can be compressed in time to ~672 fs which corresponds to a peak power of ~11 TW. Preliminary measurements indicate an achievable conversion efficiency of ~50 % to the second harmonic at 515 nm which is required to pump the OPCPA stages of PFS.

The three developed amplifiers of this thesis are called "SuperBooster", "The Cube" and "Big-Mama". The SuperBooster is the amplifier with the lowest output energy of all three. It is based on Yb:KYW as gain medium and allows for energies of up to 140 mJ at a repetition rate of 10 Hz. Due to the broader amplification bandwidth of Yb:KYW compared to Yb:YAG, no gain narrowing occurs during amplification and the spectral bandwidth of the input of ~4.2 nm is maintained. Together with a suitable pre-shaping, the output spectrum can be efficiently used to counteract gain narrowing in the subsequent Yb:YAG based 10 J amplifier. Extensive theoretical studies and experiments also show that Yb:KYW is a potential drop-in replacement for Yb:YAG in high energy amplifiers. Due to its beneficial absorption and emission properties Yb:KYW can be efficiently pumped with the same infrastructure. Besides the new gain medium, the SuperBooster also implements a new optical imaging system termed "Type 2 imaging" which outperforms the classical 4f-imaging. It enables a more compact amplifier size, up to 18 amplification passes and a high quality of the output beam.

The Cube is an amplifier based on Yb:YAG that allows for an output energy of up to 2 J at a repetition rate of 10 Hz. It served as the main amplifier of the PFS pump laser for several experiments with the OPCPA stages of PFS and for SHHG experiments. The Cube is a replacement of the original 1 J amplifier "The Tube" and shares the 4f-imaging concept of the optical system. Besides this, several improvements were implemented such as a higher quality pump module, a modular vacuum chamber and new Yb:YAG crystals as well as Yb:YAG ceramics with ASE absorbing cladding. The Cube also served as an experimental platform for new, custom-developed heatsinks for the implemented gain media. First heatsink prototypes based on the sinter-alloy MoCu 70/30 or liquid metal showed a superior cooling performance and allowed for an exceptional quality of the amplified beam profile and wavefront.

The BigMama is the final main amplifier of the PFS pump laser with an output energy of up to 10 J at 2.5 Hz, or 5 J at 10 Hz. It can be seeded directly with the broadband SuperBooster which enables a comparably broad output spectrum of more than 3 nm at 10 J, despite the typical gain narrowing of the implemented Yb:YAG. The BigMama also incorporates the latest heatsink design which is based on vacuum injected liquid metal as the thermal interface between the crystal and the heatsink. This new design enables a reversible assembly, a superior cooling performance and a negligible influence on the amplified beam profile and wavefront.

The BigMama shares the new Type 2 imaging concept of the SuperBooster. Extensive theoretical and experimental studies were conducted to evaluate the performance with either one or two Yb:YAG crystals in the amplifier. While the setup with one crystal shows an exceptional quality of the output beam profile and wavefront, it suffers from a strong impact of transverse ASE. Due to the current lack of suitable countermeasures the maximum achievable output energy is limited to ~7 J. The two crystal setup exhibits an inherently lower impact of ASE because of the lower excitation per crystal. Furthermore, the thermal management is more relaxed since the thermal load of each crystal is reduced. As a result, an output energy of up to 10 J can be achieved even without sophisticated countermeasures for ASE. This performance with two crystal comes at the price of an amplifier setup with twice the amount of optics and an additional introduction of strong astigmatism and coma.

Outlook

The operation of the BigMama at a repetition rate of 10 Hz is currently limited to an energy of 5 J by the occurrence of laser induced damages. The main source of these damages is a strongly non-spherical thermal lens at 10 Hz which cannot be properly compensated in the setup with two crystals. Several solutions exist to solve this issue in future activities. The most promising one is a switch to the setup with one crystal. This setup allows for a greater freedom to shape the temperature profile across the crystal by properly overlapping both pump modules on a single crystal. As a result, a better mitigation of the strongly non-spherical shape of the thermal lens is expected. A side effect of using the setup with only one crystal is a much higher quality of the output beam wavefront without the occurrence of strong astigmatism and coma. This also potentially enables applications where the focus of the pump laser is used instead of the unfocused beam profile.

Preliminary measurements with a newly designed ASE absorber of the heatsink show promising results to sufficiently suppress the transverse ASE in the Yb:YAG crystals. This potentially allows to push the output energy of the setup with one crystal towards 10 J. In addition, a better suppression of ASE also enables the use of a thinner, more efficient Yb:YAG crystal in this setup which was not done yet due to the inherently higher impact of ASE.

Despite the current limitation of the energy at a repetition rate of 10 Hz, the overall performance of the PFS pump laser makes it the most powerful Yb:YAG laser in the world. It is an ideal pump source for the OPCPA stages of the PFS system which finally enables the upgrade of PFS with a third OPCPA stage in order to reach the final goal of an output energy of 500 mJ at a compressed pulse duration of ~6 fs. Furthermore, the high energy stability and the exceptional quality of the beam profile of the pump laser maximize the usability of the amplified, few-cycle pulses of PFS. Other potential applications of the PFS pump laser are for example a high energy colliding pulse in a Thomson-scattering experiment [109] or the generation of high energy terahertz pulses [110].

Appendix A

More evaluations of the gluing method

Several trials were done to examine the sources of failure when the gluing method is applied to attach a crystal to a heatsink. For this purpose, a separate "diagnostic" multi-pass was built in the Type 2 geometry which enables 6 imaging passes on the heatsink. With it, the influence of the gluing method on the beam profile and the wavefront can be investigated before, during and after hardening the UV glue.

Figure A.1 shows a trial where a standard 1", 1030 nm, 0° HR test mirror was glued with the coating face down onto a flat and polished MoCu 70/30 metal plate with Panacol Vitralit 6127 UV glue. A distinctive feature of the polished surface in figure A.1 a) is a round stain from a drop of the UV glue. This drop was applied to the surface but wiped away before hardening due to a bubble in the glue. Although the metal plate was thoroughly cleaned mechanically and chemically, the glue diffused into the porous MoCu 70/30 material and left a stain with different reflectivity. An elevation of the surface due to the stain was not observed. The test mirror was attached afterwards in a second gluing attempt.

Apart from the stain, also some oxidation is seen on the surface of the metal plate which originates from an Yb:YAG crystal that was glued onto the plate before and which was removed with temperatures above 300 °C. In the process, the surface was furthermore slightly scratched in the center area.

Upon initiating the UV hardening of the ~1 µm thick glue layer below the mirror, a series of features with intensity modulations in the range of ~30 % emerged in the beam profile of the image plane, see figure A.1 b). After 1 m of free space propagation, these modulations grow extraordinarily high to almost 500 %. The shape of the features is identical to the stain of the removed glue drop. Also, a trail of the stain is observed which was caused by rotating the mirror in the first, failed gluing trial over the liquid glue drop for a better positioning . This trail is barely visible on the surface by eye but particularly pronounced in the beam profile.

Another observation is a consistently lower intensity of the beam profile within the area of the glue stain. This cannot be explained by mechanical effects only, for example from an elevation of the stain or the shrinking of the glue. Both would only induce a bending of the crystal surface around the edges of the stain and therefore, a change of the beam profile only in this region. Thus, the theory of a mechanical origin is sufficient to explain the strong wavefront deformations around the edges of the stain but not the constant decrease of the intensity over the entire area of the stain.

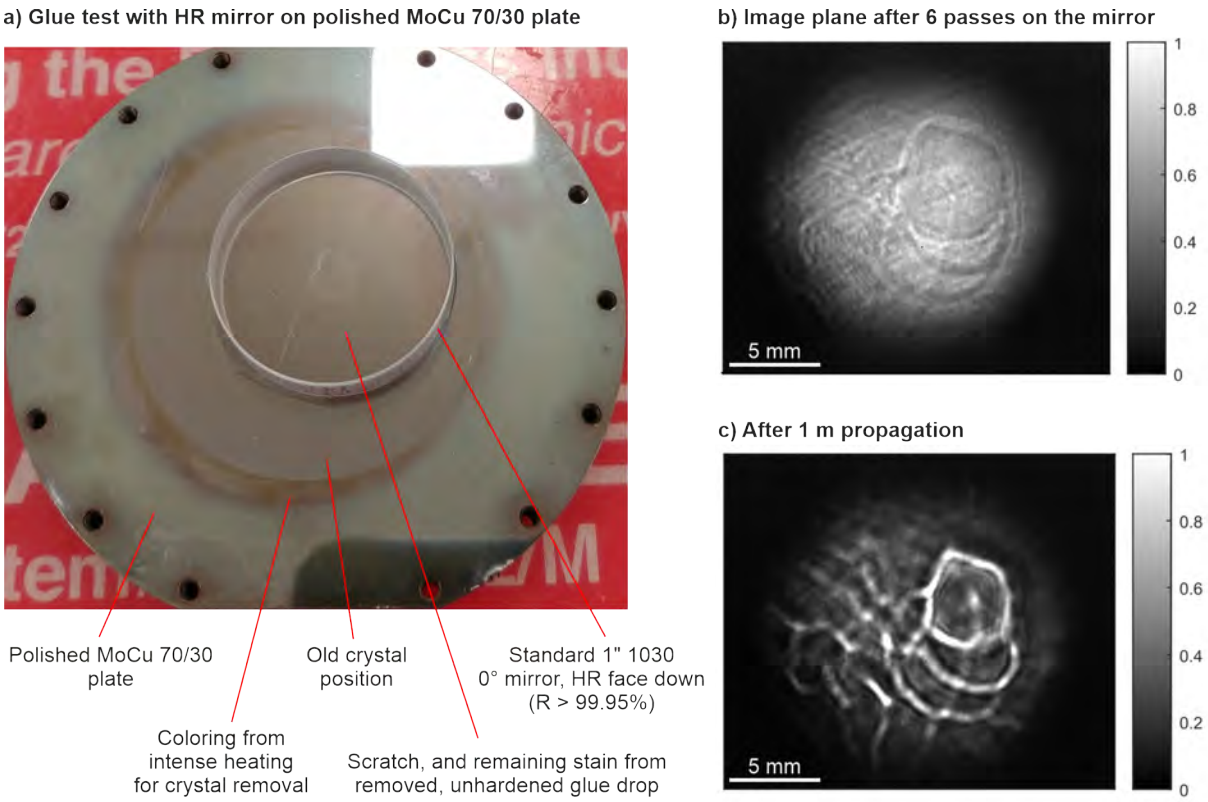

Figure A.1: *Features appearing in the beam profile when gluing a HR 1030 0° test mirror with the coating face down onto a polished and uncoated MoCu 70/30 metal plate that exhibits several imperfections. a) Test mirror glued onto metal plate, with a visible stain from an old, unhardened drop of UV glue that was thoroughly cleaned prior to the actual gluing. b) Beam profile after 6 imaging passes on the test mirror in the image plane and c) beam profile* 1 m *after the image plane, with large features and modulations in the shape of the glue stain.*

This contradiction is also consistent with the influence of the scratch. Although it caused a pit and possibly also an elevation of the surface, no modulation of the beam profile exist that can be clearly attributed to the scratch. The theory of an additional optical effect like the etalon-effect between the HR coating of the crystal and the reflective metal plate could solve this contradiction.

A third gluing trial with the same metal plate was done, but with another test mirror and Epotek OG 142-82 UV glue. This trial showed no features in the beam profile at all, also not several weeks after hardening the glue. Although this can be partially attributed to the lower shrinking ratio of the Epotek glue, the explanation is still not conclusive and further investigations are necessary to exclude e.g. other beneficial properties of the glue or a beneficial setting of the etalon-effect.

More trials with different imperfections on the surface of the metal plate were conducted: a test mirror was glued partially over the edge of the metal plate, the plate was blasted with glas beads, scratches were applied and others. The results were all similar: the Vitralit UV glue caused strong features and modulations in the beam profile immediately after starting the hardening process, while the Epotek UV glue did not show any effect at first.

However, it turned out that this was a misconception and the Epotek glue often only delayed the appearance of features in the beam profile. Figure A.2 shows a trial where a test mirror was glued partially over the edge of a polished metal plate. Before and during the hardening with UV light, no features appeared in the beam profile. After 7 hours a slight shadow evolved in the position of the edge which grew in intensity and sharpness over time. It took more than 72 hours after UV exposure for the process to stop. As a comparison, the datasheet of the Epotek glue states a maximum of 24 hours for the hardening to be finished. At the end of the process, the edge of the metal plate caused severe modulations in the beam profile and also in the wavefront. This was further proven with an interferometer.

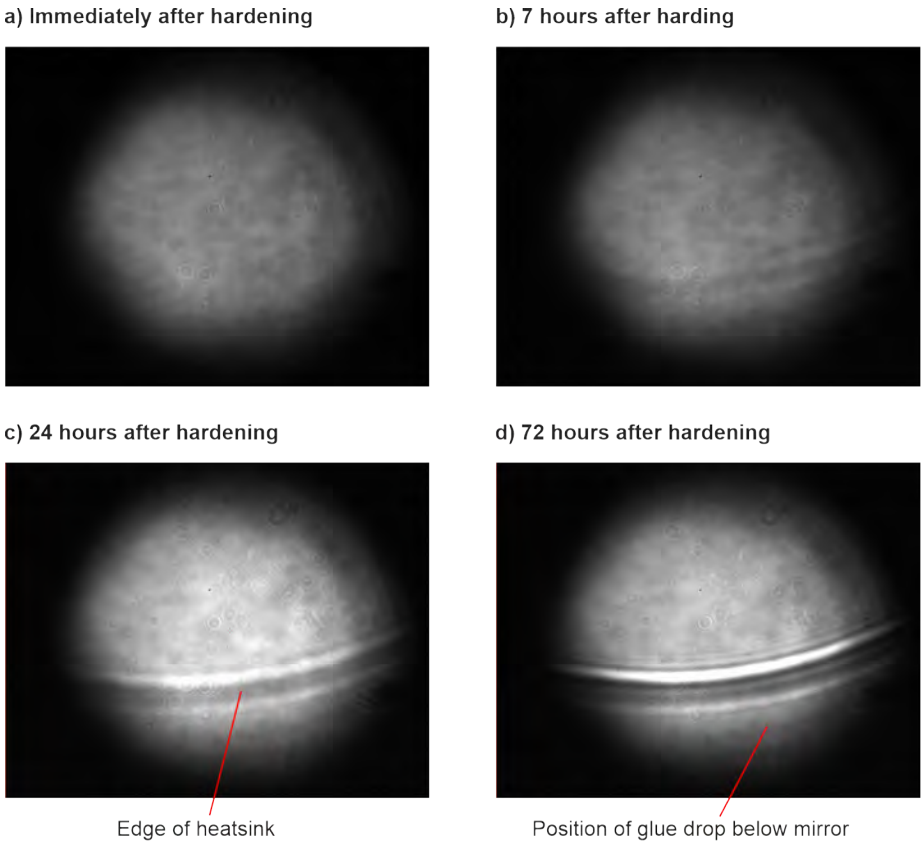

Figure A.2: *Long-term study of a HR 1030 0° test mirror that is glued face down over the edge of a 2" metal plate with Epotek OG 142-82 UV glue. a) to d) Beam profiles in the image plane after 6 imaging passes on the test mirror for different time stamps after hardening of the UV glue, with the edge becoming more visible over time. Note: The different brightness of the beam profiles originates from different settings of the measurements.*

In contrast to the clearly visible edge of the metal plate, an excessive glue drop below the free hanging part of the test mirror in figure A.2 did not cause any feature in the beam profile, even though it should cause a mechanical force due to the shrinking of the glue.

Other trials to resemble the etalon-effect, like different wedge angles of the glue layer, were not successful and did not reproduce all the wavefront and beam profile features which were seen after gluing crystals. This can be explained with the high sensitivity of the etalon-effect to the thickness of the glue layer and the general misalignment. It is therefore important to decouple any influence of the assembly from the investigation. A more promising approach for future activities on this topic is a simulation of the etalon-effect with the help of a software that allows to determine the properties of the HR coating. This could be achieved for example with the OptiLayer software of OptiLayer GmbH.

As a conclusion from all test trials, a clear source of the failures of the gluing method was not found. The contribution of a mechanical effect due to the shrinking of the UV glue is probable, but it does not explain all features that emerged after hardening the glue. Applying Epotek OG 142-82 UV glue instead of Panacol Vitralit 6127 reduces the impact of emerging features in the beam profile but still causes frequent failures of the gluing process. However, the investigation results are still ambiguous. For some trials no features at all were observed for the Epotek glue, even after weeks, whereas with Vitralit significant modulations of the beam profile emerged under the same conditions. Therefore, the next step of future investigations will be a simulation of the etalon-effect which could potentially explain the additional, yet unknown source of emerging features.

Appendix B

Prototype of the 10 J amplifier

The first version of the BigMama was built at MPQ in a 20-pass rotational symmetric 4f-imaging geometry similar to that of The Cube. All optics were scaled by a factor of ~1.5 and the setup allowed to implement two crystals to account for the required increase of the output energy to 10 J.

Although the prototype setup eventually got replaced by the final version with a Type 2 geometry, it provided valuable experimental results:

- The new 8-pass pump geometry was extensively evaluated and improved
- Several iterations of new heatsinks were implemented and evaluated
- All temperature measurements of the Yb:YAG crystals were conducted with this setup
- The impact of ASE was characterized for several crystal thicknesses and pump parameters

The most important result was the first amplification to an output energy of 10 J, see figure B.1 a). The measurement was conducted in a single-shot campaign due to several features in the amplified beam profile and wavefront which caused strong intensity modulations and eventually the breakdown of optics. Two Ø38 × 3 mm, 2 % doped Yb:YAG crystals were implemented in the setup. Each crystal was pumped at 27 kW and 1000 µs. Since the measurement was conducted with single shots, the crystals were at the cooling water temperature of 15 °C. To evaluate the achievable output energy, the input energy was gradually increased with every pump shot.

An output energy of 10 J was achieved at an input energy of 51 mJ. Due to the single-shot operation and the crystal temperature of only 15 °C a stronger saturation than what was simulated in section 8.2 occured. The maximum achievable output energy was mostly limited by the onset of transverse oscillations of ASE which prevented longer pump durations than 1000 µs. A suitable ASE absorber of the heatsink to suppress the impact of ASE was not available at the time of the measurement. The spectrum in figure B.1 b) shows the issue of a strong gain narrowing if two Yb:YAG based amplifiers are cascaded. The initial bandwidth of the regenerative amplifier of 4.2 nm is reduced to 3 nm after the Yb:YAG-based Booster and eventually to 1.8 nm after an amplification to 10 J.

Figure B.2 shows the amplified beam profiles for two different output energies. It also shows the strong modulations in the beam profile which eventually caused a breakdown of one of the crystals as well as several optics within the amplifier at an output energy of 10 J.

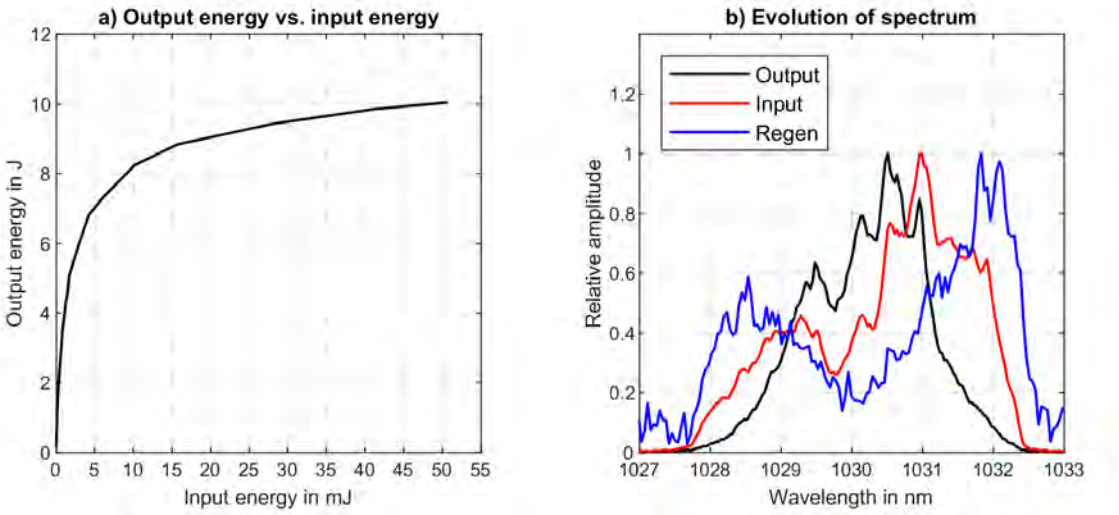

Figure B.1: *First measurement of an output energy of* 10 J *with the BigMama, in a 20-pass 4f-imaging geometry and with two* 3 mm *thick,* 2 % *doped Yb:YAG crystals. The crystals are mounted in MKIII heatsinks without ASE absorbers or index-matching liquids. Each crystal is pumped at* 27 kW*, within a FWHM diameter of* 24.5 mm *and at a pump duration of* 1000 µs*. The cooling water temperature is* 15 °C*. All measurements are taken with single shots due to the certainty of laser induced damages during the measurement. a) Dependency between the output energy and the input energy. An output of* 10 J *is achieved at an input energy of* 51 mJ*, with additional depolarization losses of* 200 mJ*. b) Evolution of the spectrum throughout the pump laser, with a bandwidth of* 4.2 nm *after the regenerative amplifier,* 3 nm *after the Yb:YAG based Booster pre-amplifier and finally* 1.8 nm *at an output energy of* 10 J*.*

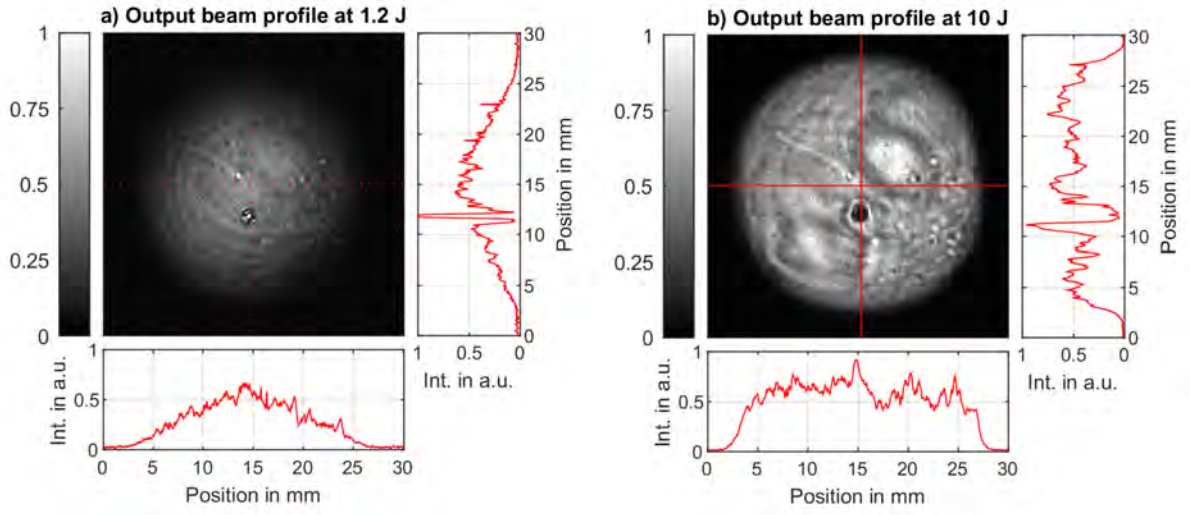

Figure B.2: *Output beam profiles for the* 10 J *measurement shown in the previous figure. Both Yb:YAG crystals are mounted in MKIII heatsinks. a) Output beam profile at an energy of* 1.2 J*. Visible rings and bright spots in the beam profile are caused by issues related the gluing technique of the MKIII heatsink. b) Output beam profile at the maximum energy of* 10 J *showing several laser induced damages. The large black spot is a damage in the HR coating of the crystal and is related to the bright spot in a). The two bright lobes around the black spot are correlated damages of a concave mirror within the amplifier.*

The modulations in the beam profile originated from the crystal-heatsink assemblies and are identical to the ones presented in the troubleshooting of the MKIII heatsink in section 4.4. For the measurement, both crystals were glued onto an MKIII heatsink. Due to the common issues with the gluing technique, several features of the heatsink surface were imprinted into the beam profile. One remaining nickel flake on the surface of one heatsink caused a particularly strong intensity spike in the beam profile which eventually led to a damage of the crystal.

The liquid metal interfaced AMKI heatsink that avoids the beam profile issues of the gluing technique could not be used for the experiments due the mechanical instabilities of the AMKI design. Once the evacuation of the amplifier started, the combined misalignment of both heatsinks caused a severe beam drift that could not be compensated or pre-compensated sufficiently.

Due to these issues, the opto-mechanical design was eventually switched to the final Type 2 geometry that allows to place the two crystals outside of vacuum and therefore to avoid possible misalignments during evacuation. Also, the final MKX heatsink design was developed to further increase the stability and the reliability of the crystal-heatsink assembly while maximizing the achievable quality of the amplified beam profile and wavefront.

Schematic of the opto-mechanical design

The detailed optical assembly of the prototype is presented in figure B.3.

Seed and pump beam paths
The core of the assembly is the rotational symmetric arrangement of 10 4f-imaging telescopes. Each telescope consists of two concave mirrors (CM) with a 1.5” diameter and a focal length of 1000 mm. All mirrors are mounted on fixed rings, also called ”mirror wheels”. Two Ø190 mm folding mirrors (FM) relay the beam to the two image planes of the system. Together with two active-mirror Yb:YAG crystals (Xt), a maximum of 40 amplification passes is achieved.

Both crystals are pumped with the new 8-pass pump geometry that was presented in section 8.3.

Control of ASE and stray light
Several water cooled beam stops are implemented in the system to increase the stability. Beam blocks in front of the large folding mirrors avoid a lasing of the cavity that is formed between the crystals and the folding mirrors. A pinhole plate in the focus plane of the amplifier filters out parasitic reflections and the majority of ASE. Additional beam stops are placed between the pump optics and the mirror wheels to block any stray pump light and thus, to decrease the heat load throughout the amplifier.

Input and output beam manipulation and detection
The input and output beams are separated by a 55° thin film polarizer (TFP). An arbitrary polarization state of the input beam can be created with the combination of a quarter-wave plate (QWP) and a half-wave plate (HWP). This allows for an optimized state of polarization that compensates the depolarization losses inside the amplifier.

Upon exiting the vacuum chamber, the waveplates convert the output beam to a linear polarization that is rotated by 90° relative to that of the input beam which is eventually reflected off the TFP. The remaining depolarization losses are transmitted through the TFP and reflected out of the beam path by a Ø35 mm optical isolator. The depolarization losses are minimized by measuring the energy of this rejected beam and fine adjusting the polarization state of the input beam.

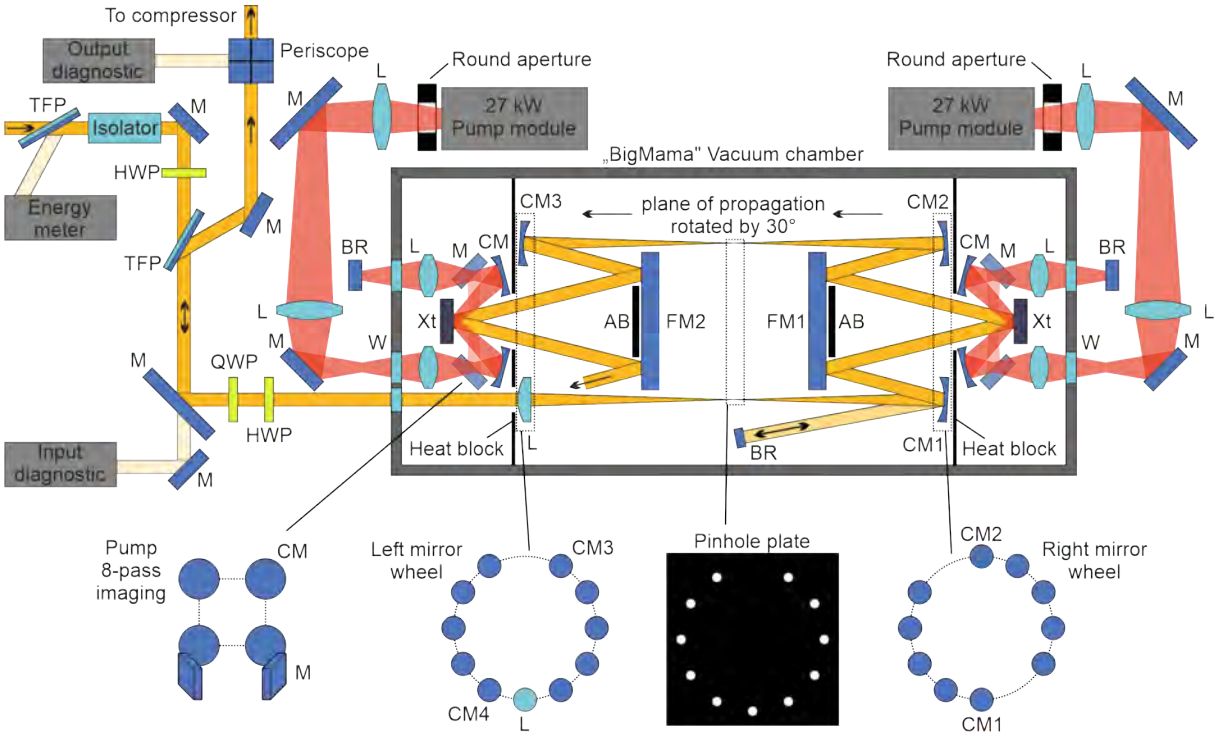

Figure B.3: *Schematic of the prototype of the BigMama. The fundamental geometry is the 20-pass 4f-imaging concept of The Cube amplifier. The input and output beams are divided by a* 55° *thin film polarizer (TFP). A quarter-wave plate (QWP) and a half-wave plate (HWP) generate an elliptical input polarization that counteracts depolarization inside the amplifier. They also cause a* 90° *rotated, linear polarization of the output beam on its way back. Inside the vacuum chamber, all concave mirrors (CM) as well as the input lens (L) are* 1.5" *in diameter with a focal length of* 1000 mm. *They are mounted on two fixed wheels, separated by a pinhole plate that filters out unwanted parasitic reflections and ASE. One active-mirror Yb:YAG crystal (Xt) is placed in each image plane of the amplifier. Both crystals are pumped by an 8-pass 4f-imaging geometry that incorporates four* 3" *concave mirrors with* 150 mm *focal lengths. The seed beam propagates for 5 roundtrips and is reflected back by a mirror (BR) for another 5 roundtrips. The plane of propagation is tilted by* 30° *after each roundtrip. Input and output diagnostics record the beam profiles through leakages of* 45° *mirrors (M). W: Window, AB: ASE block, FM: Folding mirror.*

Mechanical implementation of the prototype

A 3D render of the mechanical implementation of the prototype is shown in figure B.4. The setup consists of two large vacuum chambers, each with an almost identical optical setup inside. The smaller chamber in the center allows access to the focus plane of the amplifier. The total footprint including the pump beam delivery is $\sim 3250 \times 750\,\mathrm{mm}^2$. This does not include the input and output optics, which further increase the overall amplifier length. Since the BigMama is mainly an upscaled version of The Cube, many similarities can be seen. All optics are mounted in massive, reinforced aluminum mounts that can be shifted along alignment rails. All breadboards are mechanically decoupled from the vacuum chamber and screwed directly to the optical table.

A major redevelopment was done for the holders of the large folding mirrors to account for their increased weight of 2.5 kg. In order maximize the mechanical stability the typical spring-loaded kinematic mounts were scrapped and new solid metal-joint mirror mounts were designed and implemented. The metal-joints are optimized for an alignment range of $\pm 2°$, while withstanding the heavy load and avoiding unfavorable resonance frequencies.

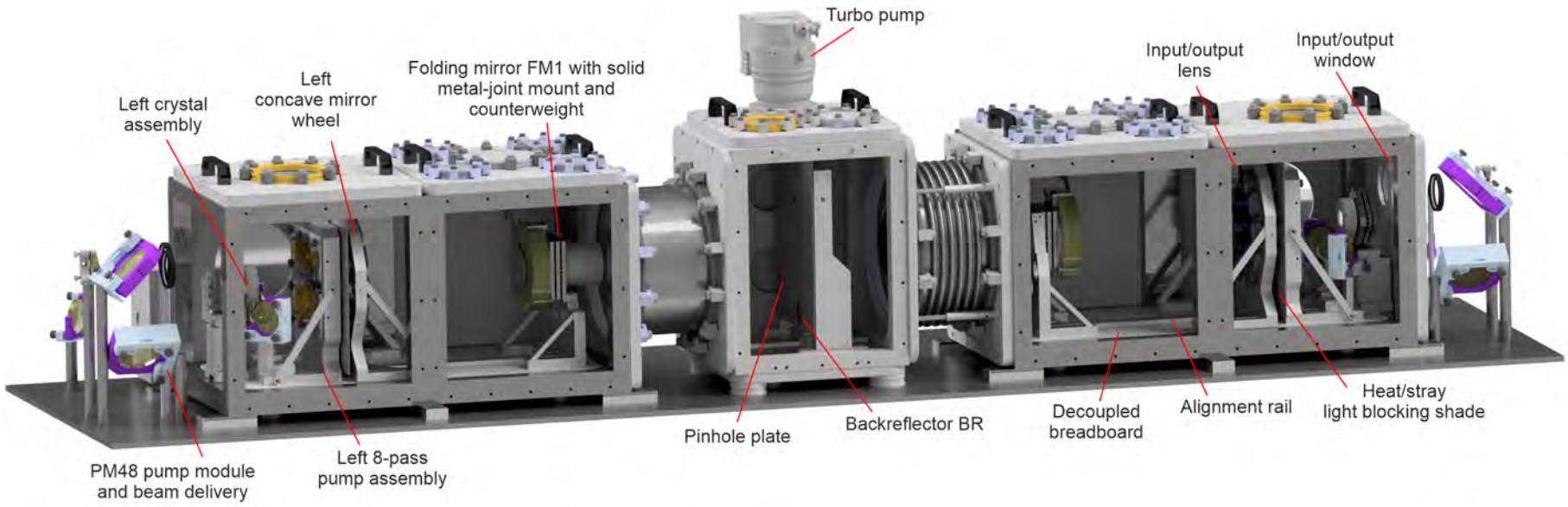

Figure B.4: *Rendered image of the vacuum chamber and complete opto-mechanical assembly of the BigMama prototype, generated with Autodesk Inventor. The overall size including the pump beam delivery is* $\sim 3250 \times 750 \times 500\,\mathrm{mm}^3$*. Additional space is required for the input and output optics, either left or right of the amplifier. The vacuum chamber consists of three sub chambers: two identical ones left and right with the (mirrored) optical setup inside and a "focus chamber" in the center that contains the pinhole plate and the backreflector. Each sub-chamber contains a breadboard that is mechanically decoupled from the chambers and screwed directly to the optical table. All optics are mounted on solid, reinforced aluminum mounts that can be shifted along alignment rails without losing the angular alignment.*

List of acronyms

β	relative material excitation
σ	absorption or emission cross-section
AR	anti-reflective
ASE	amplified spontaneous emission
CAD	computer aided design
CPA	chirped pulse amplification
DKDP	potassium dideuterium phosphate KD_2PO_4
FOD	fourth-order disperion
FROG	frequency-resolved optical gating
FWHM	full width at half maximum
GDD	group delay dispersion
HR	high-reflective
LBO	lithium triborate LiB_3O_5
LIDT	laser induced damage threshold
M_{ASE}	fluorescence lifetime correcting factor for ASE
MoCu 70/30	70 % molybdenum 30 % copper sinter-alloy
MLA	microlens array
OPA	optical parametric amplification
OPCPA	optical parametric chirped pulse amplification
PFS	Petawatt-Field-Synthesizer
SHG	second-harmonic generation
SHHG	high harmonic generation on solid surfaces
TFP	thin-film polarizer
Ti:Sa	titanium doped sapphire $Ti:Al_2O_3$
TOD	third-order dispersion
XPW	cross-polarized wave
Xtal, Xt	crystal
Yb:FP	ytterbium doped fluoride phosphate glas
Yb:CaF_2	ytterbium doped calcium fluoride
Yb:KYW	ytterbium doped potassium yttrium tungstate $Yb^{3+}:KY(WO_4)_2$
Yb:YAG	ytterbium doped yttrium aluminum garnet $Yb^{3+}:Y_3Al_5O_{12}$

Data Preservation

The measured raw data, the data processing files, and the original figure files utilized in this thesis can be reached via the Data Archive Server (DAS) of the Laboratory for Attosecond Physics (LAP) at the Max-Planck-Institut für Quantenoptik (MPQ): `//AFS/ipp-garching.mpg.de/mpq/lap/publication_archive`.

Bibliography

[1] A. L. Schawlow and C. H. Townes, "Infrared and Optical Masers," *Phys. Rev.*, vol. 112, pp. 1940–1949, Dec 1958. doi:10.1103/PhysRev.112.1940.

[2] T. H. MAIMAN, "Stimulated Optical Radiation in Ruby," *Nature*, vol. 187, pp. 493–494, Aug 1960. doi:10.1038/187493a0.

[3] G. H. Miller, E. I. Moses, and C. R. Wuest, "The National Ignition Facility," *Optical Engineering*, vol. 43, no. 12, pp. 2841 – 2853, 2004. doi:10.1117/1.1814767.

[4] D. Du, X. Liu, G. Korn, J. Squier, and G. Mourou, "Laser-induced breakdown by impact ionization in SiO2 with pulse widths from 7 ns to 150 fs," *Applied Physics Letters*, vol. 64, no. 23, pp. 3071–3073, 1994. doi:10.1063/1.111350.

[5] D. Strickland and G. Mourou, "Compression of amplified chirped optical pulses," *Optics Communications*, vol. 56, no. 3, pp. 219–221, 1985. doi:10.1016/0030-4018(85)90120-8.

[6] J. W. Yoon, C. Jeon, J. Shin, S. K. Lee, H. W. Lee, I. W. Choi, H. T. Kim, J. H. Sung, and C. H. Nam, "Achieving the laser intensity of $5.5\text{x}10^{22}$ W/cm^2 with a wavefront-corrected multi-PW laser," *Opt. Express*, vol. 27, pp. 20412–20420, Jul 2019. doi:10.1364/OE.27.020412.

[7] R. Szipöcs, K. Ferencz, C. Spielmann, and F. Krausz, "Chirped multilayer coatings for broadband dispersion control in femtosecond lasers," *Opt. Lett.*, vol. 19, pp. 201–203, Feb 1994. doi:10.1364/OL.19.000201.

[8] A. Wirth, R. Santra, and E. Goulielmakis, "Real time tracing of valence-shell electronic coherences with attosecond transient absorption spectroscopy," *Chemical Physics*, vol. 414, pp. 149–159, 2013. doi:10.1016/j.chemphys.2012.06.003.

[9] U. Morgner, F. X. Kärtner, S. H. Cho, Y. Chen, H. A. Haus, J. G. Fujimoto, E. P. Ippen, V. Scheuer, G. Angelow, and T. Tschudi, "Sub-two-cycle pulses from a Kerr-lens mode-locked Ti:sapphire laser," *Opt. Lett.*, vol. 24, pp. 411–413, Mar 1999. doi10.1364/OL.24.000411.

[10] J. A. Armstrong, N. Bloembergen, J. Ducuing, and P. S. Pershan, "Interactions between Light Waves in a Nonlinear Dielectric," *Phys. Rev.*, vol. 127, pp. 1918–1939, Sep 1962. doi:10.1103/PhysRev.127.1918.

[11] G. Cerullo and S. De Silvestri, "Ultrafast optical parametric amplifiers," *Review of Scientific Instruments*, vol. 74, no. 1, pp. 1–18, 2003. doi:10.1063/1.1523642.

[12] L. Veisz, D. Rivas, G. Marcus, X. Gu, D. Cardenas, J. Xu, J. Mikhailova, A. Buck, T. Wittmann, C. Sears, D. Herrmann, O. Razskazovskaya, V. Pervak, and F. Krausz, "Multi-10-TW sub-5-fs optical parametric synthesizer," in *2014 IEEE Photonics Conference, IPC 2014*, (United States), pp. 510–511, Institute of Electrical and Electronics Engineers Inc., Dec. 2014. doi:10.1109/IPCon.2014.6995473.

[13] S. Karsch, Z. Major, J. Fülöp, I. Ahmad, T.-J. Wang, A. Henig, S. Kruber, R. Weingartner, M. Siebold, J. Hein, C. Wandt, S. Klingebiel, J. Osterhoff, R. Horlein, and F. Krausz, "The Petawatt Field Synthesizer: A new Approach to Ultrahigh Field Generation," in *Advanced Solid-State Photonics*, p. WF1, Optical Society of America, 2008. doi:10.1364/ASSP.2008.WF1.

[14] Z. Major, S. A. Trushin, I. Ahmad, M. Siebold, C. Wandt, S. Klingebiel, T.-J. Wang, J. A. Fülop, A. Henig, S. Kruber, R. Weingartner, A. Popp, J. Osterhoff, R. Hörlein, J. Hein, V. Pervak, A. Apolonski, F. Krausz, and S. Karsch, "Basic Concepts and Current Status of the Petawatt Field Synthesizer - New Approach to Ultrahigh Field Generation," *The Review of Laser Engineering*, vol. 37, no. 6, pp. 431–436, 2009. doi:10.2184/lsj.37.431.

[15] G. D. Tsakiris, K. Eidmann, J. Meyer-Ter-Vehn, and F. Krausz, "Route to intense single attosecond pulses," *New J. Phys.*, vol. 8, 2006. doi:10.1088/1367-2630/8/1/019.

[16] U. Teubner and P. Gibbon, "High-order harmonics from laser-irradiated plasma surfaces," *Rev. Mod. Phys.*, vol. 81, pp. 445–479, Apr 2009. doi:10.1103/RevModPhys.81.445.

[17] E. Goulielmakis, M. Schultze, M. Hofstetter, V. S. Yakovlev, J. Gagnon, M. Uiberacker, A. L. Aquila, E. M. Gullikson, D. T. Attwood, R. Kienberger, F. Krausz, and U. Kleineberg, "Single-Cycle Nonlinear Optics," *Science*, vol. 320, no. 5883, pp. 1614–1617, 2008. doi:10.1126/science.1157846.

[18] A. Kessel, V. E. Leshchenko, O. Jahn, M. Krüger, A. Münzer, A. Schwarz, V. Pervak, M. Trubetskov, S. A. Trushin, F. Krausz, Z. Major, and S. Karsch, "Relativistic few-cycle pulses with high contrast from picosecond-pumped OPCPA," *Optica*, vol. 5, pp. 434–442, Apr 2018. doi:10.1364/OPTICA.5.000434.

[19] O. Jahn, V. E. Leshchenko, P. Tzallas, A. Kessel, M. Krüger, A. Münzer, S. A. Trushin, G. D. Tsakiris, S. Kahaly, D. Kormin, L. Veisz, V. Pervak, F. Krausz, Z. Major, and S. Karsch, "Towards intense isolated attosecond pulses from relativistic surface high harmonics," *Optica*, vol. 6, pp. 280–287, Mar 2019. doi:10.1364/OPTICA.6.000280.

[20] V. E. Leshchenko, A. Kessel, O. Jahn, M. Krüger, A. Münzer, S. A. Trushin, L. Veisz, Z. Major, and S. Karsch, "On-target temporal characterization of optical pulses at relativistic intensity," *Light: Science & Applications*, vol. 8, p. 96, Oct 2019. doi:10.1038/s41377-019-0207-1.

[21] C. Skrobol, "High-Intensity, Picosecond-Pumped, Few-Cycle OPCPA," *PhD thesis, Ludwig-Maximilians-Universität München*, 2014.

[22] A. Kessel, "Generation and Parametric Amplification of Few-Cycle Light Pulses at Relativistic Intensities," *PhD thesis, Ludwig-Maximilians-Universität München*, 2017. doi:10.1007/978-3-319-92843-2.

[23] C. Wandt, "Development of a Joule-class Yb:YAG amplifier and its implementation in a CPA system generating 1TW pulses," *PhD thesis, Ludwig-Maximilians-Universität München*, 2014.

[24] S. Klingebiel, "Picosecond Pump Dispersion Management and Jitter Stabilization in a Petawatt-Scale Few-Cycle OPCPA System," *PhD thesis, Ludwig-Maximilians-Universität München*, 2013.

[25] I. Ahmad, "Development of an optically synchronized seed source for a high-power few-cycle OPCPA system," *PhD thesis, Ludwig-Maximilians-Universität München*, 2011.

[26] S. Klingebiel, C. Wandt, C. Skrobol, I. Ahmad, S. A. Trushin, Z. Major, F. Krausz, and

S. Karsch, "High energy picosecond Yb:YAG CPA system at 10 Hz repetition rate for pumping optical parametric amplifiers," *Opt. Express*, vol. 19, pp. 5357–5363, Mar 2011. doi:10.1364/OE.19.005357.

[27] F. Verluise, V. Laude, Z. Cheng, C. Spielmann, and P. Tournois, "Amplitude and phase control of ultrashort pulses by use of an acousto-optic programmable dispersive filter: pulse compression shaping," *Opt. Lett.*, vol. 25, pp. 575–577, Apr 2000. doi:10.1364/OL.25.000575.

[28] C. Wandt, S. Klingebiel, S. Keppler, M. Hornung, M. Loeser, M. Siebold, C. Skrobol, A. Kessel, S. A. Trushin, Z. Major, J. Hein, M. C. Kaluza, F. Krausz, and S. Karsch, "Development of a Joule-class Yb:YAG amplifier and its implementation in a CPA system generating 1 TW pulses," *Laser & Photonics Reviews*, vol. 8, no. 6, pp. 875–881, 2014. doi:10.1002/lpor.201400040.

[29] E. Treacy, "Optical pulse compression with diffraction gratings," *IEEE Journal of Quantum Electronics*, vol. 5, no. 9, pp. 454–458, 1969. doi:10.1109/JQE.1969.1076303.

[30] D. Ehrt, "Fluoroaluminate glasses for lasers and amplifiers," *Current Opinion in Solid State and Materials Science*, vol. 7, no. 2, pp. 135–141, 2003. doi:10.1016/S1359-0286(03)00049-4.

[31] M. Siebold, J. Hein, C. Wandt, S. Klingebiel, F. Krausz, and S. Karsch, "High-energy, diode-pumped, nanosecond Yb:YAG MOPA system," *Opt. Express*, vol. 16, pp. 3674–3679, Mar 2008. doi:10.1364/OE.16.003674.

[32] C. Wandt, S. Klingebiel, R. Hörlein, I. Ahmad, T.-J. Wang, S. Trushin, Z. Major, M. Siebold, J. Hein, F. Krausz, and S. Karsch, "High-energy, diode-pumped CPA to the Joule-level based on Yb-doped materials," in *Advanced Solid-State Photonics*, p. WA4, Optical Society of America, 2009. doi:10.1364/ASSP.2009.WA4.

[33] D. E. Zelmon, D. L. Small, and R. Page, "Refractive-index measurements of undoped yttrium aluminum garnet from 0.4 to 5.0 μm," *Appl. Opt.*, vol. 37, pp. 4933–4935, Jul 1998. doi:10.1364/AO.37.004933.

[34] X. Mateos, R. Solé, J. Gavaldà, M. Aguiló, J. Massons, and F. Díaz, "Crystal growth, optical and spectroscopic characterisation of monoclinic KY(WO4)2 co-doped with Er3+ and Yb3+," *Optical Materials*, vol. 28, no. 4, pp. 423–431, 2006. doi:10.1016/j.optmat.2004.12.024.

[35] D. S. Sumida and T. Y. Fan, "Effect of radiation trapping on fluorescence lifetime and emission cross section measurements in solid-state laser media," *Opt. Lett.*, vol. 19, pp. 1343–1345, Sep 1994. doi:10.1364/OL.19.001343.

[36] J. Körner, M. Krüger, J. Reiter, A. Münzer, J. Hein, and M. C. Kaluza, "Temperature dependent spectroscopic study of Yb3+-doped KG(WO4)2, KY(WO4)2, YAlO3 and YLiF4 for laser applications," *Opt. Mater. Express*, vol. 10, pp. 2425–2438, Oct 2020. doi:10.1364/OME.398740.

[37] J. Koerner, C. Vorholt, H. Liebetrau, M. Kahle, D. Kloepfel, R. Seifert, J. Hein, and M. C. Kaluza, "Measurement of temperature-dependent absorption and emission spectra of Yb:YAG, Yb:LuAG, and Yb:CaF2 between 20°C and 200°C and predictions on their influence on laser performance," *J. Opt. Soc. Am. B*, vol. 29, pp. 2493–2502, Sep 2012. doi:10.1364/JOSAB.29.002493.

[38] R. L. Aggarwal, D. J. Ripin, J. R. Ochoa, and T. Y. Fan, "Measurement of thermo-optic properties of Y3Al5O12, Lu3Al5O12, YAIO3, LiYF4, LiLuF4, BaY2F8, KGd(WO4)2,

and KY(WO4)2 laser crystals in the 80–300K temperature range," *Journal of Applied Physics*, vol. 98, no. 10, p. 103514, 2005. doi:10.1063/1.2128696.

[39] Y. Sato and T. Taira, "Highly accurate interferometric evaluation of thermal expansion and dn/dT of optical materials," *Opt. Mater. Express*, vol. 4, pp. 876–888, May 2014. doi:10.1364/OME.4.000876.

[40] C. Ltd., "Datasheet Yttrium Aluminium Garnet (YAG)." `https://www.crystran.co.uk/optical-materials/yttrium-aluminium-garnet-yag`. Accessed: 2021.04.27.

[41] P. Loiko, K. Yumashev, N. Kuleshov, G. Rachkovskaya, and A. Pavlyuk, "Detailed characterization of thermal expansion tensor in monoclinic KRe(WO4)2 (where Re=Gd, Y, Lu, Yb)," *Optical Materials*, vol. 34, no. 1, pp. 23–26, 2011. doi:10.1016/j.optmat.2011.07.007.

[42] P. A. Loiko, K. V. Yumashev, N. V. Kuleshov, and A. A. Pavlyuk, "Thermo-optical properties of pure and Yb-doped monoclinic KY(WO4)2 crystals," *Applied Physics B*, vol. 106, pp. 663–668, Mar 2012. doi:10.1007/s00340-011-4749-z.

[43] K. Yumashev and P. Loiko, "Thermal stress and end-bulging in monoclinic crystals: the case study of double tungstates," *Appl. Opt.*, vol. 56, pp. 3857–3866, May 2017. doi:10.1364/AO.56.003857.

[44] W. Koechner, *Solid-State Laser Engineering*. Springer Series in Optical Sciences, Springer, 2006. doi:10.1007/0-387-29338-8.

[45] A. Brenier, Y. Guyot, H. Canibano, G. Boulon, A. Ródenas, D. Jaque, A. Eganyan, and A. G. Petrosyan, "Growth, spectroscopic, and laser properties of Yb3+-doped Lu3Al5O12 garnet crystal," *J. Opt. Soc. Am. B*, vol. 23, pp. 676–683, Apr 2006. doi:10.1364/JOSAB.23.000676.

[46] P. Lacovara, H. K. Choi, C. A. Wang, R. L. Aggarwal, and T. Y. Fan, "Room-temperature diode-pumped Yb:YAG laser," *Opt. Lett.*, vol. 16, pp. 1089–1091, Jul 1991. doi:10.1364/OL.16.001089.

[47] J. Körner, *Effizienzsteigerung Yb3+ basierter Kurzpuls-Laserverstärker*. Sierke, 2014.

[48] J. Körner, "Laser Engineering, Lecture notes WS 2019/2020, Friedrich-Schiller-Universität Jena," 2020. Accessed: 2021-04-27.

[49] G. L. Bourdet, "Comparison of pulse amplification performances in longitudinally pumped Ytterbium doped materials," *Optics Communications*, vol. 200, no. 1, pp. 331–342, 2001. doi:10.1016/S0030-4018(01)01622-4.

[50] L. M. Frantz and J. S. Nodvik, "Theory of Pulse Propagation in a Laser Amplifier," *Journal of Applied Physics*, vol. 34, no. 8, pp. 2346–2349, 1963. doi:10.1063/1.1702744.

[51] D. Albach, *Amplified Spontaneous Emission and Thermal Management on a High Average Power Diode Pumped Solid State Laser – The Lucia Laser System*. Theses, Ecole Polytechnique X, Apr. 2010. HAL ID: tel-00504915.

[52] L. Allen and G. Peters, "Amplified spontaneous emission III. Intensity and saturation," *Journal of Physics A*, vol. 4, no. 4, p. 564, 1971. doi:10.1088/0305-4470/4/4/020.

[53] G. J. Linford, E. R. Peressini, W. R. Sooy, and M. L. Spaeth, "Very Long Lasers," *Appl. Opt.*, vol. 13, pp. 379–390, Feb 1974. doi:10.1364/AO.13.000379.

[54] K. Ertel, C. Hooker, S. J. Hawkes, B. T. Parry, and J. L. Collier, "ASE suppression in a high energy Titanium sapphire amplifier," *Opt. Express*, vol. 16, pp. 8039–8049, May

2008. doi:10.1364/OE.16.008039.

[55] J. Speiser, "Scaling of thin-disk lasers—influence of amplified spontaneous emission," *J. Opt. Soc. Am. B*, vol. 26, pp. 26–35, Jan 2009. doi:10.1364/JOSAB.26.000026.

[56] D. Albach, J.-C. Chanteloup, and G. le Touzé, "Influence of ASE on the gain distribution in large size, high gain Yb3+:YAG slabs," *Opt. Express*, vol. 17, pp. 3792–3801, Mar 2009. doi:10.1364/OE.17.003792.

[57] E. Esarey, C. B. Schroeder, and W. P. Leemans, "Physics of laser-driven plasma-based electron accelerators," *Rev. Mod. Phys.*, vol. 81, pp. 1229–1285, Aug 2009. doi:10.1103/RevModPhys.81.1229.

[58] A. Macchi, M. Borghesi, and M. Passoni, "Ion acceleration by superintense laser-plasma interaction," *Rev. Mod. Phys.*, vol. 85, pp. 751–793, May 2013. doi:10.1103/RevModPhys.85.751.

[59] S. Keppler, A. Sävert, J. Körner, M. Hornung, H. Liebetrau, J. Hein, and M. C. Kaluza, "The generation of amplified spontaneous emission in high-power CPA laser systems," *Laser & Photonics Reviews*, vol. 10, no. 2, pp. 264–277, 2016. doi:10.1002/lpor.201500186.

[60] D. Albach, J.-C. Chanteloup, and G. le Touzé, "Influence of ASE on the gain distribution in large size, high gain Yb3+:YAG slabs," *Opt. Express*, vol. 17, pp. 3792–3801, Mar 2009. doi:10.1364/OE.17.003792.

[61] HASEonGPU, "High performance Amplified Spontaneous Emission on GPU." `https://github.com/ComputationalRadiationPhysics/haseongpu`. Accessed: 2021.04.27.

[62] S. Guch, "Parasitic suppression in large aperture disk lasers employing liquid edge claddings," *Appl. Opt.*, vol. 15, pp. 1453–1457, Jun 1976. doi:10.1364/AO.15.001453.

[63] K. Ertel, C. Hooker, S. J. Hawkes, B. T. Parry, and J. L. Collier, "ASE suppression in a high energy Titanium sapphire amplifier," *Opt. Express*, vol. 16, pp. 8039–8049, May 2008. doi:10.1364/OE.16.008039.

[64] A. Ikesue and Y. L. Aung, "Synthesis and Performance of Advanced Ceramic Lasers," *Journal of the American Ceramic Society*, vol. 89, no. 6, pp. 1936–1944, 2006. doi:10.1111/j.1551-2916.2006.01043.x.

[65] H. Yagi, J. Bisson, K. Ueda, and T. Yanagitani, "Y3Al5O12 ceramic absorbers for the suppression of parasitic oscillation in high-power Nd:YAG lasers," *Journal of Luminescence*, vol. 121, no. 1, pp. 88–94, 2006. doi:10.1016/j.jlumin.2005.10.006.

[66] A. Ikesue and Y. L. Aung, "Ceramic laser materials," *Nature Photonics*, vol. 2, pp. 721–727, Dec 2008. doi:10.1038/nphoton.2008.243.

[67] D. Albach and J.-C. Chanteloup, "Large size crystalline vs. co-sintered ceramic Yb3+:YAG disk performance in diode pumped amplifiers," *Opt. Express*, vol. 23, pp. 570–579, Jan 2015. doi:10.1364/OE.23.000570.

[68] M. Divoky, J. Pilar, M. Hanus, P. Navratil, M. Sawicka-Chyla, M. D. Vido, P. J. Phillips, K. Ertel, T. Butcher, M. Fibrich, J. T. Green, M. Koselja, J. Preclikova, J. Kubat, J. Houzvicka, B. Rus, J. Collier, A. Lucianetti, and T. Mocek, "Performance comparison of Yb:YAG ceramics and crystal gain material in a large-area, high-energy, high-average power diode-pumped laser," *Opt. Express*, vol. 28, pp. 3636–3646, Feb 2020. doi:10.1364/OE.379713.

[69] D. Kouznetsov and J.-F. Bisson, "Role of undoped cap in the scaling of thin-disk lasers," *J. Opt. Soc. Am. B*, vol. 25, pp. 338–345, Mar 2008. doi:10.1364/JOSAB.25.000338.

[70] L. E. Zapata, H. Lin, A.-L. Calendron, H. Cankaya, M. Hemmer, F. Reichert, W. R. Huang, E. Granados, K.-H. Hong, and F. X. Kärtner, "Cryogenic Yb:YAG composite-thin-disk for high energy and average power amplifiers," *Opt. Lett.*, vol. 40, pp. 2610–2613, Jun 2015. doi:10.1364/OL.40.002610.

[71] D. Albach, G. LeTouzé, and J.-C. Chanteloup, "Deformation of partially pumped active mirrors for high average–power diode–pumped solid–state lasers," *Opt. Express*, vol. 19, pp. 8413–8422, Apr 2011. doi:10.1364/OE.19.008413.

[72] O. Antipov, O. Eremeykin, A. Savikin, V. Vorob'ev, D. Bredikhin, and M. Kuznetsov, "Electronic changes of refractive index in intensively pumped Nd:YAG laser crystals," *IEEE Journal of Quantum Electronics*, vol. 39, no. 7, pp. 910–918, 2003. doi:10.1109/JQE.2003.813188.

[73] O. L. Antipov, D. V. Bredikhin, O. N. Eremeykin, A. P. Savikin, E. V. Ivakin, and A. V. Sukhadolau, "Electronic mechanism for refractive-index changes in intensively pumped Yb:YAG laser crystals," *Opt. Lett.*, vol. 31, pp. 763–765, Mar 2006. doi:10.1364/OL.31.000763.

[74] S. Chénais, F. Druon, S. Forget, F. Balembois, and P. Georges, "On thermal effects in solid-state lasers: The case of ytterbium-doped materials," *Progress in Quantum Electronics*, vol. 30, no. 4, pp. 89–153, 2006. doi:10.1016/j.pquantelec.2006.12.001.

[75] J. F. Nye, *Physical Properties of Crystals*. Clarendon Press — Oxford, 1985. doi:10.1002/crat.2170211204.

[76] W. Koechner and D. Rice, "Effect of birefringence on the performance of linearly polarized YAG:Nd lasers," *IEEE Journal of Quantum Electronics*, vol. 6, no. 9, pp. 557–566, 1970. doi:10.1109/JQE.1970.1076529.

[77] M. SWIRKOWICZ, A. BAJOR, E. Tymicki, and B. KACZMAREK, "Investigation of structural, optical and lasing properties of YAG:Yb single crystals," *Opto-electronics Review*, vol. 13, 01 2005.

[78] M. Koželja, B. Rus, J. Kubát, and J. Houžvička, "Core Free Yb:YAG Crystals for High Power Laser Systems," in *Laser Ignition Conference*, p. T4A.4, Optical Society of America, 2015. doi:10.1364/LIC.2015.T4A.4.

[79] Y. Chen, B. Chen, M. Patel, and M. Bass, "Calculation of thermal-gradient-induced stress birefringence in slab Lasers-I," *IEEE Journal of Quantum Electronics*, vol. 40, no. 7, pp. 909–916, 2004. doi:10.1109/JQE.2004.830188.

[80] O. Puncken, H. Tünnermann, J. J. Morehead, P. Weßels, M. Frede, J. Neumann, and D. Kracht, "Intrinsic reduction of the depolarization in Nd:YAG crystals," *Opt. Express*, vol. 18, pp. 20461–20474, Sep 2010. doi:10.1364/OE.18.020461.

[81] I. Shoji and T. Taira, "Intrinsic reduction of the depolarization loss in solid-state lasers by use of a (110)-cut Y3Al5O12 crystal," *Applied Physics Letters*, vol. 80, no. 17, pp. 3048–3050, 2002. doi:10.1063/1.1475365.

[82] W. A. Clarkson, N. S. Felgate, and D. C. Hanna, "Simple method for reducing the depolarization loss resulting from thermally induced birefringence in solid-state lasers," *Opt. Lett.*, vol. 24, pp. 820–822, Jun 1999. doi:10.1364/OL.24.000820.

[83] R. Kandasamy, M. Yamanaka, Y. Izawa, and S. Nakai, "Analysis of Birefringence Com-

pensation Using a Quarter-Wave Plate in Solid-State Lasers," *Optical Review*, vol. 7, pp. 149–151, Mar 2000. doi:10.1007/s10043-000-0149-z.

[84] R. Fluck, M. R. Hermann, and L. A. Hackel, "Birefringence compensation in single solid-state rods," *Applied Physics Letters*, vol. 76, no. 12, pp. 1513–1515, 2000. doi:10.1063/1.126080.

[85] M. Krüger, R. Kampmann, R. Kleindienst, and S. Sinzinger, "Time-resolved combination of the Mueller-Stokes and Jones calculus for the optimization of a twisted-nematic spatial-light modulator," *Appl. Opt.*, vol. 54, pp. 4239–4248, May 2015. doi:10.1364/AO.54.004239.

[86] Q. Lü, N. Kugler, H. Weber, S. Dong, N. Müller, and U. Wittrock, "A novel approach for compensation of birefringence in cylindrical Nd: YAG rods," *Optical and Quantum Electronics*, vol. 28, pp. 57–69, Jan 1996. doi:10.1007/BF00578551.

[87] T. Bürer and L. Katzin, "Dipole strengths and rotational strengths from dispersion for quartz," *Journal of Inorganic and Nuclear Chemistry*, vol. 29, no. 11, pp. 2715–2722, 1967. doi:10.1016/0022-1902(67)80009-5.

[88] M. D. Vido, K. Ertel, A. Wojtusiak, P. D. Mason, P. J. Phillips, S. Banerjee, J. M. Smith, T. J. Butcher, and C. Edwards, "Optical rotatory power of quartz between 77 K and 325 K for 1030 nm wavelength," *Opt. Mater. Express*, vol. 9, pp. 2708–2715, Jun 2019. doi:10.1364/OME.9.002708.

[89] T. Nubbemeyer, M. Kaumanns, M. Ueffing, M. Gorjan, A. Alismail, H. Fattahi, J. Brons, O. Pronin, H. G. Barros, Z. Major, T. Metzger, D. Sutter, and F. Krausz, "1 kW, 200 mJ picosecond thin-disk laser system," *Opt. Lett.*, vol. 42, pp. 1381–1384, Apr 2017. doi:10.1364/OL.42.001381.

[90] J. Novák, J. T. Green, T. Metzger, T. Mazanec, B. Himmel, M. Horáček, Z. Hubka, R. Boge, R. Antipenkov, F. Batysta, J. A. Naylon, P. Bakule, and B. Rus, "Thin disk amplifier-based 40 mJ, 1 kHz, picosecond laser at 515 nm," *Opt. Express*, vol. 24, pp. 5728–5733, Mar 2016. doi:10.1364/OE.24.005728.

[91] J. Körner, S. Zulić, D. Rostohar, A. Lucianetti, and T. Mocek, "Novel unstable resonator configuration for highly efficient cryogenically cooled Yb:YAG Q-switched laser," *Opt. Express*, vol. 27, pp. 21622–21634, Jul 2019. doi:10.1364/OE.27.021622.

[92] J. W. Goodman, *Introduction to Fourier Optics, 2nd Edition*. Stanford, McGraw-Hill, 1996.

[93] D. Albach, M. Loeser, M. Siebold, and U. Schramm, "Performance demonstration of the PEnELOPE main amplifier HEPA I using broadband nanosecond pulses," *High Power Laser Science and Engineering*, vol. 7, p. e1, 2019. doi:10.1017/hpl.2018.59.

[94] S. Keppler, C. Wandt, M. Hornung, R. Bödefeld, A. Kessler, A. Sävert, M. Hellwing, F. Schorcht, J. Hein, and M. C. Kaluza, "Multipass amplifiers of POLARIS," in *High-Power, High-Energy, and High-Intensity Laser Technology; and Research Using Extreme Light: Entering New Frontiers with Petawatt-Class Lasers* (G. Korn, L. O. Silva, and J. Hein, eds.), vol. 8780, pp. 96 – 101, International Society for Optics and Photonics, SPIE, 2013. doi:10.1117/12.2019248.

[95] J. Körner, J. Hein, and M. C. Kaluza, "Compact Aberration-Free Relay-Imaging Multi-Pass Layouts for High-Energy Laser Amplifiers," *Applied Sciences*, vol. 6, no. 11, 2016. doi:10.3390/app6110353.

[96] T. Gonçalvès-Novo, D. Albach, B. Vincent, M. Arzakantsyan, and J.-C. Chanteloup, "14

J / 2 Hz Yb^{3+}:YAG diode pumped solid state laser chain," *Opt. Express*, vol. 21, no. 1, pp. 855–866, 2013. doi:10.1364/OE.21.000855.

[97] A. Bayramian, P. Armstrong, E. Ault, R. Beach, C. Bibeau, J. Caird, R. Campbell, B. Chai, J. Dawson, C. Ebbers, A. Erlandson, Y. Fei, B. Freitas, R. Kent, Z. Liao, T. Ladran, J. Menapace, B. Molander, S. Payne, N. Peterson, M. Randles, K. Schaffers, S. Sutton, J. Tassano, S. Telford, and E. Utterback, "The Mercury Project: A High Average Power, Gas-Cooled Laser for Inertial Fusion Energy Development," *Fusion Science and Technology*, vol. 52, no. 3, pp. 383–387, 2007. doi:10.13182/FST07-A1517.

[98] K. Ertel, S. Banerjee, P. D. Mason, P. J. Phillips, M. Siebold, C. Hernandez-Gomez, and J. C. Collier, "Optimising the efficiency of pulsed diode pumped Yb:YAG laser amplifiers for ns pulse generation.," *Opt. Express*, vol. 19, pp. 26610–26626, Dec 2011. doi:10.1364/OE.19.026610.

[99] S. Banerjee, K. Ertel, P. D. Mason, P. J. Phillips, M. D. Vido, J. M. Smith, T. J. Butcher, C. Hernandez-Gomez, R. J. S. Greenhalgh, and J. L. Collier, "DiPOLE: a 10 J, 10 Hz cryogenic gas cooled multi-slab nanosecond Yb:YAG laser," *Opt. Express*, vol. 23, pp. 19542–19551, Jul 2015. doi:10.1364/OE.23.019542.

[100] M. Divoky, S. Tokita, S. Hwang, T. Kawashima, H. Kan, A. Lucianetti, T. Mocek, and J. Kawanaka, "1-J operation of monolithic composite ceramics with Yb:YAG thin layers: multi-TRAM at 10-Hz repetition rate and prospects for 100-Hz operation," *Opt. Lett.*, vol. 40, pp. 855–858, Mar 2015. doi:10.1364/OL.40.000855.

[101] A. Dobosz, T. Daeneke, A. Zavabeti, B. Y. Zhang, R. Orrell-Trigg, K. Kalantar-Zadeh, A. Wójcik, W. Maziarz, and T. Gancarz, "Investigation of the Surface of Ga–Sn–Zn Eutectic Alloy by the Characterisation of Oxide Nanofilms Obtained by the Touch-Printing Method," *Nanomaterials*, vol. 9, no. 2, 2019. doi:10.3390/nano9020235.

[102] M. Zimmermann, N. Lindlein, R. Voelkel, and K. J. Weible, "Microlens laser beam homogenizer: from theory to application," in *Laser Beam Shaping VIII* (F. M. Dickey and D. L. Shealy, eds.), vol. 6663, pp. 9 – 21, International Society for Optics and Photonics, SPIE, 2007. doi:10.1117/12.731391.

[103] M. Hornung, H. Liebetrau, S. Keppler, A. Kessler, M. Hellwing, F. Schorcht, G. A. Becker, M. Reuter, J. Polz, J. Körner, J. Hein, and M. C. Kaluza, "54 J pulses with 18 nm bandwidth from a diode pumped chirped pulse amplification laser system," *Opt. Lett.*, vol. 41, pp. 5413–5416, Nov 2016. doi:10.1364/OL.41.005413.

[104] R. Trebino, K. W. DeLong, D. N. Fittinghoff, J. N. Sweetser, M. A. Krumbügel, B. A. Richman, and D. J. Kane, "Measuring ultrashort laser pulses in the time-frequency domain using frequency-resolved optical gating," *Review of Scientific Instruments*, vol. 68, no. 9, pp. 3277–3295, 1997. doi:10.1063/1.1148286.

[105] V. E. Leshchenko, "Slava-FROG reconstruction." `https://github.com/leschenkos/Slava-FROG`. Accessed: 2021.04.27.

[106] N. Didenko, A. Konyashchenko, A. Lutsenko, and S. Tenyakov, "Contrast degradation in a chirped-pulse amplifier due to generation of prepulses by postpulses," *Opt. Express*, vol. 16, pp. 3178–3190, Mar 2008. doi:10.1364/OE.16.003178.

[107] D. Blázquez-Sánchez, B. Weichelt, A. Austerschulte, A. Voss, T. Graf, A. Killi, H.-C. Eckstein, M. Stumpf, A. L. Matthes, and U. D. Zeitner, "Improving the brightness of a multi-kilowatt single thin-disk laser by an aspherical phase front correction," *Opt. Lett.*, vol. 36, pp. 799–801, Mar 2011. doi:10.1364/OL.36.000799.

[108] S. Piehler, B. Weichelt, A. Voss, M. A. Ahmed, and T. Graf, "Power scaling of fundamental-mode thin-disk lasers using intracavity deformable mirrors," *Opt. Lett.*, vol. 37, pp. 5033–5035, Dec 2012. doi:10.1364/OL.37.005033.

[109] K. Khrennikov, J. Wenz, A. Buck, J. Xu, M. Heigoldt, L. Veisz, and S. Karsch, "Tunable All-Optical Quasimonochromatic Thomson X-Ray Source in the Nonlinear Regime," *Phys. Rev. Lett.*, vol. 114, p. 195003, May 2015. doi:10.1103/PhysRevLett.114.195003.

[110] J. A. Fülöp, L. Pálfalvi, G. Almási, and J. Hebling, "High Energy THz Pulse Generation by Tilted Pulse Front Excitation and Its Nonlinear Optical Applications," *Journal of Infrared, Millimeter, and Terahertz Waves*, vol. 32, pp. 553–561, May 2011. doi:10.1007/s10762-010-9667-3.

Acknowledgments

At the end of this thesis, I would like to thank a few, particularly important people that were involved in creating it.

First of all, I cannot express enough gratitude to my co-workers of the MPQ workshop and their remarkable skills. I will not name any, because I don't want to miss any. Beyond doubt, the development of the PFS pump laser and PFS in general would have been much less successful without the workshop and especially, it would have taken significantly longer. I highly enjoyed the many technical discussions and particularly the opportunity to gain invaluable firsthand knowledge of how all the mechanical components were manufactured. This was a tremendous help for improving my machine engineering skills and for optimizing all of my designs. Besides, I always felt welcome by everyone and I personally enjoyed every single visit, including some off duty beers with refreshing, non-physics related chats!

Similar to that, I would like to express my gratitude to the purchasing department and the technical staff of MPQ and CALA who helped in building the PFS system and maintaining it. A special thanks to Martin Triphahn who I consider more as a part of the PFS team than of the technical staff because of all the invaluable help and joyful moments in and outside of the laboratory over the years!

Many thanks to Jörg Körner for all the fruitful conversations, the help with Yb:KYW and the optical systems, and especially for the permission to use and improve the V4 simulation tool. The cooperation showed me that it is indispensable for the progress and success of any project to cooperate with external people that have different views and skills!

I would like to thank all the people of the HEC:DPSSL community. The workshops were clearly some of the most memorable moments during this thesis. They gave me the opportunity to connect to so many different people and to learn firsthand knowledge about building and troubleshooting state-of-the-art, high energy lasers, which can hardly be found in any literature. This helped me to quickly catch up in the field of laser development and in particular, to improve the PFS pump laser over the years. I highly enjoyed every single workshop. Frankly speaking, the people that were involved and the way the workshops were organized around building the community really sets my personal bar for future, scientific conferences.

A special thank you to my former professor and head of the department "Technische Optik" at the TU Ilmenau, Prof. Dr. Stefan Sinzinger, for encouraging me to leave my comfort zone and to take the job offer at MPQ, despite losing a (hopefully) valuable member of the department. In hindsight I also want to say that studying "Optronik" at the TU Ilmenau for my bachelor's and master's degree was the perfect choice and an invaluable help for this thesis since I gained exactly the broad knowledge of physics, machine engineering and optical engineering that is required to develop and advance state-of-the-art lasers.

Thanks a lot to Gaia Barbiero for tirelessly deciphering the first drafts of this thesis and canceling out all those colloquial terms.

Many thanks also to Vyacheslav Leshchenko for the help with the FROG retrieval and the contrast measurements, and for conducting important measurements which I otherwise would have forgotten but which nicely add to the content of this thesis.

And last, of course, my gratitude to the entire team of the PFS project under the supervision of Prof. Dr. Stefan Karsch and Dr. Zsuzsanna Slattery-Major: Olga Jahn, Alexander Kessel, Vyacheslav Leshchenko, Andreas Münzer, Alexander Schwarz, Christoph Skrobol and Sergei Trushin. It was a highly joyful and fruitful time in and, most importantly, also outside of the laboratory. In particular a big thanks to Andreas Münzer for developing and building the PFS pump laser together with me over the years, and for all the memorable and fun moments.